AEROSOL INDIRECT EFFECTS IN A COUPLED GLOBAL AEROSOL AND ATMOSPHERIC CIRCULATION MODEL

by

Minghuai Wang

A dissertation submitted in partial fulfillment
of the requirements for the degree of
Doctor of Philosophy
(Atmospheric and Space Sciences)
in The University of Michigan
2009

Doctoral Committee:

Professor Joyce E. Penner, Chair
Professor Richard B. Rood
Associate Professor Christopher J. Poulsen
Assistant Professor Xianglei Huang

ACKNOWLEDGEMENTS

This dissertation could not be written without many people's help. The first person I would like to thank is my academic advisor Prof. Joyce E. Penner. Her broad knowledge and sharp vision in the field help me to define my research questions, and her scientific excitement and her patience encourages me to finally finish my research. Her scientific attitude will be a great beneficial to me in my future career.

I would also like to thank Dr. Xiaohong Liu and his wife for their many helps during past several years. They help me substantially not only on my research but also on many aspects of my life.

I would also like to say thank you to Dr. Leon Rotstayn. It was a great experience to have collaboration with Dr. Rotstayn in the early years of my PhD study, and I learned a lot from him about how to conduct research.

It is great experience to work with so many wonderful people in our group here: Sandy, Michael, Akinori, Natalia, Sophia, Yan, Christiane, Huan, Yang, Li, Xi, Yuxing, Erica, Guangxin, Roy. I am very grateful to Roy for his many coding work, which save me a lot of time and help me focus more on scientific questions.

Finally, special thanks to my family. Thank my wife for her trust, and for her patience, and for her sacrifice in past several years and for her taking care of our new born son in last nine months. This dissertation can not be done without her. Thank my parents for

their loves. They raised me and educated me and I own them everything I have. Thank my mom for coming to States to take care of my son in last four months so that I can have time to write my dissertation.

TABLE OF CONTENTS

ACKNOWLEDGEMENTS ……..ii

LIST OF FIGURES ……..vii

LIST OF TABLES……xiii

ABSTRACT……xv

CHAPTER

I. INTRODUCTION 1

1.1 The climate system and our changing climate 1
1.2 Climate forcing and climate sensitivity 5
1.3 Atmospheric aerosols and their climate effects 8
1.4 Aerosol indirect effects 11
1.5 Modeling aerosol indirect effects in global climate models 13
1.6 Overview of the dissertation 16

II. THE COUPLED IMPACT AEROSOL AND NCAR CAM3 MODEL: EVAULATION OF PREDICTED AEORSOL NUMBER AND SIZE DISTRIBUTION ……23

2.1 Introduction 23
2.2 Model description 25
2.2.1 LLNL IMPACT aerosol model 26
2.2.2 NCAR CAM3 29
2.2.3 Emission data 30
2.3 Sensitivity tests 32
2.3.1 Primary emission of sulfate particles to represent sub-grid scale nucleation……..33
2.3.2 Boundary layer nucleation 35
2.3.3 Three-mode representation for sulfate aerosol 39
2.4 Model results 41
2.4.1 Annual and global budgets 41
2.4.2 Global and vertical distributions 47

2.5 Comparison with observations: aerosol mass 52
2.5.1 Surface observations 52
2.5.2 Vertical Profiles 62
2.6 Comparison with observations: aerosol number and size distribution……....65
2.6.1 Aerosol size distributrion.....65
2.6.2 Vertical profile of aerosol number concentration 72
2.7 Sensitivity of aerosol size and number to model formulation 75
2.7.1 Primary emission of sulfate particles.....76
2.7.2 Boundary layer nucleation 77
2.7.3 Three-mode representation for sulfate aerosol 80
2.8 Summary and discussion.....84
Appendix 2.A Coupling of LLNL/Umich IMPACT and NCAR CAM3 model……..88
Appendix 2.B Simulated aerosol size distribution and number concentration……..91

III. AEROSOL INDIRECT FORCING IN A GLOBAL MODEL WITH PARTICLE NUCLEATION……93

3.1 Introduction.....94
3.2 Methods.....95
3.2.1 The coupled IMPACT/CAM model 99
3.2.2 Nucleation mechanisms 101
3.2.3 Primary-emitted sulfate particles 103
3.2.4 Calculation of cloud droplet number and the first indirect forcing……..104
3.2.5 Overview of the model experiments 108
3.3 Global aerosol mass budgets in PD and PI simulations.....110
3.4 Present day CCN concentration 111
3.5 Anthropogenic contribution to CCN concentrations 118
3.6 Cloud droplet number concentration and the first aerosol indirect forcing……..126
3.7 Summary and discussion.....134

IV. CIRRUS CLOUDS IN A GLOBAL CLIMATE MODEL WITH A STATISTICAL CIRRUS CLOUD SCHEME……140

4.1 Introduction.....140
4.2 Model descriptions and set-up of simulations 148
4.2.1 The IMPACT aerosol model……...148
4.2.2 NCAR CAM3……149
4.2.3 Set-up of simulations and experimental design……..165
4.3 Model results in the case of HOM 166
4.4 Effects of heterogeneous IN and mesoscale temperature perturbation……..187
4.4.1 Effects of heterogeneous IN.....187
4.4.2 Effects of mesoscale temperature perturbation.....198

4.5 Conclusions and discussions.....200
Appendix 4.A Equations used in the cirrus cloud scheme….....205
Appendix 4.B A two-moment treatment of cloud microphysics for warm and mixed-phase clouds…….....207
Appendix 4.C Aerosol optical properties…….213

V. SUMMARY AND FUTURE WORK 216

5.1 Summary.....216
5.2 Future work.....224

APPENDIX…….228

BIBLIOGRAPHY …….239

LIST OF FIGURES

Figure

1.1 Records of changes in atmospheric three major green house gases: carbon dioxide (red line), methane (blue line), and nitrous oxide (black line) over the last 2000 years. Source: Intergovernment Panel on Climate Change, 2007…...3

1.2 Figure 1.2 Temperature changes relative to the corresponding average for 1901-1950 (°C) from decade to decade from 1906 to 2005 over the entire globe. The black line indicates observed temperature change, while the colored bands show the range covered by 90% of recent model simulations. Red indicates simulations that include natural and human factors, while blue indicates simulations that include only natural factors. Source: Intergovernmental Panel on Climate Change, 2007……...4

1.3 Global, annual mean radiative forcings due to a number of processes for the period from the start of the industrial era (about 1750) to 2005. Contoured bars represent the best estimates of the radiative forcings for each process. Red bars represent positive forcing (warming), and blue bars represent negative forcing (negative). Error bars represents range of uncertainty. Source: Intergovernmental Panel on Climate Change (IPCC), 2007……...7

1.4 Scheme of the microphysical processes that influence the size distribution and chemical composition of atmospheric aerosol. The scheme highlights the large range of sizes that are involved in the formation and evolution of aerosol particles. Source: Raes et al. (2000)……8

2.1 Vertically integrated annual mean concentrations (mg m^{-2}) of total sulfate, sulfate associated with nonsulfate aerosols, and OM, BC, dust, and sea salt predicted by the model……..48

2.2 Annual averaged zonal mean concentration (μg/m^3) of OM, BC, dust, and sea salt predicted by the model. CAM3 used a hybrid vertical coordinate and the pressure at the kth model level is given by $p(k)=A(k)p_0+B(k)p_s$, where p_s is surface pressure, p_0 is a specified constant pressure (1000 hPa), A and B are coefficients. Data are plotted as a function of this hybrid vertical coordinate times 1000 and labeled 'Approximate Pressure'……..49

2.3 Model predicted zonal mean number concentration (#/cm^3) of pure sulfate aerosol in the nuclei (upper panel) and accumulation mode (lower panel) in January (right) and July (left). 'Approximate Pressure' is defined in the caption to Figure 2.2. ……51

2.4 Monthly average sulfate concentration at selected sites that are part of an ocean network operated by a group at the University of Miami (Prospero et al., 1989; Arimoto et al., 1996; Savoie et al., 1989, 1993). Model results are in solid lines, and observed data are in dots with one standard deviation…….52

2.5 BC concentration at various sites (Liu et al., 2005): (a) Amundsen-Scott, South Pole (Bodhaine, 1995), (b) Halley, Antarctica (Wolff and Cachier, 1998), (c) Amsterdam Island, France (Wolff and Cachier, 1998), (d) Mauna Loa, Hawaii (3.4 km asl) (Bodhaine, 1995), (e) Jungfraujoch, Switzerland (3.5 km asl) (Nyeki et al., 1998), (f) Mace Head, Ireland (Cooke et al., 1997), (g) Barrow, Alaska (Bodhaine, 1995), (h) Alert, Canada (Hopper et al., 1994). Model results are in solid lines, and observed data are in dots……54

2.6 Annual average simulated OC and BC concentrations vs. observations from the IMPROVE network. The solid lines are 1:1, and the dashed lines are 2:1 or 1:2. ……55

2.7 (a-h): Monthly average total sea salt concentrations at selected sites that are part of an ocean network operated by a group at the University of Miami (Prospero et al., 1989; Arimoto et al., 1996; Savoie et al., 1989, 1993); (i) monthly fine sea salt particles (d < 1.5 μm) at Mace Head, Ireland (Yoon et al., 2007). Model results are in solid lines, and observed data are in dots with one standard deviation…….56

2.8 Monthly average dust concentration at selected sites that are part of an ocean network operated by a group at the University of Miami (Prospero et al., 1989; Arimoto et al., 1996; Savoie et al., 1989, 1993). Model results are in solid lines, and observed data are in dots with one standard deviation…….59

2.9 Monthly average fine mode dust concentration (d < 2.5 μm) at the IMPROVE network stations listed in Table 2.8. (a) Florida (80.68W, 25.39N, at surface); (b) Alaska (148.97W, 63.72N, 658 m); (c) Hawaii (156-155W, 19.5N, 1258-3439 meter); (d) Midwest North America (105-100W, 28-44N, 736-1672 meter); (e) Western North America (120-105W, 28-44N, 1000-3000 meter). 60

2.10 Vertical profiles of total aerosol (left panel) and BC (right panel) mass mixing ratios. Observations are from Schwartz et al. (2006) and took place on November 10 (stars) and November 12 (open circles), 2004, over Houston, Texas. The error bars represent the sample standard deviation. All simulation cases are defined in Table 2.2……...64

2.11 Aerosol size distribution in the marine boundary layer. Observations ('Obs') are from Heintzenberg et al. (2000). All simulated cases are defined in Table 2.2. ……67

2.12 Aerosol size distribution over sites in Europe. Observations ('Obs') are from Putaud et al. (2003). All simulated cases are defined in Table 2.2. …….68

2.13 Aerosol size distribution in the free troposphere. Observations ('Obs') are from Putaud et al. (2003) (Jungfraujoch), Raes et al. (2000) (Tenerife); Frindlind et al. (2004) (Crystal-Face, Florid). All simulated cases are defined in Table 2.2…….70

2.14 Vertical profiles of the number concentration of ultrafine particles (diameter > 3 nm) averaged for latitude bands 70ºS-20ºS (left panel), 20ºS-20ºN (middle panel) and 20ºN-70ºN (right panel) over the Pacific Ocean. Observations (star) are from Clark and Kapustin (2002), and the error bars represent 50% of the standard deviation. Model results are annual means over the same grid squares as the observations (175º-270ºE for the tropics, 200º-240ºE for the NH and 135º-180ºE for the SH). All simulated cases are defined in Table 2.2. ……...72

2.15 Vertical profiles of the number concentration of Aitken mode particles (diameter > 14 nm, left panel) and accumulation mode particles (diameter > 100 nm, right panel) over Punta Arenas, Chile, in March/April (upper panel) and over Prestwick, Scotland, in Sept./Oct. (lower panel). Observations are from Minikin et al. (2003): median (star), 25- and 75-percentiles (left end and right end of error bars). Model results are averaged over 60º-50ºS, 70º-85ºW for Chile, and over 50º-60ºN, 10ºW-5ºE for Scotland. All simulated cases are defined in Table 2.2. ……74

3.1 Diagram showing the processes included in the estimation of the first aerosol indirect effect……..103

3.2 Present day zonal annual-average CCN concentrations (cm^{-3}) at 0.2% supersaturation for all six cases. CAM3 used a hybrid vertical coordinate and the pressure at the *k*th model level is given by $p(k)=A(k)p_0+B(k)p_s$, where p_s is surface pressure, p_0 is a specified constant pressure (1000 hPa), A and B are coefficients. Data are plotted as a function of this hybrid vertical coordinate times 1000 and labeled 'Approximate Pressure'. ……..112

3.3 Present day annual-average CCN concentrations (cm^{-3}) at 0.2% supersaturation near 930 hPa (the third model level) for all six cases. ……...114

3.4 Ratio of present day annual-average CCN concentrations (at 0.2% supersaturation) near 930 hPa (the third model level) between different cases……....116

3.5 Annual-average anthropogenic fraction of CCN concentration at 0.2% supersaturation near 930 hPa (the third model level) for all six cases……120

3.6 Present day zonal annual-average anthropogenic fraction of CCN concentration at 0.2% supersaturation. 'Approximate pressure' is defined in the caption to Figure 3.2……...122

3.7 Difference in annual-average anthropogenic fraction of CCN concentrations between difference cases……124

3.8 Annual-average cloud top droplet number concentrations (cm^{-3}) derived from (a) MODIS (Quaas et al., 2006), (b) BHN, (c) BHN_PRIM and (d) BHN_EMP_PRIM……..127

3.9 (a) The change in the annual-average cloud top effective radius from anthropogenic emissions and (b) Annual-average 1st AIE in the BHN_PRIM case. The values given in the title are global averages……...129

3.10 Change in the simulated annual-average 1st AIE from including the empirical boundary layer nucleation mechanism in five regions: N_L: over Northern Hemisphere land; N_O: over Northern Hemisphere oceans; S_L: over Southern Hemisphere land; S_O: over Southern Hemisphere oceans; Global: global average (Red bar: the difference between BHN_EMP and BHN; Blue bar: the difference between BHN_EMP_PRIM and BHN_PRIM)……131

3.11 (a) Change in the zonal mean annual-average 1st AIE and (b) the change in the zonal annual-average anthropogenic fraction of CCN (right panel) from including primary-emitted sulfate particles (Red line: the difference between BHN_PRIM and BHN; Blue line: the difference between BHN_EMP_PRIM and BHN_EMP)……..132

3.12 The 1st AIE from 5 different model configurations (w/m^2): BHN_PRIM, using the average from four months (January, April, July and October); WARM: the same as BHN_PRIM but with only warm clouds (warmer than 273.15K) included; STRAT: the same as BHN_PRIM but with only stratiform clouds included; N40: the same as BHN_PRIM but with the minimum cloud droplet number set to $40/cm^3$; N10: the same as BHN_PRIM but with the minimum cloud droplet number set to $10/cm^3$. ……..134

4.1 Annual zonal means of liquid water path (LWP, g/m^2), ice water path (IWP, g/m^2), cloud top droplet number concentration (N_l, #/cm^3), cloud top droplet effective radius (R_l, μm), cirrus cloud top ice crystal number (N_i, #/cm3), and cirrus cloud top ice crystal radius (R_i, μm), short wave cloud forcing (SWCF, W/m^2), and long wave cloud forcing (LWCF, W/m^2) in four cases: HOM, HMTH_0.01IN, HMHT_0.1IN, HMHT_1IN…….171

4.2 Annual zonal mean latitude versus pressure plots of grid-mean cloud liquid water content (CLDLIQ, mg/m^3), cloud ice water content (CLDICE, mg/m^3), cloud liquid droplet number (LIQNUM, #/cm^3), cloud ice crystal number (ICENUM, #/L) and cloud fraction (CLOUD)……...174

4.3 Annual zonal mean latitude versus pressure plots of ice water content (mg/m^3) (a) that measured by the Aura MLS instrument, (b) that predicted by HOM, and (c) that predicted by HMHT_0.01IN……176

4.4 Annual zonal mean latitude versus pressure plots of (a) ice crystal number concentration (#/cm^3) predicted by the prognostic ice crystal equation and (b) that calculated from homogeneous freezing parameterization in the case of HOM……...177

4.5 In-cloud ice crystal number concentration (ICNC, #/cm^3) and ice crystal effective radius (REI, μm) versus temperature. Model results are sampled every six hours over six flight regions (Kiruna, Sweden in January and February; Hohn, Germany in November and December; Forli, Italy in Octorber; Mahe, Seychelles, in February and March; Darwin, Australia, in November; Aracabuta, Brazil in January and February) where the observation reported in Krämer et al. (2008) were collected (See Table 3 in Krämer et al. (2008) for the flight information). The 50 percentile (green line), 25% percentile (blue line), and 75% percentile (red line) are shown for each 1 K temperature bins. The upper panel is for the HOM case; the middle panel is for the HMHT_0.01IN case; and the low panel is for the HMHT_0.1IN case....179

4.6 Frequency of occurrence of RHi in the SH middle latitudes (60ºS-30ºS) (SH MID, left panel), in the tropics (30ºS-30ºN) (TROPIC, middle panel), and the NH middle latitudes (30ºN-60ºN) (NH MID, right panel) at 100-200 hPa (upper panel) and at 200-300 hPa (lower panel) from all simulations listed in Table 4.1. Observations from MOZAIC data in the tropics and in the NH middle latitudes are also shown……..181

4.7 Annual-average frequency of occurrence of ice supersaturation from MLS data (upper panel) and the case of HOM (lower panel) at 147 hPa (139 hPa for model) (left panel) and 215 hPa (192 hPa for model) (lower panel)……..184

4.8 Regionally-averaged frequency of occurrence of ice supersaturation from MLS data and from three simulations: HOM, HMHT_0.01IN, and HMHT_0.1IN, (a) at 149 hPa (139 hPa for model) and at (b)215 hpa (192 hPa for model) over five regions: Global (80ºS-80ºN), NH(North Hemisphere, 30ºN-80ºN), TROPICS (30ºN-30ºS), SH(Southern Hemisphere, 55ºS-30ºS), and Antarctic (80ºS-55ºS)……..186

4.9 Annual zonal mean latitude versus pressure plots of (a) soot and (b) dust particles number concentration (#/cm^3)……..187

4.10 Annual zonal mean latitude versus pressure plots of ice crystal number concentration in all five cases that allow the competition between homogeneous freezing and heterogeneous freezing. All cases are described in Table 4.1……..190

LIST OF TABLES

Table

2.1 Size Distribution Parameters for Non-sulfate Aerosols (Table 1 in Liu et al., 2005)…….28

2.2 Description of cases……..40

2.3 Global budget for sulfate aerosol……..41

2.4 Global budget for OM and BC…….42

2.5 Global budget for dust……..44

2.6 Global budget for sea salt…….45

2.7 Simulated and observed fine and coarse mode sea salt aerosols ($\mu g\ m^{-3}$)……58

2.8 IMPROVE Sites used in Figure 2.9…….61

3.1 Hygroscopicity and density for each aerosol component……...107

3.2 Description of cases……108

3.3 Aerosol emissions and burdens in the present day and preindustrial simulations for the BHN_PRIM case…….110

3.4 Global annual-averaged CCN concentration in the boundary layer in the PD simulation, cloud top effective radius in the PD simulation, change in the cloud top effective radius from anthropogenic emissions, anthropogenic fraction of CCN in the boundary layer, column-integrated anthropogenic fraction of CCN, and the 1st AIE for all six cases……...119

4.1 Descriptions of simulations…….166

4.2 Annual global mean cloud properties and their interannual variations (standard deviations). The liquid water path (LWP, g/m^2) observations are from SSM/I (for the years 1987-1994, Ferraro et al., 1996; for August 1993 and January 1994, Weng and Grody, 1994; and for August 1987 and February 1988, Greenwald et al., 1993) and ISCCP for the year 1987 (Han et al., 1994). SSM/I data are restricted to oceans. Ice water path (IWP, g/m^2) has been derived from ISCCP data for the years 1983-2000 (Storelvmo et al., 2008). N_d and N_i refer to the vertically integrated cloud droplet and ice crystal number concentration (10^{10}/m^2), and r_{effl} (μm) refers to the cloud top effective radius. Observations of N_d are obtained from ISCCP for the year 1987 (Han et al., 1998) and observations of r_{effl} are obtained from ISCCP for the year 1987 (Han et al, 1994) and from MODIS (version 4) for the year 2001 (Platnick et al., 2003), and are limited to 50ºN to 50ºS. r_{effi} and N_{itop} refer to ice crystal radius and number at the top of cirrus clouds, respectively. Observations of r_{effi} are from MODIS data (version 4) for the year 2001. Total cloud cover (TCC) was obtained from ISCCP for the years 1983-2001 (Rossow and Schiffer, 1999) and MODIS data for the years 2001-2004 (Platnick, 2003). High cloud cover (TCCHGH) was obtained from ISCCP data for the years 1983-2001. TCCLOW refers to low level cloud cover.……169

4.3 Annual global mean shortwave cloud forcing (SWCF, W/m^2), longwave cloud forcing (LWCF, W/m^2), net cloud forcing (CF, W/m^2), total precipitation (Ptot, mm/day), water vapor mass (WVM, kg/m^2), net incoming radiation at the top of the atmosphere (FNT, W/m^2), and clear sky net long wave radiation at the top of the atmosphere (FLNTC, W/m^2, negative values mean outgoing) and their interannual variations (standard deviations). The shortwave (SWCF) and longwave cloud forcing (LWCF) estimates are taken from ERBE for the years 1985-1989 (Kiehl and Trenberth, 1997) and CERES for the years 2000-2005 (http://science.larc.nasa.gov/ceres). Total precipitation (P_{tot}) is taken from the Global Precipitation Data Set for the years 1979-2002 (http://precip.gsfc.nasa.gov). Water vapor mass (WVM) data is from MODIS for the years 2001-2004 (King et al., 2003)……170

4.4 Comparison of measured ice crystal number concentration ('Obs') during the INCA campaign (Gayet et al., 2004) over the SH (Punta Arenas, Chile, in March/April) and over the NH (Prestwick, Scotland, in September/October) with those simulated from the prognostic ice crystal equations in the model. Median values from the observations are shown. For the model simulations, monthly mean results are used, and are averaged over 60°-50°S, 70°-85°W, from March to May in Chile, and over 50°-60°N, 10°W-5°E, from September to November in Scotland. Model results are restricted to pressure levels from 200 hpa to 300 hPa, and to temperatures from -35°C to -60°C……..180

4.B1 Size distribution parameters for aerosols……209

4.C1 Physical and optical properties at 550 nm for aerosol species……214

ABSTRACT

The aerosol indirect effect remains one of the largest uncertainties in the projection of the future climate change. In this dissertation we improve both aerosol and cloud treatments in a coupled aerosol and atmospheric circulation model to advance our understanding of aerosol indirect effects.

An empirical aerosol nucleation parameterization is implemented into the coupled model to better represent observed nucleation events in the boundary layer and is shown to improve the comparison of simulated aerosol size distributions with observations. Simulated cloud condensation nuclei (CCN) concentrations in the boundary layer range from 70 to 169 /cm^3 from different nucleation mechanisms. Primary-emitted sulfate has the largest effect on simulated CCN concentration, while the effect of the boundary layer nucleation on CCN concentration strongly depends on the number of simulated primary particles. The first indirect forcing from various treatments of aerosol nucleation ranges from -1.22 to -2.03 W/m^2. Including primary-emitted sulfate particles significantly increases the first aerosol indirect forcing, while whether particle formation from aerosol nucleation increases or decreases aerosol indirect effects largely depends on the relative change of primary particles and SO_2 emissions from the preindustrial to the present day atmosphere.

To better represent subgrid-scale supersaturation, a statistical cirrus cloud scheme is implemented into the coupled model and is shown to simulate the observed probability distribution of relative humidity well. Heterogeneous ice nuclei (IN) are shown to affect not only high level cirrus clouds through their effect on ice crystal number concentration but also low level liquid clouds through the moistening effect of settling and evaporating ice crystals. The change in net cloud forcing is less sensitive to the change in ice crystal concentrations because changes in high cirrus clouds and low level liquid clouds tend to cancel, while the net radiative flux change at the top of the atmosphere is still large because of changes in the greenhouse effect of water vapor. Changes in the assumed mesoscale temperature perturbation are shown to change ice crystal number and radiative fluxes with a magnitude that is similar to that from a factor of 10 change in the heterogeneous IN number.

CHAPTER I

INTRODUCTION

1.1 The climate system and our changing climate

The climate system consists of the atmosphere, land surface, snow and ice, oceans and other bodies of water, and living things. Many physical, chemical, and biological processes and interactions occur among the various components of the climate system. Fluxes of mass, heat, and momentum are exchanged among different components. The atmosphere is most readily identifiable as intertwined with climate, in the sense of one definition thereof ('average weather'). The atmospheric component is also the main body of this dissertation.

The sun provides the energy that drives the climate system. On average, 342 Watts of solar radiation reaches the top of the Earth's atmosphere for each square meter of the surface area (Kiehl and Trenberth, 1997). 31% of this energy is immediately reflected back into the space by the Earth's surface (9%) and the atmosphere (clouds, aerosol particles and other gas species) (22%). The remaining 235 W/m^2 of solar energy is absorbed by the Earth's surface (168 W/m^2) and by the atmosphere (67 W/m^2). To maintain energy balance, the Earth and its atmosphere must emit, on average, the same amount of energy into the space. The thermal radiation emitted by the Earth and its

atmosphere is determined by their individual temperatures. Due to the presence of greenhouse gases and clouds in the atmosphere, only a small part (40 W/m^2) of the thermal radiation (390 W/m^2) emitted by the Earth's surface escapes into the space directly, and the remaining (350 $Watts/m^2$) is emitted back to the Earth's surface. This is the so-called greenhouse effect, which leads to a global mean temperature of 14^o C on the Earth's surface that is 33 degrees higher than it would be (-19^o C) were it not for the greenhouse effect. Most of the thermal energy is emitted back into space by the greenhouse gases (165 Watts) and clouds (30 Watts) at a lower temperature (Kiehl and Trenberth, 1997).

Over the long-term evolution of life on Earth, solar energy, the Earth's surface, atmospheric constituents (greenhouse gases, aerosol particles), and clouds have maintained a sophisticated energy balance for the Earth climate system. Any perturbation in one of these will cause energy imbalance and may potentially lead to climate change. A perturbation in the climate system can include changes in solar irradiance, the land surface, atmospheric constituent concentrations, or clouds. Among these changes, variations in solar irradiance occur naturally, and changes in the land surface, atmospheric constituents, and/or clouds can occur either naturally or by human-induced means. For example, aerosol particles in the atmosphere can be increased significantly either by fossil fuel burning from human activities or by a major volcanic eruption (e.g., Mt. Pinatubo in 1991).

Since the start of the industrial era (about 1750), human activities have significantly changed atmospheric constituents, greenhouse gases, and aerosol particle concentrations. Figure 1.1 shows the change of three major greenhouse gases (carbon dioxide [CO_2],

methane [CH_4], and nitrous oxide [N_2O]) concentrations over the past 2005 years. The three major green house gas concentrations have increased significantly over the past 250 years. For example, [CO2] has increased globally by about 100 ppm (36%) over the last 250 years, from a range of 275 to 285 ppm in the pre-industrial era to 379 ppm in 2005.

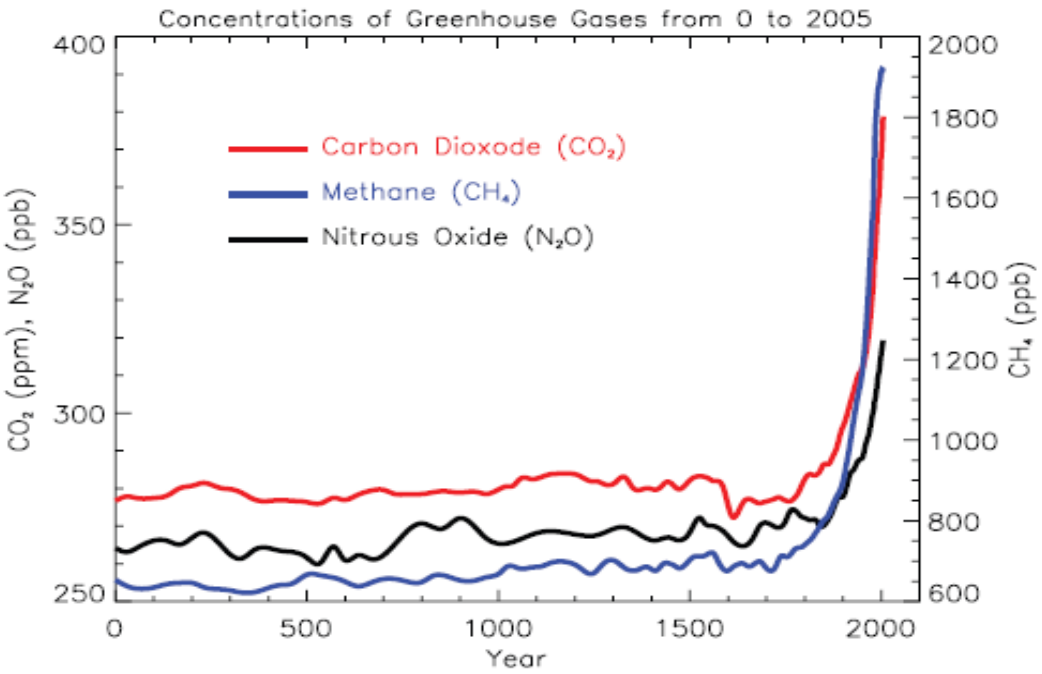

Figure 1.1: Records of changes in atmospheric three major green house gases: carbon dioxide (red line), methane (blue line), and nitrous oxide (black line) over the last 2000 years. Source: Intergovernment Panel on Climate Change, 2007.

The increase in greenhouse gases is believed to be the predominant cause for observed temperature increases in the 20th century, as concluded in the Intergovernmental Panel on Climate Change (IPCC) 2007 report. Figure 1.2 shows observed global mean surface temperature changes from 1906 to 2005, along with those simulated by numerical models with and without human-induced changes in the Earth climate system. Observed global mean temperature has risen about 0.74^{o} C over the last 100 years. As shown in Figure 1.2, this observed increase in global mean temperature can not be reproduced by numerical models that only include natural perturbations, such as variations in solar irradiance and

the effects of volcanic eruptions, and can only be reproduced by those models which simulate human-induced change in the atmosphere.

Global warming gives rise to a series of consequences, such as rising sea levels, change in the amount and pattern of precipitation, reduction of snow and ice coverage, thawing of permafrost, and searing heat waves. These problems pose significant threats to human communities and ecosystems, and global warming is believed to be the most important environmental crisis the world faces. A better understanding of the underling physical mechanisms and more accurate prediction of future climate change are urgently needed to navigate this crisis.

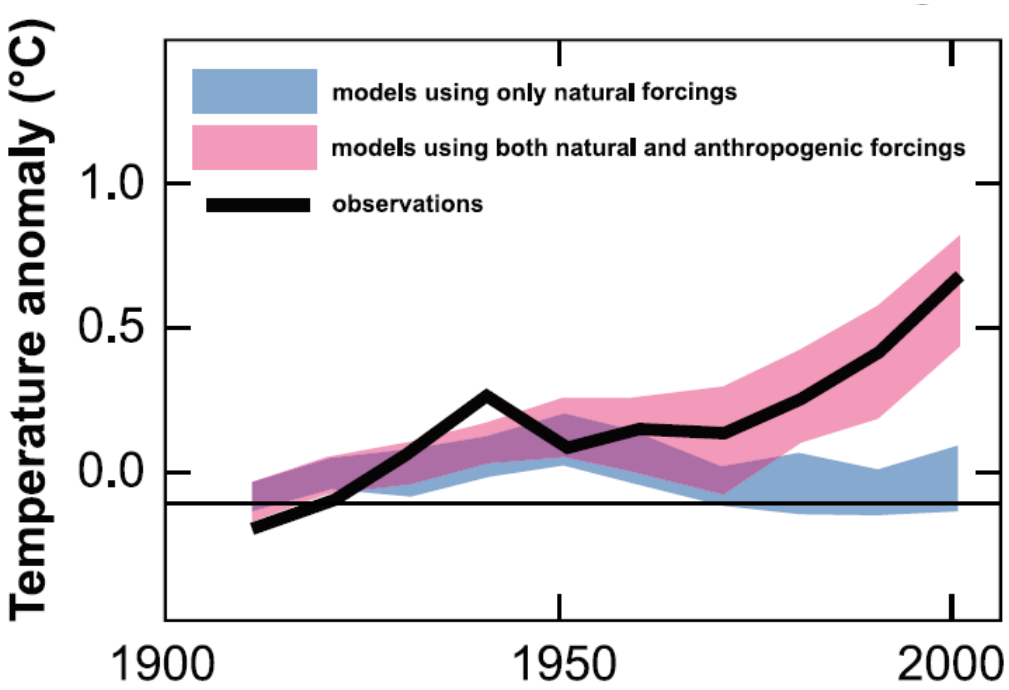

Figure 1.2: Temperature changes relative to the corresponding average for 1901-1950 (°C) from decade to decade from 1906 to 2005 over the entire globe. The black line indicates observed temperature change, while the colored bands show the range covered by 90% of recent model simulations. Red indicates simulations that include natural and human factors, while blue indicates simulations that include only natural factors. Source: Intergovernmental Panel on Climate Change, 2007.

1.2 Climate forcing and climate sensitivity

The magnitude of a perturbation to the energy balance caused by natural or human-induced change is measured in terms of climate forcing, which is defined as the net radiative flux change at the tropopause after the changes in radiative forcing agents (e.g., greenhouse gases, aerosols, land use, solar activity, and due to volcanic eruptions). Radiative forcing (ΔF) can be related to the global mean equilibrium temperature change (ΔT_s) at the surface, which is a response of the climate system to external forcing, through the following linearized relationship:

$$\Delta T_s = \lambda \Delta F \,, \tag{1.1}$$

where λ is the climate sensitivity parameter, which indicates how much the global average surface temperature will change will occur per unit radiative forcing, and therefore is the object of much current research on climate change. Although radiative forcing is a simple measure (it does not attempt to represent the climate response) for both quantifying and ranking the many different influences on climate change, it has the advantage of being more readily calculable and comparable than estimates of the climate response to different forcings. Therefore, it has widely used to compare and assess the influence of different radiative forcing agents since first being introduced in early studies of the climate response to change in solar irradiance and CO_2 in simple radiative-convective models (Manabe and Moller, 1961; Manabe and Wetherald, 1967).

Figure 1.3 shows estimated radiative forcing between 1750 and 2005 for a variety of forcing agents that include both human-induced changes and natural changes (IPCC, 2007). Radiative forcing from natural changes (here, restricted to solar irradiance alone) is 0.12±0.06 W/m^2, which is much smaller than that from human-induced changes. The

total anthropogenic radiative forcing has a best estimate of 1.6 W/m^2 and ranges from 0.6 to 2.4 W/m^2. Although the greenhouse gases contribute most to the total anthropogenic radiative forcing, with a magnitude of 2.63±0.24 W/m^2, their forcing is well defined with an uncertainty of only about 10% because of their long residence times and their homogeneous distribution in the atmosphere and their absorption spectrum. The large uncertainty in the estimated total anthropogenic forcing is mainly caused by the uncertainty in radiative forcing of aerosols. The total radiative forcing of aerosol is estimated to be -1.2 W/m^2 with a range from -0.2 to -2.3 W/m^2 that represents 5% to 95% confidence range.

The large uncertainty in the estimation of aerosol radiative forcing limits the evaluation of global climate models and useful empirical inferences of climate sensitivity. Although a large spread of climate sensitivity in global climate models results primarily from differences in simulated cloud feedbacks (Randall et al., 2007), the climate sensitivity of global climate models could be constrained by the models' capability to reproduce observed temperature trends in the 20^{th} century alone if the radiative forcings were accurately known. Because of the large uncertainty in the estimated total aerosol radiative forcing in the 20^{th} century, this constraint fails to narrow the spectrum of climate sensitivity. The combination of a small anthropogenic forcing and a large climate sensitivity or the combination of a large anthropogenic forcing and a small climate sensitivity could both have produced the observed 20^{th} century temperature record (e.g., Penner 2004). As shown in Kiehl (2007), global climate models with large climate sensitivity tend to have a small total anthropogenic forcing, which is usually associated with a large negative aerosol forcing. The wide spread of climate sensitivity limits our

capability to project future climate change. So reduction in the uncertainty in aerosol forcing, specifically, is essential to better constrain the uncertainty in climate sensitivity overall, and to improve our projections of future climate change.

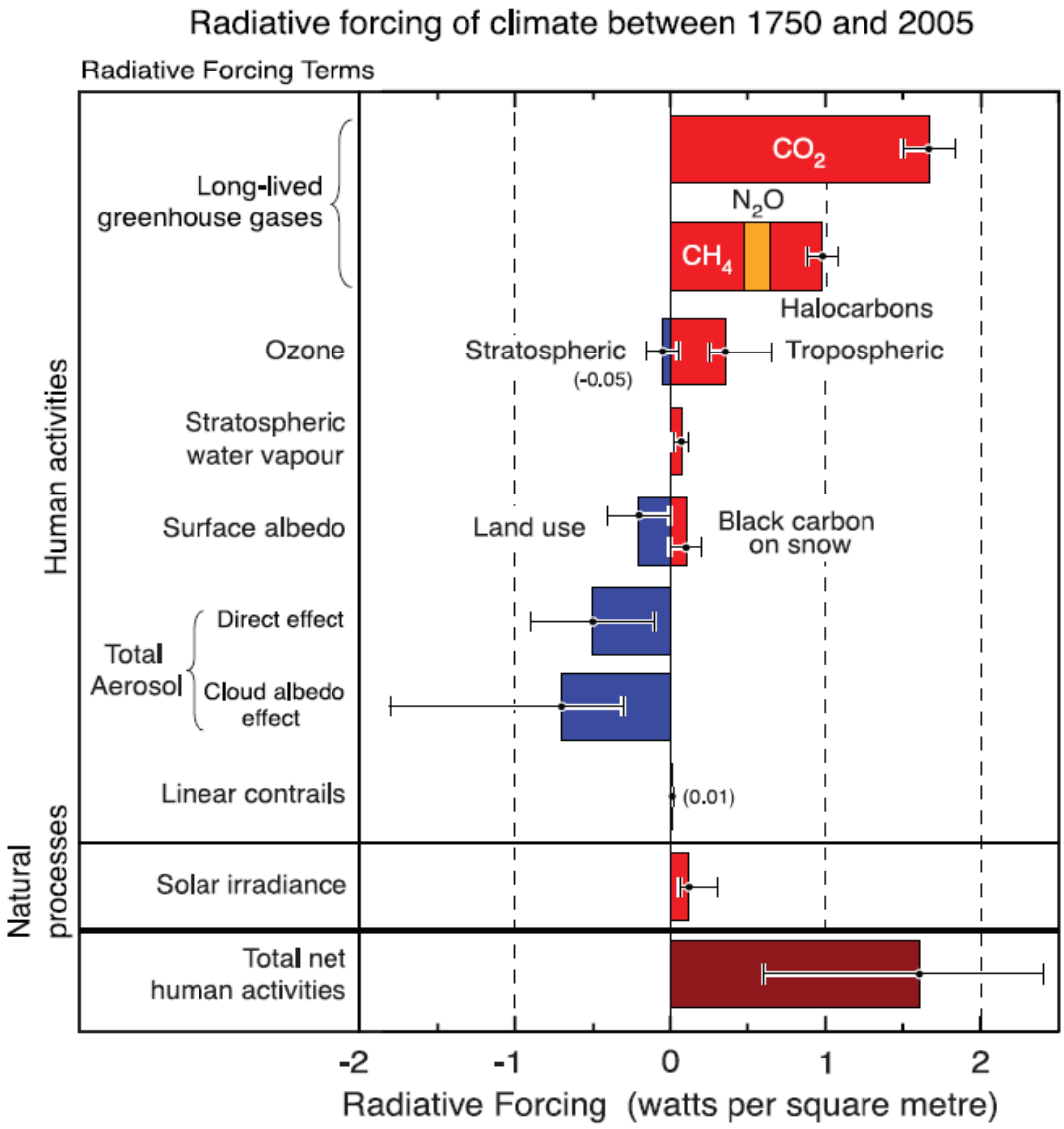

Figure 1.3 Global, annual mean radiative forcings due to a number of processes for the period from the start of the industrial era (about 1750) to 2005. Contoured bars represent the best estimates of the radiative forcings for each process. Red bars represent positive forcing (warming), and blue bars represent negative forcing (negative). Error bars represents range of uncertainty. Source: Intergovernmental Panel on Climate Change (IPCC), 2007.

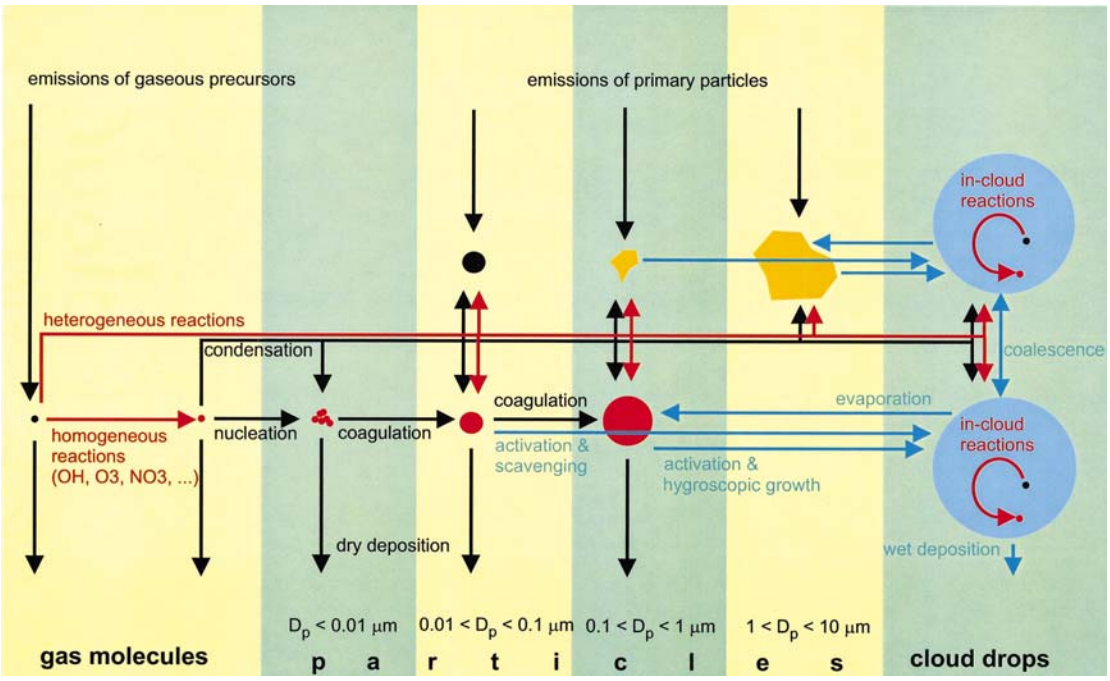

Figure 1.4: Scheme of the microphysical processes that influence the size distribution and chemical composition of atmospheric aerosol. The scheme highlights the large range of sizes that are involved in the formation and evolution of aerosol particles. Source: Raes et al. (2000).

1.3 Atmospheric aerosols and their climate effects

Aerosols are solid or liquid particles that are suspended in the atmosphere. They have both natural and anthropogenic sources. For example, wind-borne dust, sea salt, and volcanic aerosols are natural aerosols; soot and organic carbonaceous particles from fossil fuel burning and biomass burning are anthropogenic aerosols. Aerosol concentrations in the atmosphere vary from location to location, and can be as little as $10^2/cm^3$ in remote marine regions and as high as $10^8/cm^3$ in heavy polluted urban regions. The size of these aerosol particles can span over four orders of magnitude, from a few nanometers to around 100 µm. Their presence in the atmosphere and their chemical and physical properties are determined by complicated processes that involve the generation, growth, and removal of aerosols. These include emissions, chemical reactions, nucleation,

coagulation, condensation, cloud processing, dry deposition, and wet deposition, as illustrated in Figure 1.4.

Aerosol particles that are directly emitted as particles from their sources are termed primary particles. Wind-borne dust, sea salt, and soot particles formed through combustion are all primary particles. Aerosol particles that are generated in the atmosphere through the nucleation of gas phase species, such as sulfuric acid gas and water vapor, are termed secondary particles. Nucleation occurs when the concentration of the gas phase species exceeds its equilibrium vapor pressure above molecular clusters formed by random collisions, and is favored primarily in an environment where pre-existing aerosol surface area is low.

After aerosol particles are added into the atmosphere, through either direct emissions or secondary generation, they grow through condensation, coagulation, and cloud processes. Condensation of gas species on aerosol surfaces is efficient for small particles (e.g., freshly nucleated particles and freshly emitted soot particles from combustion), but condensation becomes diffusion limited and slows down when particles reach a diameter of the order of the mean free path length of the condensing molecule (typically about 60 nm) (Raes et al., 2000). Coagulation strongly depends on particle concentration and eventually quenches as number concentration falls. Cloud processing is another important microphysical process in which particles grow. Large aerosol particles (with a diameter of around 100 nm) can activate into non-precipitating droplets in a supersaturation environment. Once a droplet is formed, aqueous oxidation of compounds within the drop will add mass to the pre-existing particles. When the cloud droplets evaporate, the residual aerosol particles are larger than original aerosol particles.

Aerosol particles are removed from the atmosphere through wet deposition, dry deposition and gravitational settling. Small particles (with diameters less than 1 μm) diffuse to the Earth's surface (dry deposition), a process that becomes less efficient when particle size increases. Large particles (with diameters larger than 1 μm) settle gravitationally, a process that becomes less efficient when particle size decreases. In the range 0.1 to 1 μm in diameter, dry removal is very slow, and the formation and growth processes discussed above tend to accumulate the aerosol in this size range. These particles, when they have the right hygroscopic properties, will be removed mainly by activation in clouds and subsequent precipitation (wet deposition).

Aerosol particles can be separated into four modes based on their size, which are closely related to the production and removal mechanisms discussed above: nucleation mode particles (with diameters less than 10 nm); Aitken mode particles (with diameters between 10 nm and 100 nm), accumulation mode particles (with diameters between 0.1 μm to 1 μm), and coarse mode particles (with diameters larger than 1 um). Among these four modes, accumulation mode particles are most relevant to aerosol's climate effect, for these category of aerosols have the most important contribution to the number concentration of cloud condensation nuclei (CCN) and to light scattering.

Although aerosols are tiny particles in the atmosphere, they have important climate effects. They can affect climate directly by scattering solar radiation or absorbing solar or thermal radiation. For example, sulfate particles can scatter solar radiation back into space and cool the Earth, while soot particles can absorb solar radiation. These are termed aerosol direct effects. Aerosol particles can also indirectly affect climate through modifying cloud properties by acting as CCN or ice nuclei (IN). These are termed aerosol

indirect effects. Aerosol can also change snow albedo when dark aerosol particles (e.g., soot and dust particles) deposit on snow surfaces. Absorbing aerosol particles can heat the atmosphere, and thus tend to reduce large-scale cloud fraction (Hansen et al., 1997), which is termed a semi-direct effect. Whether this effect warms or cools the earth strongly depend where soot particles are injected in the atmosphere (Penner et al., 2003). Aerosol particles also contribute to numerous other climatically important processes. For example, aerosol particles can fertilize the land and ocean through the deposition of nitrates, iron, and other nutrients, therefore affecting biogeochemical cycles. Through their effect on cirrus clouds, aerosol particles may also affect water vapor concentrations in the stratosphere (Sherwood 2002). Among all these effects, aerosol indirect effects can potentially have large magnitude but also large uncertainty, and this is the focus of the dissertation at hand.

1.4 Aerosol indirect effects

Clouds are an extremely important climate regulator. They have a large impact on the Earth's energy budget since they are highly reflective of solar radiation, yet strongly absorbing of long wave thermal radiation. Globally, on average, clouds reflect about 50 W/m^2 of solar radiation into space and trap 30 W/m^2 of terrestrial thermal radiation, thus exerting a net cooling effect of about 20 W/m^2. In addition, clouds play a central role in the hydrological cycle, which is coupled to the energy budget through the release of latent heat that results from water condensation or evaporation. This, in turn, influences atmospheric circulation on a variety of scales.

By acting as CCN or IN, aerosol particles, along with other meteorological conditions, determine cloud droplet number concentration and ice crystal number concentration. By

changing cloud droplet number concentration and ice crystal number concentration, anthropogenic aerosols can affect cloud optical and physical properties, which will change short wave and long wave cloud radiative forcing and the hydrological cycle, further affecting atmospheric circulation. This is the aerosol radiative indirect effect. Note that the aerosol semi-direct effect is also included as an aerosol indirect effect listed in the IPCC 2007 report, but is not included in this definition. Here, aerosol indirect effects are strictly limited to aerosol's impact on clouds by acting as CCN or IN.

Several aerosols indirect effects have been identified (Denman et al., 2007). For a given cloud liquid water content, increases in cloud droplet number concentration from anthropogenic aerosols will decrease droplet size, and will increase cloud optical depth and cloud albedo. This is called the 'first aerosol indirect effect' (e.g., Ramaswamy et al., 2001) or the 'Twomey effect' (e.g., Twomey, 1977) or the 'cloud albedo effect' (Lohmann and Feichter, 2005). Increases in cloud droplet number concentration and decreases in cloud droplet size are also hypothesized to reduce the precipitation efficiency and to increase the cloud water path, prolonging cloud lifetimes. This is called the 'second aerosol indirect effect' (e.g., Ramaswamy et al., 2001) or the 'Albrecht effect' (Albrecht, 1989), or the 'cloud lifetime effect' (Lohmann and Feichter, 2005). The glaciation effect refers to the effect of an increase in IN resulting in a rapid glaciation of a super-cooled liquid water clouds due to the difference in vapor pressure over ice versus water (Lohmann, 2002; Lohmann and Diehl, 2006). Unlike cloud droplets, these ice crystals grow in an environment of high supersaturation with respect to ice, quickly reaching precipitation size, with the potential to turn a non-precipitating cloud into a precipitating cloud. The thermodynamic effect refers to a delay in freezing by the smaller

droplets, causing super-cooled clouds to extend to colder temperatures (Rosenfeld, 1999; Rosenfeld and Woodley, 2000; Khain et al., 2005). Aerosols can also potentially affect cirrus clouds (pure ice clouds at temperatures below 238 K) by acting as IN. When a few efficient heterogeneous IN are present in an otherwise homogeneous frozen-dominated environment, these few IN can lead to early formation of cirrus clouds, which can lead to changes in ice crystal number concentration, cloud fraction, and ice water content. The magnitude of these effects is not fully established (Penner et al., 2009).

1.5 Modeling aerosol indirect effects in global climate models

Global climate models are the primary tool for studying aerosol indirect effects on a global scale, and for studying aerosol effects on the hydrological cycle and the atmospheric circulation, and for further projecting aerosol's impact on future climate change. Although satellite data is another way to study aerosol indirect effects globally, they are usually used to constrain model estimations (e.g., Lohmann and Lesins, 2002) and have also been used to estimate aerosol indirect effects alone very recently (Quaas et al., 2008). Problems have been identified with satellite estimates, particularly with the use of a column integrated aerosol parameter (such as aerosol optical depth or the product of aerosol optical depth and Angstrom coefficient) as a proxy for CCN (Feingold et al., 2003). Furthermore, there are no coincident retrievals for aerosol and cloud properties, and there may be short-term meteorological effects on satellite derived relationships between aerosol and cloud properties that could incorrectly affect the interpretation of those relationships relative to longer-term climatic effects (e.g., Lohmann et al., 2006). There are also problems with estimating droplet size and cloud optical depth from broken

clouds (Marshak et al., 2006), and with separating the anthropogenic component of aerosols from the natural component (Diner et al., 2004).

Although global models are the primary tool in estimating aerosol indirect effects, large uncertainties remain in model estimates. As shown in Figure 1.3, the best estimate for the cloud albedo effect carries a very large uncertainty range. No best estimate is available for other aerosol indirect effects, and no consensus exists for even the signs of indirect forcing for some of the aerosol indirect effects, such as aerosol indirect effects on cirrus clouds. Improvements in both aerosol and cloud treatments in GCMs are imperative to advancing our understanding of aerosol-cloud interactions and to decreasing the uncertainties in estimated aerosol indirect effects. These improvements include a better representation of aerosols, a better treatment of cloud microphysics and cloud dynamics, and a better understanding of aerosol's capability to act as CCN and IN. Specific key areas where better representation/understanding is needed are:

1. Time-resolved aerosol emission inventories. In particular, biogenic sources and emissions from biomass burning are highly uncertain. Aerosols emissions in pre-industurial times are also highly uncertain. Several model studies show large uncertainties in simulated aerosol indirect effects based on the unknown ratio of pre-industrial to present-day aerosol number concentration.
2. Aerosol size distribution and evolution. Aerosol sizes span four order of magnitude and are determined by their generation and removal mechanisms (section 1.3), and vary significantly from one place to another; however, in most studies of aerosol indirect effects, only a single size distribution is assumed for each aerosol category.

The aerosol size distribution has been shown to be important to in the estimation of aerosol indirect effects (Chen and Penner, 2005).

3. Chemical pathways for aerosol particles in the atmosphere. For example, organic particles result both from primary emissions and from gas-to-particle conversion in the atmosphere (secondary organic aerosol), but the latter process is not well understood, and simulated organic aerosol concentrations are substantially underestimated (Heald et al., 2005; Volkamer et al., 2005). The presence of organic particles, owing to their distinct hygroscopic and absorption properties, can be particularly important for cloud albedo effects (Ming et al., 2007). Simulating nitrate particles also remains problematic because of their semi-volatile nature.
4. Mixing states between different aerosol components. Aerosol particles in nature tend to be composed of several compounds and can be internally or externally mixed. The actual conditions are difficult to simulate in climate models, and most global models simply assume external mixing or internal mixing. The aerosol mixing state affects their capability to act as CCN or IN.
5. Convective cloud microphysics. There is currently a substantial discrepancy between the degree of sophistication in cloud microphysics in large-scale clouds and the very rudimentary treatment of cloud microphysics in convective clouds. Evidence has emerged to show that enhanced droplet concentrations from aerosol particles may affect convective clouds (e.g., Rosenfeld, 1999; Andreae et al., 2004).
6. Cloud dynamic processes, such as entrainment, which are critical to aerosol-cloud interactions. For example, the cloud lifetime effect is hypothesized to increase cloud liquid water due to reduced precipitation efficiency (Albrecht, 1989), which is

indeed simulated in most climate models, but in observations the opposite can occur, as well. By using a cloud resolving model, Ackerman et al. (2004) showed that a decrease in liquid water in polluted clouds can be caused by the enhanced entrainment of dry air in polluted clouds, with subsequent evaporation of cloud droplets.

7. Subgrid-scale features of clouds. Aerosol-cloud interactions take place on the microscale, and are at best crudely represented in global climate models. Thus, subgrid scale features are desirable for many microphysical processes, such as droplet activation and autoconversion. For example, cloud scale vertical velocity is needed to calculate droplet activation and ice freezing, which is currently absent in most climate models.
8. The capabilities of aerosol particles to act as CCN or IN. Organic particles can be important CCN, but their effects on cloud droplet formation are still under debate (Feingold and Chuang, 2002; Nenes et al., 2002, Lance et al., 2004). Much more has to be learned about aerosol particles' capabilities to act as IN (Kärcher et al., 2007).

Other than the problems listed above, any improvements in cloud treatments in global climate models in general would be welcomed regarding aerosol indirect effects, since these effects strongly depend on how cloud, and their radiative and hydrological properties are represented in GCMs, and since accurate model representation of clouds and cloud influences on radiation and hydrology remains particularly challenging.

1.6 Overview of this dissertation

In this dissertation, improved aerosol and cloud treatments in a coupled aerosol and atmospheric circulation model are introduced to study the aerosol indirect effect. In the

first half of the dissertation (Chapters II and III), the focus is on the aerosol treatment, and in particular, the treatment of the nucleation of aerosols in the aerosol model component of the coupled model, to see how different treatments affect aerosol indirect effects. In the second half of this dissertation (Chapter IV), the focus is on the cloud treatment, and in particular, subgrid-scale treatment of supersaturation and cloud formation in cirrus clouds in the atmospheric circulation model component of the coupled model.

To meet the need to better represent aerosol size evolution in global models, as discussed in section 1.5, global aerosol models with detailed aerosol microphysics modules have been recently developed (Wilson et al., 2001; Adams and Seinfeld, 2002; Gong et al., 2003; Easter et al., 2004; Lauer et al., 2005; Liu et al., 2005; Spracklen et al., 2005a; Stier et al., 2005). Generally, these aerosol microphysics modules include sulfate aerosol nucleation, condensation, and coagulation, and cloud-aerosol particle processes (section 1.3). The inclusion of these microphysical processes in a global aerosol model permits the model to predict the evolution of aerosol sizes and its mixing states, which are critical to the estimation of aerosol indirect effects.

Although these models are shown to improve the modeling of aerosol sizes and mixing states and have been used to study aerosol indirect effects and CCN concentration, large uncertainties remain, particularly with the treatment of the generation mechanism for secondary particles. Binary homogenous nucleation is the only mechanism to generate secondary particles in most models, but it can not explain the observed nucleation rates in the boundary layer (e.g., Clarke et al., 1998). Partly to compensate for the inefficient generation of secondary particles in the boundary layer, a small fraction of anthropogenic

sulfur is assumed to be emitted in particulate form with a prescribed size distribution in some global models. Although this treatment increases secondary particles in models, it adds new uncertainties because of the absence of constraints on this treatment in global models. Therefore a better representation of aerosol nucleation in the boundary layer is needed. Moreover, the effects of simulated size-resolved aerosol composition on the estimate of aerosol indirect effects have not been quantified. Several studies have used the size-resolved aerosol composition predicted from their aerosol models to estimate the aerosol indirect effects (Ghan et al., 2001a; Lohmann et al., 2007; Storelvmo et al., 2006). But these studies did not examine how different treatments in the prediction of the aerosol size and number concentration, especially different generation mechanisms of secondary particles, affect the estimate of the aerosol indirect forcing. Given the fact that more and more global models with size-resolved aerosol composition have been used to estimate aerosol indirect effects and that large uncertainties remain in the treatment of the secondary particles, it will be important to quantify how different generation mechanisms of secondary particles affect the estimate of aerosol indirect effects. On the one hand, this can tell us whether the efforts in representing aerosol size evolution in global models can improve our understanding of the aerosol indirect effects. On the other hand, this can also point to the need for the further future improvement.

The first half of this dissertation discusses the representation of aerosol nucleation in the boundary layer and quantifies the effects of different aerosol nucleation mechanisms on the estimate of the first aerosol indirect forcing. An aerosol nucleation parameterization is first implemented in the aerosol model component of the coupled model to simulate boundary layer nucleation. This parameterization was based on an

empirical fit to newly formed particles and their dependence on sulfuric acid vapor based on long-term observations of aerosol formation events at Hyytiälä, Finland (Kulmala et al., 2006; Sihto et al., 2006; Riipinen et al., 2007). This parameterization also fits the records of nucleation events measured in a variety of continental and marine atmospheric environments well (Kuang et al., 2008). With this new nucleation mechanism, the coupled model is then used to address the following questions in Chapters II and III:

Q1. How well does this empirical nucleation mechanism reproduce observed aerosol sizes and number concentration?

Q2. How do different generation mechanisms of secondary particles (primary-emitted sulfate, nucleation in the upper troposphere, and nucleation in the boundary layer) contribute to CCN concentration?

Q3. How do different generation mechanisms of secondary particles affect the estimation of aerosol indirect effects?

The second half of the dissertation deals with the cirrus cloud treatment. Our understanding of the aerosol indirect effects on cirrus clouds is still very poor and no consensus exists for even the sign of the indirect forcing on cirrus clouds as discussed in section 1.5. One of the primary challenges in studying aerosol indirect effects on cirrus clouds in global models arises from the representation of supersaturation. The supersaturation level in global models is important because it determines when ice nucleation occurs and which freezing modes dominate. In previous global model studies of aerosol indirect effects on cirrus clouds (Lohmann et al., 2002; Hendricks et al., 2005, Liu et al., 2007, and Liu et al., 2009), only grid-mean supersaturation was predicted. But the use of grid-mean supersaturation is not sufficient for ice nucleation in cirrus clouds,

because subgrid-scale fluctuations from small scale motions such as gravity waves are critical in cirrus cloud generation and in determining cirrus cloud properties (Hoyle et al., 2005; Kärcher and Ström, 2003; Hagg and Kärcher, 2004; Jensen and Pfister, 2004).

The subgrid-scale treatment is not only needed for ice supersaturation, but also is desirable in many other processes involved in cirrus cloud formation and decay. Ice crystal number concentration is extremely sensitive to the subgrid-scale cooling rate. Subgrid-scale humidity fields determine whether sublimation or deposition occurs, since both super- or sub-saturation conditions can exist in cirrus clouds. Subgrid-scale ice water information is needed to determine how much of the cloud fraction dissipates in sublimation. However, this kind of subgrid-scale feature is still absent in cirrus cloud treatments in most global models, and this hinders our ability to study aerosol indirect effects on cirrus clouds.

In the second half of the dissertation (Chapter IV), a statistical cirrus cloud scheme is implemented (Kärcher and Burkhardt, 2008, hereafter KB08) in the atmospheric circulation model component (NCAR CAM3) of a coupled model to better represent the subgrid-scale supersaturation. This statistical cirrus cloud scheme has subgrid-scale features for clear sky supersaturation and in-cloud total water, which improves the treatment of ice freezing and cloud decay. This scheme also has a consistent treatment for cloud fraction and ice freezing, which is absent in most indirect effect studies on cirrus clouds (e.g., Lohmann et al., 2002; Hendricks et al., 2005; Liu et al., 2009). The consistent treatment between cloud fraction and ice freezing makes the study of heterogeneous IN effects on cloud fraction possible. With this new cloud scheme, the coupled model is then used to address the following questions:

Q4. How well does the model reproduce observed supersaturation? Supersaturation levels are important since this determines whether freezing occurs and which freezing mode dominates.

Q5. How do different IN concentrations change cirrus cloud properties (e.g., ice crystal number concentration, effective radius, ice water, and cloud fraction)?

Q6. How do changes in mesoscale dynamics (i.e., subgrid-scale temperature perturbations) affect cirrus cloud properties, and how does this effect compare with changes induced by different IN concentrations?

In Chapter II, the coupled aerosol and atmospheric circulation model used in this dissertation is described. The empirical boundary layer nucleation mechanism mentioned above is implemented into the aerosol model component. Simulated size-resolved aerosol fields from the coupled model are evaluated by comparing them with observations. The effects of the boundary layer nucleation mechanism, primary emitted particulate sulfate, and a three-mode sulfate aerosol representation of simulated aerosol size and number are evaluated by sensitivity tests.

In Chapter III, we further study how different secondary particle generation mechanisms, include binary homogeneous nucleation in the free troposphere, the empirical nucleation parameterization in the boundary layer, and primary emitted anthropogenic sulfate all contribute to CCN concentration, and to the determination of the fraction of CCN concentration which is anthropogenic. Finally, their impacts on the estimation of the first aerosol indirect effect are investigated.

In Chapter IV, the statistical cirrus cloud scheme in KB08 is implemented in the atmospheric circulation model component of a coupled model. Model results are

evaluated by comparison with observations. In particular, an evaluation of simulated supersaturation is presented by comparing model results with satellite data and aircraft observations. By varying IN number concentrations, we study how different IN concentrations affect cirrus cloud properties. And by varying subgrid scale temperature perturbations, we study how changes in mesoscale dynamics affect cirrus cloud properties. The relative importance between IN concentration and dynamics is then quantified.

The dissertation concludes with a summary of the main results and an outlook for future work in the final chapter.

CHAPTER II

THE COUPLED IMPACT AEROSOL AND NCAR CAM3 MODEL: EVALUATION OF PREDICTED AEROSOL NUMBER AND SIZE DISTRIBUTION

2.1 Introduction

Atmospheric aerosols are an important component of the global climate system and have important climate effects (e.g., direct effects, indirect effects), as discussed in Chapter I. Their climate effects are complicated to study, not only because of the complicated nature in determining aerosol size, number and composition, but also because of dynamical feedbacks involved. Ackerman et al. (2004) showed that increased cloud droplet number concentrations caused by an increase in atmospheric aerosol number concentrations can enhance the entrainment of overlying dry air into stratocumulus clouds in the marine boundary layer, while Guo et al. (2007) showed that when the large-scale subsidence is strong, the growth of cloud tops is suppressed and entrainment drying makes no significant difference. Andreae et al. (2004) showed that the delay in the onset of precipitation, which can be caused by smaller cloud droplets from enhanced aerosol number concentrations, leads to invigoration and restructuring of

clouds. Ramanathan et al. (2005) and Rotstayn et al. (2007) showed that the change in temperature gradients created by anthropogenic aerosols in the Indian Ocean may change the monsoon precipitation in South Asia and Australia. Zhang et al. (2007) showed that enhanced storm track activities in the Pacific Ocean may be related to the increase in anthropogenic aerosol number concentration.

A fully-coupled climate-aerosol model is required to evaluate these rather complicated climate effects. In this chapter, we describe the coupled IMPACT aerosol model (Rotman et al., 2004; Liu et al., 2005) and NCAR CAM3 atmospheric circulation model (Collins et al., 2006a) (see Appendix 2.A for a description of the coupling method). This coupled IMPACT/CAM3 model is the main research tool in this dissertation, and will be used in Chapters III and IV. Aerosol fields from the version of IMPACT that uses a sulfate aerosol microphysics module (Liu et al., 2005) and the standard version of the NCAR CAM3 model are evaluated and some uncertainties associated with the simulation of the aerosol number concentration and its size distribution are investigated. In particular, effects of different generation mechanisms of secondary particles, and effects of different number of modes to represent sulfate particles are examined.

Sub-grid scale nucleation and aerosol growth near strong sources of sulfur emissions are usually represented as pre-existing primary sulfate particles in global aerosol models (Adams and Seinfeld, 2002). Therefore, Liu et al. (2005) assumed that 2% of the emitted anthropogenic sulfur formed sulfate particles prior to mixing within a grid box. Particles also formed as a result of nucleation events in the upper troposphere associated with binary homogeneous nucleation. Boundary layer nucleation events have been postulated to occur as a result of a number of mechanisms (Yu and Turco, 2000; Korhonen et al.,

1999; O'Dowd et al., 2002; Zhang et al., 2004; Kulmala et al., 2006). Here, we add the boundary layer nucleation mechanisms from Kulmala et al. (2006) and Sihto et al. (2006) to the IMPACT model to explore the effect of additional nucleation events on the predicted aerosol size and number concentration. In addition, we explore the impact of different choices for the fraction of sulfate emitted as primary particles. Finally, we investigate the size and number concentration of aerosols associated with using three modes to represent sulfate aerosol instead of the 2-mode representation described in Liu et al. (2005).

The coupled model and emission data are described in section 2.2. Sensitivity tests using different representations for nucleation and primary emissions of sulfate aerosols, as well as the number of sulfate modes included in the microphysics module, are described in section 2.3. Model results from our base case are presented in section 2.4 (global budget and spatial distributions), section 2.5 (comparison with observed mass fields), and section 2.6 (comparison with observed aerosol size and number), respectively. Results from the sensitivity tests are shown in section 2.7. Finally, a summary is presented in section 2.8.

2.2 Model Description

The coupled IMPACT/CAM model used in this study consists of two components: the LLNL/UMich IMPACT aerosol model, and the NCAR CAM3 atmospheric circulation model. The two components of the coupled system are run concurrently using the MPMD (Multiple Processors Multiple Data) mode to exchange aerosol fields and meteorological fields at each advection time step of the IMPACT model. We used 26 vertical levels and a horizontal resolution of 2x2.5 for both CAM3 and IMPACT. The time step for CAM3

was 30 minutes, and that for advection in IMPACT was 1 hour. The time step for aerosol microphysics in IMPACT is dynamically adjustable and can be shorter than one second during a strong nucleation event (Liu et al., 2005; Herzog et al., 2004). In this section, we describe both model components and the emission data used in this study.

2.2.1 LLNL/UMich IMPACT aerosol model

The aerosol model component is based on the LLNL/UMich IMPACT model (Rotman et al., 2004; Penner et al., 1998). In these studies, the IMPACT model was driven by archived meteorological fields from either a general circulation model or assimilated data. In our coupled model system, we replaced these offline meteorological fields with fields generated from the coupled atmospheric general circulation model (NCAR CAM3). Thus, the temperature, pressure, wind speeds, humidity, cloud fraction, cloud water, precipitation, convective mass flux, detrainment rate, and boundary layer height from CAM3 were made available at each time step of the IMPACT model.

The LLNL/UMich IMPACT model (Rotman et al., 2004; Penner et al., 1998) was developed using massively parallel computer architecture, and was extended in Liu and Penner (2002) to treat the mass of sulfate aerosol as a prognostic variable. It was further extended in Liu et al. (2005) to treat the microphysics of sulfate aerosol and the interactions between sulfate and non-sulfate aerosols based on the aerosol module developed by Herzog et al. (2004). The model uses the flux-form semi-Lagrangian (FFSL) advection algorithm of Lin and Rood (1996). Cumulus transport was described in detail by Penner et al. (1998) and vertical diffusion is based on an implicit scheme from Walton et al. (1998).

The LLNL/UMich IMPACT model simulates the microphysics of sulfate aerosol (nucleation, condensation, coagulation) and its interactions with primary emitted non-sulfate aerosols: organic matter (OM), black carbon (BC), dust, and sea salt, using a modal representation of sulfate aerosol microphysics with an arbitrary number of modes (Herzog et al., 2004; Liu et al., 2005). Both mass and number for pure sulfate aerosol are predicted. Here two modes are used for the base case: the nucleation/Aitken mode with particle radius less than 0.05 μm and the accumulation mode with particle radius larger than 0.05 μm. Mineral dust and sea salt are predicted in four bins with radii varying from 0.05-0.63 μm, 0.63-1.26 μm, 1.26-2.5 μm, and 2.5-10 μm. The size distribution within each size bin follows a predefined, fixed distribution with the size distribution of dust represented by a superposition of three lognomal distributions and that of sea salt represented by a superposition of two lognomal distributions. See Table 1, and Liu et al. (2005) for details. This representation results in slight discontinuities in the number concentrations at the edges of the different size bins. Carbonaceous aerosols (OM and BC) are currently represented by a single submicron size bin with separate distributions assumed for biomass burning OM/BC and natural OM and for fossil fuel OM/BC. Both of these are represented by a superposition of three lognormal distributions (Table 2.1).

Sulfuric acid gas (H_2SO_4(g)), which is produced from gas phase chemistry, can nucleate to form new sulfate particles in the nucleation/Aitken mode or condense onto the preexisting sulfate and non-sulfate aerosol particles. In the base case, only binary homogeneous nucleation of H_2SO_4-H_2O following the parameterization of Vehkamäki et al. (2002) is considered. Sulfate particles can coagulate with each other or with non-sulfate particles. The volume mean radius of each mode (pure sulfate aerosol) and each

bin (non-sulfate aerosols) is used to calculate particle diffusion coefficients and coagulation kernels (Herzog et al., 2004). The size distribution for non-sulfate aerosols is fixed and is used to calculate the rates of condensation and coagulation. A separate prognostic variable is used to track the amount of sulfate that condenses or coagulates with the non-sulfate aerosols. The hydrophilic and hydrophobic properties of non-sulfate aerosols are determined by the amount of sulfate coating that is produced through coagulation and condensation of pure sulfate as well as any aqueous phase formation on the non-sulfate particles (Liu et al., 2005). Carbonaceous or mineral dust aerosol particles were assumed to be hygroscopic when there is a coating of more than 10 layers of sulfate molecules (Liu et al., 2005). The sulfate produced from aqueous phase reactions is assumed to be equally distributed among the hygroscopic aerosol particles that are larger than 0.05 μm in radius.

Table 2.1: Size Distribution Parameters for Non-sulfate Aerosols (Table 1 in Liu et al., 2005).

Aerosol component	Ni[a]	Ri, μm	sigma
Fossil fuel OM/BC	0.428571	0.005	1.5
	0.571428	0.08	1.7
	1.0e-6	2.5	1.65
Biomass OM/BC and natural OM	0.9987	0.0774	1.402
	1.306e-3	0.3360	1.383
	2.830e-3	0.9577	1.425
Sea Salt	0.965	0.035	1.92
	0.035	0.41	1.70
Dust	0.854240	0.05	1.65
	0.145687	0.27	2.67
	7.3e-5	4.0	2.40

[a]Ni is the fraction of the total particle number in a given size range and is dimensionless.

Dry deposition is calculated using the module developed by Wang et al. (1998), which employs a resistance-in-series approach to calculate the dry deposition velocity from the aerodynamic resistance and surface resistance (Wesely et al., 1985). Gravitational settling

is taken into account for aerosol species. Wet deposition is calculated using the scavenging module developed by Mari et al. (2000) and Liu et al. (2001) which includes scavenging in convective updrafts and first-order rainout and washout in precipitating columns. The horizontal fractional area of each grid box that experiences precipitation is based on Giorgi and Chamiedes (1986) by assuming a cloud liquid water content of 1.5 g m^{-3} for stratiform clouds and 2.0 g m^{-3} for convective clouds.

Scavenging efficiencies for the accumulation mode sulfate and sea salt are assumed to be 1.0 and the scavenging efficiency of nucleaiton/Aitken mode sulfate is calculated from the Brownian coagulation coefficient (Liu et al., 2005). The scavenging efficiencies of BC, OM, and mineral dust depend on the amount of sulfate coating and the sizes of these aerosols (Liu et al., 2005), but we set the upper and lower limits for scavenging efficiencies in liquid clouds to the scavenging efficiencies for soluble and insoluble species, respectively, from Stier et al. (2005), which are based on the measurements of Henning et al. (2004). The upper (lower) limits are 0.80 (0.30), 0.85 (0.40), and 0.99 (0.6) for BC/OM, fine mode dust (0.06–0.625 μm), and coarse mode dust (0.625-10 μm), respectively. For cirrus clouds, the scavenging efficiencies are set to 0.1 for all aerosol species (Feichter et al., 2004). Variations in this efficiency have a significant impact on upper tropospheric aerosol burdens (Hendricks et al., 2004), but is not considered further in this study. For mixed phase clouds, the cloud water or ice-weighted mean scavenging efficiencies from liquid clouds and cirrus clouds are used.

2.2.2 NCAR CAM3

The NCAR Community Atmospheric Model (CAM3) is a part of the Community Climate System Model (CCSM3) (Collins et al., 2006a, 2006b). We employed CAM3

here in its stand-alone version. The model may be run using one of three dynamical cores, with either an Eulerian spectral, semi-Lagrangian, or finite volume advection scheme. Here the finite volume dynamical core is used. In CAM3, the physics and the finite volume dynamical core are coupled in a time splitting approximation (Williamson, 2002). Cloud liquid and cloud ice are prognostic variables in CAM3 (Boville et al., 2006), which replaced the diagnostic scheme in NCAR CCM3. Since cloud liquid is separated from cloud ice, it is possible to treat the differences in radiative properties and sedimentation properties between liquid and ice clouds. A prescribed aerosol concentration from an off-line calculation of a chemical transport model constrained by an assimilation of satellite retrievals was used to calculate the aerosol optical properties (Collins et al., 2001; Rasch et al., 2001). Cloud droplet number concentrations were prescribed in the precipitation process and in calculating the radiative properties of clouds.

In the coupled CAM-IMPACT aerosol model, the prescribed aerosol concentration from CAM3 was replaced with concentrations calculated in the IMPACT aerosol model; however, in this chapter, the simulated aerosol fields had no effect on the radiation fields or the predicted meteorology because we wished to focus on evaluating the aerosol fields in the coupled model.

2.2.3 Emission data

The emissions of anthropogenic sulfur were developed based on an updated and extended version of the emission data of Smith et al. (2001) (see Smith et al., 2004). In our base case, 98% of anthropogenic sulfur is emitted as gas phase SO_2. The remaining 2% of anthropogenic sulfur is assumed to be emitted as sulfate particles. 85% of the mass is emitted in the accumulation mode with a modal diameter of 70 nm and a geometric

standard deviation of 2.0. The remaining 15% of the mass is emitted in the nucleation/Aitken mode with a modal diameter of 10 nm and a geometric standard deviation of 1.6 (Whiteby, 1978).

Volcanic SO_2 emissions are a 25-year average of sporadic and continuously emitting volcanoes based on Andres and Kasgnoc (1998). Marine DMS fluxes are the average of the high and low estimates from Kettle and Andreae (2000) who used the ocean DMS field compiled by Kettle et al. (1999) and flux formulations based on Liss and Merlivat (1986) and Wanninkhof **(**1992**)**. The natural OM fluxes were derived by assuming that 9% of the terpene emissions developed by Guenther et al. (1995) were rapidly converted to OM (Penner et al., 2001). Emissions of fossil fuels and biofuel carbonaceous aerosols were from the year 2000 emissions of Ito and Penner (2005), with some adjustments. In particular, we compared the simulated surface concentrations from IMPACT using the fossil fuel emissions in 2000 with surface observations and derived a scaling factor of 2.3 over East Europe and a scaling factor of 1.45 over Asia. Fossil fuel BC emissions are highly uncertain (Bond et al., 2004; Novakov et al., 2003; Ito and Penner, 2005). The fossil-fuel inventory we use is an update to the year 2000 data developed by Bond et al. (2004), and is about a factor of two lower than inventories that are thought to give smaller absorption in the atmosphere than that deduced from the analysis of sun-photometer data (Sato et al., 2003). We assumed that both fossil fuels and biofuel aerosols are emitted into the surface layer. The year 2000 open biomass burning emissions were developed using the inverse method described by Zhang et al. (2005), together with an a priori estimate of the emissions for the year 2000 based on scaling the bottom-up aerosol emission inventory estimate of Ito and Penner (2005) with the ratio of

the CO emissions from the inverse study of Arellano et al. (2004) and the bottom-up study of Ito and Penner (2005). The open biomass emissions were emitted uniformly into the boundary layer.

Sea salt emissions are calculated online in the coupled model using the method defined in Gong et al. (1997) based on the 10 m wind speeds from CAM3, with sea salt particles injected into the lowest model layer. Dust emissions were not calculated based on the CAM3 model wind speeds, but from emission fluxes provided by Ginoux (private communication, 2004) at a 6 hour interval. These emission fluxes were developed using the method described in Ginoux et al. (2001) based on the 10 m wind speed and soil wetness calculated by the GFDL GCM nudged by NCEP meteorological fields. The emission flux is similar to that described by Ginoux et al. (2001) with the formula for the threshold wind velocity defined as in Ginoux et al. (2004). These prescribed dust fluxes were used because the use of the Ginoux et al. (2001) emission parameterization with CAM3 wind speeds did not capture the right seasonal variation of dust concentrations near the Sahara desert. Dust is assumed to be uniformly injected into the boundary layer.

2.3 Sensitivity tests

There are large uncertainties in simulated aerosol particle number concentrations and size in global model studies (Spracklen et al., 2005a). We used five additional simulations to study the sensitivity of aerosol number and size to the use of primary emitted sulfate particles used to simulate nucleation in sub-grid scale plumes, to the inclusion of boundary layer nucleation mechanisms, and to the use of a three-mode representation of sulfate aerosol. The descriptions of these five runs are presented here,

and comparisons with the base case, as well as with observations, are presented in section 2.7.

2.3.1 Primary emission of sulfate particles used to represent the effect of sub-grid scale nucleation

In the base case, 2% of anthropogenic sulfur is assumed to be emitted as primary sulfate particles. Most global model studies that predict both aerosol mass and number have included some fraction of sulfate emissions as primary-emitted sulfate to represent nucleation in sub-grid scale plumes (Liu et al., 2005; Easter et al., 2004; Stier et al., 2005; Adams and Seinfeld, 2002; Spracklen et al., 2005a, 2007; Pierce and Adams, 2006, 2007). The size distribution and total amount of the primary-emitted particulate sulfate should account for all microphysical processes that occur within sub-grid scale plumes (nucleation, condensational growth, and coagulation) (Adams and Seinfeld, 2003), as well as any sulfate particles emitted directly from the source. In the model of Adams and Seinfeld (2002), the primary-emitted particulate sulfate is also used as a surrogate for other non-sulfate primary particles.

Observations provide little constraint on how much sulfur should be emitted as primary particles or what size to assume in a global model. Observed mass conversion rates from gas-phase SO_2 to particulate sulfate in power plant plumes range from near zero to 6%/hour in clear conditions (Hewitt et al., 2001), and most of the H_2SO_4 that is formed undergoes condensation rather than nucleation. The mass conversion rate also strongly depends on sunlight exposure.

The absence of constraints by observations leads to large uncertainties with respect to the treatment of the amount of the sulfur and the size distribution of particles emitted as

particulate sulfate in global model studies. Some models have used the size distribution from Whitby (1978) (two modes: 0.01 μm and 0.07 μm in diameter) for anthropogenic particulate sulfate emissions, but different amounts are assumed (2% of anthropogenic sulfur in Liu et al., (2005) and Easter et al., (2005); 3% in Adams and Seinfeld (2002), Pierce and Adams (2006; 2007), and Spracklen et al., (2007)). Stier et al. (2005; 2006) used larger sizes for ship, industrial, and power plant emissions (two modes: 0.15 μm and 1.5 μm in diameter) and smaller sizes for other sources (two modes: 0.06 μm and 0.15 μm in diameter), and assumed that 2.5% of anthropogenic sulfur is emitted as particles. Lauer et al. (2005) did not assume any primary-emitted particle sulfate, but this was partly compensated for by the large number concentrations of primary fossil fuel BC particles which were very small in their model (75% of the fossil fuel BC mass had a modal diameter of 0.02 μm).

Although primary-emitted sulfate particles have little impact on the simulated sulfate aerosol mass, they can have a large impact on the simulated sulfate aerosol number (Adams and Seinfeld, 2002, 2003; Spracklen et al., 2005a). Adams and Seinfeld (2002) used a model that only included sulfate and showed that the inclusion of 3% of the sulfur emissions as primary-emitted particulate sulfate almost doubled the predicted number concentration of CCN in the planetary boundary layer and improved the comparison between the model and the observations compared to a case with no primary emissions. Spracklen et al. (2005a) used a model that only included sulfate and sea salt and confirmed the large increase in the aerosol number concentration when 3% of the sulfur emissions were treated as primary-emitted sulfate particles. Stier et al. (2006), on the other hand, used a size distribution for primary-emitted sulfate aerosols that was more

aged than that used by Spracklen et al. (2005a) and Adams and Seinfeld (2002). They showed that anthropogenic sulfate increases the global mean number burden of the soluble nucleation, Aitken, and accumulation modes by 8%, 20%, and 27%, respectively. They did not specifically analyze the increase in the number concentration associated with the primary emission of sulfate particles. The specific impact of primary sulfate particles on number concentrations is likely a function of the assumed size distribution and the degree of aging. Here, our use of the Whitby size distribution is guided by the fact that it represents an average continental size distribution which would account for aging during sub-grid scale processes, but we cannot rule out that either less or more aging of the distribution might be appropriate within the grid box in which they are emitted.

In order to examine the sensitivity of the simulated aerosol size distribution to the assumed primary-emitted particulate sulfate fraction, we examined a case (denoted as '0%SO2') in which no sulfur is emitted as primary particles and all sulfur is emitted as gas phase SO_2. In contrast to the studies by Adams and Seinfeld (2002, 2003) and Spracklen et al. (2005a), our model study includes all major primary aerosol particle types: organic carbon, black carbon, dust, and sea salt.

2.3.2 Boundary layer nucleation

In the base case, only binary homogeneous nucleation (Vehkamäki et al., 2002) is included. Nucleation by this mechanism occurs most frequently in the upper troposphere and over polar regions, where favorable conditions (low temperature and low pre-existing particle surface area) occur (Lucas and Akimoto, 2006). However, a variety of observations have shown that nucleation events are common in the planetary boundary

layer (Kulmala et al., 2004; Koponen et al., 2003; Vehkamäki et al., 2004; Dal Maso et al., 2005; Laaksonen et al., 2005; O' Dowd et al., 1999). Several nucleation mechanisms, including ion-mediated nucleation (Yu and Turco, 2000), ternary homogeneous nucleation involving ammonia, sulfate, and water (Korhonen et al., 1999), nucleation involving iodine species (O'Dowd et al., 2002), and nucleation involving organics (Zhang et al., 2004) have been suggested as being important in the boundary layer, but no agreement has been reached about the relative importance of different nucleation mechanisms.

Sihto et al. (2006) fit the observed time rate of change of particles in the 3 to 6 nm range at Hyytiälä, Finland, with either a linear or a quadratic function of the observed sulfuric acid gas concentration. The quadratic empirical fit is appropriate for a kinetic nucleation mechanism, in which two molecules containing sulfuric acid collide to form a stable cluster (McMurry and Friedlander, 1979). The linear fit is appropriate for an activation nucleation mechanism (Kulmala et al., 2006) in which a cluster containing a single sulfuric acid molecule together with other molecules is activated by heterogeneous nucleation or heterogeneous chemical reactions. Spracklen et al. (2006) applied the linear empirical formula from Kulmala et al. (2006) to relate the nucleation rate in the boundary layer to the sulfuric acid concentration in their global aerosol model, and demonstrated that this mechanism could be important in determining the regional and global aerosol number concentration.

We implemented both the linear and quadratic empirical formulas in the global model to examine their impacts on the aerosol number concentration. Following Spracklen et al.

(2006), we first calculate the nucleation rate of 1 nm particles from Kulmala et al. (2006) and Sihto et al. (2006) as:

$$j_{1nm}=A(H_2SO_4) \quad (2.1)$$

or

$$j_{1nm}=K(H_2SO_4)^2, \quad (2.2)$$

where A (1.0^{-6}/s) and K (1.0^{-12} cm^3/s) are rate constants chosen from the median values derived in case studies (Sihto et al., 2006). Then we used the formula from Kerminen and Kulmala (2002) to calculate the rate of formation of 3 nm particles:

$$j_{3nm}=j_{1nm}\, exp(-0.66\gamma CS/GR), \quad (2.3)$$

where CS is the reduced condensation sink (m^{-2}), GR is the growth rate (nm/h), and γ is a proportionality factor (m^{2}nm/h). The reduced condensation sink (CS) is calculated by summing over all aerosol modes and/or bins j:

$$CS = \sum_j \beta_j r_j N_j \,, \quad (2.4)$$

where β_j is the transitional correction factor for the condensational mass flux, N_j is the number concentration in the size class j, and r_j is the volume-mean particle radius. The growth rate (GR) is calculated as in Kerminen and Kulmala (2002) by summing over all condensable gases i:

$$GR = \frac{3.0*10^{-9}}{\rho} \sum c_i M_i C_i \,, \quad (2.5)$$

where c_i is the mean molecular speed of the condensing vapor (m s^{-1}), M_i is the molecular weight (g mole^{-1}), C_i is the gas phase concentration of condensing vapor (molecules cm^{-3}), and ρ is the density of the nuclei (kg m^{-3}). In this study, the only condensing vapor is

sulfuric acid gas. The proportionality factor γ is the semi-empirical formula derived in Kerminen and Kulmala (2002):

$$\gamma = 0.23(\frac{d_{mean}}{150})^{0.048}(\frac{\rho_{nuc}}{1000})^{-0.33}(\frac{T}{293})^{-0.75}. \quad (2.6)$$

Here d_{mean} is the number mean diameter of the pre-existing particle population (nm), ρ_{nuc} is the density of the nuclei (kg/m^3), and T is the ambient temperature (K). In this study we assume γ=0.23 m^{2}nm/h as an approximation.

Three additional simulations are added to investigate how these boundary layer nucleation mechanisms affect the simulated aerosol size and number. In the case denoted as '2%SO2+Act', the boundary layer nucleation mechanism in Equation 2.1 (known as the activation mechanism) is added to the base case. Spracklen et al. (2005b) showed that binary homogeneous nucleation has little effect on simulated marine boundary layer aerosol number concentrations, so we have replaced the binary homogeneous nucleation mechanism with the empirical boundary layer nucleation scheme in the boundary layer, and have disallowed competition between binary nucleation and the empirical boundary layer nucleation mechanisms. This approximation may miss some areas (such as polar regions in winter) where binary homogeneous nucleation may dominate the empirical boundary layer nucleation scheme used here, but these areas are relatively small. In the case denoted as '0%SO2+Act', the empirical boundary layer nucleation in Equation 2.1 is added to the case of '0%SO2', replacing the binary homogeneous nucleation mechanism in the boundary layer. In the case denoted as '0%SO2+Kin' (known as the kinetic mechanism), Equation 2.2 instead of Equation 2.1 is used to replace the binary homogeneous nucleation rate in the boundary layer.

2.3.3. The three-mode representation for sulfate aerosol

In our base case, two modes are used to represent pure sulfate aerosol: a nucleation/Aitken mode (radius < 0.05μm) and an accumulation mode (radius > 0.05μm), which is similar to the study of Lauer et al. (2005). While our 2-mode representation is able to capture some of the variability of the aerosol size distribution (Liu et al., 2005), a 3- or 4-mode representation would be more realistic and, therefore, expected to perform better compared with observations. For example, a 4-mode version of our aerosol microphysics module was shown to be in better agreement with a sectional model than the 2-mode version in box model intercomparisons (Herzog et al., 2004). Lauer et al. (2005) also suggested that a 3-mode representation of the aerosol size distribution with an additional mode representing nucleation sizes (i.e., radius < 5 nm), to attempt to better simulate an aged Aitken mode. Therefore, in the '3-mode' case, we used the 3-mode version of our aerosol microphysics module in the IMPACT aerosol model with an additional mode at nucleation sizes. Aerosol particles from nucleation are grouped into the nucleation mode and the primary-emitted sulfate particles are grouped into the Aitken mode (5 nm < radius < 50 nm) and the accumulation mode (radius > 50 nm).

Table 2.2 lists all sensitivity tests along with the base case. In addition to the above cases, the case 'NOBHN' was included. This is the same as the base case except that binary homogeneous nucleation is turned off above the boundary layer. This case is examined to study the extent to which binary homogeneous nucleation above the boundary layer affects the simulated mass profile in the upper troposphere in section 2.5.2.

Table 2.2: Description of cases.

Case name	Within BL[a]	Within FT[b]	Primary sulfate	Number of modes for pure sulfate	Integration time (years)
Base-5yrs	BHN[c]	BHN	2%SO2[f]	2	5
Base-1yr	BHN	BHN	2%SO2	2	1
0%SO2	BHN	BHN	0%SO2[g]	2	1
0%SO2+Act	BL1st[d]	BHN	0%SO2	2	1
0%SO2+Kin	BL2nd[e]	BHN	0%SO2	2	1
2%SO2+Act	BL1st	BHN	2%SO2	2	1
3-mode	BHN	BHN	2%SO2	3	1
NOBHN	BHN	No FT nucleation	2%SO2	2	1

[a]Boundary layer.
[b]Free troposphere.
[c]Binary homogeneous nucleation (scheme of Vehkamäki et al., 2002).
[d]Boundary layer nucleation using Equation 2.1.
[e]Boundary layer nucleation using Equation 2.2.
[f]2% of anthropogenic SO_2 emissions are input as primary sulfate.
[g]0% of anthropogenic SO_2 emissions are input as primary sulfate.

All simulations used climatological sea surface temperatures. In the base case the coupled model was integrated for 5 years after an initial spin-up time of four months and monthly average data were used. In the sensitivity tests, the model was only integrated for 1 year after an initial spin-up of four months in order to save computational costs. Since the aerosol fields are not allowed to change heating rates or droplet number concentrations in the climate model, the aerosol fields do not affect the simulated meteorological fields. Therefore, the meteorological fields are the same for all the first year simulations, which allows us to make comparisons of different cases from only one year of simulation.

Table 2.3: Global budget for sulfate aerosol.

	This study	AeroCom
Sources (Tg S yr^{-1})	60.03	59.67[a](22[b])
Emission	1.23	
Gas-phase SO_2 oxidation	18.01	
Aqueous-phase SO_2 oxidation	40.79	
Burden (Tg S)	0.84	0.66 (25)
H_2SO_4(g) (%)	0.03	
Nuclei and accu.[c] mode sulfate (%)	5.93, 72.64	
On carbonaceous aerosols (%)	15.98	
On dust bins 1-4 (%)	2.96, 0.44, 0.18, .0054	
On sea salt bins 1-4 (%)	1.69, 0.11, 0.04, .0003	
Above 5km(%)	39.90	32.23 (36)
Polar (%)[d]	1.30	5.91 (55)
Lifetime (days)	5.08	4.12 (18)
Rate coefficient for removal ($days^{-1}$)	0.20	0.25 (18)
Wet	0.18	0.22 (22)
Dry	0.01	0.03 (55)
Wet (%)	93.41	88.50 (8)

[a]The mean value from available models in AeroCom. See Textor et al. (2006), Table 10 for details.
[b]The coefficient of variation x100 (standard deviation/model-mean expressed as a percentage) in AeroCom. See Textor et al. (2006), Table 10 for details.
[c]accu.: Accumulation.
[d]South of 80ºS and north of 80ºN.

2.4 Model Results

2.4.1 Annual and global budgets

The global budgets of the simulated aerosols and their precursor species are shown in Tables 2.3-2.6. Also listed are the average, median, and standard deviation of all available models from the model intercomparison study in the Aerosol Model Intercomparison Initiative (also known as AeroCom). See Textor et al. (2006), Table 10 for details. More than a dozen models were included in the AeroCom intercomparison study.

Table 2.4: Global budget for OM and BC.

	this study	AeroCom
OM		
Sources (Tg yr^{-1})	77.52	96.60[a](26[b])
Fossil fule emission	15.67	
Biomass burning emission	47.39	
Photochemistry from terpenes	14.46	
Burden (Tg)	0.99	1.70 (27)
Above 5km(%)	14.46	20.40 (56)
Polar[c] (%)	0.29	3.27 (76)
Lifetime (days)	4.66	6.54 (27)
Rate coefficient for removal ($days^{-1}$)	0.21	0.16 (4)
Wet	0.19	0.14 (32)
Dry	0.02	0.03 (49)
Wet(%)	89.21	79.90 (16)
BC		
Sources (Tg yr^{-1})	10.51	11.90 (23)
Fossil fuel emission	5.80	
Biomass burning emission	4.71	
Burden (Tg)	0.13	0.24 (42)
Above 5km (%)	14.25	21.20 (52)
In polar[c] (%)	0.38	4.18 (71)
Lifetime (days)	4.39	7.12 (33)
Removable rate ($days^{-1}$)	0.23	0.15 (21)
Wet	0.20	0.12 (31)
Dry	0.03	0.03 (55)
Wet (%)	88.17	78.60 (18))

[a]The mean value from available models in AeroCom. See Textor et al. (2006), Table 10 for details.
[b]The coeffiecient of variation ×100 (standard deviation/model-mean expressed as a percentage in AeroCom. See Textor et al. (2006), Table 10 for details.
[c]South of 80ºS and north of 80ºN.

The model predicts that 78.6% of the total sulfate mass is pure sulfate aerosol (5.9% in the nucleation/Aitken mode and 72.6% in the accumulation mode) with the remaining sulfate mass (21.4%) coated on non-sulfate aerosols (16% on carbonaceous aerosol, 3.6% on dust, and 1.8% on sea salt). The model predicts a smaller sulfate fraction in the nucleation/Aitken mode (5.9% vs. 9.7%) than in Liu et al. (2005) in part because there is a smaller contribution of gas-phase SO_2 oxidation to the sulfate source (30% vs. 34% in

Liu et al. (2005)). The total source of sulfate is 60.03 Tg/year, similar to the mean of the AeroCom models (Textor et al., 2006). The model has a larger burden of sulfate aerosol, 0.84 Tg S, compared to 0.60 Tg S in the AeroCom models, which is due to smaller wet and dry removal rate coefficients in our model.

39.9% of the sulfate mass is located above 5 km, which is similar to the mean of the AeroCom models (32.23%). But the model predicts much less sulfate in polar regions (south of 80ºS and north of 80ºN) compared to that in the AeroCom models: only 1.30% compared to 5.91% for AeroCom. This is also true for the other aerosol species (see below). This may point to differences in the wet removal mechanism as well as to differences in the efficiency of transport to the poles between our model and the other models that participated in AeroCom.

Table 2.4 shows the budget for carbonaceous aerosols. The OM burden is 0.99 Tg, which is about two-thirds that of the mean of the AeroCom models. The burden of BC is 0.13 Tg, which is about half of that in AeroCom. The smaller burdens (and shorter lifetimes) in our model are mainly due to the larger removal rate coefficients from wet scavenging. The hygroscopic properties of carbonaceous aerosols in our model are based on the amount of sulfate coated on these initially hydrophobic aerosols. As pointed out in Liu et al. (2005), most carbonaceous aerosols in our model are internally mixed with sulfate and generally hygroscopic except near the source regions, which makes the wet removal rate of carbonaceous aerosols larger than that in many other models. Liu et al. (2005) showed that the global mean aging time for carbonaceous aerosols using our treatment is about 1.8 days which is smaller than the aging time of 2-4 days typically used in models that do not account for the physical processes that lead to the coating of

Table 2.5: Global budget for dust.

	this study					AeroCom
Size (μm)	0.05-0.63	0.63-1.25	1.25-2.50	2.50-10.0	Total	Total
Emission (Tg yr^{-1})	76.57	291.54	662.59	1325.20	2355.90	1840.00[a] (1640.00[b], 49[c])
Burden (Tg)	1.60	5.99	10.92	4.62	23.14	19.20 (20.50, 40)
Fine mass[d] (%)	-	-	-	-	3.76	20.80 (10.80, 114)
Above 5km(%)	11.12	10.71	9.28	4.04	8.73	14.10 (14.10, 51)
Polar[e] (%)	0.30	0.29	0.24	0.05	0.22	1.54 (1.00, 102)
Lifetime (days)	7.65	7.51	6.02	1.27	3.59	4.14 (4.04, 43)
Removal rate coefficient ($days^{-1}$)	0.13	0.13	0.17	0.79	0.28	0.31 (0.25, 62)
Wet	0.11	0.11	0.12	0.11	0.12	0.08 (0.09, 42)
Dry	0.02	0.02	0.05	0.68	0.16	0.23 (0.16, 84)
Wet (%)	87.65	86.01	71.00	13.97	41.31	33.00 (31.70, 54)

[a]The mean value from available models in AeroCom. See Textor et al. (2006), Table 10 for details.
[b]The median value from available models in AeroCom. See Textor et al. (2006), Table 10 for details.
[c]The coefficient of variation x100 (standard deviation/model-mean expressed as a percentage) in AeroCom. See Textor et al. (2006), Table 10 for details.
[d]Particles with radius < 0.5 μm.
[e]South of 80ºS and north of 80ºN.

Table 2.6: Global budget for sea salt.

	this study					AeroCom
Size (μm)	0.05-0.63	0.63-1.25	1.25-2.50	2.50-10.0	Total	Total
Emission (Tg yr^{-1})	114.18	437.71	947.62	1097.90	2597.41	166000.00[a] (6280.00[b], 199[c])
Burden (Tg)	0.43	1.59	2.62	0.47	5.10	7.52 (6.37, 54)
Fine mass[d] (%)	-	-	-	-	4.79	14.60 (8.72, 118)
Above 5km (%)	3.45	3.15	2.39	0.49	2.54	8.65 (6.94, 92)
Polar[e] (%)	1.26	1.13	0.78	0.07	0.86	3.32 (1.88, 140)
Lifetime (days)	1.37	1.32	1.01	0.16	0.71	0.48 (0.41, 58)
Removal rate coefficient ($days^{-1}$)	0.73	0.76	0.99	6.35	1.39	5.07 (2.50, 188)
Wet	0.65	0.66	0.70	1.09	0.72	0.79 (0.68, 77)
Dry	0.08	0.10	0.29	5.26	0.67	4.28 (1.40, 219)
Wet (%)	89.16	87.27	71.02	17.20	51.80	30.50 (30.30, 65)

[a]The mean value from available models in AeroCom. See Textor et al. (2006), Table 10 for details.
[b]The median value from available models in AeroCom. See Textor et al. (2006), Table 10 for details.
[c]The coefficiet of variation x100 (standard deviation/model-mean expressed as a percentage) in AeroCom. See Textor et al. (2006), Table 10 for details.
[d]Particles with radius < 0.5 μm.
[e]South of 80ºS and north of 80ºN.

hydrophobic aerosols by sulfate. The rate coefficient for wet removal of carbonaceous aerosols is about 0.19/day in the model, compared with 0.13/day for the mean of the AeroCom models. In addition, the emissions of carbonaceous aerosols in our model are smaller than the mean of the emissions in the AeroCom models, which also contributes to the smaller burden. About 14% of the carbonaceous aerosol burden is above 5 km in our model, compared with about 21% in AeroCom. This is consistent with the larger rate coefficient for wet removal in our model. The mass fractions of OM and BC at the poles are 0.29% and 0.38%, respectively, which is much smaller than the corresponding fractions (3.27% for OM and 4.18% for BC) in AeroCom. The differences at the poles are associated with the larger rate coefficient for wet removal of carbonaceous aerosols in the model, but are probably also due to transport differences.

The total burden of mineral dust (Table 2.5) is 23.14 Tg, which is slightly larger than that from the mean of the AeroCom models (19.20 Tg). The mass fraction of fine-mode mineral dust (diameter < 1μm) is 3.76 % in our model compared with 20.80 % for the mean of the AeroCom models. The smaller fine-mode mass fraction in our model partly results from the larger rate coefficient for wet removal. Wet scavenging is the dominant removal mechanism for fine-mode mineral dust particles but is less important relative to settling and dry deposition for coarse-mode particles. Therefore, a larger wet removal rate will lead to a smaller fine-mode mass fraction. The larger wet removal rate is caused by the coating of dust particles by sulfate. Sulfate coated on mineral dust increases its hygroscopicity and increases the rate coefficient for wet removal, which is 0.12/day and contributes 41.31% to the total removal rate coefficient for dust in the model. The wet removal rate coefficient in the AeroCom models is 0.08/day, or 33% of the total removal

rate coefficient for dust. The size range of the emitted particles in our model can also result in a smaller fine-mode mass fraction. As shown in Textor et al. (2006), the PNNL model used the same Ginoux et al. (2001) total emission flux as in our model, but they assumed that dust particles are emitted at only two sizes: 0.31 and 2.81 μm in diameter, resulting in a much higher fine-mode mass fraction (34%). The mass fraction for dust above 5 km is 8.73% compared to a mean of 14.1% in AeroCom. The mass fraction at the poles is 0.22%, which is only about one-seventh that of the value in AeroCom (1.54 %).

The total burden for sea salt aerosol (Table 2.6) is 5.10 Tg, which is smaller than the mean in the AeroCom models (7.52 Tg). The mass fraction of sea salt aerosol in the fine-mode is 4.79 % compared to 14.6% in the AeroCom models. The larger mass fraction in AeroCom mainly results from the large mass fraction of fine-mode aerosols in the GISS model, which is about 70%. The lifetime of sea salt aerosols is 0.71 days, which is 50% larger than the mean of the AeroCom models (0.48 day). The longer lifetime in our model is from the smaller rate coefficient for dry removal. The total rate coefficient for wet removal is almost the same as that for dry removal in our model, but in the AeroCom models the dry removal rate coefficient is several times that of the wet removal rate coefficient. This may partly result from the smaller mass fraction (9.2%) in the supercoarse mode (radius > 2.5 μm) in our model. The mass fraction for sea salt above 5 km is 2.54% compared to 8.65% in the AeroCom models and the mass fraction at the poles is 0.86% compared to 3.32% in the AeroCom models.

2.4.2 Global and vertical distributions

Figures 2.1 and 2.2 show the vertically integrated annual mean mass concentrations and zonally averaged annual mean mass concentrations for sulfate, OM, BC, dust, and

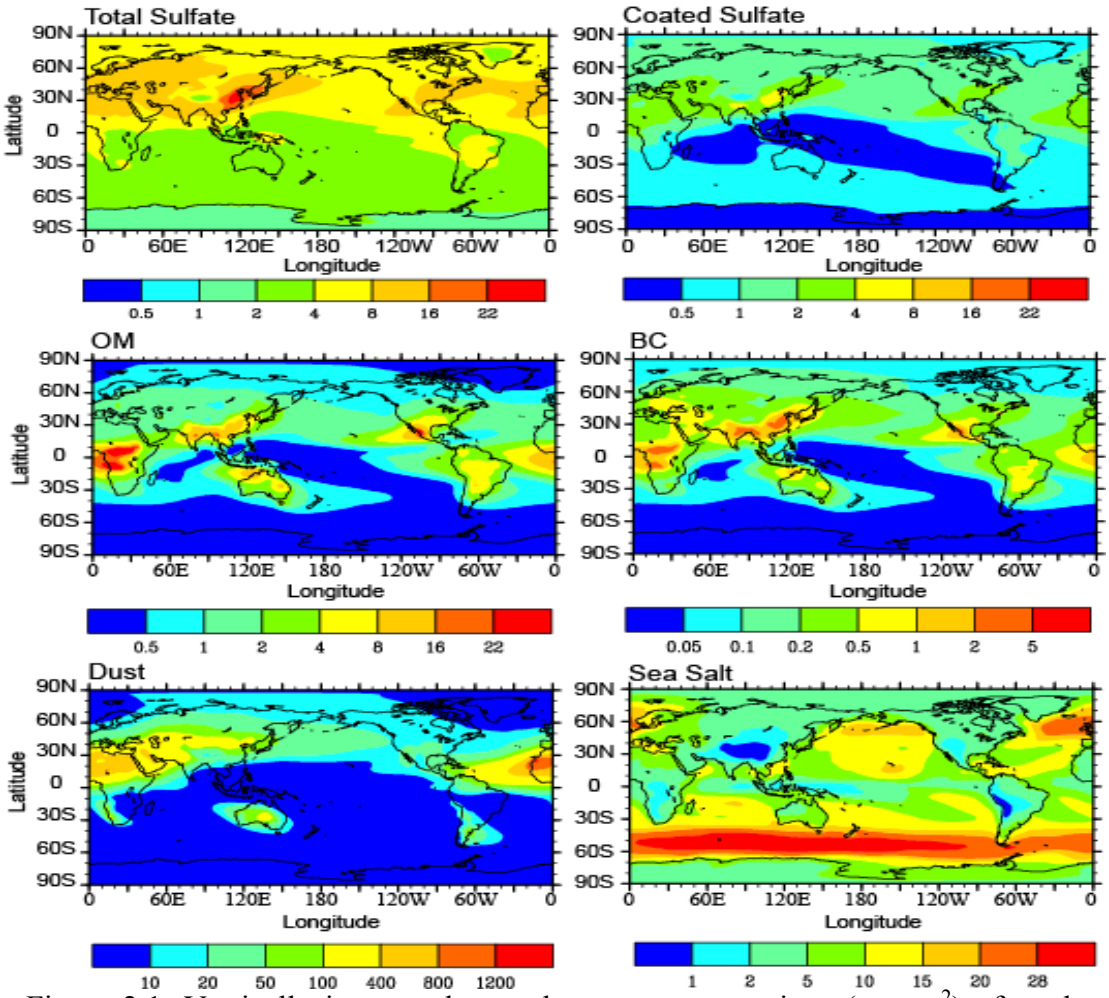

Figure 2.1: Vertically integrated annual mean concentrations (mg m^{-2}) of total sulfate, sulfate associated with nonsulfate aerosols, and OM, BC, dust, and sea salt predicted by the model.

sea salt aerosols. The dominant contributions to the burden and concentrations of total sulfate come from anthropogenic sources, which are mainly located in the industrial regions in the Northern Hemisphere (NH). As a secondary aerosol, the sulfate concentrations extend further north than the primary particles (OM, BC, dust, and sea salt). Carbonaceous aerosols show strong contributions from both biomass burning emissions (e.g., Central Africa, Central and South America, and Australia) and fossil fuel emissions (e.g., China, India, Turkey, and Eastern Europe). The vertical transport of

carbonaceous aerosols is efficient, in part because of the uniform injection of biomass

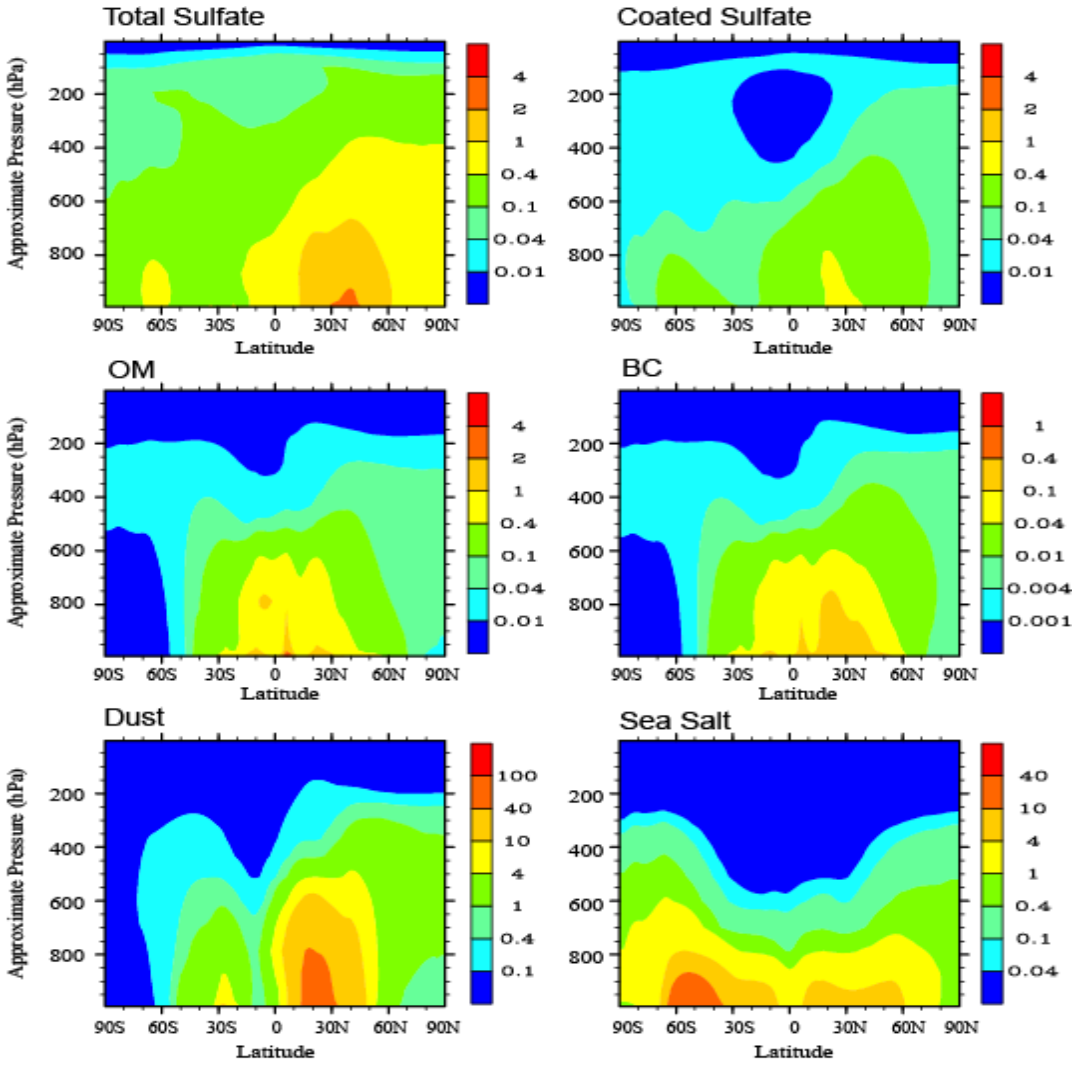

Figure 2.2: Annual averaged zonal mean concentration (μg/m^3) of OM, BC, dust, and sea salt predicted by the model. CAM3 used a hybrid vertical coordinate and the pressure at the kth model level is given by $p(k)=A(k)p_0+B(k)p_s$, where p_s is surface pressure, p_0 is a specified constant pressure (1000 hPa), A and B are coefficients. Data are plotted as a function of this hybrid vertical coordinate times 1000 and labeled 'Approximate Pressure'.

burning carbonaceous aerosols in the boundary layer and in part because they are smaller than dust and sea salt aerosols and do not experience as much gravitational settling. They also show strong transport towards the poles in the middle troposphere, which results in higher concentration in the middle troposphere than in the lower troposphere over polar

regions. Dust aerosol shows a distinct maximum extending from sources in the African Sahara towards the Atlantic Ocean and Central America, and a second maximum extending from the middle of Asia towards the North Pacific. Dust also has strong vertical transport. Sea salt aerosol shows large concentrations over the storm tracks in the middle latitudes of both hemispheres where surface wind speeds are large. Its concentration decays rapidly with altitude, in part because of the large settling velocity of these aerosols as well as their effective wet removal. Sulfate aerosol coated on non-sulfate aerosols depends on the concentrations of both sulfuric acid gas and non-sulfate aerosols. It is not surprising that the amount of sulfate aerosol coated on non-sulfate aerosols is large over East Asia, India, North Africa, the Eastern U.S., and the 60ºS latitude belt, where the concentrations of both non-sulfate aerosols and sulfuric acid gas concentrations are large.

Figure 2.3 shows the model predicted zonal mean number concentrations of pure sulfate aerosol in the nucleation/Aitken and accumulation modes in January and July. There is a distinct maximum in the number concentration of the nucleation/Aitken mode in the tropical upper troposphere in both January and July. This maximum results from strong nucleation events in the upper troposphere, due to the favorable conditions there (very low temperature and low pre-existing aerosol surface area, see Liu and Penner (2002)). Another maximum can be seen at NH middle latitudes in the region close to the surface, which is due to the direct emission of primary sulfate from anthropogenic sources. The depletion of aerosol particles in the nucleation/Aitken mode in the lower troposphere of the Southern Hemisphere (SH) near 60°S comes from the scavenging of H_2SO_4 gas and the coagulation of nucleation/Aitken mode particles with sea salt particles,

which have large concentrations there (Figures 2.1 and 2.2). Large concentrations in the accumulation mode in the NH lower troposphere come from the direct primary emissions of anthropogenic sulfate particles, and from the growth of particles in the nucleation/Aitken mode.

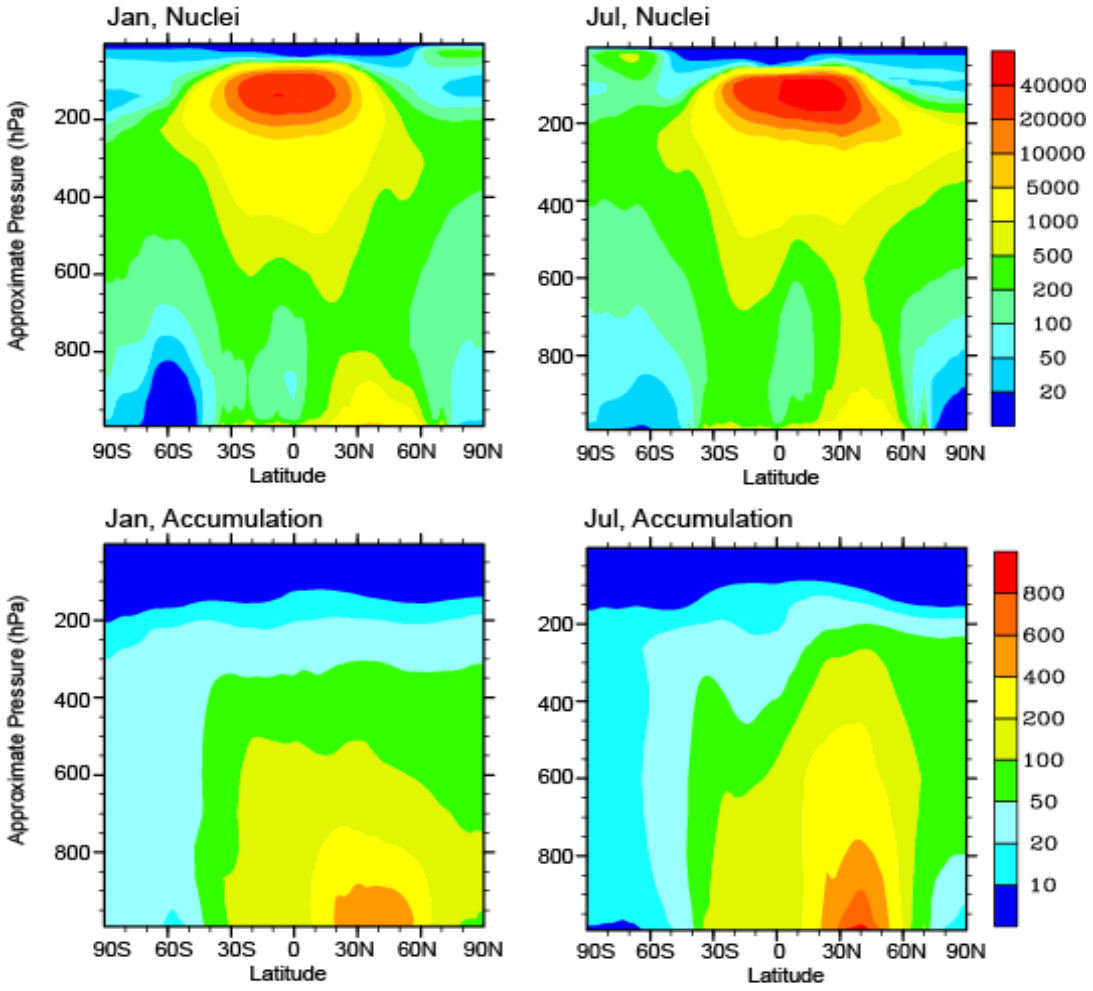

Figure 2.3: Model predicted zonal mean number concentration (#/cm^3) of pure sulfate aerosol in the nuclei (upper panel) and accumulation mode (lower panel) in January (right) and July (left). 'Approximate Pressure' is defined in the caption to Figure 2.2.

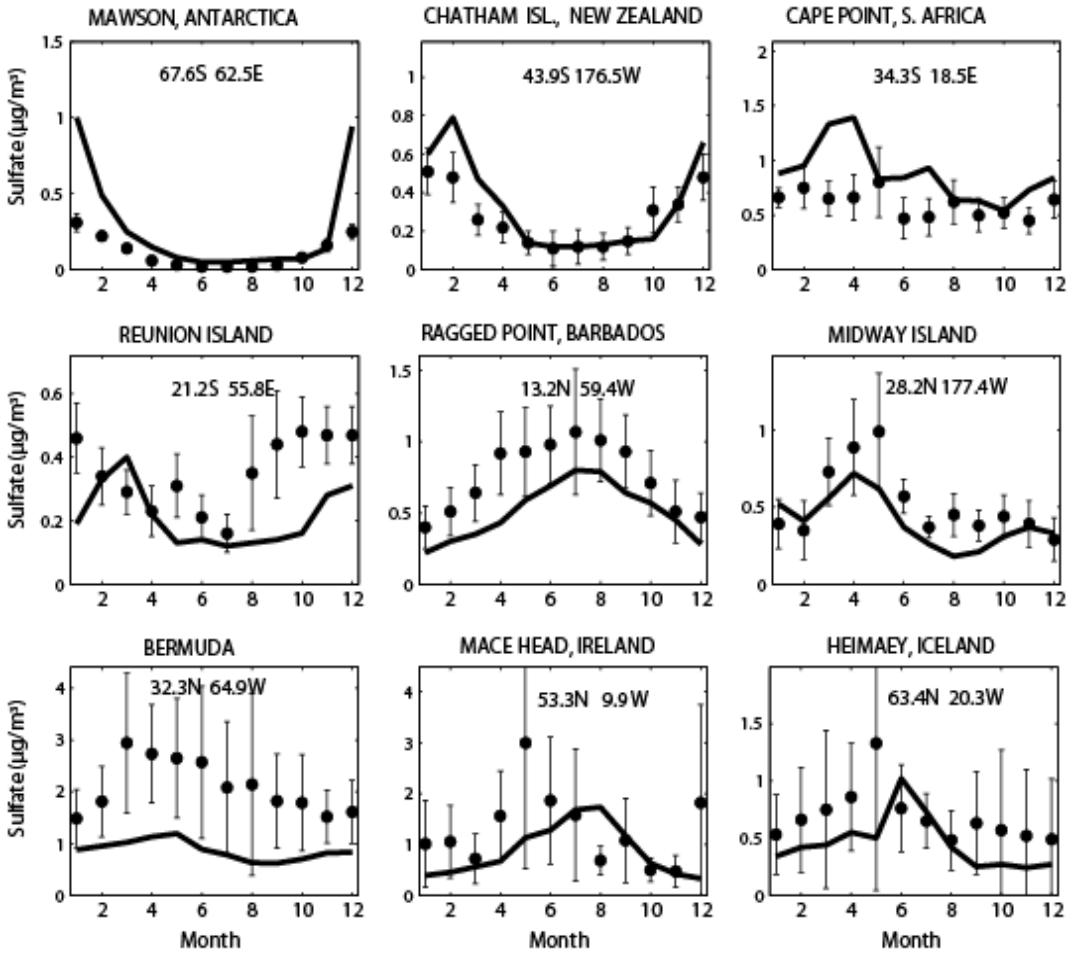

Figure 2.4: Monthly average sulfate concentration at selected sites that are part of an ocean network operated by a group at the University of Miami (Prospero et al., 1989; Arimoto et al., 1996; Savoie et al., 1989, 1993). Model results are in solid lines, and observed data are dotted, with one standard deviation error bars.

2.5 Comparison with observations: Aerosol mass

2.5.1 Surface observations

Figure 2.4 shows the simulated monthly average sulfate concentrations at nine selected sites. At Southern Hemisphere (SH) high latitudes (Mawson, Antarctica), the model reproduces the observed seasonal cycle, but it overestimates the sulfate concentration in summer, which may be due to the high DMS emissions used in the model (see also Liu et al. (2005)). The observed sulfate concentrations are reproduced well at Chatham Island,

New Zealand. At Cape Point, South Africa, the model overestimates sulfate concentrations in spring, but reproduces observations well in other months. At Reunion Island, the model underestimates sulfate concentrations in the fall and winter. At Ragged Point, Barbados, the model reproduces the seasonal cycle with a peak in the summer. At Bermuda, the model underestimates sulfate concentrations in spring and summer, which may be caused by a bias in the westward transport in CAM, since concentrations at Bermuda are primarily associated with the transport of sulfate and precursors from North America (Savoie et al., 2002). Hurrell et al. (2006) showed that summertime NH tropical easterlies in CAM3 are too strong (by ~4 m/s) and extend too far poleward, which may lead to a bias in the westward transport in the subtropics over the eastern U.S. At Midway Island, in the Pacific Ocean, the model reproduces sulfate concentrations well. At the two higher latitude sites (Mace Head, Ireland; Heimaey, Iceland), the model reproduces the seasonal cycle reasonably well. The peak values in the summer result from the transport of pollution from Europe.

Figure 2.5 shows the simulated monthly average concentrations of BC at selected sites. At high latitude sites (South Pole; Halley, Antarctica; Barrow, Alaska; Albert, Canada), the model largely underestimates the BC concentrations. This underestimation is consistent with the smaller mass fractions in the polar regions compared to other models that was presented in section 2.4 and can be due to the larger wet scavenging efficiency of BC in the model, together with possible stronger precipitation or weaker poleward transport. At Jungfraujoch, Switzerland, the model reproduces the observations well. At Amsterdam Island, the model underestimates the BC concentration. At Mace Head, Ireland, the model also underestimates the BC concentration except in the summer. At

Mauna Loa, Hawaii, which is located in the lower free troposphere, the simulated BC concentration is reasonable in winter, but is overestimated in summer. The global distribution shows that this overestimation in summer comes from the very strong biomass burning emissions in Central America. The overestimation may also come from the tropical easterly winds which are too strong (by ~4 m/s) in CAM3 (Hurrell et al., 2006).

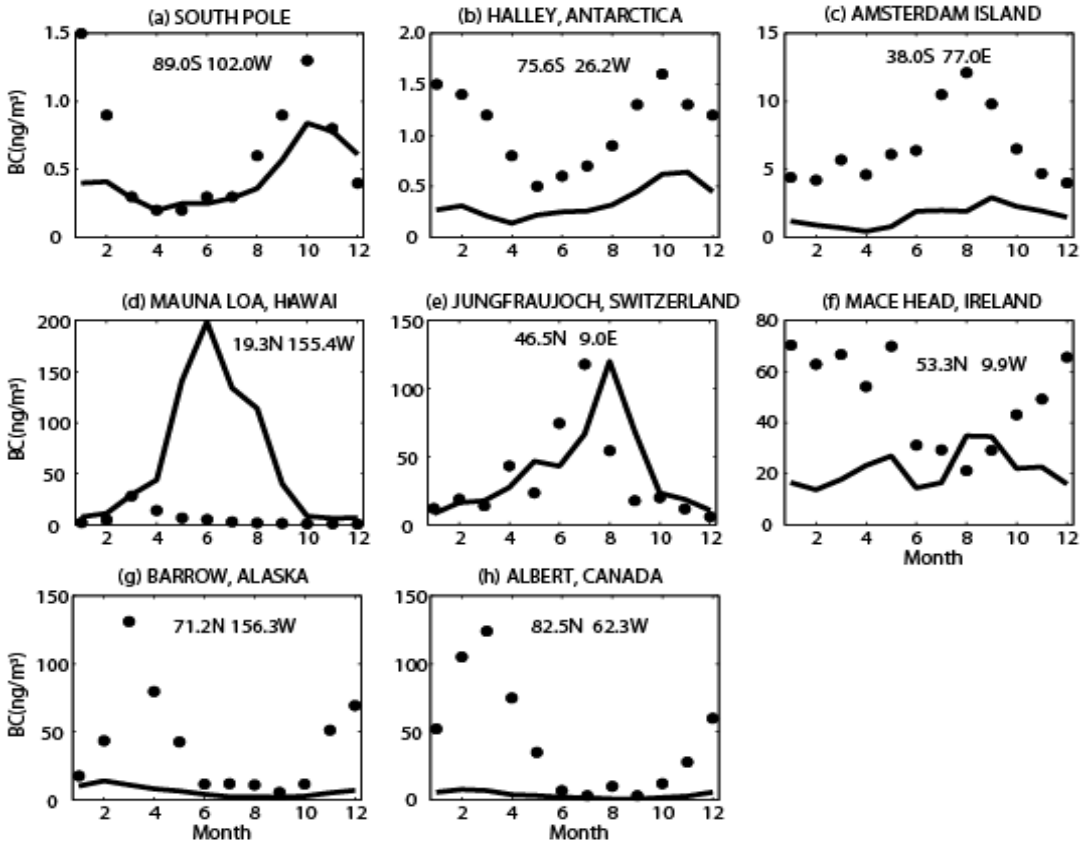

Figure 2.5: BC concentration at various sites (Liu et al., 2005): (a) Amundsen-Scott, South Pole (Bodhaine, 1995), (b) Halley, Antarctica (Wolff and Cachier, 1998), (c) Amsterdam Island, France (Wolff and Cachier, 1998), (d) Mauna Loa, Hawaii (3.4 km asl) (Bodhaine, 1995), (e) Jungfraujoch, Switzerland (3.5 km asl) (Nyeki et al., 1998), (f) Mace Head, Ireland (Cooke et al., 1997), (g) Barrow, Alaska (Bodhaine, 1995), (h) Alert, Canada (Hopper et al., 1994). Model results are in solid lines, and observed data are dotted.

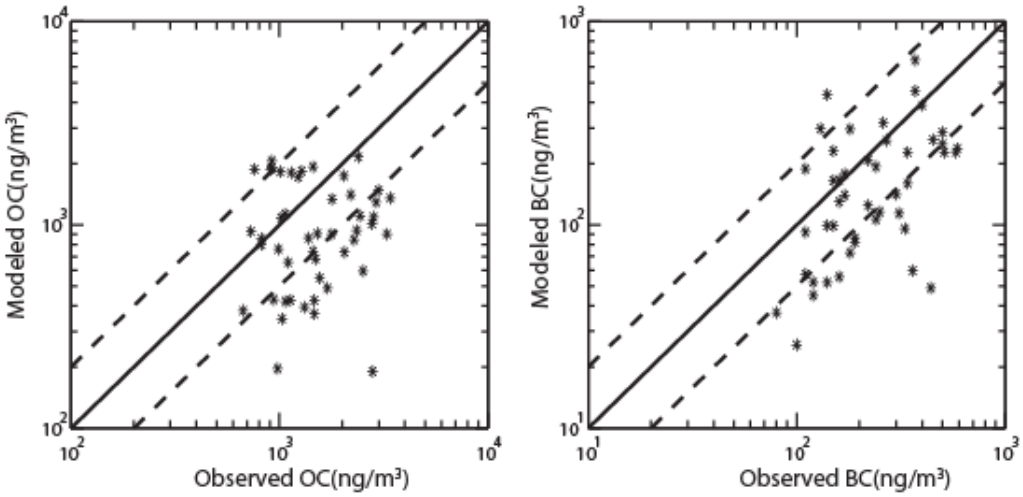

Figure 2.6: Annual average simulated OC and BC concentrations vs. observations from the IMPROVE network. The solid lines are 1:1, and the dashed lines are 2:1 or 1:2.

Figure 2.6 shows a scatter plot of the annual average simulated and observed OC and BC for 3 years (from March 1996 to February 1999) from 48 sites in the Inter-agency Monitoring of Protected Visual Environments (IMPROVE) network (Malm et al., 2000). The simulated concentrations at most sites are within a factor of two of the observed concentrations. However, the model generally underestimates the concentrations of both BC and OC, a feature which also appears in other models (e.g., Easter et al., 2004; Chung and Seinfeld, 2002).

The first eight plots in Figure 2.7 show the monthly average sea salt concentrations at eight selected sites. The model represents the NH sites well compared with observations. At higher latitudes (Mace Head, Ireland and Heimaey, Iceland), the model captures the observed seasonal variations with a maximum in winter and a minimum in summer. But the model underestimates the maximum sea salt concentrations in winter at Heimaey, Iceland and therefore underestimates the seasonal variation. At the mid-latitude sites (Cheju and Bermuda), the model reproduces the seasonal variation of the observations,

but it underestimates the magnitude of sea salt concentrations. In the SH, at Cape Point, South Africa, the model reproduces the observed sea salt concentrations reasonably well, but it overestimates the sea salt concentrations at Invercargill, New Zealand. As shown below, this overestimation is mainly caused by coarse sea salt particles. At Mawson, Antartica, the model also overestimates the concentration, especially during the Southern Hemisphere winter.

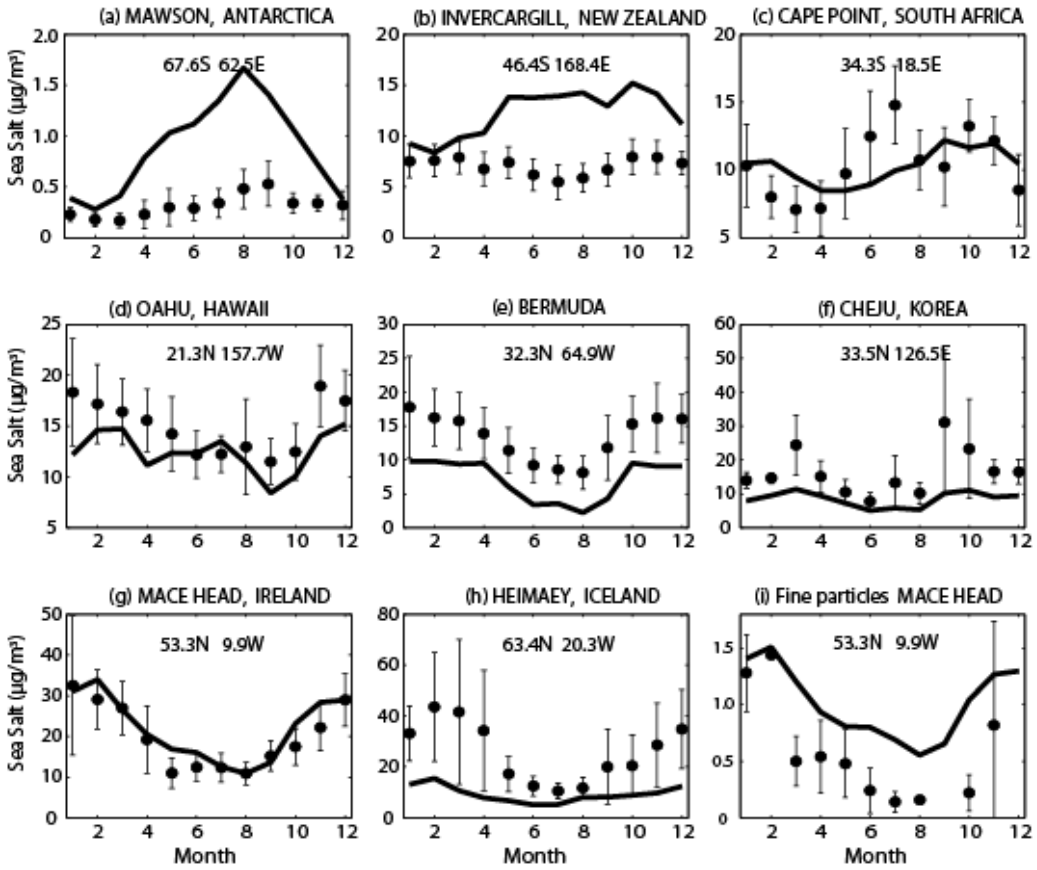

Figure 2.7. (a-h): Monthly average total sea salt concentrations at selected sites that are part of an ocean network operated by a group at the University of Miami (Prospero et al., 1989; Arimoto et al., 1996; Savoie et al., 1989, 1993); (i) monthly fine sea salt particles (d < 1.5 μm) at Mace Head, Ireland (Yoon et al., 2007). Model results are in solid lines, and observed data are dotted with one standard deviation error bars.

Although the coarse mode accounts for most of the sea salt mass, sea salt in the fine mode has the most important contribution to the number of CCN and to light scattering by the aerosol. The last plot in Figure 2.7 compares the simulated monthly average sea salt concentration in the fine mode (with diameter < 1.5 μm) with observations at Mace Head, Ireland (Yoon et al., 2007). The model reproduces the observed seasonal variation well, with a maximum in winter and a minimum in summer. But the model overestimates the magnitude of the fine mode sea salt aerosol, especially in summer, where the model predicts values that are two or three times larger than the observations.

Table 2.7 compares the simulated and observed fine and coarse mode sea salt mass concentrations at several locations. In the SH middle to high latitudes, the model is in good agreement with observations for the fine mode (RIST 93 South, RIST 94 South, and ACE-1). In tropical regions, the model underestimates observed fine mode sea salt concentrations by a factor of two or three (RIST93 Tropical, RIST 94 Tropical, and MAGE 92), but it is within one standard deviation of the observations. It also underestimates the fine mode sea salt concentrations in the NH middle latitudes, but to a lesser extent. In the SH middle latitudes, the model also underestimates the observed fine mode sea salt concentrations (Cape Grim JJA, Cape Grim DJF). The model overestimates the coarse mode sea salt concentrations in the SH middle to high latitudes, consistent with its overestimation of the total sea salt concentrations (Figure 2.7).

Table 2.7. Simulated and observed fine and coarse mode sea salt aerosols (μg m^{-3}).

		Fine particles (d<1.4 μm)[c]		Coarse particles (d>1.4 μm)[c]	
		Model	Observations	Model	Observations
RITS 1993[a]	70S-40S, 80W-140W, Mar-May	0.83	0.84±0.64	19.49	4.8±2.3
	20S-20N, 140W, Mar-May	0.23	0.56±0.50	7.11	7.4±3.8
	30N-54N, 140W, Mar-May	0.45	0.84±0.96	11.74	7.3 ±4.6
RITS 1994[a]	70S-40S, 80W-140W, Nov-Dec	0.80	0.7±0.31	16.96	5.0±2.0
	20S-20N, 140W, Nov-Dec	0.26	0.82±0.90	8.31	8.8±2.6
	30N-54N, 140W, Nov-Dec	0.54	0.71±0.15	15.40	5.3±2.5
MAGE 1992[a]	12S-20N, 140W, Feb-Mar	0.28	0.75±0.55	8.55	12.0±6.0
PSI 1991[a]	48N, 127W, Apr-May	0.36	0.33±0.29	9.85	3.3±2.3
ACE-1 1995[a]	46S, 110W, Nov-Dec	0.72	1±0.56	20.09	9.3±5.4
Cape Grim 1988-1990[b]	41S, 145E, Jun-Aug	0.43	1.4	13.14	17.5
	41S, 145E, Dec-Feb	0.36	1.09	9.80	13.7

[a]From Quinn and Coffman (1999).
[b]From Andreae et al. (1999).
[c]Wet size at 70% relative humidity.

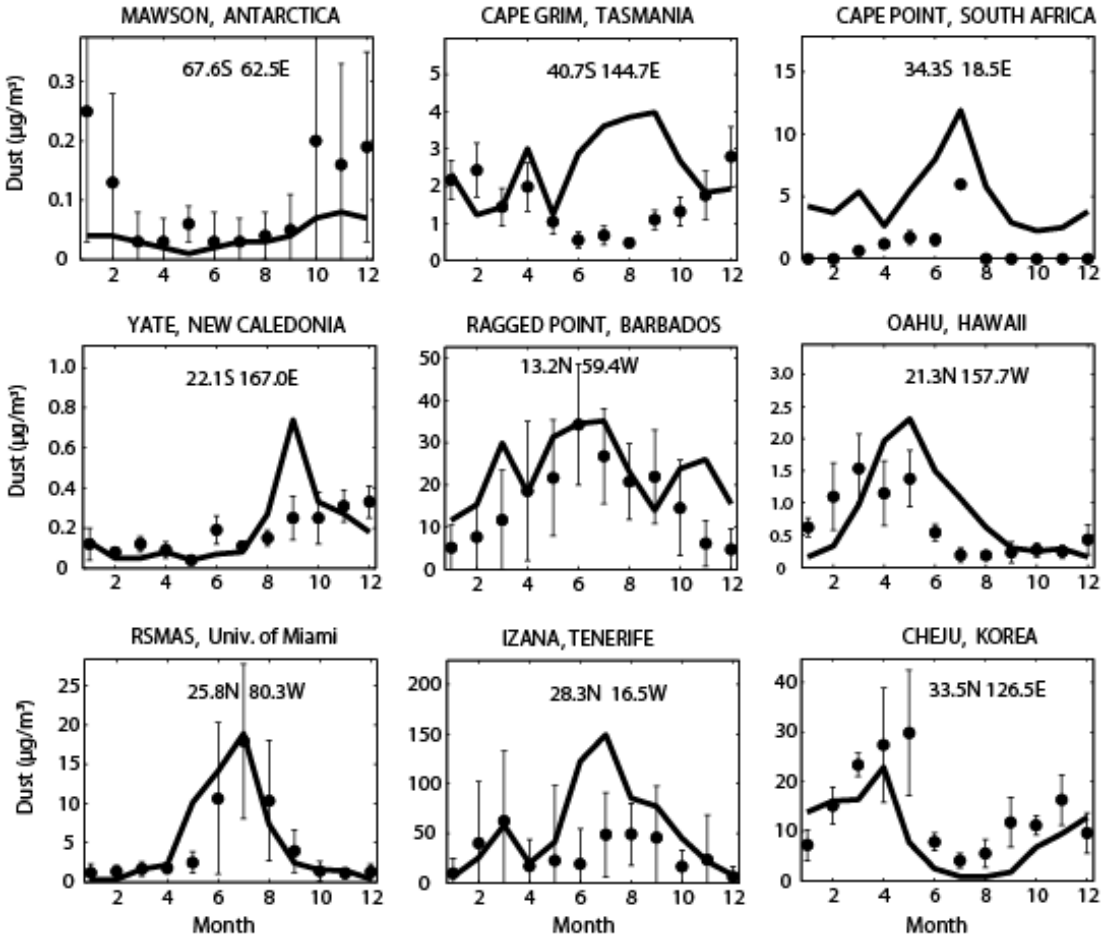

Figure 2.8. Monthly average dust concentration at selected sites that are part of an ocean network operated by a group at the University of Miami (Prospero et al., 1989; Arimoto et al., 1996; Savoie et al., 1989, 1993). Model results are in solid lines, and observed data are dotted with one standard deviation error bars.

Figure 2.8 compares the simulated and observed total monthly-averaged dust concentrations at nine selected sites. At Mawson, Antarctica, the model reproduces the concentrations during winter months, but it underestimates dust concentrations during the summer, which was also true for BC concentrations. At Cape Grim, which is located southeast of the dust source in Australia, the model is not able to simulate the seasonal cycle. The largest dust concentrations in the model occur during the winter, whereas the observations have a minimum concentration at that time. At New Caledonia, downwind of the dust source in Australia, the modeled seasonal cycle is reasonable, although the

concentration in September is still overestimated. At Cape Point, South Africa, which is located at the southern most tip of the African dust source, the model simulates the seasonal cycle reasonably well, but it overestimates dust concentrations. At Tenerife, which is close to the Saharan dust source, the model overestimates dust concentrations in the summer months (June-August), but simulates the observed concentrations well in other months. At downwind sites from the African dust source (Barbados and University of Miami), the model reproduces the seasonal cycle in the dust concentration: high concentrations in summer months, and lower concentrations in winter months. At sites downwind of the Asian dust source (Cheju, Korea and Oahu, Hawaii), the model simulates the observed maximum in the spring. At Cheju, it reproduces the observed dust

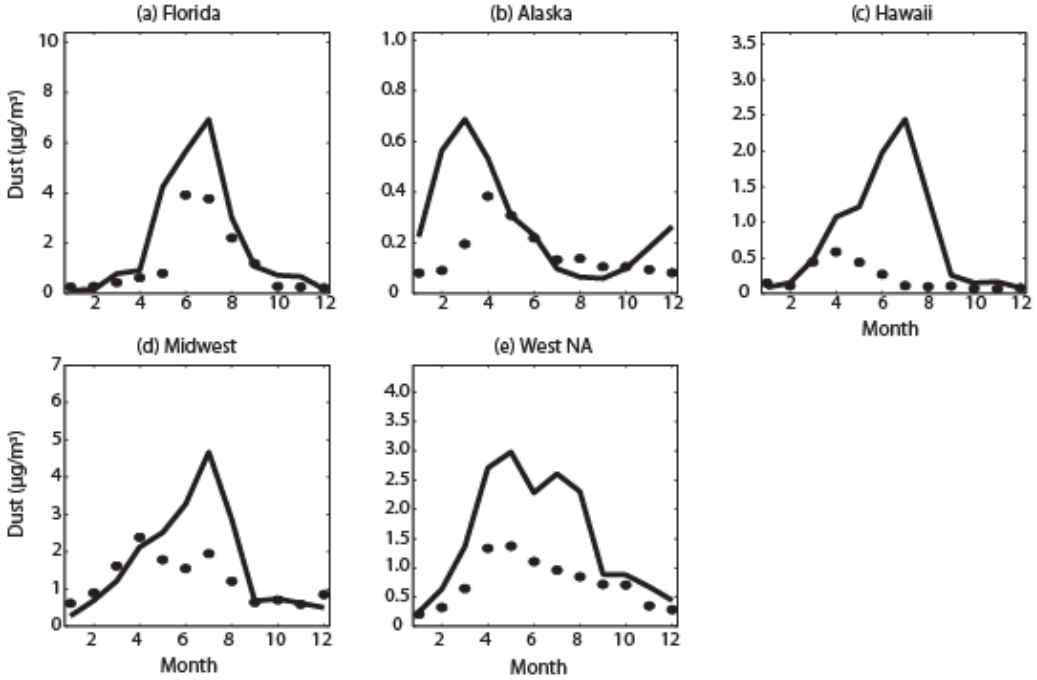

Figure 2.9. Monthly average fine mode dust concentration (d < 2.5 μm) at the IMPROVE network stations listed in Table 2.8. (a) Florida (80.68W, 25.39N, at surface); (b) Alaska (148.97W, 63.72N, 658 m); (c) Hawaii (156-155W, 19.5N, 1258-3439 m); (d) Midwest North America (105-100W, 28-44N, 736-1672 m); (e) Western North America (120-105W, 28-44N, 1000-3000 m).

Table 2.8: IMPROVE Sites used in Figure 2.9.

Location	ID	Longitude	Latitude	Elevation (meter)
Figure 9a: Florida				
Everglades N. P.[a]	Ever1	80.68W	25.39N	1
Figure 9b: Alaska				
Denali N. P.	Dena1	148.97W	63.72N	650
Figure 9c: Hawaii				
Hawaii Volcanoes N. P.	Havo1	155.26W	19.43N	1258
Mauna Loa Observatory #1	Malo1	155.58W	19.54N	3439
Mauna Loa Observatory #2	Malo2	155.58W	19.54N	3439
Figure 9d: Midwest				
Badlands N.P.	badl1	101.9W	43.7N	736
Big Bend N.P.	bibe1	103.2W	29.3N	1066
Guadalupe Mountains N.P.	gumo1	104.8W	31.8N	1672
Figure 9e: Western North America				
Bandelier N.M[b].	band1	106.3W	35.8N	1988
Bliss S.P.[c]	Blis1	120.1W	39.0N	2130
Bryce Canyon N.P.	brca1	112.2W	37.6N	2481
Bridger Wilderness	Brid1	109.8W	43.0N	2626
Canyonlands N.P.	cany1	109.8W	38.5N	1798
Chiricahua N.M.	chir1	109.4W	32.0N	1554
Gila Cliff Dwellings N.P.	gicl1	108.2W	33.2N	1775
Great Basin N.P.	grba1	114.2W	39.0N	2065
Great Sand Dunes N.M.	grsa1	105.5W	37.7N	2499
Jarbidge Wilderness	Jarb1	115.4W	41.9N	1869
Lone Peak Wilderness	lope1	111.7W	40.4N	1768
Mesa Verde N.P.	meve1	108.5W	37.2N	2172
Mount Zirkel Wilderness	mozi1	106.7W	40.5N	3243
Petrified Forest N.P.	pefo1	109.8W	35.1N	1766
Rocky Mountain N.P.	romo1	105.6W	40.3N	2760
San Gorgonio N.P.	sago1	116.9W	34.2N	1726
Sequoia N.P.	sequ1	118.8W	36.5N	519
Tonto N.M.	tont1	111.1W	33.7N	775
Weminuche Wilderness	wemi1	107.8W	37.7N	2750
Yellowstone N.P.	yell2	110.4W	44.6N	2425
Yosemite N.P.	yose1	119.7W	37.7N	1603

[a]N.P., National Park.
[b]N.M.: National Monument.
[c]S.P.: State Park.

concentrations in winter, but underestimates somewhat the dust concentrations in other months. At Oahu, it overestimates the observed dust concentrations from May to August.

Figure 2.9 shows the monthly averaged dust concentrations in the fine mode (with radius < 1.25μm) compared to observations in the U.S., from data in the IMPROVE network. Overall, the model captures the seasonal variation of observed dust concentrations, but there are some months in which the model overestimates the fine dust concentration. In Florida, the model reproduces the peak concentration in summer, which is associated with the African dust source. In Alaska, the model overestimates the dust concentrations in winter and spring. In Hawaii, the model simulates well the observed concentrations in winter, but overestimates the concentrations in summer. Moreover, the peak concentration occurs in summer rather than in spring as observed. As noted previously, the easterlies in the CAM3 model are too far north and too strong (Hurrell et al., 2006), and this causes a maximum in the concentrations of dust in summer in Hawaii, based on sources in Africa and North America. In the mid-western U.S. and in western North America, the observations have their peak concentrations in spring, which may indicate the influence of the Asian dust source. Our model produces a peak concentration in the summer in the mid-west and in April in western North America. The overestimation in the model is consistent with that found by Cakmar et al. (2006). They suggested that the optimal fraction of fine particles (radius < 1μm) that fits observations best is lower than current model estimates.

2.5.2 Vertical profiles

Figure 2.10 compares vertical profiles of the total aerosol and BC mixing ratios over Houston, Texas from observations (Schwarz et al., 2006) with monthly averaged data

from the model in November. The observations took place on November 10, 2004 and November 12, 2004. A Single Particle Soot Photometer (SP2) was used to measure aerosol particles in the size range from 0.15-0.7 μm volume equivalent diameter. Schwartz et al. (2006) scaled the raw observations of BC mass by a factor of 1.7. The factor of 1.7 is determined by comparing the normalized integral of the average size distribution measured by the SP2 with the normalized integral of the average size distribution from several other airborne campaigns, to determine the aerosol mass for the entire size spectrum. Both the BC mass mixing ratio and the total aerosol mass mixing ratio from the observations decrease strongly with altitude from the surface to the lower troposphere. The mixing ratios reach a minimum in the middle troposphere and increase slightly with altitude from the middle troposphere to the lower stratosphere.

The model simulates a near constant mixing ratio for BC and total aerosol from the surface to 700 hPa and a maximum in the BC mixing ratio from 700-800 hPa which is not seen in the observations. Vertical profiles of the simulated individual aerosol components indicate that the mixing ratio of aerosol species from fossil fuel emissions decrease with altitude from the surface to lower free troposphere, while the mixing ratio of biomass burning aerosols and dust increase with altitude from the surface to about 700 hPa and reach a maximum near 700 hPa (not shown). The maximum in the mixing ratio of dust and biomass aerosols at 700 hPa is associated with their uniform injection in the boundary layer and their long range transport in the lower free troposphere. Biomass burning explains the maximum mixing ratio of BC from 700-800 hPa. Compensating effects from the decrease with altitude of fossil fuel aerosols, and the increase with altitude of dust, produces a near constant mixing ratio for total aerosol.

While the model predicts a reasonable magnitude for the total aerosol and BC mixing ratios near the surface and in the upper troposphere, it overestimates the mixing ratio in the lower and middle free troposphere. This may be caused by either vertical transport that is too strong, by assumed injection heights for biomass burning and dust aerosols that are too high, or by wet deposition that is too weak in the model. However, it may also be due to the fact that there are only two days of observational data, which may not be representative.

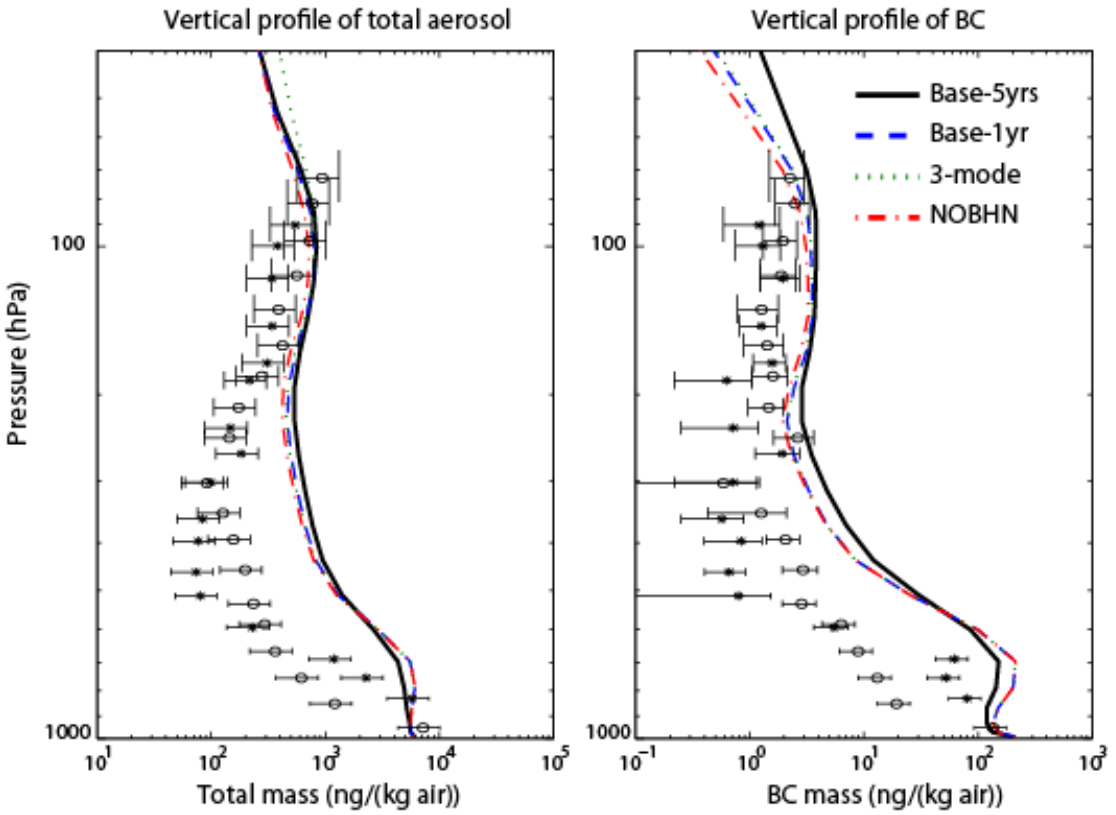

Figure 2.10: Vertical profiles of total aerosol (left panel) and BC (right panel) mass mixing ratios. Observations are from Schwartz et al. (2006) and took place on November 10, 2004 (stars) and November 12, 2004 (open circles), over Houston, Texas. The error bars represent the sample standard deviation. All simulation cases are defined in Table 2.2.

Figure 2.10 also shows simulated profiles from two other model cases. One is from the '3-mode' case, and the other is from the base case with binary homogeneous nucleation

switched off above the boundary layer ('NOBHN'). The differences between the mass mixing ratio profiles from these two cases and those from the base case are minor, despite the fact that the simulated aerosol number concentrations for these two cases differ significantly from those in the base case. For example, the NOBHN case has far smaller aerosol number concentrations in the upper troposphere than those in the base case due to the absence of nucleation, and the size of aerosol particles is much larger as a result of coating of pre-existing aerosols by sulfate. This suggests that different treatments in aerosol microphysics as described here and the effects of microphysics on scavenging have only a small effect on the vertical profile of either the total aerosol mass or the black carbon mass.

2.6 Comparison with observations: Aerosol number and size distribution

2.6.1 Aerosol size distribution

Figure 2.11 shows the aerosol size distribution in the marine boundary layer from the model and observations (Heintzenberg et al., 2000). The observational data were compiled and aggregated onto a 15º×15º grid. We sampled the model over the same regions as those of the observations (see Appendix B for a description of the derivation of the simulated size distribution and number concentration from the mode and bin structure in the model). Generally, the model simulates a bimodal distribution for aerosols over the marine boundary layer, with an Aitken mode having a geometric diameter of 20 nm and an accumulation mode having a diameter of 150 nm. The observed size distribution is also bimodal, but the model underestimates both the accumulation mode radius and mode

number at all latitudes except 45-60ºN, where it somewhat overestimates the aerosol number (by about 50%). The largest underestimate of accumulation mode aerosol number (by a factor of 2 to 3) occurs over SH middle latitudes and tropical regions (45ºS-15ºN). The underestimate of the accumulation mode aerosol number is consistent with the underestimate of the total sea salt aerosol mass at Cheju and Bermuda (Figure 2.7). This underestimation may not be due to the use of the 2-mode aerosol representation, since it also occurs in the model results of Pierce and Adams (2006; 2007) and, to a lesser extent, in the results of Spracklen et al. (2007). They both used a sectional representation for aerosol size distributions (30 bins in Pierce and Adams (2006; 2007); 20 bins in Spracklen et al. (2007)). As pointed out by Pierce and Adams (2006) there are large differences between the various sea salt source function they assayed. Nevertheless, none of the different source functions applied in Pierce and Adams (2006) leads to a significant improvement in their models' agreement with observations, possibly because of a bias in the wind speeds in the GISS model that they were using. The sea salt source function has also been implicated in possible disagreements between model aerosol optical depths over the southern oceans and observations (e.g., Penner et al., 2002). Further work is needed to improve the representation of sea salt in global models.

The model also underestimates both the Aitken mode radius and number concentration in the marine boundary layer outside regions that are heavily influenced by continental sources (e.g., 75ºS-15ºN, 75ºN-90ºN). The absence of ultrafine sea salt particles (radius < 0.05 μm) in our source representation may contribute somewhat to the underestimation of the aerosol number in the Aitken mode in the model, especially at high latitudes. Pierce and Adams (2006) found better agreement at high latitudes (45ºS-75ºS) when they used

the Martensson et al. (2003) sea salt source function though other latitudes were not improved. In addition, the absence of a boundary layer nucleation scheme in the base case simulation, as well as its absence in the simulations of Pierce and Adams, may also bias the results. Indeed, including a boundary layer nucleation mechanism improves the comparison of the model with observations over the tropics and over the SH middle latitudes (section 2.7.2).

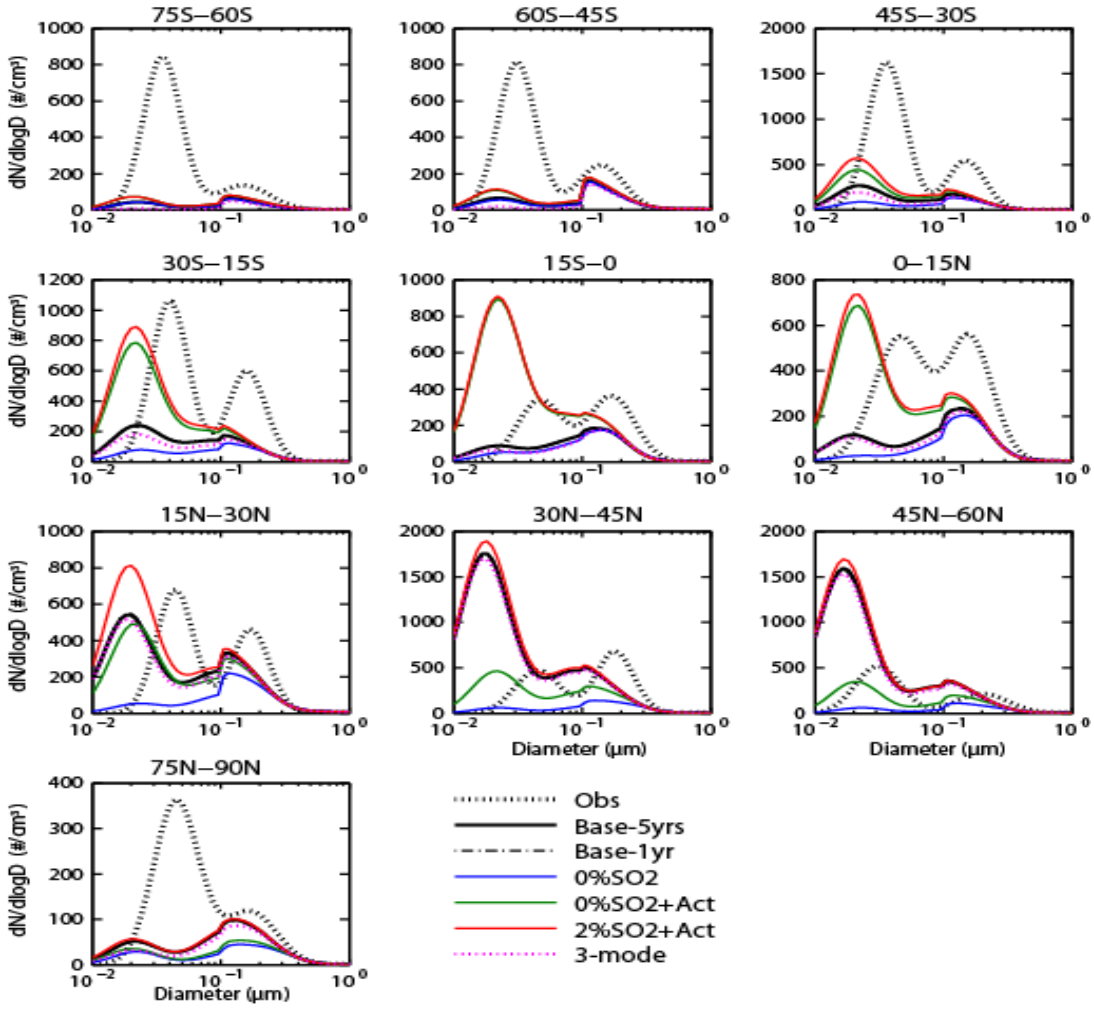

Figure 2.11: Aerosol size distribution in the marine boundary layer. Observations ('Obs') are from Heintzenberg et al. (2000). All simulated cases are defined in Table 2.2.

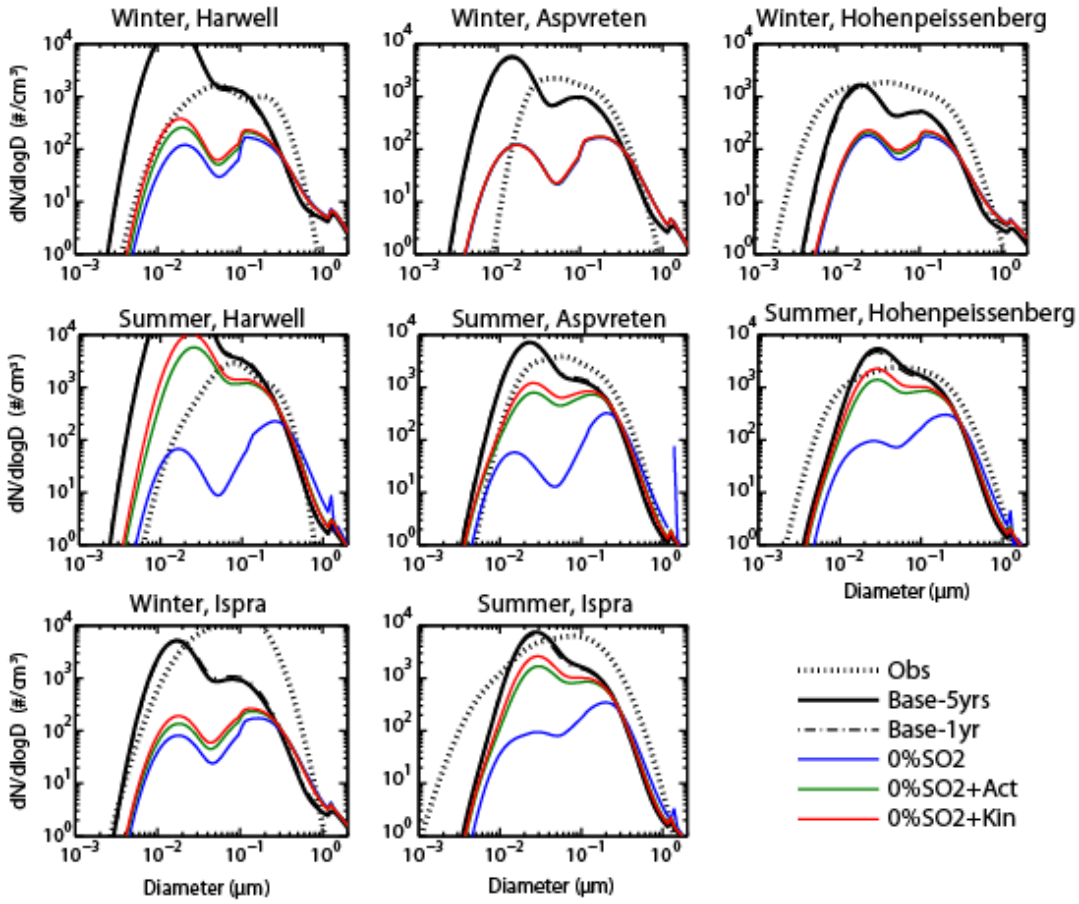

Figure 2.12: Aerosol size distribution over sites in Europe. Observations ('Obs') are from Putaud et al. (2003). All simulated cases are defined in Table 2.2.

Over regions that are heavily affected by continental sources (30ºN-60ºN), the base case model overestimates aerosol number concentrations and underestimates the mode radius in the Aitken mode, which may be associated with the assumed size distribution and number concentration of primary-emitted sulfate particles. A larger emitted size and smaller fraction in the Aitken mode would provide a better agreement between the model and observations. The role of the primary-emitted sulfate particles is further discussed in section 2.7.1.

Figure 2.12 shows the aerosol size distribution from the model and observations at four sites in Europe in winter and summer in the continental boundary layer (Putaud et al.,

2003). Aspvreten is located in a region with background continental conditions 50 km from any large pollution source. Harwell and Hohenpeissenberg are located in a rural location 10 to 50 km from large pollution sources, and Ispra is a polluted site less than 10 km from a large pollution source. The observed number concentrations at Aspvreten are smaller and have larger sizes than those at the more polluted site, Ispra. The aerosol at this background site represents a more aged aerosol than observed at Ispra. There is also a narrower size spectrum and smaller number concentration in winter compared to summer, which result from additional nucleation events during summer, when the rate of production of sulfate is larger. At Aspvreten, the model is in better agreement with the observations in summer than in winter, when the simulated Aitken mode size is too small. Apparently, the assumed fixed size distribution and fraction (2%) of primary-emitted sulfate particles in the base case is not able to represent the seasonal variations in subgrid scale nucleation events which depend on the rate of production of sulfate gas and its variation with sunlight.

Given the model's resolution (about 200 km), it is not surprising that the simulation overestimates the aerosol number concentrations at Harwell because the grid box at this location includes the emissions from London. The Hohenpeissenberg site is located at an altitude of about 1km, and the model is in better agreement with the observed size distribution in summer than it is in winter. The model underestimates the total aerosol number concentration in winter.

At Ispra, we would expect the model to give smaller aerosol number concentrations compared to the observations, since the grid box near Ispra includes some rural regions.

In both winter and summer, the model underestimates aerosol number concentrations in both the accumulation and Aitken modes.

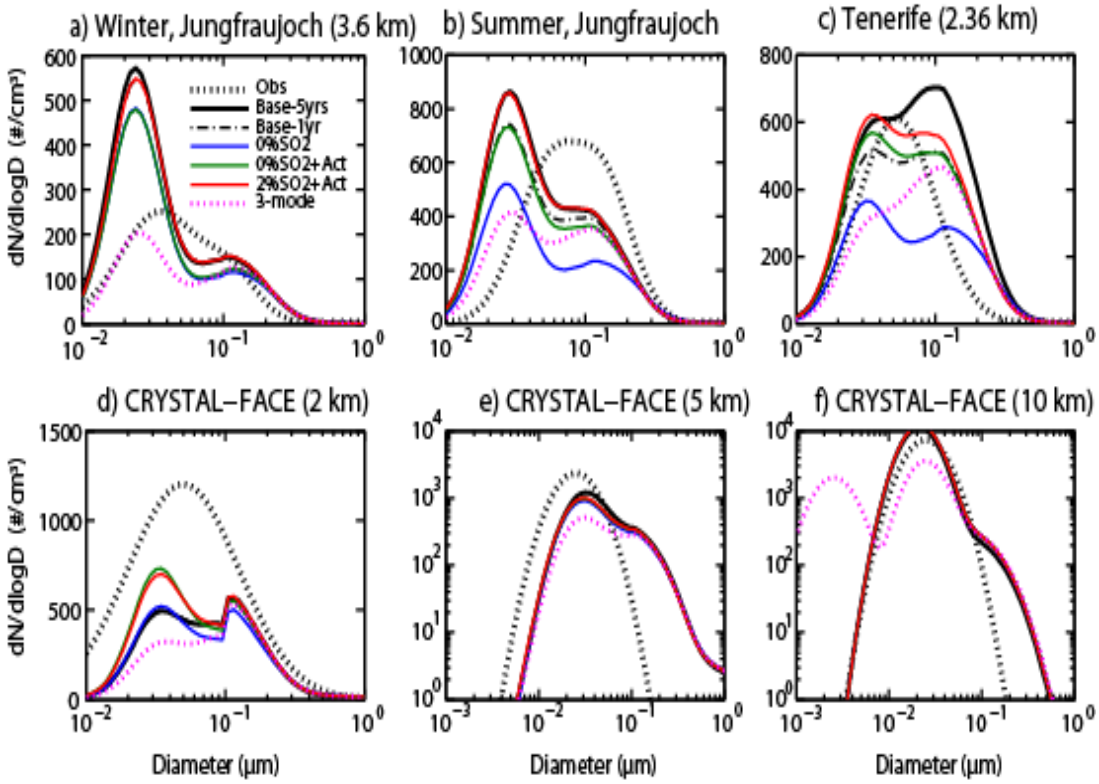

Figure 2.13: Aerosol size distribution in the free troposphere. Observations ('Obs') are from Putaud et al. (2003) (Jungfraujoch), Raes et al. (2000) (Tenerife); Frindlind et al. (2004) (Crystal-Face, Florid). All simulated cases are defined in Table 2.2.

Figure 2.13 (a-d) shows aerosol size distributions in the lower free troposphere from the model and observations at three sites (Jungfraujoch, 3580 m, Putaud et al. (2003); Florida during the Crystal-Face experiment, 2-5 km, (Frindlind et al., 2004); Tenerife, 2360 m, (Raes et al., 1997)). The observations show a monomodal distribution at all sites. This has been argued to result from descending aerosol particles from the upper troposphere and the depletion of accumulation mode particles from the boundary layer by wet and dry deposition (Raes et al., 2000). The model predicts a prominent Aitken mode together with a less prominent accumulation mode. The accumulation mode in the model

is associated with both accumulation mode aerosols transported from the boundary layer (such as dust, which is especially prominent at the Tenerife site) and with coagulation and the condensational growth of aerosols. The observations at Jungfraujoch have a higher aerosol number concentration and a larger mode radius in spring than in winter, which may result from the higher H_2SO_4 production rate in spring. The model simulates these features well. Over South Florida (Crystal-Face), the model underestimates the aerosol number concentration at 2 km. However, it should be noted that the observations only represent a single date.

At both 5 km and 10 km, the observed aerosol size distributions are monomodal with higher number concentrations at higher altitudes, indicating that nucleation may be playing a significant role in determining number concentrations. The model reproduces the number concentration of the mode near 0.02 – 0.03 μm well in the upper troposphere. However, it overestimates the Aitken mode radius in the middle troposphere. The observed mode radius in the middle troposphere is similar to that in the upper troposphere. In the model, the mode radius increases as aerosol particles descend from the upper troposphere. There is a large discrepancy between modeled and observed accumulation mode number concentrations in the middle and upper troposphere.

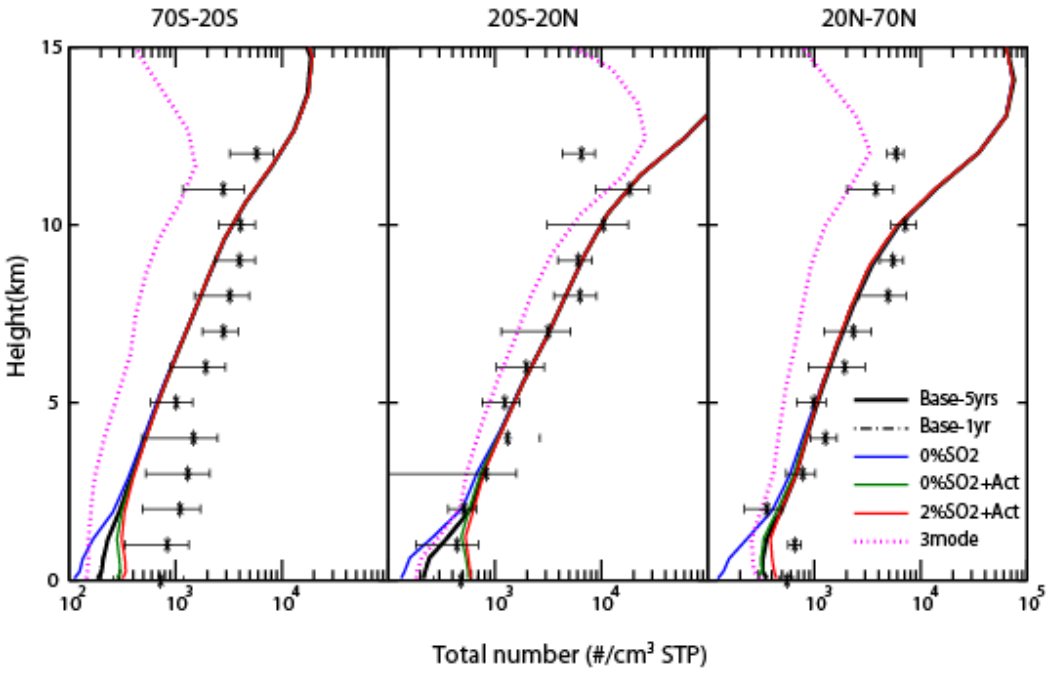

Figure 2.14. Vertical profiles of the number concentration of ultrafine particles (diameter > 3 nm) averaged for latitude bands 70ºS-20ºS (left panel), 20ºS-20ºN (middle panel) and 20ºN-70ºN (right panel) over the Pacific Ocean. Observations (stars) are from Clark and Kapustin (2002), and the error bars represent 50% of the standard deviation. Model results are annual means over the same grid squares as the observations (175º-270ºE for the tropics, 200º-240ºE for the NH and 135º-180ºE for the SH). All simulated cases are defined in Table 2.2.

2.6.2 Vertical profiles of aerosol number concentrations

Figure 2.14 shows vertical profiles of ultrafine particles (diameter > 3nm) from the model and the observations of Clarke and Kapustin (2002). Clarke and Kapustin (2002) compiled field data taken over the Pacific Ocean over several decades, and separated them into three regions: the South Pacific (70ºS-20ºS), Tropical Pacific (20ºS-20ºN), and North Pacific (20ºN-70ºN). All profiles show an increase in the ultrafine particle number concentration with altitude, which is associated with nucleation events in the upper troposphere. The observations also show a larger aerosol number concentration in the upper troposphere over the tropics than over the South Pacific or the North Pacific. The

model reproduces the increase in the aerosol number concentration with altitude. The model also predicts larger aerosol number concentrations in the upper troposphere over the tropics than over higher latitudes. However, the ultrafine aerosol number concentration in the model is larger than in the observations at the highest altitudes. As we will show in section 2.7.3, the use of the 3-mode aerosol representation decreases the simulated ultrafine particle number concentration. Over the South Pacific, the model underestimates the aerosol number concentration between the surface and 5 km. The observational data over the South Pacific is mainly derived from ACE-1 observations, which may be biased toward strong convective regions with higher aerosol number concentrations (Clarke and Kapustin, 2002). Over the tropics, the observational data are nearly constant with altitude in the boundary layer, but the model simulates a factor of two increase in the aerosol number concentration with altitude. As we will show in section 2.6.2, the inclusion of a boundary nucleation mechanism can improve this comparison.

Figure 2.15 shows vertical profiles of the aerosol number concentration in the Aitken mode (diameter > 14 nm) and in the accumulation mode (diameter > 100 nm) from both the model and observations at Punta Arenas, Chile and Prestwick, Scotland (Minikin et al., 2003). The observed aerosol number concentrations in the Aitken mode are nearly constant with altitude in the free troposphere at both locations. Model results increase with altitude in the free troposphere and decrease with altitude in the boundary layer near Scotland. The model overestimates the Aitken mode number concentration at the altitudes from 8-12 km, a feature that is improved in the 3-mode representation (section 2.7.3).

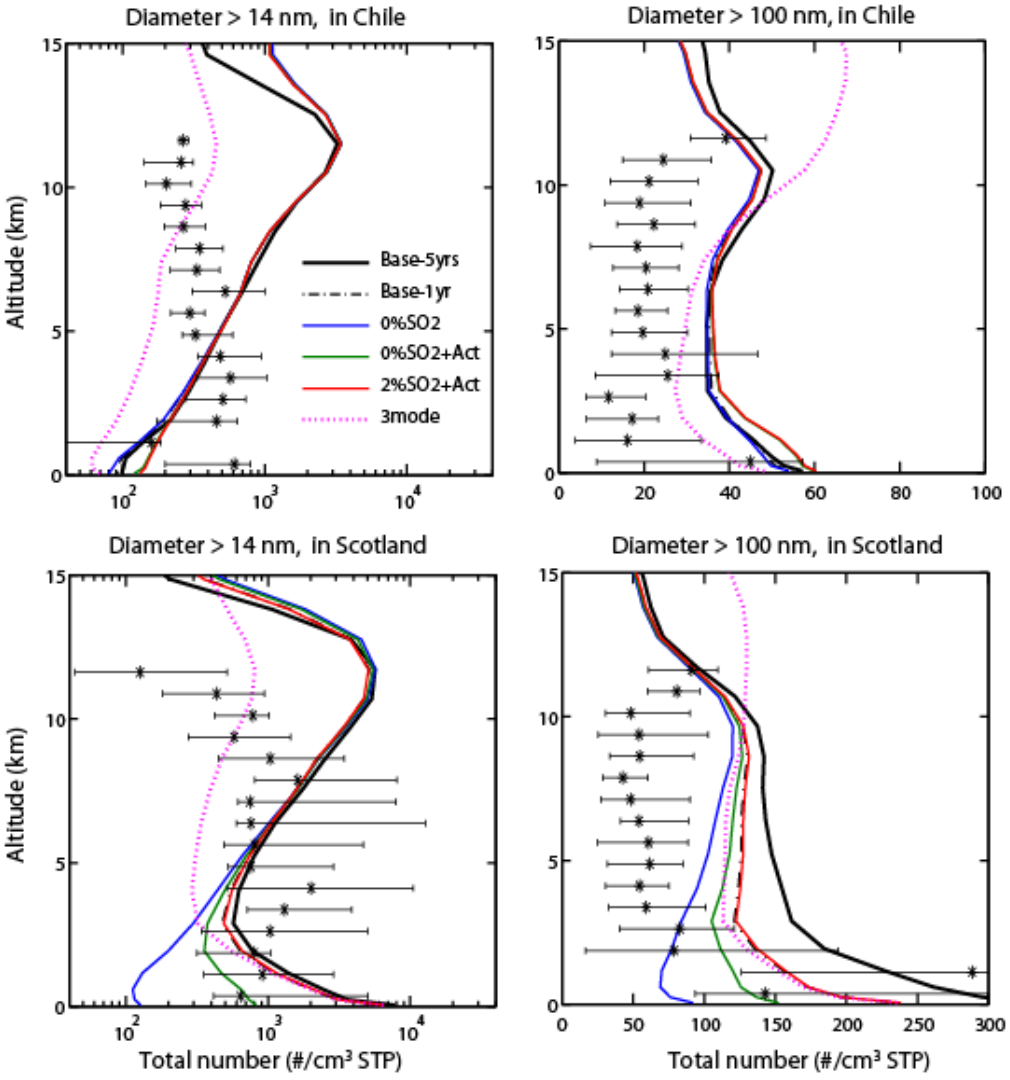

Figure 2.15. Vertical profiles of the number concentration of Aitken mode particles (diameter > 14 nm, left panel) and accumulation mode particles (diameter > 100 nm, right panel) over Punta Arenas, Chile in March/April (upper panel) and over Prestwick, Scotland, in Sept./Oct. (lower panel). Observations are from Minikin et al. (2003): median (stars). Error bars show the interquartile range. Model results are averaged over 60º-50ºS, 70º-85ºW for Chile, and over 50º-60ºN, 10ºW-5ºE for Scotland. All simulated cases are defined in Table 2.

Observed accumulation mode aerosol number concentrations near Scotland decrease with altitude from surface to the lower free troposhere, are nearly constant with altitude in the middle troposphere, and increase slightly in the upper troposphere. The model reproduces this trend in the lower and middle troposphere, though the decrease in the boundary layer is somewhat smaller than observed. However, the increase in the upper troposphere is not reproduced by the model. This feature, too, is improved with the 3-mode representation (see section 2.7.3). The observed vertical profile of accumulation mode aerosol number concentration near Punte Arenas is similar to that near Scotland. The model also reproduces near constant concentrations in the lower and middle troposphere, with a very small decrease in concentration with height in the boundary layer. This very small decrease with height is the result of an increase in the sulfate aerosol number with height and a decrease in the sea salt aerosol number with height. The increase in accumulation mode aerosol number (by a factor of two) from Punta Arenas to Scotland is reproduced by the model.

2.7 Sensitivity of aerosol size and number to model formulation

In this section, five additional one year simulations as described in section 2.3 are compared with the first year simulation of the base case and with observations, to study how the simulated aerosol size and number varies with the assumed fraction of primary emitted sulfate particles, with the inclusion of a boundary layer nucleation mechanism, and with the use of a 3-mode representation of aerosol size.

2.7.1 Primary emission of sulfate particles

The primary-emitted sulfate particles in the model have a significant influence on the aerosol number in both the Aitken mode and the accumulation mode over the SH middle latitudes (45ºS-15ºS) and over the NH middle to high latitudes (15ºN-90ºN) in the marine boundary layer (Figure 2.11) and over the continental boundary layer in Europe (Figure 2.12), where the influence of continental sources is large. While the inclusion of the primary-emitted sulfate particles improves the comparison with observations at most latitudes, it overestimates the Aitken aerosol number concentration in NH middle latitudes (30ºN-60ºN).

Including primary-emitted sulfate improves the agreement of the model with observations in the lower free troposphere at Junfraujoch in spring and at Tenerife, but has almost no effect in the middle and upper free troposphere (Figure 2.13). The influence of primary particles transported from surface sources decreases with altitude, while the influence from homogeneous binary aerosol nucleation increases.

The vertical profiles of aerosol number concentrations (Figure 2.14 and Figure 2.15) demonstrate the importance of primary sulfate particles in the boundary layer and in the lower free troposphere. Without primary sulfate particles (or a boundary layer nucleation scheme), the model is not able to simulate the decrease in the aerosol number concentration with altitude in the boundary layer over Scotland.

Since the contribution of the assumed primary-emitted sulfate particles to the aerosol particle number concentration is large, and since there is a poor understanding of the amount of sub-grid scale nucleation which should be represented in the form of primary-emitted sulfate particles, the development of a more rigorous method of representing

these processes is needed. The treatment of these processes in a global aerosol model still constitutes one of the largest uncertainties in the modeling of aerosol size distributions in a global model (Adams and Seinfeld, 2003).

2.7.2 Boundary layer nucleation

In the marine boundary layer, inclusion of the activation mechanism in the model (Equation 2.1) for boundary layer nucleation increases the simulated aerosol number and improves the comparison with observations over the tropics and over the SH middle latitudes (45ºS-15ºN, in Figure 2.11). Over these regions, the concentration of sulfuric acid gas is high and the concentration of primary particles are low, both of which favor new particle formation. In tropical regions, the aerosol number in the Aitken mode can be of order 10 times that simulated without boundary layer nucleation, and the aerosol number in the accumulation mode can increase by 50%. Boundary layer nucleation also improves the comparison with the observed vertical profile of ultrafine particles in the tropical and southern Pacific (Figure 2.14). Without boundary layer nucleation, the model is unable to simulate the nearly constant number concentration with altitude in the boundary layer in the tropical and southern Pacific.

Over the marine boundary layer in regions that are influenced by pollution such as the NH middle latitudes (e.g., 15ºN-60ºN in Figure 2.11, 20ºN-70ºN in Figure 2.14), and over continental sites influenced by pollution (e.g., Scotland in Figure 2.15 and continental European sites (not shown)), the effect of including the activation mechanism for boundary layer nucleation largely depends on whether or not primary-emitted sulfate particles are included. The comparison of the base case (with 2% of the anthropogenic sulfur emitted as particulate sulfate) with the '2%SO2+Act' case shows that including the

boundary layer nucleation mechanism has almost no effect on the simulated aerosol number and size. In these regions, the inclusion of primary-emitted sulfate particles produces a high pre-existing surface area, which depletes the sulfuric acid gas concentration, and slows or inhibits boundary layer nucleation. In contrast, when there are no primary-emitted sulfate particles (compare '0%SO2' with '0%SO2+Act'), boundary layer nucleation increases the aerosol number concentration significantly in the boundary layer of the remote NH (e.g., 15ºN-60ºN in Figure 2.11; 20ºN-70ºN in Figure 2.14, and Scotland in Figure 2.15). This is also true for polluted continental sites during spring (Figure 2.12). However, during winter, boundary layer nucleation has little effect (Figure 2.12) because the sulfuric acid gas production rate is low at these continental sites.

Over regions either with very low sulfuric acid concentrations (75º-60ºS and 75º-90ºN in Figure 2.11) or with very large burdens of primary particles (60º-45ºS in Figure 2.11 and Chile in Figure 2.15, from sea salt aerosol), the boundary layer nucleation mechanism has little effect on the simulated aerosol number concentration, which does not depend on primary sulfate particles. The boundary layer nucleation effect has a small impact on the simulated aerosol number and size in the lower free troposphere, and has almost no effect in the middle and upper troposphere.

Figure 2.12 compares the effects from the kinetic boundary layer nucleation mechanism (which is 2^{nd} order in the H_2SO_4 concentration, '0%SO2+kin') and the activation boundary layer nucleation mechanism (which is 1^{st} order in the H_2SO_4 concentration, '0%SO2+Act'). Both mechanisms produce similar aerosol number concentrations, with only slightly higher concentrations in the Aitken mode from the kinetic nucleation mechanism.

Although the empirical boundary layer nucleation mechanism used in this study was derived from long-term observations at Hyytiälä, there are large differences between the nucleation rates observed at other sites. Riipinen et al. (2007) showed that the rate constant derived from a site in Heidelberg is about one order of magnitude larger than that derived from Hyytiälä. Yu et al. (2008) showed that an ion-mediated nucleation model can explain three of the nucleation events from Hyytiälä that were reported by Riipinen et al. (2007), but they did not examine cases from Heidelberg. The extent to which different mechanims contribute at different sites, is not known. Different nucleation rates or different mechanisms may result in different contributions of boundary layer nucleation to the simulated aerosol size and number.

The contribution of gases other than sulfate to the growth of nucleation-size particles is also unknown. In the results shown above, the only condensing vapor was sulfuric acid gas. However, observational data has shown that other species may also contribute to the growth of nanoparticles (e.g., Stolzenburg et al., 2005). In particular, a number of theoretical (Kerminen et al., 2000; Zhang and Wexler, 2002) and experimental (e.g., Allan et al., 2006; Smith et al., 2008) studies support the notion that organic species play a crucial role in the growth of nanoparticles. For example, Smith et al. (2008) showed that the condensation of sulfuric acid gas could have accounted for only about 10% of the growth that was observed in their measurements, and that oxygenated organics and nitrogen-containing organics can play a dominant role in the growth of nanoparticles. Including the contribution of condensational growth of organic compounds in the model will increase the growth rate of nanoparticles, which will lead to an increase in the

number of larger particles (e.g., CCN) and may also improve the comparison with observations.

2.7.3 The 3-mode representation for sulfate aerosol

The 3-mode version of the sulfate aerosol model is significantly different than the 2-mode version in the upper troposphere where aerosol nucleation is the dominant source of particles. The 3-mode version produces a distinct nucleation mode with a mode diameter of 2.5 nm, which is not present in the 2-mode version. This nucleation mode in the upper troposphere is also evident in the model study of Stier et al. (2005), who also separated the nucleation mode from the Aitken mode. Although this nucleation mode is not seen in the measurements that we examined, the size cut-off of the instruments used to measure aerosols in the upper troposphere limits any observation of this mode. In addition, the 3-mode version results in fewer aerosol particles in the Aitken mode (Crystal-Face at 10 km in Figures 2.13 and 2.15) because freshly nucleated particles are no longer injected into this mode and also because coagulation of the nucleation mode particles has moved Aitken mode particles into the accumulation mode. This improves the comparison of Aitken mode concentrations with observations at altitudes from 8-12 km (Figure 2.15). Finally, the 3-mode version produces higher aerosol number concentrations in the accumulation mode in the upper troposphere (Figure 2.15). In the upper troposphere over high latitudes in both hemispheres, the predicted accumulation mode aerosol number concentrations in the 3-mode version are about 2-3 times that in the 2-mode version. This version of the model may somewhat overestimate the accumulation mode aerosol number concentration compared with observations (Figure 2.15).

Nevertheless, this version of the model is expected to be more physically realistic at high altitudes (see also Weisenstein et al., (2007)).

In the middle and lower troposphere, the 3-mode version produces fewer aerosol particles in both the Aitken and accumulation modes (Figure 2.15). The descent of aerosols from the upper troposphere is an important source of particles in the Aitken mode in the lower and middle troposphere (Clarke and Kapustin, 2002). Since the 3-mode version produces fewer aerosol particles in the Aitken mode in the upper troposphere, it is not surprising that it also results in fewer Aitken aerosol particles in the middle and lower troposphere. This makes the comparison of the model with observations worse, especially over the SH (in Chile), but the comparison in Chile is improved when boundary layer nucleation is included in the 3-mode version (not shown). Including ultrafine sea salt emissions (Pierce and Adams, 2006) may also improve the comparison of the 3-mode version with the observations in these parts of the troposphere. The accumulation mode aerosol particles in the 3-mode version in the middle and lower troposphere are also smaller in number than in the 2-mode version, despite the fact that there are more accumulation mode particles in the upper troposphere. In the middle and lower troposphere, the growth of aerosol particles in the Aitken mode by condensation, coagulation, and cloud processing may be a more important source of accumulation mode particles than the source from the descent of accumulation particles directly from the upper troposphere. Then, fewer Aitken mode aerosol particles in the middle and lower troposphere would lead to fewer accumulation mode particles.

In the boundary layer, the 3-mode version produces results that are similar to the 2-mode version for the aerosol size distribution over the regions where primary particles

have a large contribution to the aerosol particle population, such as for the continental sites over Europe (Figure 2.12) and marine sites over tropical and midlatitude regions of both hemispheres (45ºS-60ºN, Figure 2.11). Over these regions, the aerosol size distribution is mainly determined by the primary-emitted particles, and since there are no primary-emitted particles in the nucleation mode (radius < 0.005μm), the additional nucleation mode in the 3-mode version has little effect on the simulated aerosol size distribution. The difference between the 3-mode and 2-mode versions in the boundary layer is slightly larger over regions far from pollution sources (e.g., 75ºS-45ºS, 75ºN-90ºN in Figure 2.11). Over these regions, aerosol particles entrained from the free troposphere are important sources of Aitken particles, and since the Aitken mode number concentration in the free troposphere is in general lower in the 3-mode version than in the 2-mode version, the concentrations in the boundary layer are also smaller (Figure 2.15).

The 3-mode version and the 2-mode version are also similar in the boundary layer when boundary layer nucleation is included in both versions (not shown). In our treatment, the aerosol particles that are generated from boundary layer nucleation are added to the size range with radius > 3nm due to growth by condensation (Equation 2.3), whereas the particles produced through binary homogeneous nucleation in the upper troposphere are assumed to have a critical size of around 1 nm. The particles from boundary layer nucleation also have lower number concentrations in the nucleation mode than those formed in the upper troposphere from binary homogeneous nucleation. In addition, the concentration of primary particles is much larger in the boundary layer than it is in the upper troposphere, which decreases the role of aerosol nucleation in the

simulated aerosol size distribution in the boundary layer, and thus decreases the differences between the 2-mode and 3-mode versions of the model.

The 3-mode version reproduces the observed trend in the change of the accumulation mode number with altitude (Figure 2.15). In both hemispheres, observations show that the accumulation mode number concentration first decreases in the boundary layer and lower free troposphere, and then remains constant, and finally increases with altitude. The 3-mode version captures these features well, while the 2-mode version does not.

Large scale transport also plays a role in determining the difference between the 2- and 3-mode versions. The separation of freshly nucleated particles from Aitken mode particles in the 3-mode version has a large effect in the upper troposphere (i.e., Aitken mode particles decrease significantly and accumulation mode particles increase in concentration) because there is a strong source of freshly nucleated particles there. These effects are moved downward by the large scale transport, and this affects the simulated aerosol size distribution in the middle troposphere.

Our results show that it is important to separate the nucleation mode from the Aitken mode when a large number of freshly nucleated particles is produced with very small sizes, as is the case for aerosol particles generated from binary homogeneous nucleation in the upper troposphere in our study. But inclusion of a separate nucleation mode has only a small effect on the simulated aerosol size distribution when particle growth from condensation is also partially parameterized and particles are added into the model in a more aged size distribution with lower number concentrations (e.g., aerosol particles from the boundary layer nucleation scheme in this study). This parameterization of the growth of newly formed particles by condensation could also improve the number of

Aitken particles without the introduction of an additional nucleation mode (e.g., Easter et al., 2004). In Easter et al. (2004), the nucleation of H_2SO_4 and water vapor was treated using the nucleation and growth model of Harrington and Kreidenweis (1998), which calculates the formation of nanometer-sized particles during a nucleation burst and their subsequent growth to Aitken mode sizes (larger than 10 nm). However, the method of Harrington and Kreidenweis (1998) cannot separate the parameterization of the subsequent growth of the newly formed particles from the parameterization of nucleation, which makes it difficult to use other nucleation parameterizations (e.g., Vehkamäki et al., 2002). The growth parameterization used here for aerosol particles generated from boundary layer nucleation (Equation 2.3, Kerminen et al. (2004) and Kerminen and Kulmala (2002)) is independent of the parameterization of the nucleation rate of critical clusters. The application of this method in global models allows one to simulate the development of a more aged particle distribution from nucleation and condensation events even though the size resolution of the model is limited, although more study may be needed to quantify the limitations of using this formula.

2.8 Summary and discussion

In this chapter, the IMPACT aerosol model was coupled to the NCAR CAM3 climate model. The version of IMPACT with aerosol microphysics was evaluated. Differences in the simulation of aerosol number and size from treating sub-grid scale nucleation events as primary-emitted sulfate particles, the inclusion of boundary layer aerosol nucleation mechanisms, and a 3-mode aerosol representation are discussed.

The annual and global budgets from the model are in the range of results from other models included in the AeroCom intercomparison. But the burden of BC is only about

half of the mean of the AeroCom models and the burden of OM is only about two-thirds of the mean, which is mainly due to increased wet removal owing to the treatment of sulfate coatings on otherwise initially hydrophobic aerosols, such as BC, OM, and dust. This also partly explains the simulated smaller fine mode mass fraction for dust (7.11% vs. 20.8% in AeroCom). Our simulated mass fraction in polar regions is much less than in AeroCom for all aerosol species, which may result from either differences in poleward transport or from differences in the treatment of wet removal processes.

The comparison of the model with surface observations shows that the model simulates the observed concentrations and seasonal cycles reasonably well. Over Hawaii, the model overestimates BC and fine dust concentrations in summer, which can be partly explained by the bias in the tropical easterlies in CAM3. The model only simulates about one half or one-third of the observed concentration of fine mode sea salt aerosol in the tropics, and it also underestimates the concentration in middle latitudes in both hemispheres. The model overestimates the concentration of fine mode dust aerosols over the United States.

The model reproduces BC and total aerosol mixing ratios between the upper troposphere and lower stratosphere (Figure 2.10). But there is a maximum in the biomass burning aerosols and dust aerosols near 700 hPa which results in a near constant mixing ratio of the total aerosol mass from the surface to 700 hPa over Houston, Texas, a feature that is not present in the observations. Our sensitivity tests show that different treatments of the aerosol microphysics as described here and the effects of microphysics on scavenging have only a small effect on the vertical profile of either the total aerosol mass or the black carbon mass.

In the marine boundary layer (Figure 2.11), the base case simulation overestimates the Aitken mode aerosol number concentrations in regions heavily influenced by pollution, but underestimates the Aitken mode in all other regions. The inclusion of the empirical boundary layer nucleation mechanisms improves the comparison with observations in the middle and low latitudes. At high latitudes, the comparison with observations may be improved by the inclusion of sea salt particles in the ultrafine size range (Pierce and Adams, 2006), which are neglected in the current model. The model also underestimates aerosol number concentrations in the accumulation mode in the marine boundary layer, especially at middle and low latitudes, which is consistent with the underestimation of fine mode sea salt particles in these regions.

At sites located in the continental boundary layer in Europe (Figure 2.12), primary-emitted sulfate particles contribute significantly to the aerosol number concentration in both the Aitken and accumulation mode,s since these sites are strongly influenced by anthropogenic emissions. When primary sulfate particles are included, boundary layer nucleation has little effect in polluted regions. Boundary layer nucleation improves the correspondance to observations compared to the simulation without primary sulfate, but still underestimates the aerosol number concentration significantly, especially in winter. This may suggest that it is important to represent additional sub-grid scale particulate formation in global models.

In the lower free troposphere, the model simulates a prominent Aitken mode and a less prominent accumulation mode, which are not seen in the observations. This may be caused by the wet removal mechanism, vertical transport, or particle nucleation in the upper troposphere. The model simulates a single mode distribution in the middle

troposphere over Florida, as observed during the Crystal-Face experiment. Both primary-emitted sulfate particles and boundary layer nucleation mechanisms have less impact on the aerosol number concentration in the free troposphere than in the boundary layer.

The vertical profile of CN number is simulated well between the lower free troposphere and about 10 km in the base case (Figure 2.14), but is overestimated above 10 km. The simulated CN number concentrations are significantly reduced in the 3-mode representation. In the boundary layer, the CN number concentration in the Northern Hemisphere in the base case agrees with observations, but is underestimated in the Southern Hemisphere and in the tropics. This feature is improved when a boundary nucleation mechanism is included (Figure 2.14). The inclusion of a boundary layer nucleation mechanism also improves the simulation of the Aitken and accumulation mode particles in the boundary layer (Figure 2.15).

The 3-mode representation agrees with the observed increases in accumulation mode aerosol number with altitude in the upper troposphere, in contrast to the 2-mode representation. The concentrations are 2 or 3 times those in the 2-mode representation, and are somewhat overestimated in comparison to observations. The 3-mode representation also decreases the Aitken mode number concentration.

Our study suggests that simulated aerosol size and number concentrations are sensitive to the different assumptions used in the model. The large contribution of primary particulate sulfate to aerosol particle number concentration together with poor constraints on its treatment from either observations or fine-resolution models make this treatment undesirable until further constraints can be developed. More studies are needed to quantify the size and composition of directly emitted sulfate particles, newly formed

particles in source plumes, and their growth on sub-grid temporal and spatial scales. Boundary layer nucleation mechanisms are appealing, but the fact that the mechanism used in this study cannot yet capture all of the variations in the observed nucleation events prevents us from making further conclusions. More studies are needed to quantify how different nucleation mechanisms and how other condensable gases affect modeled Aitken and accumulation mode aerosol numbers. The results from the 3-mode model show that it is important to separately represent freshly nucleated particles. This may also be achieved through a parameterization of nucleation together with the subsequent growth of the newly formed particles to larger size.

Uncertainties in the simulated aerosol number and size distribution can have important implications for CCN concentrations, and aerosol indirect forcing, which is the focus of Chapter III.

Appendix 2.A Coupling of LLNL/Umich IMPACT and NCAR CAM3

In this appendix, we explain the method used to couple the LLNL/Umich IMPACT aerosol model and the NCAR CAM3 atmospheric circulation model.

Coupling between an aerosol model and an atmospheric circulation model can be accomplished directly, by adding the equations that describe the transport and transformation of aerosols directly to the atmospheric component of a climate model (e.g., Lohmann et al., 2007), or by coupling a separate aerosol transport and transformation model to an atmospheric circulation and climate model (e.g., Easter et al., 2004; Chuang et al., 2002; Penner et al., 2003; Taylor and Penner, 1994). Here we chose the second method and coupled the IMPACT aerosol model and the NCAR CAM3 atmospheric circulation model. In this strategy, water vapor, liquid, and ice are transported by the

CAM3 model, while aerosols are transported in the IMPACT model (the water associated with the aerosol is dealt with in the IMPACT model in steady state with the relative humidity from CAM). Both CAM and IMPACT use the finite volume numerical transport algorithm, so the large-scale transport in the two models is consistent. In addition, the instantaneous convective mass flux fields are passed to IMPACT at each time step to calculate the convective transport of aerosols, while the cloud and precipitation fields from CAM are used to calculate wet scavenging.

This coupling strategy allows separate groups to update each component separately, and allows us to easily change aerosol model versions depending on the complexity that we wish to include. In addition, the same aerosol model can be run using off-line assimilated meteorological fields as in Liu et al. (2005), facilitating the examination of the predicted aerosol fields for specific years. We currently have three configurations of the IMPACT aerosol model: a version that only predicts aerosol mass, but not aerosol number (e.g., Liu et al., 2002); a version with an aerosol microphysical module, which includes nucleation of gas phase H_2SO_4, condensation, and coagulation among pure sulfate aerosols and between sulfate aerosols and other components (Liu et al., 2005); and a version that includes the thermodynamics of the nitrate-ammonium-sulfuric acid-dust-sea salt and water system (Feng and Penner, 2007). We also have several versions of NCAR CAM model: the standard version of the NCAR CAM3 model (Collins et al., 2006a); a version with detailed ice microphysics (Liu et al., 2007; Liu et al., 2009); and a version with both detailed liquid and ice microphysics (Chapter IV in this dissertation).

The method we chose to couple the two model components was determined by the unique features of each model component. The CAM3 and IMPACT models have

different parallel schemes, and different domain decomposition methods. CAM3 uses a hybrid message passing MPI/OpenMP scheme, which is able to fully exploit the advantages of supercomputers with both shared and distributed memory. The model domain is decomposed nearly equally and distributed to each processor which communicates with other processors via MPI message passing. Each individual processor includes multiple threads which use OpenMP to speed calculation. The IMPACT model uses only MPI to parallelize the code. The master processor of IMPACT is used for all input and output, and to transfer data to and from all other ('slave') processors. The model domain is nearly equally decomposed in latitude/longitude blocks and distributed to the slave processors. These very different parallel schemes for the two components suggest that we need a coupler or a hub to facilitate communication between the two model components. In addition, there is a massive amount of data that must be exchanged between the two model components (about 30 3-D variables needing about 80 Megabytes for each time step), which suggests that direct communication between the two model components through the master processor of IMPACT would save computer time.

Thus, we used the master processor of IMPACT as a 'virtual' coupler, since, as noted above, the master processor of IMPACT was already used to control output and input for the IMPACT model and was not used for any additional model integrations. This 'virtual' coupler receives the meteorological data from CAM3 and sends them to the slave processors used by IMPACT. After each time step of the aerosol model, it receives the aerosol field from the slave processors, and sends appropriate data back to the individual processors used by the CAM3 model. The two model components of the coupled system run as separate executables in MPMD (Multiple Processors Multiple Data) mode, and

communicate via MPI. The MPH (Multi-component Handshaking) Library (He and Ding, 2005) is used to initialize the communication channels between the two model components and to map the processors to the model components. Because of the concurrent execution (i.e., operator splitting) of the two component models, there is a one time step lag between them.

In this study, CAM3 and IMPACT use an identical global grid with 26 vertical levels and a 2º×2.5º horizontal resolution. The time steps are 30 minutes for CAM3 and and 1 hour for IMPACT. Thus, at every other CAM3 time step, there is an exchange of data between CAM3 and IMPACT. Since the computational cost of IMPACT is high, the communication time between the two model components is only a small fraction of the total computational cost for the coupled model. By assigning the appropriate number of processors to each model component, we can minimize the idle time of each model component that results from waiting for the data from the other component. In doing this, the total computational cost of the coupled system is only slightly larger than the sum of the costs of each model component when they run as stand-alone versions. It takes about 1.5 hours for a one month integration using three 32-thread nodes (2 MPI processors that each include 16 threads are assigned to CAM3 and 64 MPI processors are assigned to IMPACT) on the Bluefire machine at NCAR, which is an IBM clustered Symmetric MultiProcessing (SMP) system based on the POWER6^{TM} processor.

Appendex 2.B Simulated aerosol size distribution and number concentration

In Figures 2.11-2.15, we compared our simulated aerosol size distribution and number concentration with a variety of observations. Here, we describe how we derive the

continuous simulated aerosol size distribution and the number concentration from the values in each of the size bins or modes. For each prognostic sulfate mode (three lognormal modes in the simulation with three modes, and two lognormal modes in all other cases), the median diameter can be derived from the predicted mass and number with along the geometric standard deviations from each mode. Then, the size distribution of sulfate aerosol can be obtained from a superposition of all predicted sulfate modes. For non-sulfate aerosols, the assumed size distributions in Table 2.1 are used to calculate the number concentration of aerosols in each size bin (one bin for carbonaceous aerosols, four bins for dust and sea salt aerosols). The size distribution of total aerosol is the sum of the size distribution of pure sulfate aerosol and non-sulfate aerosols. The simulated aerosol number concentrations in Figures 2.14 and 2.15 are derived by integrating the simulated size distribution over the appropriate size range of the observation. Since the smallest size for dust and sea salt is 0.1 μm in diameter, there is a discontinuity in the simulated size distribution at around 0.1 μm in diameter. Slight discontinuities can also occur at the edges of the four bins used to approximate the dust and sea salt size distributions.

CHAPTER III

AEROSOL INDIRECT FORCING IN A GLOBAL MODEL WITH PARTICLE NUCLEATION

3.1 Introduction

Atmospheric aerosols are an important component of the global climate system. One of the primary effects of aerosols is to modify cloud properties by acting as cloud condensation nuclei (CCN). This so-called aerosol indirect effect is one of the largest uncertainties in our understanding of climate change. One major challenge in the study of the aerosol indirect effect is to determine the source of the CCN-size particles, which involves the accurate treatment of both aerosol microphysics and large scale atmosphere dynamics (Raes et al., 2000).

The processes that determine the number of CCN particles include emissions, photochemistry, nucleation, coagulation, condensation, and wet removal. Some particles are primary particles, i.e. emitted directly from sources, such as carbonaceous particles from open fires (Ito and Penner, 2005), sea salt particles from the bubble-bursting process of whitecaps (Clarke et al., 2006), and dust particles from wind erosion of dry soils (Ginoux et al., 2001). Some of these particles are large enough to act as CCN, such as

some sea salt particles (Clarke et al., 2006), but other particles, such as hydrophobic soot particles, must first add soluble compounds and grow by condensation and coagulation to sizes that are large enough to act as CCN (Rissler et al., 2006). Secondary particles may be generated from the nucleation of gas phase species, such as sulfuric acid gas and water vapor (Kulmala et al., 2007). These freshly nucleated particles begin as nanometer sized particles, and need substantial growth to become CCN-sized particles. New particle formation events capable of producing CCN-size particles have been observed at locations including the sub-Arctic boreal forest (Lihavainen et al., 2003), coastal areas (O'Dowd et al., 2002a), continental regions (McNaughton et al., 2004; Laaksonen et al., 2005), cloud outflow regions (Twohy et al., 2002), and in the upper free troposphere (Singh et al., 2002). Primary particles and secondary particles interact with each other by coagulation, and compete for gas phase species which may condense or form new particles through nucleation.

Cloud processing is another important microphysical process that may produce CCN-sized particles (Hoppel et al., 1994). In an environment with high supersaturations, some ultrafine particles (< 0.05 μm in radius) can activate into non-precipitating cloud droplets. Once a droplet is formed, aqueous oxidation of compounds within the drop will add mass to the pre-existing particles. When the cloud droplets evaporate, the residual aerosol particles are larger than original aerosol particles and can be activated more readily with a more modest supersaturation.

The concentration of CCN-sized particles that are available for cloud formation also depends on the transport between different atmospheric compartments (e.g., the marine boundary layer (MBL) and the free troposphere (FT)) because the residence time of

aerosols within a typical atmospheric compartment is shorter than the characteristic time of many aerosol microphysical processes (Raes et al., 2000). For example, observations have shown that subsidence from the FT may be an important process controlling MBL aerosol number concentrations. Clarke et al., 1996; Van Dingenen, 1999; Clarke et al., 2006). Clarke et al. (2006) estimated that entrainment from the FT can provide 35-80% of the CCN flux into the MBL over regions between 40ºS and 40ºN, with the rest from sea salt aerosol.

Unraveling the role of these complicated processes in determining CCN-sized particles requires a global model that can account for both aerosol microphysical processes and large and small scale transport (Raes et al., 2000). In order to meet this need, global aerosol models with detailed aerosol microphysics modules have been recently developed (Wilson et al., 2001; Adams and Seinfeld, 2002; Gong et al., 2003; Easter et al., 2004; Lauer et al., 2005; Liu et al., 2005; Spracklen et al., 2005a; Stier et al., 2005). Generally, these aerosol microphysics modules include the formation of new aerosol particles (nucleation) from gas phase species (e.g., sulfuric acid gas and water vapor), the condensation of volatile gases on preexisting aerosol particles, the coagulation of aerosol particles, and the cloud processing of the aerosol particles. The inclusion of these microphysical processes in a global aerosol model permits prediction of the formation and cycling of aerosols in the global atmosphere and determination of the source of CCN-sized particles.

Several studies have used these global aerosol models to investigate how different sources contribute to CCN concentrations. Adams and Seinfeld (2002; 2003) used a model that only included sulfate and showed that primary emissions of sulfate were more

efficient at increasing CCN concentration per unit mass of SO_2 emissions than gas-phase emissions. Pierce and Adams (2006) and Pierce et al. (2007) extended the Adams and Seinfeld model, adding primary-emitted aerosol particles from sea salt and carbonaceous aerosols. Pierce and Adams (2006) showed that including the emissions of ultrafine sea salt (<0.05 μm in radius) can increase CCN concentrations at 0.2% supersaturation over the Southern Ocean by 20% to 60%, depending on the sea salt emission parameterization which was used. Assuming an internal mixture of sulfate, sea salt, black carbon (BC), and organic matter (OM) in their model, Pierce et al. (2007) showed that the inclusion of carbonaceous aerosol particles can increase CCN concentrations (at 0.2% supersaturation) by 65-90% in the globally averaged surface layer depending on the carbonaceous emissions inventory used. In another study, Stier et al. (2006) included all major aerosol types and separately tracked soluble and insoluble particles. They found that the column-integrated soluble accumulation mode number concentration only decreased by 4.6% when anthropogenic carbonaceous emissions were excluded. In contrast, when anthropogenic emissions from both carbonaceous particles and sulfur were excluded, the column-integrated soluble accumulation mode number concentration was decreased by 42.3%. Spracklen et al. (2005a) used a model that only included sulfate and sea salt aerosols and simulated a larger decrease (60%) in the CCN concentration at the surface when anthropogenic sources of sulfur were excluded. They also found that in the tropical oceanic marine boundary layer, sea spray contributes less than 10% of the total CCN and that the remaining 90% were derived mostly from sulfate particles that formed in the FT by binary homogeneous nucleation (BHN).

The model studies summarized above only considered binary homogenous nucleation (BHN). Although BHN can explain observed nucleation rates in the upper troposphere, it cannot explain the observed nucleation rates in the boundary layer (e.g., Clarke et al., 1998). Several nucleation mechanisms have been suggested to explain boundary layer nucleation events (Kulmala et al., 2006; Sihto et al., 2006; Yu, 2006). Spracklen et al. (2006) include a boundary layer nucleation mechanism from Kulmala et al. (2006) in their global aerosol model and studied its effect on CCN concentrations (Spracklen et al., 2008). They demonstrated that the inclusion of the boundary layer nucleation scheme improves the comparison of the simulated nucleation events with observations in Hyytiälä, Finland, and improves the simulated particle size distribution and total particle number concentrations at three continental sites in Europe. Their global calculation also showed that boundary layer nucleation increases springtime boundary layer global mean CCN concentrations at 0.2% supersaturation by 3-20%.

Large uncertainties remain in these model studies, however, especially in terms of the representation of primary-emitted particles. For example, Pierce et al. (2007) assumed that all carbonaceous aerosols were emitted in a size distribution with a number median diameter (d_g) of 0.023μm and a geometric standard deviation (σ) of 2.00, while Stier et al. (2006) assumed a d_g of 0.06μm for carbonaceous aerosols from fossil-fuel and bio-fuel emissions and a d_g of 0.15μm for those from vegetation fires, with a σ of 1.59 for all carbonaceous aerosols. These models also differ with respect to whether or not primary-emitted sulfate particles were included. Spracklen et al. (2005a, 2006) did not include any primary-emitted sulfate particles, while Stier et al. (2006), Pierce et al. (2007) and

Spracklen et al. (2008) included these particles, but assumed different amounts and sizes for the emitted particulate sulfate.

More importantly, the effects of modeling different sources of CCN particles on the estimation of the aerosol indirect forcing have not been studied. Several studies have used the size-resolved aerosol composition predicted from their aerosol models to estimate the aerosol indirect effect (Ghan et al., 2001a; Lohmann et al., 2007; Storelvmo et al., 2006). But these studies did not examine how different treatments in the prediction of the aerosol size and number concentration affect the estimation of the first indirect forcing. Ghan et al. (2001a) showed that the aerosol indirect forcing calculated on the basis of their predicted aerosol size was smaller than that calculated on the basis of a prescribed size distribution, because anthropogenic sulfate contributed less to the simulated CCN particles in the case of the predicted aerosol size due to its condensation on other primary particles. Their conclusion, however, may be affected by the prescribed size chosen in their sensitivity test because, as noted in Chen and Penner (2005), the choice of the prescribed aerosol size has a large impact on the aerosol indirect forcing. Furthermore, their conclusion was drawn based on the aerosol indirect forcing from anthropogenic sulfate only. The concurrent increase in both anthropogenic sulfate and other non-sulfate aerosols may have different effects (Stier et al. 2006). Moreover, they did not investigate how the treatment of individual processes affect the calculated aerosol indirect forcing, e.g., how the primary-emitted sulfate particles included in their model affect the simulated aerosol indirect forcing.

Using a global aerosol model with a detailed aerosol microphysics module to simulate both aerosol size and number, we showed in Chapter II that the inclusion of a boundary

layer nucleation mechanism provides a better agreement with long-term observations of aerosol size distributions than do models that only include primary-emitted sulfate or BHN, especially over the MBL and over the Southern Hemisphere (SH). We also showed that the simulated effect of the boundary layer nucleation on the aerosol number concentration depends on whether primary-emitted sulfate particles are or are not included.

Here we extend the work in Chapter II. The goals of this Chapter are threefold: 1) to study the effects of including a boundary layer nucleation mechanism on CCN concentrations; 2) to revisit the effects of BHN in the FT and primary-emitted sulfate particles on CCN concentrations, given the new results concerning inclusions of boundary layer nucleation in the model; and 3) to further examine the effects of nucleation and the emission of primary sulfate particles on the indirect forcing by anthropogenic aerosols. Section 3.2 describes our methods. The global mass budget for all cases is described in section 3.3. The effects on simulated CCN concentrations are explored in section 3.4. The effects on the anthropogenic fraction of CCN are presented in section 3.5. Impacts on cloud droplet number concentration and the first indirect effect are explored in section 3.6. Finally, section 3.7 presents a discussion and our conclusions.

3.2 Methods

3.2.1 The coupled IMPACT/CAM model

The model used here consists of two components as described in detail in Chapter II: the NCAR CAM3 atmospheric circulation model (Collins et al., 2006a), and the LLNL/Umich IMPACT aerosol model (Liu et al., 2005). The aerosol model component

(IMPACT) includes an aerosol microphysics module that simulates the dynamics of the sulfate aerosol size distribution (nucleation, condensation, coagulation) and its interactions with primary emitted non-sulfate aerosols: OM, BC, dust, and sea salt (Herzog et al., 2004). Both the mass and number of pure sulfate aerosol in an arbitrary number of modes are predicted. Here, we chose the 2-mode version of the model, which includes a nucleation/Aitken mode (r<0.05μm) and an accumulation mode (r>0.05 μm). Non-sulfate aerosols are assumed to follow predefined background size distributions (Table 2.1). Sulfuric acid gas (H_2SO_4(g)) is produced from the gas phase oxidation of DMS and SO_2. H_2SO_4(g) can nucleate to form new sulfate particles in the nucleation mode or can condense onto preexisting sulfate or non-sulfate aerosol particles. Sulfate aerosol particles can also coagulate with other particles. The hydrophilic and hydrophobic properties of non-sulfate aerosols are determined by the amount of sulfate coating that is produced through coagulation and condensation. The aqueous production of sulfate is equally distributed among the hygroscopic aerosol particles that are larger than 0.05μm in radius.

The atmospheric general circulation model (GCM) component (NCAR CAM3) is a part of the Community Climate System Model (CCSM3) (Collins et al., 2006b). Cloud water and cloud ice are separate prognostic variables in CAM3, which makes it possible to treat the difference in radiative and sedimentation properties between cloud water and cloud ice. Cloud droplet number concentrations are prescribed in the precipitation process and in calculating the radiative properties of clouds. Boville et al. (2006) and Collins et al. (2006a) document the physical parameterizations used in the model and its performance.

We used 26 vertical levels and a horizontal resolution of 2 × 2.5 degrees for both the CAM3 and IMPACT models in this study. The time step for CAM3 was 30 minutes, and the time step for advection in IMPACT was 1 hour.

3.2.2 Nucleation mechanisms

In the original IMPACT aerosol model (Liu et al., 2005), only BHN using the parameterization of Vehkamäki et al. (2002) was included. As mentioned above, BHN cannot explain the observed nucleation rate in the boundary layer (e.g., Clarke et al., 1998). Moreover, the model study of Lucas and Akimoto (2006) has shown that the simulated nucleation rate from BHN is negligible in the boundary layer. In addition Spracklen et al. (2005a) showed that there was very little change in the simulated MBL aerosol number concentration when BHN was switched off in the lowest 3 km of their model.

In Chapter II, we implemented a parameterization to simulate boundary layer nucleation in the IMPACT model. This parameterization was based on an empirical fit to newly formed particles and their dependence on sulfuric acid vapor from long-term observations of aerosol formation events at Hyytiälä, Finland (Kulmala et al., 2006; Sihto et al., 2006; Riipinen et al., 2007). This parameterization also fits nucleation events measured in a variety of continental and marine atmospheric environments (Kuang et al., 2008). The nucleation rate of 1 nm particles (j_{1nm}) is first calculated using the parameterizations from Kulmala et al. (2006) and Sihto et al. (2006) (Equation 2.1 and Equation 2.2 in Chapter II). In the model, 3 nm particles are added to the nucleation mode at each time step (which is dynamically determined based on the accuracy of the solution) instead of 1 nm particles. The rate of formation of 3 nm particles (j_{3nm}) is

calculated from j_{1nm} using the formula from Kerminen and Kulmala (2002) (see Equation 2.3 in Chapter II).

For the rate coefficients A and K in Equation 2.1 and Equation 2.2, we adopt the median values derived from the case studies in Sihto et al. (2006), which were 1.0×10^{-6}/s and 1.0×10^{-12} cm^3/s, respectively. In Chapter II, we showed that the inclusion of these boundary layer nucleation mechanisms improved the comparison of simulated aerosol size distributions with observations in the MBL. Furthermore, the use of Equations 2.1 and 2.2 gave similar results, especially in terms of the number concentration of the accumulation mode particles. Here, we choose Equation 2.1 to represent boundary layer nucleation. The contribution of BHN and the nucleation mechanism represented by Equation 2.1 to the CCN concentration and to the first aerosol indirect forcing will be quantified.

Although the form of the empirical parameterization for nucleation is generally applicable, variations of several orders of magnitude in the prefactors *A* and *K* have been observed, depending on location and the environmental conditions (Sihto et al.; 2006; Riipinen et al., 2007; Kuang et al., 2008). This indicates that species other than sulfuric acid may play a role in nucleation. For example, biogenic iodine oxides (O'Dowd et al., 2002b), organic species (Zhang et al., 2004), and ammonia (Korhonen et al., 1999) can be important in particle formation. In addition, ion mediated nucleation may be also important (Yu et al., 2008a). Nevertheless, this simple empirical parameterization is still useful for exploring the effects of boundary layer nucleation in global models, given our poor understanding of the mechanisms behind particle formation.

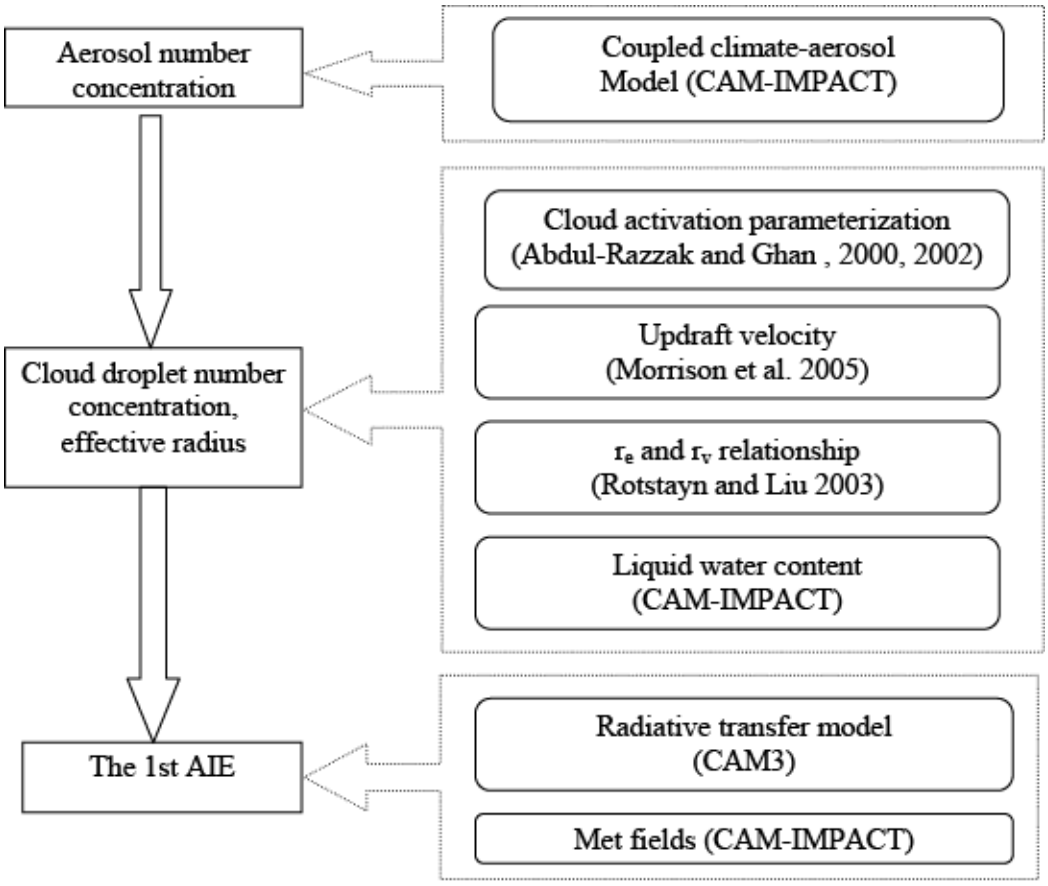

Figure 3.1: Diagram showing the processes included in the estimation of the first aerosol indirect effect.

3.2.3 Primary-emitted sulfate particles

Most global model studies that predict both aerosol mass and number have included some fraction of sulfur emissions as primary emitted sulfate particles to represent sub-grid scale nucleation (Liu et al., 2005; Easter et al., 2004; Stier et al., 2005; Adams and Seinfeld, 2002; Spracklen et al. 2005b; Pierce et al., 2007). The amount and size of these particles is chosen to represent the condensational growth and coagulation of both sulfate particles emitted directly from the source and those nucleated shortly after emission (Adams and Seinfeld, 2003).

In the IMPACT aerosol model (Liu et al., 2005), 2% of anthropogenic sulfur was assumed to be emitted as primary sulfate particles, with 85% of the mass residing in the accumulation mode with a mode diameter of 70 nm and a geometric standard deviation of 2.0 nm, and the remaining 15% of the mass in the Aitken mode having a mode diameter of 10 nm and a geometric standard deviation of 1.6 nm. We showed in Chapter II that, this primary-emitted sulfate has a large impact on the simulated aerosol number concentrations, consistent with the results from Adams and Seinfeld (2002) and Spracklen et al. (2005b). In this study, we will further examine how these primary-emitted sulfate particles affect the CCN number concentration and the first indirect forcing.

3.2.4 Calculation of cloud droplet number and the first indirect forcing

We used a procedure similar to that used by Chen and Penner (2005) to calculate the aerosol indirect forcing (Figure 3.1). First, the aerosol fields calculated from the coupled model are used to calculate the cloud droplet number concentration using the cloud droplet activation parameterization of Abdul-Razzak and Ghan (2000; 2002). Then, the droplet number concentration is used to calculate the cloud droplet effective radius (Rotstayn and Liu, 2003). Finally, the cloud droplet effective radius is used to calculate the cloud optical depth and the first aerosol indirect forcing using an offline radiative transfer model taken from NCAR CAM3. Detailed descriptions of each step follow.

The cloud droplet number concentration was calculated from the aerosol fields using a parameterization based on Köhler theory (Abdul-Razzak and Ghan, 2000; 2002). This parameterization combines the treatment of multiple aerosol types and a sectional representation of size to deal with arbitrary aerosol mixing states and arbitrary aerosol

size distributions. Five categories of aerosols are externally mixed: pure sulfate, biomass burning OM/BC coated with sulfate, fossil fuel OM/BC coated with sulfate, sea salt with sulfate, and dust coated with sulfate; coating by sulfate is treated as internally mixed in each aerosol type. The bulk hygroscopicity parameter for each category of aerosol is the volume-weighted average of the parameters for each component taken from Ghan et al. (2001b) (see Table 3.1). The size distributions for pure sulfate, which have spatial and temporal variations, are predicted from the coupled CAM-IMPACT model, while the size distributions of the non-sulfate aerosols are prescribed as in Table 2.1. In applying the Abdul-Razzak and Ghan parameterization, the size spectrum for each aerosol category is divided into 30 bins.

The vertical velocity used in the cloud activation parameterization is calculated as

$$w = \overline{w} + c \times \sigma_w \tag{3.1}$$

(Lohmann et al., 1999; Takemura et al., 2005; Jiang and Cotton, 2005; Lohmann et al., 2007), where $\overline{w}$ is the large-scale vertical velocity, σ_w is the subgrid-scale variance of the vertical velocity, and c is a coefficient. This formula takes the non-linear dependence of the cloud droplet number on the vertical velocity into account. σ_w is diagnosed (Morrison et al., 2005) as

$$\sigma_w = K \big/ m_l , \tag{3.2}$$

where K is the eddy diffusivity from the CAM3 model and m_l is the mixing length. The mixing length is calculated based on Holtslag and Boville (1993) from the altitude z and the asymptotic scale length λ_c (m) using the following formula:

$$\lambda_c = 300 \text{ for } z \le z_{pbl} \tag{3.3}$$

and

$$\lambda_c = 30 + 270\exp(-z / z_{pbl}) \text{ for } z \geq z_{pbl}, \quad (3.4)$$

where z_{pbl} is the height of the planetary boundary layer. The minimum value of σ_w is set to 0.1 m/s, following Ghan et al. (1997) and Morrison et al. (2005).

In Lohmann et al. (1999; 2007) and Takemura et al. (2005), fixed values for *c* are used (0.7 in Lohmann et al. 1999 and Takemura et al., 2005; 1.3 in Lohmann et al., 2007). Jiang and Cotton (2005) diagnosed *c* to be 0.24 using large-eddy simulations of six observed boundary layer cases, but also showed that the value of *c* diagnosed from these simulations varied from small values for cumulus clouds (around 0.10) to two to five times larger for stratocumulus clouds (0.30-0.55) (Table 1 in Jiang and Cotton, 2005), which implies that the value of *c* may depend on other parameters, such as σ_w or $\overline{w}$. We diagnosed *c* by calculating cloud droplet number concentration and integrating over a normal vertical velocity distribution with a mean of zero and a standard deviation of σ_w and setting the computed droplet number to that obtained using Equation 3.1. Our results show that the coefficient *c* in Equation 3.1 must be treated as a function of the variance of the vertical velocity, in order to reproduce the results from the normal probability distribution, and that it should decrease for larger values of σ_w. Based on our tests, we used the following empirical formula for *c* in our droplet nucleation parameterization:

c = 0.20, when σ_w > 10 m s^{-1} ; (3.5)

$$c = \frac{\log\sigma_w - \log 0.1}{\log 10 - \log 0.1} \times 0.6 + \frac{\log 10 - \log\sigma_w}{\log 10 - \log 0.1} \times 0.1, \quad (3.6)$$

when 0.1 m s^{-1} < σ_w <10 m s^{-1} ;

c = 0.60, when σ_w < 0.1 m s^{-1}. (3.7)

Table 3.1. Hygroscopicity and density for each aerosol component

Aerosol Component	Hygroscopicity[a]	Density (g/cm^3)
Sulfate	0.51	1.7
BC	5.0e-7	1.5
OM	0.13	1.2
Sea Salt	1.16	2.2
Dust	0.14	2.6

[a]The hygroscopicity parameter depends on the number of dissolved ions per molecule, the osmotic coefficient, the soluble mass fraction, the component density, and the molecular weight, as defined by Equation 3 in Abdul-Razzak and Ghan (2000). Values are taken from Ghan et al. (2001b).

The coefficient *c* should also depend on the mean velocity and the number concentration of accumulation mode aerosol (radius > 50 nm). However, since the large scale vertical velocity in a grid box of the GCM is normally less than 0.05 m/s, we neglect the dependence of *c* on the mean velocity as an approximation. Moreover, as long as the accumulation mode aerosol concentration is less than 1000/cm^3, the cloud droplet number concentration calculated from this approximation is within 10% of that calculated by integrating over the normal vertical velocity distribution.

In part, because we suspect that our sea salt concentrations are underpredicted (see details in Chapter II), we set a lower limit on the cloud droplet number concentration of 20 cm^{-3} to represent the minimum cloud droplet concentration in the background atmosphere. As we show in section 3.6, however, the use of this minimum number concentration adds uncertainties to the calculated first aerosol indirect effect.

The volume mean radius of the cloud droplets is calculated from the cloud droplet number concentration and the liquid water content of the cloud. Then, the cloud droplet effective radius is parameterized based on Rotstayn and Liu (2003), which takes account the change in the dispersion of the cloud droplet size distribution due to the change in the

cloud droplet number. The middle curve in Figure 3.1 from Rotstayn and Liu (2003) is used in this study.

The radiative transfer model is that of NCAR CAM3 (Collins et al., 2006a), and the meteorological fields are taken from the output of the coupled CAM3/IMPACT model with a frequency of four hours. The time step for the radiative transfer model is one hour. The concentrations of the trace gases CO_2 and O_3 are the same as those in the NCAR CAM3 model. We apply the effects of aerosols on clouds to all liquid clouds, and to both large scale and convective clouds. The sensitivity of the first AIE to cloud types included in the calculation is discussed in section 3.6.

Table 3.2. Description of cases

Case name	Within BL[a]	Within FT[b]	Primary sulfate
BHN	BHN[c]	BHN	0%SO2[d]
EMP	EMP[e]	No FT nucleation	0%SO2
BLBHN	BHN	No FT nucleation	0%SO2
BHN_PRIM	BHN	BHN	2%SO2[f]
BHN_EMP	EMP	BHN	0%SO2
BHN_EMP_PRIM	EMP	BHN	2%SO2

[a]Boundary layer.
[b]Free troposphere.
[c]Binary homogeneous nucleation (scheme of Vehkamäki et al., 2002).
[d]0% of anthropogenic SO_2 emissions are input as primary sulfate.
[e]The empirical parameterization for boundary layer nucleation from Equation 2.1.
[f]2% of anthropogenic SO_2 emissions are input as primary sulfate.

3.2.5 Overview of the model experiments

Table 3.2 lists all of the cases considered here. In case BHN, only binary homogeneous nucleation is included in both the boundary layer (BL) and the FT, and no primary-emitted sulfate particles are included. In case EMP, only the empirical boundary layer nucleation from Equation 2.1 is included. There is no nucleation in the FT or any primary-emitted particulate sulfate. BLBHN is the same as EMP, except that binary homogeneous nucleation replaces the nucleation parameterization based on Equation 2.1

in the boundary layer. BHN_PRIM is the same as BHN, except that 2% of the anthropogenic sulfur emissions are emitted as sulfate particles. BHN_EMP is the same as BHN, except that the boundary layer nucleation scheme from Equation 2.1 replaces the binary homogeneous nucleation in the boundary layer. Finally, BHN_EMP_PRIM is the same as BHN_EMP, except that 2% of the anthropogenic sulfur emissions are emitted as sulfate particles. BHN, BHN_PRIM, BHN_EMP, and BHN_EMP_PRIM were compared with observations in Chapter II. The EMP and BLBHN cases are added here to quantify the effect of BHN in the FT on CCN concentrations and on the AIE.

The role of nucleation in the boundary layer on CCN concentrations can be quantified by comparing BHN_EMP with BHN and BHN_EMP_PRIM with BHN_PRIM. The role of nucleation in the FT can be quantified by comparing BHN with BLBHN and BHN_EMP with EMP. Finally, the role of representing nucleation in the boundary layer by primary-emitted sulfate particles can be quantified by comparing BHN_PRIM with BHN and BHN_EMP_PRIM with BHN_EMP.

We ran two simulations for each of the cases in Table 3.2: one with the present day (PD) emissions and one with preindustrial emissions (PI). In each simulation, the coupled model was integrated for 1 year after an initial spin-up of four months. Since the aerosol fields are not allowed to change heating rates or droplet number concentrations in the climate model, the aerosol fields do not affect the simulated meteorological fields, which allows us to compare the aerosol fields from different cases from these one-year simulations, as in Chapter II. Then the resulting aerosol fields from the coupled model are used to calculate cloud droplet number concentration and the first indirect forcing, following the procedure described in section 3.2.4.

Table 3.3: Aerosol emissions and burdens in the present day and preindustrial simulations for the BHN_PRIM case.

Aerosol types	Sources (Tg/yr or Tg S/yr)		Burden (Tg or Tg S)	
	PD	PI	PD	PI
Sulfate	60.06	24.00	0.86	0.33
Black carbon	10.51	2.52	0.13	0.033
Organic carbon	77.52	37.44	1.02	0.47
Dust size[a] (μm)				
0.05-0.63	76.57	76.57	1.62	1.62
0.63-1.25	291.53	291.53	6.03	6.40
1.25-2.50	662.58	662.58	10.83	11.00
2.50-10.0	1325.17	1325.17	4.28	4.30
0.05-10.0	2355.86	2355.86	22.77	23.34
Sea Salt size[a] (μm)				
0.05-0.63	112.47	112.86	0.42	0.42
0.63-1.25	430.90	432.34	1.56	1.56
1.25-2.50	932.15	935.21	2.56	2.57
2.50-10.0	1079.04	1082.65	0.46	0.47
0.05-10.0	2554.57	2563.07	5.01	5.02

[a]radius.

3.3 Global aerosol mass budgets in PD and PI simulations

Anthropogenic sulfur emissions were used from Smith et al. (2001; 2004), and those for the year 2000 (61.3 Tg S per year) and the year 1850 (1.51 Tg S per year) were used for the present day (PD) and the preindustrial (PI) simulations, respectively. Anthropogenic emissions of fossil fuel and biomass burning carbonaceous aerosols were from Ito and Penner (2005), but adjusted as discussed in Chapter II. The year 2000 PD emissions include fossil fuel BC and OM (5.8 Tg BC and 15.8 Tg OM per year), and biomass burning BC and OM (4.7 Tg BC and 47.4 Tg OM per year). PI emissions were those for 1870 (23.0 Tg per year for OM and 2.52 Tg per year for BC). Natural emissions included volcanic SO_2 (4.79 Tg S per year from Andres and Kasgnoc, 1998), marine dimethyl sulfide (DMS) (26.1 Tg S per year from Kettle and Andreae, 2000), OM from vegetation (14.5 Tg per year from Penner et al., 2001), and mineral dust provided by

Ginoux (private communication, 2004) for the year 1998 based on the algorithm of Ginoux et al. (2001), and were the same for both the PD and PI simulations. Sea salt emissions (around 2560 Tg per yr) were calculated online in the coupled CAM/IMPACT model using the method defined in Gong et al. (1997).

The global aerosol mass budgets for all six cases are very similar, and only the results in the BHN_PRIM case are shown in Table 3.3. Aerosol burdens for the present day simulations are within the range of aerosol burdens simulated by other models (see Chapter II for details). The difference between the present day and preindustrial simulations is largely determined by the difference in the emissions, including both their amount and location. The difference is also affected by, but to a lesser extent, the difference in the scavenging efficiencies for the initially hydrophobic species, such as black carbon, organic carbon, and dust. For example, even though the emissions of mineral dust are the same in both the PD and PI simulations, the burden is slightly smaller in the PD simulation resulting from the larger wet scavenging efficiency of dust coated with sulfate.

3.4 Present day CCN concentration

Present day zonal annual-average CCN concentrations at 0.2% supersaturation and present day annual-average CCN concentrations at the third model level (around 930 hPa, representing the boundary layer) are shown in Figures 3.2 and 3.3, respectively, while Figure 3.4 shows the ratio of the present day annual-average boundary layer CCN concentration between different cases. As expected, the BLBHN case produces the smallest CCN concentrations and the BHN_EMP_PRIM case produces the largest concentrations. Thus, binary homogeneous nucleation is generally not very effective in

the boundary layer, whereas the introduction of primary aerosols together with the boundary layer nucleation scheme both act to increase CCN concentrations in the boundary layer over those from just BHN.

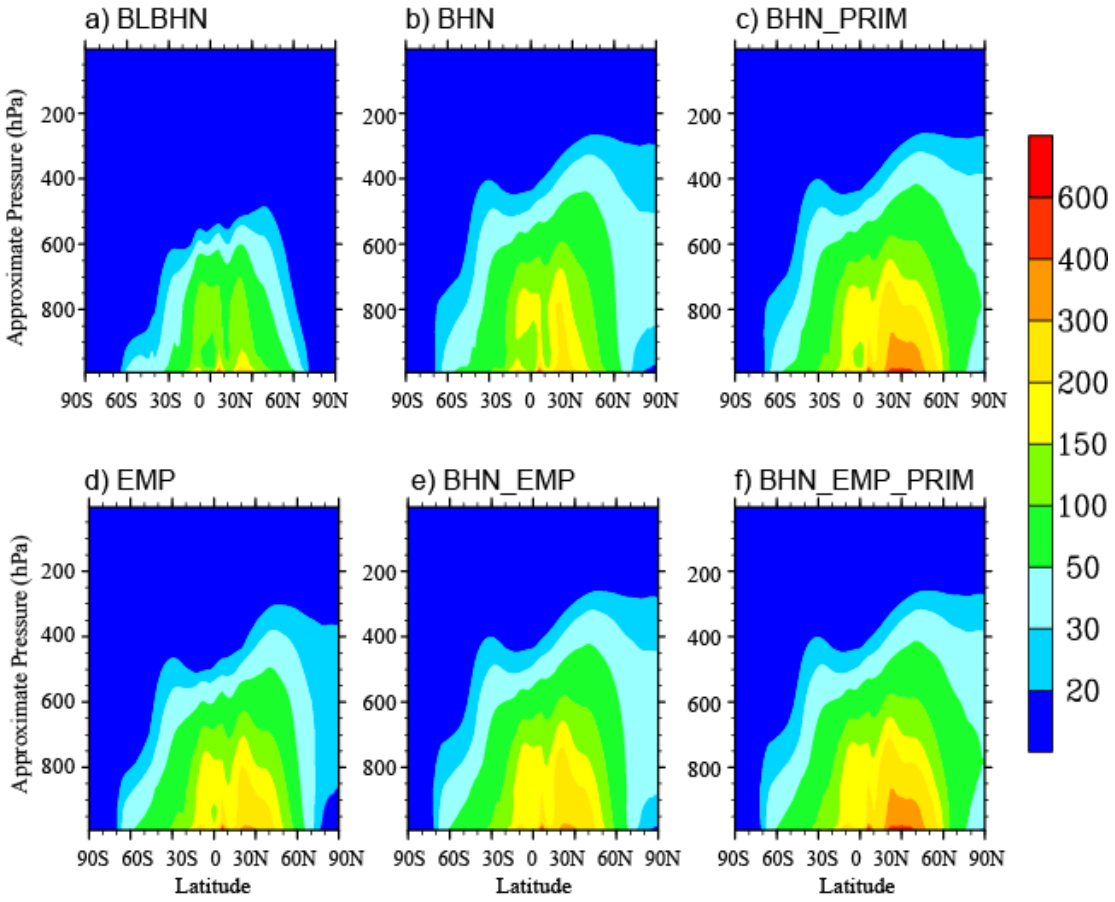

Figure 3.2: Present day zonal annual-average CCN concentrations (cm^{-3}) at 0.2% supersaturation for all six cases. CAM3 used a hybrid vertical coordinate, and the pressure at the *k*th model level is given by $p(k)=A(k)p_0+B(k)p_s$, where p_s is surface pressure, p_0 is a specified constant pressure (1000 hPa), A and B are coefficients. Data are plotted as a function of this hybrid vertical coordinate times 1000 and labeled 'Approximate Pressure'.

The effects of including the empirical boundary layer nucleation scheme can be quantified by comparing simulations with and without this nucleation mechanism. These effects are large when no primary sulfate particles are emitted, and the global average CCN concentration in the boundary layer is enhanced by 31.4% (Figure 3.4a and Table

3.4). In the MBL, boundary layer nucleation increases CCN concentrations by more than 30% (compare Figure 3.3b and e, and Figure 3.4a). In particular, CCN concentrations are increased by 75% to more than 150% over the tropical Eastern Pacific and in the middle latitudes over North America, Europe, and the North Atlantic. Over these regions, the production of sulfuric acid gas is high and the concentration of primary particles is low, which favors the occurrence of nucleation events. Over continental regions without high sulfuric acid concentrations, the increases in CCN concentrations are small (less than 10%). The effects of the empirical boundary layer nucleation mechanism are also small at high latitudes because of the lower sulfuric acid gas concentration.

In contrast, in the cases where 2% of the anthropogenic SO_2 emissions is emitted as particulate sulfate (BHN_EMP_PRIM vs. BHN_PRIM), the effects of the empirical boundary layer nucleation are much smaller and only increase global average CCN concentration in the boundary layer by 5.3% (Figure 3.4b and Table 3.4). The increases in CCN concentrations over most oceanic regions in the Northern Hemisphere (NH) and over land areas in both hemispheres are less than 10% (compare Figure 3.3d and f and Figure 3.4b). The inclusion of the empirical boundary layer nucleation scheme can even lead to a decrease in the CCN number concentrations over some regions, such as the western United States, as also shown in Spracklen et al. (2008). This is because the addition of tiny particles from boundary layer nucleation events slows the growth of particles into CCN-sized particles by competing with larger particles for the condensation of sulfuric acid gas. In the MBL over the tropical Pacific and in the SH, the effects of including the empirical boundary layer nucleation mechanism are still large since the emissions of anthropogenic primary sulfate particles are much smaller over these regions.

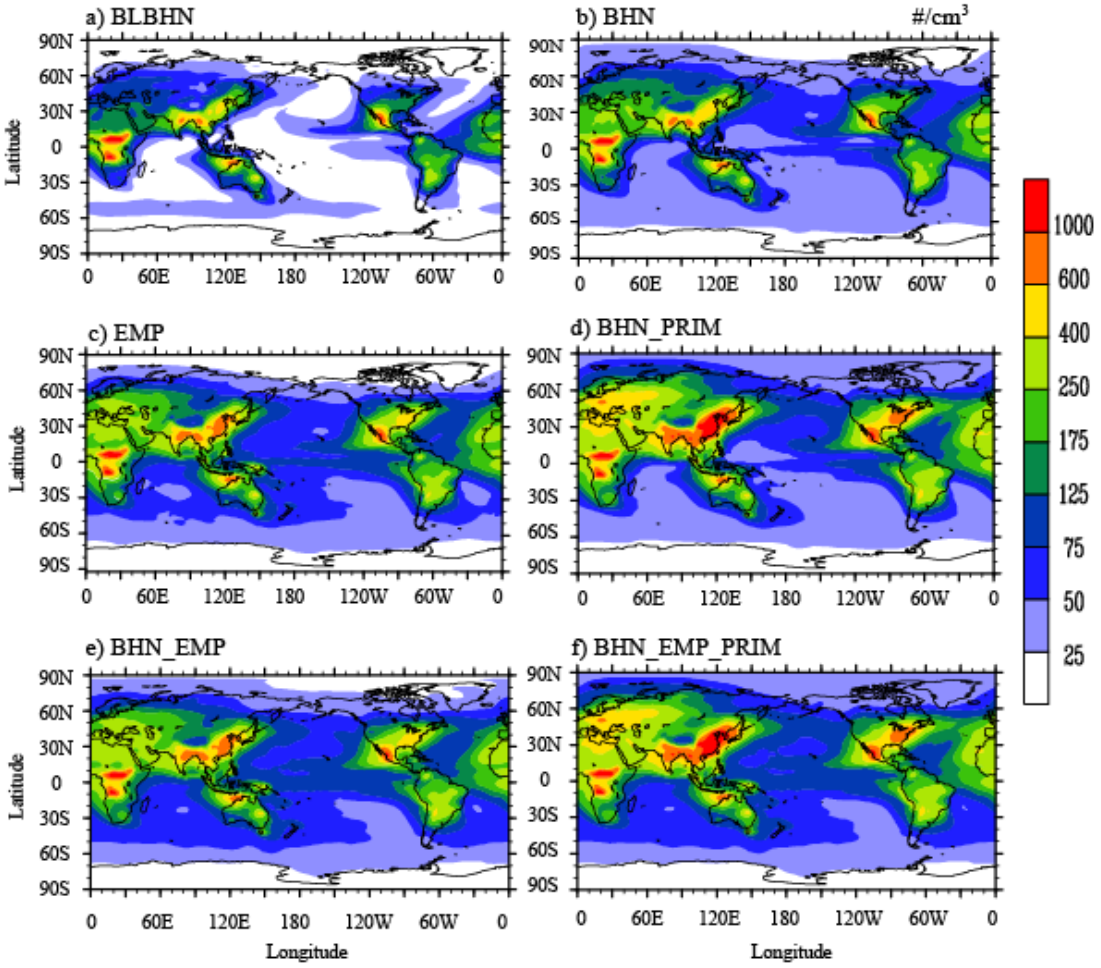

Figure 3.3: Present day annual-average CCN concentrations (cm^{-3}) at 0.2% supersaturation near 930 hPa (the third model level) for all six cases.

Spracklen et al. (2008) used the empirical nucleation rate represented by Equation 2.1, but with different rate coefficients, to study the effects of the boundary layer nucleation on CCN concentrations in spring (March-May) and how these depend on the rate coefficient. In their model, 2.5% of the anthropogenic SO_2 emissions were emitted as primary sulfate with the aged size distribution that was suggested for the AEROCOM emissions inventory (personal communication, D. Spracklen; Dentener et al., 2006). The majority (88%) of the primary anthropogenic SO_2 comes from the industrial sector and is

emitted at a diameter of 1 μm, while the remaining fraction comes from the traffic sector and is emitted at a diameter of 30 nm. Spracklen et al. (2008) showed that the enhancement in April is 9% when the rate coefficient is 2.0×10^{-6}/s. Their result is close to our annual average result (5.3% enhancement in the case when primary-emitted sulfate particles are included), although we have somewhat different emissions and concentrations of other primary particles (e.g., carbonaceous aerosol, sea salt) and have a different magnitude of emissions of the precursor species (SO_2 and DMS) of sulfuric acid gas. They also showed that the enhancement in April ranges from 3 to 20% when the rate coefficient ranges from 2.0×10^{-8} to 2.0×10^{-4}/s.

Our results suggest that the effects of including boundary layer nucleation on the CCN concentrations depend on both the rate coefficients (as shown by Spracklen et al., 2008), and in an important way on the assumed and simulated primary particles. When primary-emitted sulfate particles are included, the effect of including boundary layer nucleation is much smaller because the depletion of sulfuric acid gas from the condensational growth of primary particles decreases the frequency and intensity of nucleation events, and slows the growth of freshly nucleated particles. Although only primary particles from anthropogenic sulfate are examined here, we would expect that the effects of boundary layer nucleation on CCN concentrations also depends on the treatment of other primary particles (carbonaceous aerosols, dust, and sea salt). Given the large uncertainties in the treatment of these other primary particles in global aerosol models, the accurate determination of the effects of boundary layer nucleation on CCN concentrations may require significantly improved estimates of emissions.

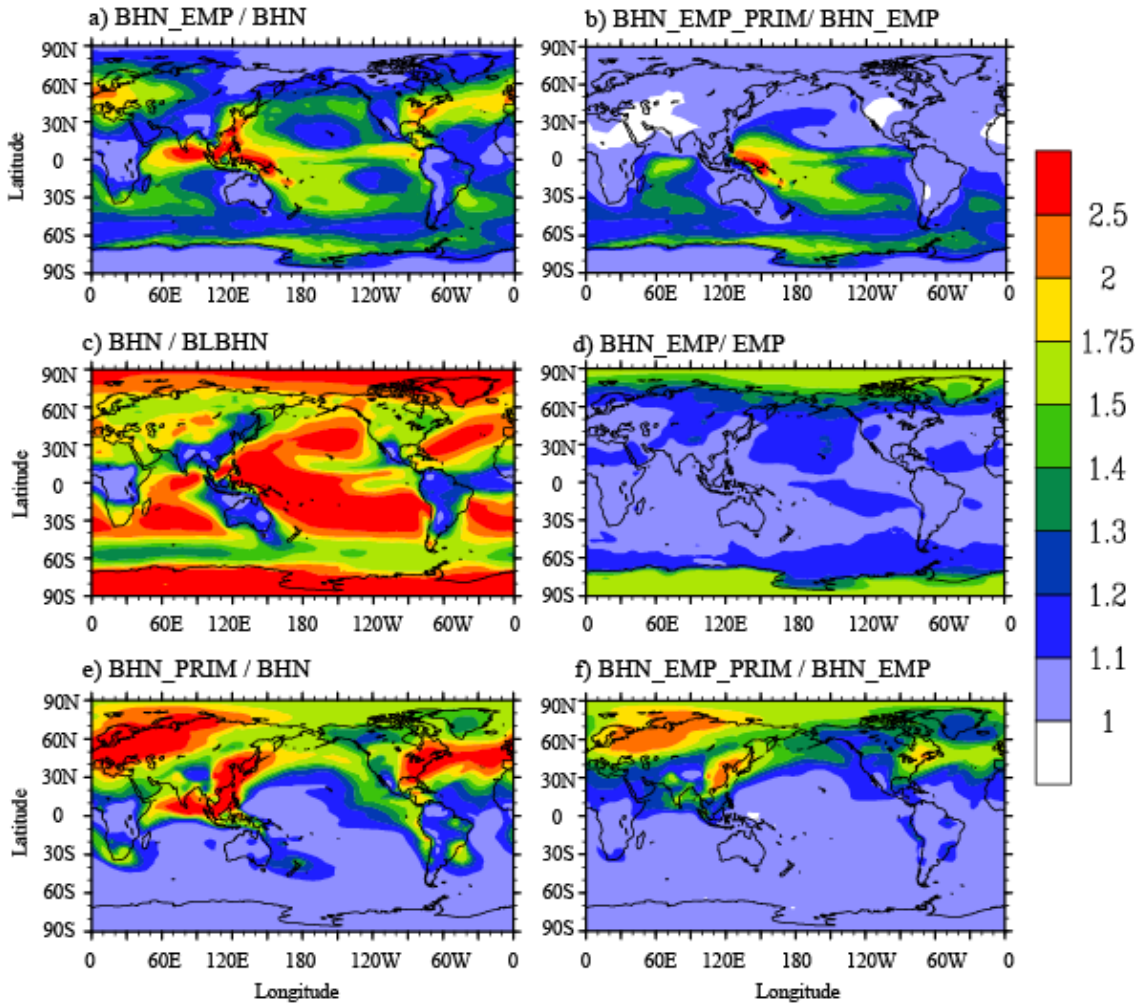

Figure 3.4: Ratio of present day annual-average CCN concentrations (at 0.2% supersaturation) near 930 hPa (the third model level) between different cases.

The effect of mixing free tropospheric aerosols into the boundary layer can be quantified by comparing cases in which binary homogeneous nucleation takes place throughout the atmosphere (case BHN or BHN_EMP) with those in which nucleation only takes place within the boundary layer (case BLBHN or EMP). Figure 3.4c shows that if only binary homogeneous nucleation is considered (BHN vs. BLBHN), the mixing of aerosols from the FT into the boundary layer has a large impact on the simulated CCN concentrations in the boundary layer. The small concentrations of CCN particles produced within the boundary layer in this case allows particles to diffuse into the

boundary layer from above, causing higher concentrations there, especially in the MBL over regions where primary particles have little influence on the CCN concentrations. In these regions, concentrations are increased by more than 200% (compare Figure 3.3a and 3.3b and Figure 3.4c). These results are consistent with the model study by Spracklen et al. (2005a). They are also consistent with the analysis of Clarke et al. (2006), who estimated that entrainment from the FT can provide 35-80% of the CCN flux into the MBL over regions between 40ºS and 40ºN.

In the case where the empirical boundary layer nucleation scheme is included (BHN_EMP vs. EMP), nucleation in the free troposphere increases boundary layer particles by less than 20% everywhere except near the poles (Figure 3.4d). This shows that if boundary layer nucleation events happen as frequently as Equation 2.1 suggests, the entrainment from the free troposphere into the boundary layer is not as important as previously thought. The effects of BHN in the FT are most important at high latitudes and in the middle troposphere (Figure 3.4d and compare Figure 3.2e and 3.2d), because the impact of the boundary layer nucleation is small in these regions (compare Figure 3.2b and 3.2e).

The inclusion of primary-emitted sulfate particles significantly increases CCN concentrations (Figure 3.4e and 3.4f). In the scenarios where the empirical boundary layer nucleation scheme is not included (BHN vs. BHN_PRIM), the inclusion of primary-emitted particulate sulfate increases CCN number concentrations in both the boundary layer and free troposphere, but the main effects are limited to the NH (compare Figure 3.2b and 3.2c, see Figure 3.4e). Over regions strongly influenced by industrial pollution, CCN concentrations are increased by more than 200%, which is consistent with the

results from previous studies (Adams and Seinfeld, 2002; Spracklen et al., 2005b). In the cases where the boundary layer nucleation scheme is included (BHN_EMP_PRIM vs. BHN_EMP), the effects of primary-emitted particles are smaller than when this effect is not included (compare Figure 3.4e and 3.4f), which is due to the competition for sulfuric acid gas between nucleation of new particles and condensation onto pre-existing particles. The decreases in the frequency and intensity of boundary layer nucleation partly offset the increases in the aerosol particles from the primary-emitted sulfate particles.

3.5 Anthropogenic contribution to CCN concentrations

It is important to understand the perturbations to the CCN concentrations between the PD and PI simulations in order to understand variations in the aerosol indirect forcing. Figures 5 and 6 show the annual-average boundary layer (third model level) and the zonal mean PD anthropogenic fraction of CCN concentrations, respectively. The PD anthropogenic fraction of CCN concentrations is calculated as the increase in the CCN concentrations from the PI to the PD case divided by the CCN concentrations in the PD case. In the BHN_PRIM case, present day anthropogenic emissions contribute 62% of the CCN concentrations in the boundary layer (~930 hPa). This fraction is comparable with that reported by Spracklen et al. (2005a) (59% in December and 61% in July at the surface) in a model that only included sulfate and sea salt aerosols, and with that reported by Adams and Seinfeld (2002) (60%) in a model that only included sulfate aerosols. Our results show that over polluted regions, such as East Asia, the eastern United States, and Europe, anthropogenic emissions contribute more than 80% of the CCN, but over remote oceanic regions the contribution from anthropogenic emissions is much smaller (Figure

Table 3.4: Global annual-averaged CCN concentration in the boundary layer in the PD simulation, cloud top effective radius in the PD simulation, change in the cloud top effective radius from anthropogenic emissions, anthropogenic fraction of CCN in the boundary layer, column-integrated anthropogenic fraction of CCN, and the 1st AIE for all six cases

Case name	CCN in the BL in PD (#/cm^3)	Reff[a] in PD (μm)	Change in Reff (μm)	f_{accn}[b] in the BL	Column-integrated f_{accn}	1st AIE (W/m^2)
BLBHN	70.34	13.50	-0.69	46.32	48.60%	-0.81
BHN	104.24	12.24	-0.86	43.88	48.76%	-1.55
EMP	128.37	11.83	-0.84	46.77	49.36%	-1.22
BHN_PRIM	159.89	11.77	-1.23	62.07	57.57%	-2.03
BHN_EMP	136.92	11.61	-0.84	46.37	50.62%	-1.49
BHN_EMP_PRIM	168.77	11.46	-0.97	46.09	55.36%	-1.65

[a]Cloud top droplet effective radius for low level warm clouds.
[b]PD Anthropogenic fraction of CCN concentrations.

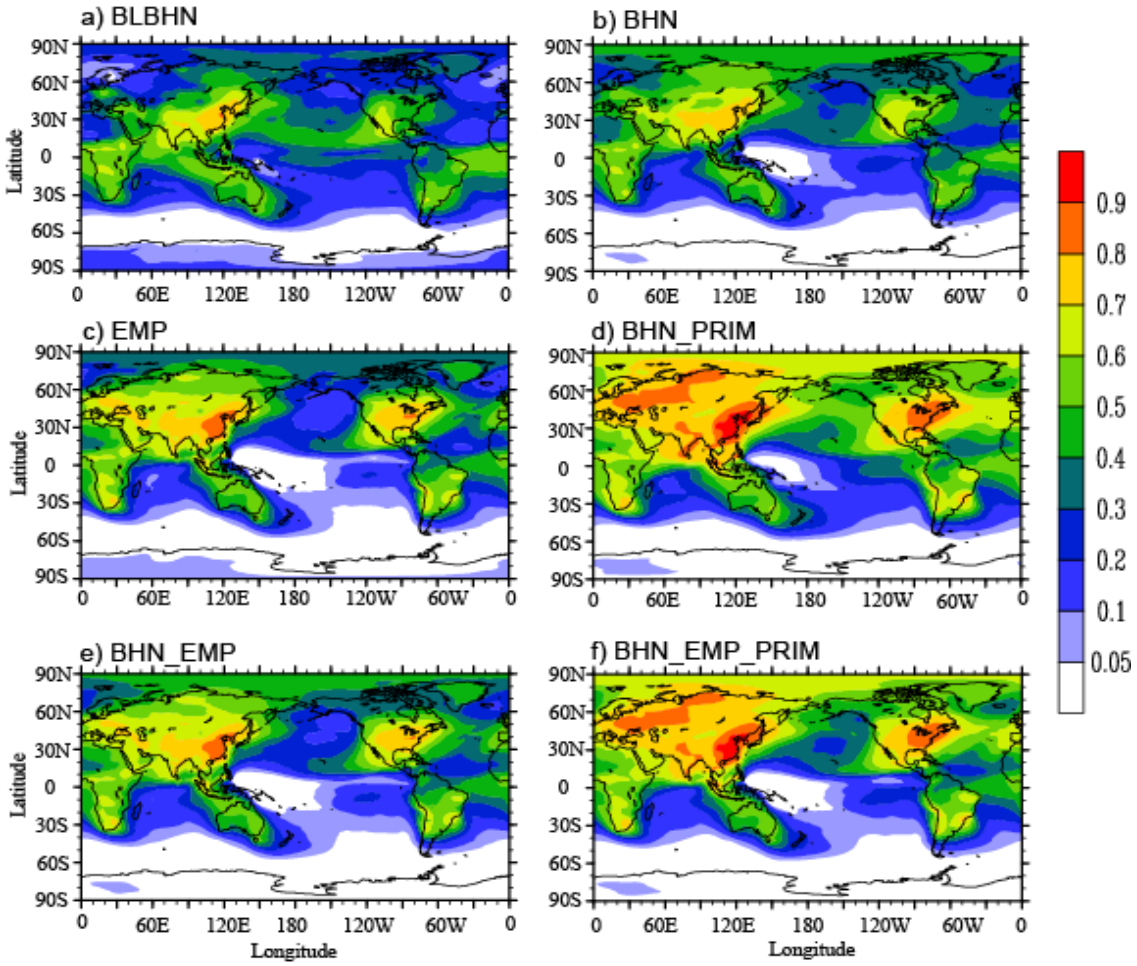

Figure 3.5: Annual-average anthropogenic fraction of CCN concentration at 0.2% supersaturation near 930 hPa (the third model level) for all six cases.

3.5d). For example, anthropogenic emissions contribute less than 5% of CCN in the SH south of 50°S.

There is a large difference in the contribution of CCN from anthropogenic emissions to the zonal mean CCN concentration between the NH and SH. In the NH middle latitudes, the anthropogenic fraction of CCN is of order ~60-80% in Figs. 3.6c, d, e, and f from the surface to the upper troposphere (200 hPa). The simulations with the largest values near surface are those that have primary-emitted sulfate particles (compare, for example, Figure 3.6c and 3.6b), and the simulations with the largest values in the upper

troposphere are those that either have BHN in the FT or have the empirical boundary layer mechanism in the BL (compare Figure 3.6b and 3.6d with 3.6a). It is interesting that the empirical boundary layer mechanism increases the anthropogenic fraction of CCN more in the upper troposphere than it does at the surface (Figure 3.6d) over the NH. This is because pure sulfate particles have a larger contribution to the anthropogenic fraction of CCN concentrations in the upper troposphere than in the lower troposphere in the NH (Figure 3.2d and 3.2a). In the SH middle and high latitudes, the anthropogenic fraction of CCN is small near the surface (less than 5% below about 700 hPa) in all simulations, and increases with altitude to ~40% around 300 hPa. The maximum at high altitudes in the SH results from the transport of pollution in the middle troposphere from the SH lower latitudes and from the NH (see also Spracklen et al., 2005a).

When the empirical boundary layer nucleation scheme is included in the BHN_EMP_PRIM case, the anthropogenic contribution to CCN concentrations in the boundary layer is 56%, a decrease of 6 percentage points from the BHN_PRIM case. The decrease is large over oceanic regions strongly influenced by continental pollution (compare Figure 3.5d and 3.5f, and Figure 3.7b). For example, over the North Pacific, the inclusion of boundary layer nucleation decreases the anthropogenic fraction from 40-60% in BHN_PRIM to 20-40% in BHN_EMP_PRIM. Over these regions, the relative increase in the SO_2 concentration from the preindustrial to the present day simulation is small due to the strong natural contribution from the oxidation of DMS, while the relative increase in the primary-emitted particles is large due to the influence from continental pollution. Both of these factors lead to a smaller relative contribution from boundary layer nucleation to the CCN concentration in the PD compared to that in the PI atmosphere,

which decreases the anthropogenic fraction of the CCN concentration. Over polluted continental regions, the effect of the empirical boundary layer nucleation scheme on the anthropogenic fraction of CCN is small.

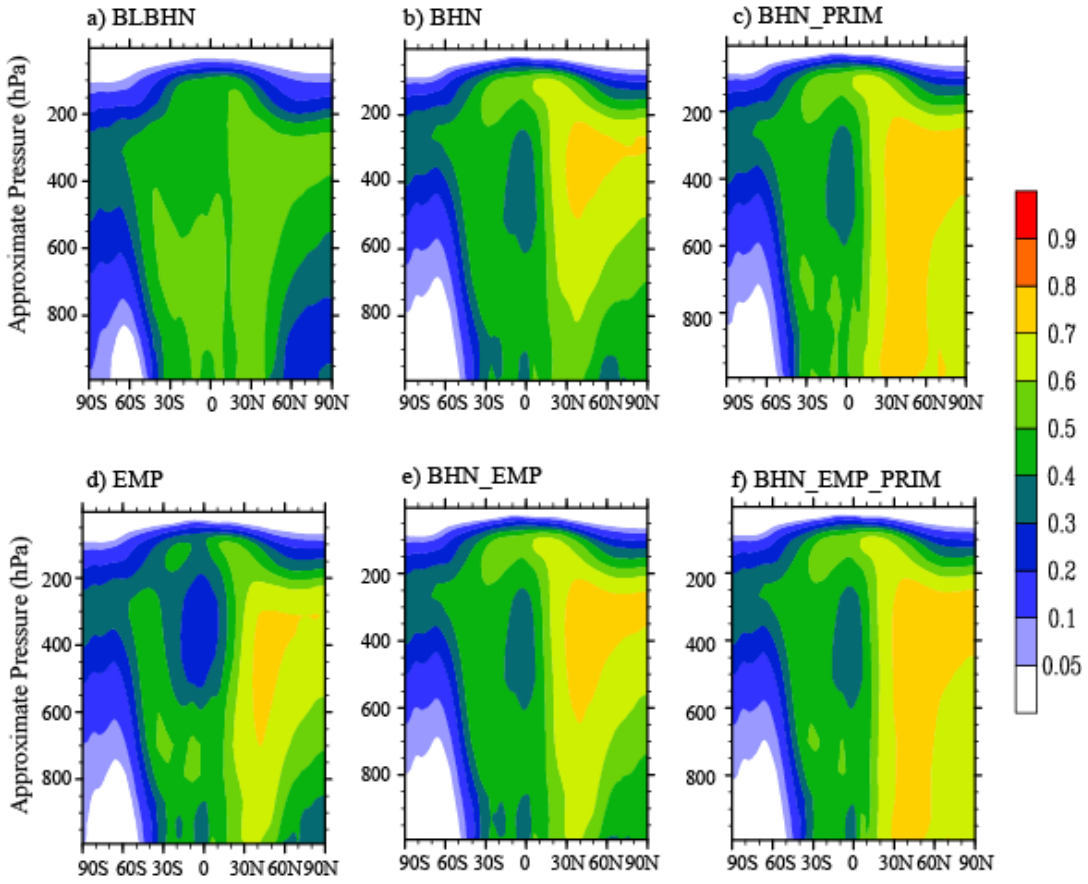

Figure 3.6: Present day zonal annual-average anthropogenic fraction of CCN concentration at 0.2% supersaturation. 'Approximate pressure' is defined in the caption to Figure 3.2.

In the cases which do not include any primary-emitted anthropogenic sulfate (BHN_EMP vs. BHN), the empirical boundary layer nucleation scheme increases the anthropogenic fraction of CCN by 1.5 percentage points from 44.9% in BHN to 46.4% in BHN_EMP in the boundary layer. This increase mainly occurs over continental regions (Figure 3.7a), which contrasts with the cases that included primary-emitted sulfate particles. Over these continental regions, the relative increase in the SO_2 concentration

from the PI to the PD simulation is larger than the relative increase in primary-emitted particles, which leads to a larger contribution to the CCN concentration in the PD than in the PI atmosphere when the boundary layer nucleation mechanism is included, thereby increasing the anthropogenic fraction of CCN. Decreases in the anthropogenic fraction of CCN over ocean regions are similar to the case when primary sulfate particles are emitted, but the decrease is not as large (compare Figure 3.7a and 3.7b).

Binary homogeneous nucleation in the free troposphere decreases the annual-average anthropogenic fraction of CCN in the boundary layer compared to the case when it is only included in the boundary layer, from 46.3% in BLBHN to 43.9% in BHN. This decrease occurs mainly over tropical regions and over the SH (Figure 3.7c). Over these regions, the relative increase in the SO_2 concentration from the PI to the PD simulation is small due to strong natural contributions from the oxidation of DMS, which leads to a relatively smaller contribution from binary homogeneous nucleation to the CCN concentration in the PD than in the PI simulation. When these particles descend from the free troposphere into the boundary layer, they decrease the anthropogenic fraction of CCN. In contrast, over polluted continental regions and over much of the NH, binary homogeneous nucleation in the free troposphere increases the anthropogenic fraction of CCN in the boundary layer. Over these continental regions, the relative increase in the SO_2 concentration from the PI to the PD simulation is larger than the relative increase in primary-emitted particles, which leads to a relatively larger contribution from binary homogeneous nucleation to the CCN concentration in the PD over the PI simulation. This leads to an increase in the anthropogenic fraction of CCN concentrations over continental regions and throughout much of the NH. For the cases that include the empirical

boundary layer nucleation scheme, the effect of binary homogeneous nucleation in the FT is much smaller and the globally-averaged anthropogenic fraction of CCN in the boundary layer is almost the same: 46.8% in EMP vs. 46.4% in BHN_EMP (Figure 3.7d) In these scenarios, the CCN concentrations in the boundary layer are mainly determined by the empirical boundary layer nucleation scheme, together with the primary-emitted particles, and therefore the effect of binary homogeneous nucleation in the FT on the CCN concentration in the boundary layer is small.

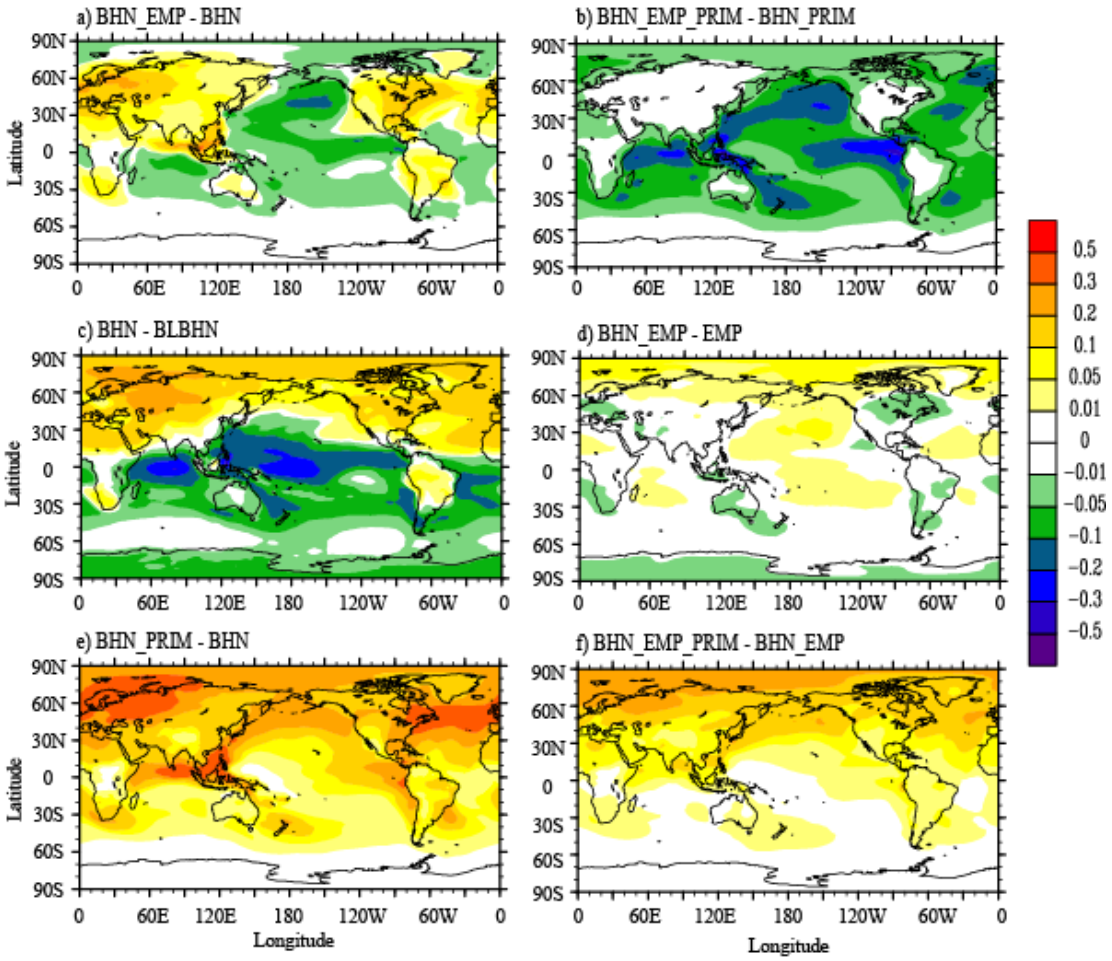

Figure 3.7: Difference in annual-average anthropogenic fraction of CCN concentrations between different cases.

Binary homogeneous nucleation in the FT has an important impact on the anthropogenic fraction of CCN in the free troposphere (Figure 3.6a vs. 3.6b and Figure

3.6d vs. 3.6e). It increases the anthropogenic fraction of CCN in the middle and upper troposphere over the NH. Over those regions, BHN is an important source of aerosol particles (Figure 3.2a vs. 3.2b and Figure 3.2d vs. 3.2e), and the relative increase in the SO_2 concentration from the PI to the PD simulation is larger than the relative increase in primary-emitted particles. For scenarios without boundary layer nucleation (Figure 3.6a vs. 3.6b), BHN in the FT decreases the anthropogenic fraction of CCN concentration over most of the SH. This is because the relative increase in the SO_2 concentration from the PI to the PD in the SH is somewhat smaller than the relative increase in primary particles.

This comparison suggests that the competition for sulfuric acid gas between primary particles and nucleation determines whether the inclusion of a nucleation mechanism (boundary layer nucleation or free troposphere nucleation) in the model increases or decreases the anthropogenic fraction of the CCN particles. When the relative increase in the precursor gas species (SO_2) is large and the relative increase in primary particles is not that large, the inclusion of nucleation tends to increase the anthropogenic fraction. In contrast, when the relative increase in the precursor gas species (SO_2) is small but the relative increase in primary particles is not that small, the inclusion of nucleation tends to decrease the anthropogenic fraction.

The effect of including primary-emitted sulfate particles on the anthropogenic fraction of CCN particles is large. For the cases that do not include the boundary layer nucleation scheme, the inclusion of primary-emitted sulfate particles increases the annual-average anthropogenic fraction of CCN from 44% in BHN to 62% in BHN_PRIM. Large increases in the anthropogenic fraction occur over Europe, South East Asia, and regions of continental outflow over the North Atlantic (Figure 3.7e). This large increase can be

explained by two factors: first, primary-emitted sulfate (at least at the sizes assumed here) forms CCN-size particles more efficiently than do particles that nucleate from gas phase H_2SO_4, and second, the percentage change in primary-emitted sulfate particles between the PD and PI simulations is larger than the percentage change in other primary particles (carbonaceous aerosols, dust, and sea salt) between the PD and PI simulations. The inclusion of the boundary layer nucleation scheme partly offsets this large increase in the anthropogenic fraction from primary-emitted sulfate, and leads to a smaller increase in the anthropogenic fraction of CCN due to primary sulfate than that in the case without boundary layer nucleation. The increase in the boundary layer is 10 percentage points (from 46% in BHN_EMP to 56% in BHN_EMP_PRIM) compared to an increase of 18 percentage points without boundary layer nucleation. The zonal annual-average anthropogenic fraction of CCN shows that the inclusion of primary-emitted sulfate particles also increases the anthropogenic fraction of CCN in the middle to upper troposphere in the NH (Figure 3.6c vs. Figure 3.6b or Figure 3.6f vs. Figure 3.6e). These results indicate that primary-emitted sulfate particles not only increase CCN concentrations in the PD significantly, but also increase the anthropogenic fraction of CCN concentrations significantly.

3.6 Cloud droplet number concentrations and the first aerosol indirect forcing

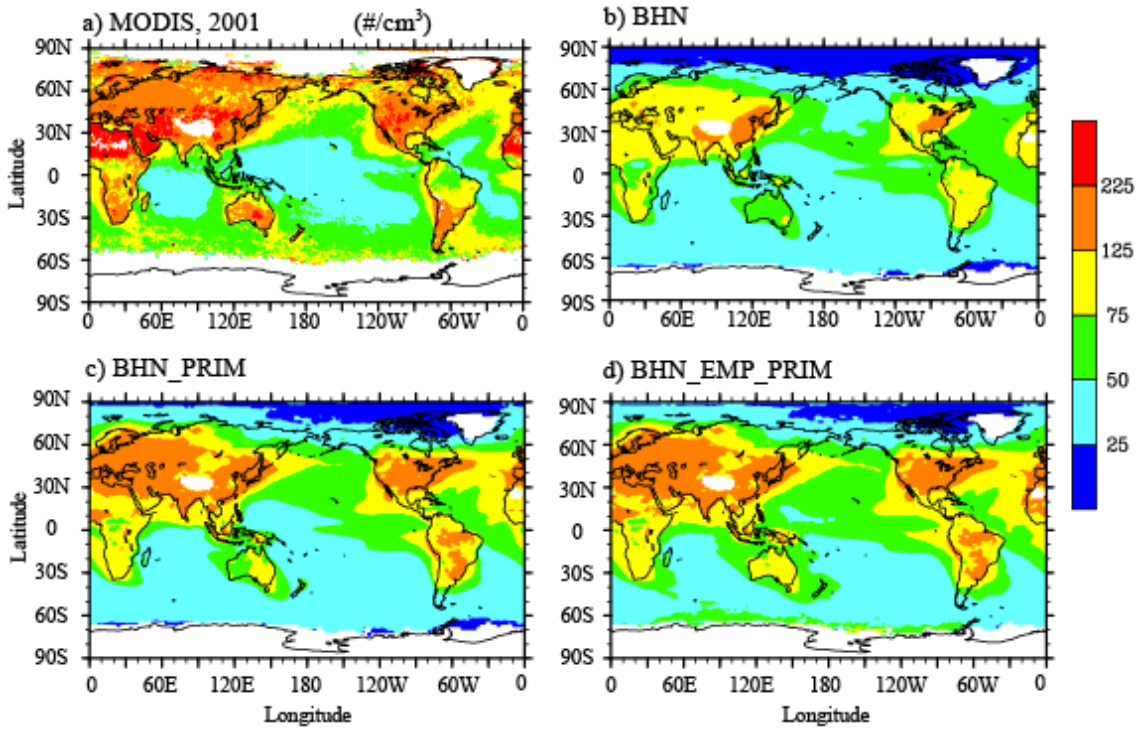

Figure 3.8: Annual-average cloud top droplet number concentrations (cm^{-3}) derived from (a) MODIS (Quaas et al., 2006), (b) BHN, (c) BHN_PRIM, and (d) BHN_EMP_PRIM.

The simulated cloud top droplet number concentration for lower level warm clouds is shown in Figure 3.8 along with satellite observations. The satellite data was derived from version 4 of the Moderate Resolution Imaging Spectroradiometer (MODIS) aboard the Terra satellite (Platnick et al., 2003) by Quaas et al. (2006). The MODIS cloud products include both cloud optical depth and cloud droplet effective radius, and Quaas et al. (2006) diagnosed droplet number from these variables assuming adiabatic clouds. The simulated cloud droplet number concentration at cloud top was diagnosed in the model using the ISCCP cloud simulator (Klein and Jacob, 1999; Webb et al., 2000) which emulates the way nadir-looking satellites measure clouds, and facilitates the comparison of the model data with satellite observations. For both the satellite and simulated data,

only warm (T>273K) and low level (pressure>640 hPa) clouds are sampled. The simulated data is sampled at each time step (every 30 minutes).

The magnitude and spatial distribution of cloud-top droplet number from the BHN_PRIM case agrees better with the MODIS data than that from the BHN case. The simulated cloud droplet number concentration is larger over land than over the ocean in BHN_PRIM, because of the larger anthropogenic emissions over land, with concentrations between 75 and 225/cm^3 over land and between 25 and 75/cm^3 over ocean. However, the model generally has a smaller cloud droplet number concentration, and simulates a smaller land/ocean contrast, than what is observed. In the SH between 40° and 60°, the simulated cloud droplet number concentration is less than 50/cm^3 while the measured cloud droplet number from MODIS is about 75/cm^3. The high cloud droplet number concentration observed over this region in MODIS is also consistent with the high number concentration of CCN derived by Vallina et al. (2007) from the MODIS aerosol optical depth.

The inclusion of the empirical boundary layer nucleation scheme (BHN_EMP_PRIM) improves the comparison with MODIS cloud drop number concentration compared to the BHN_PRIM case. However, this version also underestimates the observed cloud droplet number concentrations in the 40°-60°S latitude belt. Pierce and Adams (2006) showed that the inclusion of a source of ultrafine sea salt particles can increase the simulated cloud droplet number concentration resulting from the condensational growth of ultrafine particles into CCN-size particles. The absence of condensable organic species from biogenic emissions in the IMPACT model may also cause an underestimate of the growth of small particles into CCN-sized particles and contribute to the underestimation shown

in Figure 3.8. Recent studies (e.g., Vaattovaara et al., 2006) from observational data have shown that the formation of the secondary organic aerosols can contribute to the growth of recently formed particles.

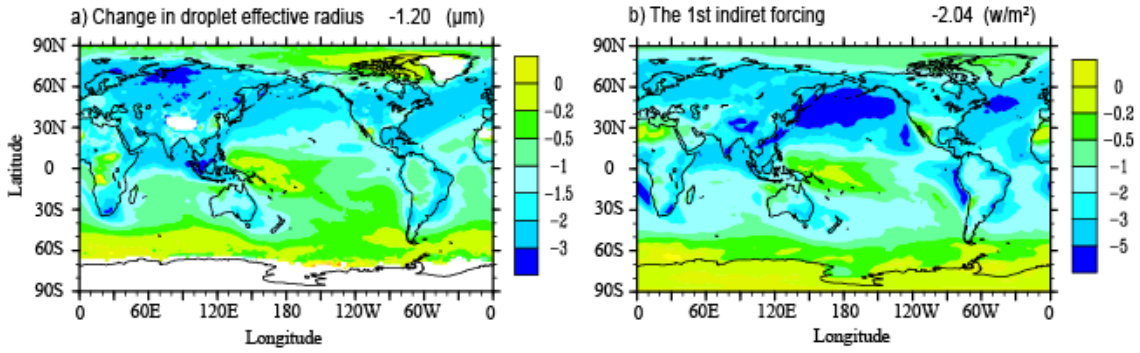

Figure 3.9. (a) The change in the annual-average cloud top effective radius from anthropogenic emissions and (b) annual-average 1st AIE in the BHN_PRIM case. The values given in the title are global averages.

Figure 3.9 shows the simulated change in cloud top effective radius from anthropogenic aerosols and the first aerosol indirect forcing for the BHN_PRIM case. Anthropogenic aerosols decrease the global average cloud top effective radius by 1.20 μm, with larger decreases over land and smaller decreases over ocean. The first aerosol indirect forcing is -2.03 W/m^2 in this case. The spatial distribution of the first indirect forcing is determined by the change in the cloud top effective radius and, to a lesser extent, by the cloud forcing. The maximum in the first aerosol indirect forcing occurs over the north Pacific, which is caused by the combination of the strong decrease in the cloud effective radius and strong cloud forcing over this region.

Figure 3.10 shows the change in the simulated first AIE from including the empirical boundary layer nucleation mechanism in five regions: NH land, NH oceans, SH land, SH oceans, and for the global average. These changes are consistent with the spatial pattern of the change in the simulated anthropogenic fraction of CCN shown in Figure 3.7a and

3.7b. The first aerosol indirect forcing is only -1.65 W/m^2 in the BHN_EMP_PRIM case, a decrease of 0.38 W/m^2 in absolute magnitude from the BHN_PRIM case, as shown in Figure 3.10 and in Table 3.4. This decrease occurs over most regions with the largest decrease over oceanic regions in the NH, which comes from the decrease in the simulated anthropogenic fraction of CCN (Figure 3.7b). In the cases without any primary-emitted sulfate particles, the inclusion of the empirical boundary layer nucleation scheme changes the global average forcing only slightly: from -1.55 W/m^2 in BHN to -1.49 W/m^2 in BHN_EMP, which is due to increases in the (negative) forcing over land and decreases over the ocean (Figure 3.10). The inclusion of the empirical boundary layer nucleation scheme changes the spatial pattern of the first indirect forcing and shifts more of the contribution of the first AIE to land (i.e., the changes are more positive over the oceans in Figure 3.10). This suggests the importance of including a boundary layer nucleation mechanism in the estimation of the global aerosol indirect forcing.

Figure 3.11 shows the change in the zonal mean annual-average first AIE and the change in the zonal annual-average anthropogenic fraction of CCN after inclusion of primary-emitted sulfate particles. The primary-emitted sulfate particles have a large impact on the first aerosol indirect forcing, which is consistent with their impact on the anthropogenic fraction of CCN as shown in Figure 3.7e and 3.7f. For the cases without the empirical boundary layer nucleation scheme, the inclusion of primary-emitted sulfate particles changes the forcing from –1.55 W/m^2 in BHN to –2.03 W/m^2 in BHN_PRIM (Table 3.4). For the scenario with the empirical boundary layer nucleation scheme, the effect of including primary-emitted sulfate particles on the first indirect forcing is smaller, only increasing the magnitude of the forcing from -1.49 W/m^2 in the BHN_EMP case to -

1.65 W/m^2 in the BHN_EMP_PRIM case (Table 3.4). The largest increases take place in the middle latitudes of the NH where anthropogenic sulfur has the largest contribution to the total sulfur (Figure 3.11). This suggests that the treatment of sub-grid scale nucleation processes by including primary-emitted sulfate particles in the model introduces a large uncertainty in the estimation of the aerosol indirect forcing.

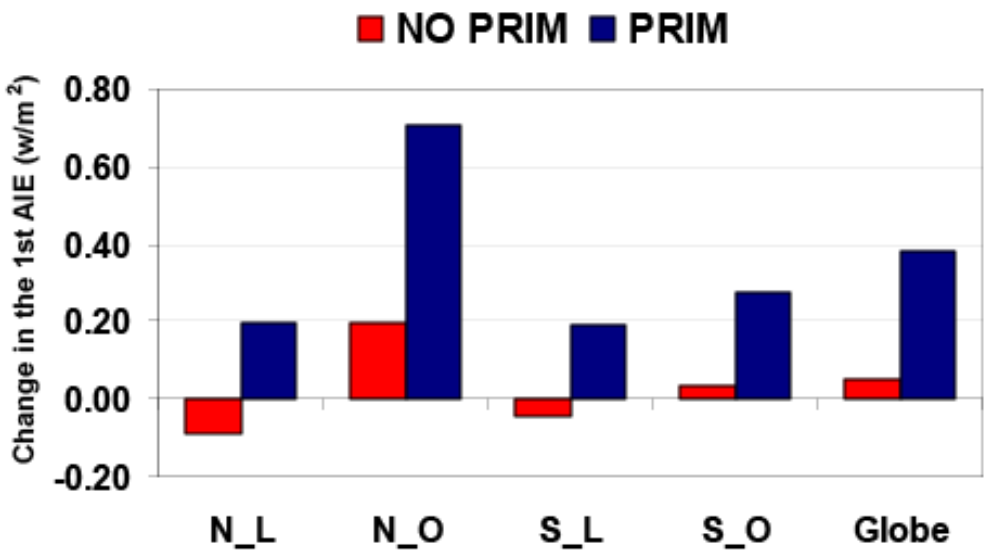

Figure 3.10: Change in the simulated annual-average 1st AIE from including the empirical boundary layer nucleation mechanism in five regions: N_L: over Northern Hemisphere land; N_O: over Northern Hemisphere oceans; S_L: over Southern Hemisphere land; S_O: over Southern Hemisphere oceans; Global: global average (red bar: the difference between BHN_EMP and BHN; blue bar: the difference between BHN_EMP_PRIM and BHN_PRIM).

Binary homogeneous nucleation in the FT increases the forcing from -1.22 W/m^2 in the EMP case to -1.49 W/m^2 in the BHN_EMP case (Table 3.4). Although the change in the anthropogenic fraction of CCN in the boundary layer is small between these two cases, the vertical profiles of the anthropogenic fraction of CCN show an increase when binary homogeneous nucleation in the FT is included (Figure 3.6d and 3.6e), which may explain the increase in the first indirect forcing. However, when there is no boundary

layer nucleation, the inclusion of binary homogeneous nucleation in the FT nearly doubles the forcing from -0.81 W/m^2 in BLBHN to -1.55 W/m^2 in BHN (Table 3.4). This large increase is caused by the unrealistically low droplet number concentrations simulated in the BLBHN case. In our calculations, we set a lower limit on the cloud droplet number concentration of 20 cm^{-3}. Due to the low cloud droplet number concentration simulated in BLBHN, most regions have a constant cloud droplet number concentration of 20 cm^{-3} in both the present day and preindustrial simulations, which decreases the first indirect forcing significantly.

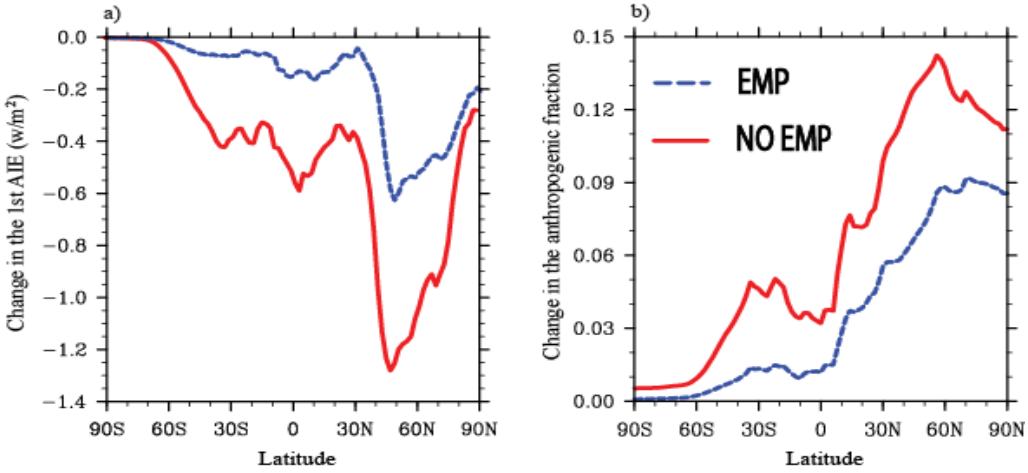

Figure 3.11. (a) Change in the zonal mean annual-average 1st AIE and (b) the change in the zonal annual-average anthropogenic fraction of CCN (right panel) from including primary-emitted sulfate particles (red line: the difference between BHN_PRIM and BHN; blue line: the difference between BHN_EMP_PRIM and BHN_EMP).

The first aerosol indirect forcing calculated in this study is higher than that of most other studies (Foster et al. 2007). Here we explore how our estimation of the first aerosol indirect forcing depends on the assumption of the cloud types included in the indirect aerosol effect and the lower limit of the cloud droplet number concentrations. We compare different choices for these factors to the forcing calculated in the BHN_PRIM

case averaged over four months (Jan, April, July, and October) in order to save computer time.

As shown in Table 2.7 in Forster et al. (2007), different models have included different cloud types in their estimation of the first AIE. Some models only include warm clouds (e.g., Ming et al., 2005; Takemura et al., 2005), but other studies include both warm and mixed-phase clouds (e.g., Penner et al., 2006; Chen and Penner, 2005). Some models include only stratiform clouds (e.g., Suzuki et al., 2004), but other studies include both stratiform and convective clouds (e.g., Jones et al., 2001). In Figure 3.12, in the simulation labeled WARM, we limited the first AIE to warm clouds only, which are clouds with temperatures warmer than 273.15 K. In the STRAT case, we limited the first AIE to stratiform clouds only. All other specifications in the WARM and STRAT cases are the same as those in the BHN_PRIM case. There are 24% and 40% decreases in the first AIE in STRAT and WARM, respectively, compared to BHN_PRIM (Figure 3.12). Thus, the estimation of the first AIE is very sensitive to the cloud types included in the simulation. The large contribution from mixed-phase clouds to the estimation of the first AIE (40%) depends, of course, on the fraction of these clouds that are assumed to remain in the liquid phase. Since this fraction is simply specified in this model, the model sensitivity to this factor could be quite different with other formulations.

In the N40 and N10 simulations, we set the minimum cloud droplet number concentration to 40 and 10/cm^3, respectively. In the N40 case, the first AIE is decreased by 40% compared with the BHN_PRIM case, and in the N10 case, the first AIE is increased by 13% compared with the BHN_PRIM case (Figure 3.12). A minimum number concentration of 40/cm^3 has been used in some model studies (e.g., Lohmann et

al., 2007). Although it may be reasonable to set a minimum cloud droplet number concentration to determine background droplet number concentrations if the predicted aerosol number concentrations are too low, our sensitivity tests show that the exact value of the minimum droplet number concentration makes a large difference in the estimated AIE. Moreover, the effect of the minimum droplet number depends on the simulated cloud droplet number.

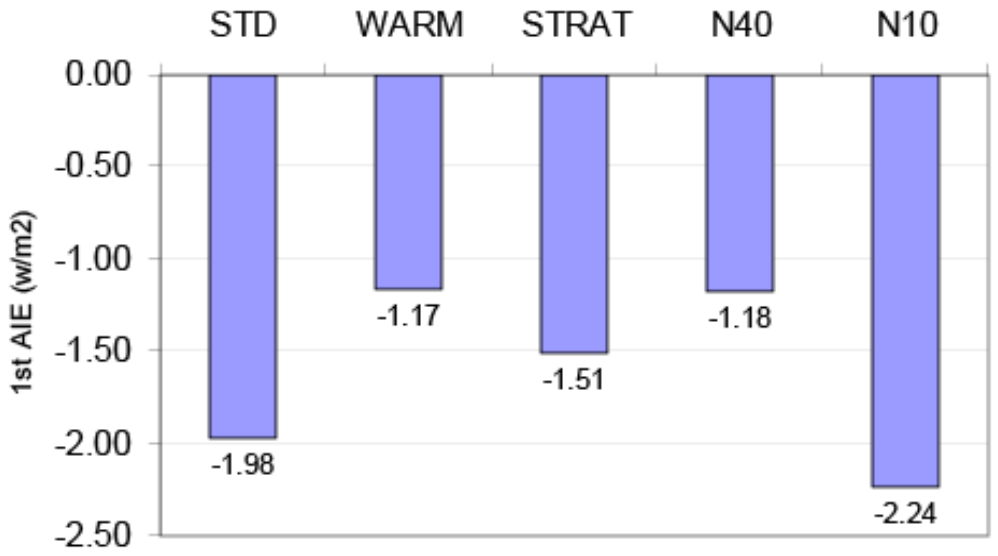

Figure 3.12: The 1st AIE from five different model configurations (W/m^2): BHN_PRIM, using the average from four months (January, April, July, and October); WARM: the same as BHN_PRIM, but with only warm clouds (>273.15K) included; STRAT: the same as BHN_PRIM, but with only stratiform clouds included; N40: the same as BHN_PRIM, but with the minimum cloud droplet number set to 40/cm^3; N10: the same as BHN_PRIM, but with the minimum cloud droplet number set to 10/cm^3.

3.6 Summary and discussion

The effects of different nucleation parameterizations have not been included in global model studies of the aerosol indirect effect. Here, we used a global aerosol model that includes an empirical boundary layer nucleation scheme, as well as binary homogeneous

nucleation, to explore how nucleation affects the concentration of CCN and aerosol indirect forcing. We also investigated how the inclusion of primary-emitted sulfate particles affects CCN concentrations and aerosol indirect forcing.

The inclusion of the empirical boundary layer nucleation scheme improved the comparison of cloud top droplet number concentrations from the model with satellite data over the Southern Oceans, but the model still underestimates cloud top droplet number concentrations in the region from 30°S to 60°S. This underestimation may come from the absence of ultrafine sea salt particles or from the absence of condensable organic species from marine biogenic emissions.

Our study showed that the effect of the empirical boundary layer nucleation scheme on CCN concentration depends in an important way on the assumed and simulated primary particles. Including empirical boundary layer nucleation increases global average CCN concentrations in the boundary layer by 31.4% when the primary sulfate particles are excluded, and by 5.3% when primary-emitted sulfate particles are included. In the MBL over the tropics and in the SH, the empirical boundary layer nucleation scheme increases CCN concentrations in the PD simulation by 30-100% and this increase has little dependence on whether primary-emitted sulfate particles are or are not included, since primary sulfate particles make only a small contribution to the primary particles over these regions. However, uncertainties in the emissions of natural primary particles (sea salt and dust) over these remote regions prevent us from making any further conclusions. For example, if the underestimation of the cloud droplet number concentration in the Southern Ocean results from an underestimation of natural primary particles (e.g.,

ultrafine sea salt particles), the effects of boundary layer nucleation may be overestimated over that region.

This study also shows that the inclusion of the empirical boundary layer nucleation scheme in the model decreases the effects of BHN in the FT on CCN concentrations in the MBL, as well as the effects of primary sulfate particles. When no boundary layer nucleation is included, the inclusion of BHN in the FT in the model increases CCN concentrations in the MBL by more than 150%, which is consistent with other model studies. However, when the empirical boundary layer nucleation scheme is included in the model, BHN in the FT has a much smaller effect on CCN concentrations. This suggests that, as long as boundary layer nucleation events occur as frequently as Equation 2.1 suggests, BHN in the FT is not a critical factor in determining the CCN concentration in the MBL. The inclusion of primary-emitted sulfate particles always increases CCN concentrations in the boundary layer, although the inclusion of the empirical boundary layer nucleation scheme decreases the percentage increases in CCN associated with primary-emitted sulfate from 53% to 23%.

Our study suggests that the effect of including a nucleation mechanism (either boundary layer nucleation or free troposphere nucleation) in the model on the anthropogenic fraction of the CCN particles and on the first aerosol indirect forcing largely depends on the competition for sulfuric acid gas between primary particles and nucleation. When the relative increase in the precursor gas species (SO_2) between the PD and PI simulations is large and the relative increase in primary particles is not that large, the inclusion of nucleation tends to increase the anthropogenic fraction and to increase the aerosol indirect forcing. This is the case for the effect of boundary layer nucleation

over the NH land when no primary sulfate is included (Figure 3.7a, and Figure 3.10) and for the effect of BHN over the NH land (Figure 3.7c). In contrast, when the relative increase in the precursor gas species (SO_2) between the PD and PI simulations is small but the relative increase in primary particles is not that small, the inclusion of nucleation tends to decrease the anthropogenic fraction and to decrease the aerosol indirect forcing. This is the case for the effect of the boundary layer nucleation over ocean regions (Figure 3.7a, 3.7b, and Figure 3.10), and for the effect of BHN over the SH (Figure 3.7c). This contrast explains why the empirical boundary layer nucleation scheme changes the spatial pattern of the first indirect forcing and shifts more of the contribution of the first AIE to land (Figure 3.10). The magnitude of the relative increase in SO_2 and primary particles between the PD and PI simulations causes a large decrease in the first indirect forcing over ocean and small decreases or even increases in the first indirect forcing over land in the simulations with boundary layer nucleation, compared to those without boundary layer nucleation.

In this study, the nucleation rate from boundary layer nucleation only depends on the sulfuric acid gas concentrations, and the meteorological fields are the same for both the PI and PD simulations. So, the primary particles and precursor gas species are the two most critical factors in determining the effects of nucleation on the anthropogenic fraction of CCN particles and on the aerosol indirect forcing. However, if boundary layer nucleation also depends on some other factors and if the meteorological fields are changed as a result of global warming, the effects of including a boundary layer nucleation mechanism on aerosol indirect forcing can differ from that calculated here. For example, the ion-mediated nucleation mechanism suggested by Yu (2006) leads to

less nucleation at higher temperatures (Yu et al., 2008b). This suggests that including a boundary layer nucleation scheme would have lead to a smaller increase and a larger decrease in the anthropogenic fraction of CCN than that in this study, if this ion-mediated nucleation mechanism were used and the increase in temperature from the PI to the PD were included.

In this study, a 2-mode representation (nucleation/Aitken mode and accumulation mode) of the sulfate aerosol size distribution is used to simulate the effects of nucleation events from both boundary layer nucleation and BHN. As shown in Chapter II, a 3-mode representation with an additional mode representing nucleation sizes (radius < 5 nm) produces fewer Aitken mode particles and more accumulation mode particles in the upper troposphere because of the large amount of freshly nucleated particles from BHN. However, the 3-mode representation has a smaller effect on the accumulation mode particles in the boundary layer even when boundary layer nucleation is included. This is partly due to the fact that the aerosol particles generated from boundary layer nucleation are grown by condensation up to a size of 3 nm and have lower number concentrations in the nucleation mode compared with those from BHN. In addition, primary particles are important sources for accumulation mode particles in the boundary layer, whereas the growth of particles from the nucleation mode is important in the free troposphere. As a result, the effects of different size distribution treatments (3-mode vs. 2-mode) is small. Since accumulation mode particles in the boundary layer are the focus of this study, we would expect the 3-mode representation to have small effects on the results reported here.

Our study also shows that the inclusion of primary-emitted sulfate increases the anthropogenic fraction of CCN concentrations and the first aerosol indirect forcing

significantly, because primary-emitted sulfate forms CCN-size particles more efficiently than do particles that nucleate from the gas phase. The percentage change in primary-emitted sulfate particles between PD and PI simulations is larger than the percentage change in other primary particles. This suggests that the treatment of sub-grid scale nucleation processes by including primary-emitted sulfate particles in the model introduces a large uncertainty in the estimation of the aerosol indirect forcing. When boundary layer nucleation is included, the effect of primary-emitted sulfate particles is smaller.

In summary, this study shows the impacts from including different nucleation mechanisms and from including primary sulfate particles on the CCN concentrations and on the aerosol indirect forcing. Better parameterizations for the treatment of sub-grid scale nucleation processes, as well as the mechanisms of aerosol nucleation, are urgently needed.

CHAPTER IV

CIRRUS CLOUDS IN A GLOBAL CLIMATE MODEL WITH A STATISTICAL CIRRUS CLOUD SCHEME

4.1. Introduction

Cirrus clouds cover about 30% of the Earth's area (Wang et al., 1996; Rossow and Schiffer, 1999; Wylie and Menzel, 1999) and are therefore important in maintaining the global radiation balance (Ramanathan and Collins, 1991). They can form through either homogeneous freezing or heterogeneous freezing. Homogeneous freezing occurs through the freezing of liquid solutions such as sulfate droplets (Koop et al., 2000), and this usually occurs at low temperature and high relative humidity over ice (*RHi*). In contrast, heterogeneous freezing is mediated by insoluble solids (Pruppacher and Klett, 1997) or surfactant layers (Zobrist et al., 2007) that lower the energy barrier for the formation of an ice germ, and therefore requires lower supersaturation and can occur at higher temperatures. Aerosol particles that contribute such surfaces and undergo heterogeneous freezing are termed ice nuclei (IN). Mineral dust, carbonaceous, and metallic particles appear to be common heterogeneous IN (Chen et al., 1998; DeMott et al., 2003; Cziczo et al., 2004).

Homogeneous freezing is believed to be the primary mechanism for cirrus cloud formation in pristine environments (e.g., Heymsfield and Sabin, 1989; Cantrell and Heymsfield, 2005), but the presence of heterogeneous IN can hinder or even prevent the occurrence of homogeneous freezing because of the consumption of water vapor by ice crystals formed from heterogeneous freezing due to the lower required *RHi* (e.g., Demott et al., 1997; Liu and Penner, 2005). This preventive effect may significantly change cirrus cloud properties and humidity in the upper troposphere. Heterogeneous freezing from a few heterogeneous IN may result in lower ice crystal number concentration and larger ice crystal particles than those from homogeneous freezing, since homogeneous freezing usually generates high concentrations of ice crystals because of the abundance of liquid haze particles. Jensen et al. (2008) suggested that it is likely that the observed presence of rather large ice crystals near the tropical tropopause in very low concentration results from ice nucleation on effective heterogeneous IN. Heterogeneous freezing from a few heterogeneous IN may also change the frequency of occurrence of cirrus clouds because of the lower required *RHi* (Jensen and Toon, 1997). Using Lagrangian microphysical aerosol-cloud model simulations, Haag and Kärcher (2004) showed that the frequency of occurrence of thin cirrus can be significantly increased as a result of the presence of a small number of IN (0.001 /cm^3) at midlatitudes, but can also be decreased when the number concentration of IN exceed 0.02/cm^3. Heterogeneous freezing from a few heterogeneous IN may change ice water content by changing ice crystal settling velocity (e.g., Haag and Kärcher et al., 2004). Heterogeneous freezing from a few heterogeneous IN may also change humidity fields in the upper troposphere. Haag et al. (2003) suggested that the difference in the probability distribution of relative

humidity between the Southern Hemisphere (SH) and the Northern Hemisphere (NH) observed during the Interhemispheric Differences in Cirrus Properties from Anthropogenic Emissions (INCA) field experiments may be explained by heterogeneous freezing that comes from increased aerosol particles in the NH.

Although the heterogeneous IN are important in determining freezing mechanisms and cirrus cloud properties, the freezing capabilities of different aerosol particles acting as IN, and in particular the freezing capabilities of anthropogenic aerosol particles, are still not well understood (Kärcher et al., 2007; DeMott, 2007). Laboratory studies of cirrus ice formation that relate ice nucleation to aerosol properties show that heterogeneous ice nucleation on mineral dust (e.g., Zuberi et al., 2002; Hung et al., 2003; Archuleta et al., 2005; Field et al., 2006; Möhler et al., 2006; Salam et al., 2006), and on soot (or black carbon, BC) particles (DeMott, 1990; DeMott et al., 1999; Gorbunov et al., 2001; Möhler et al., 2005) requires lower *RHi* than homogeneous freezing on sulfate, while coating soot with sulfate can increase the nucleation thresholds from an ice saturation ratio of about 1.3 at 230 K to 1.5 at 185 K (Möhler *et al.*, 2005). DeMott (2007) reported laboratory experiments with aircraft soot and aerosols produced from biomass burning, which showed that aircraft and biomass soot particles required RH_i of close to 155% near -55°C. Thus, these soot particles did not nucleate ice any more easily than does sulfate aerosol when it freezes homogeneously.

The role of anthropogenic aerosols on cirrus cloud properties is also complicated by the fact that dynamical processes play an important role in ice nucleation in the upper troposphere (e.g., Heymsfield, 1977; Ström et al, 1997; Kärcher and Ström, 2003; Haag and Kärcher, 2004; Jensen and Pfister, 2004; Hoyle et al., 2005). Dynamical processes

control temperature and cooling rates, which are two critical factors in the ice nucleation process, and thereby affect cirrus cloud properties. Heymsfield (1977) found that ice crystal concentration and ice water content in cirrus clouds are strong functions of the vertical velocity based on airborne measurements in the United States. Ström et al. (1997) demonstrated the potential impact of atmospheric waves on the physical properties of young cirrus clouds from airborne measurements over Southern Germany. Immler et al. (2008) found a clear correlation between temperature anomalies induced by equatorial Kelvin waves and the occurrence of thin cirrus at the tropical tropopause. The strong role of dynamical processes on ice nucleation and cirrus cloud microphysical properties make it difficult to separate the effects of aerosol changes and dynamical changes on cirrus microphysical properties (Kärcher and Ström, 2003). It is suggested that cirrus formation is at least as sensitive to changes in dynamical forcing patterns as to changes in the aerosol size and number (Kärcher and Ström, 2003).

In recent years, global models have been used to study the effect of aerosols on cirrus cloud properties. In a general circulation model (GCM) study, Lohmann and Kärcher (2002) showed that the effect of aerosols on cirrus clouds is small if only homogeneous freezing is included, but this conclusion can depend on the ice deposition coefficient and vertical velocity used in their model (Kay and Wood, 2008). As shown by Kay and Wood (2008) in a timescale analysis, ice crystal concentration from homogeneous freezing can be quite sensitive to aerosol concentration when the ice deposition coefficient is much less than 0.1, but not when a deposition coefficient of 0.5 is used as in Lohmann and Kärcher (2002). Differences in ice deposition coefficients and vertical velocities may also partly explain why Liu et al. (2009) obtained a larger positive forcing (0.5 W/m^2) when

only homogenous freezing simulations were included in their global model study. Liu et al. (2009) used a smaller deposition coefficient (0.1 vs. 0.5) and a larger vertical velocity (25 cm/s vs. 7.8 cm/s) than did Lohmann and Kärcher (2002). A large positive forcing (~0.15 W/m^2) from anthropogenic sulfate is also simulated in Penner et al. (2009) in an off-line calculation with aerosols fields archived from the same model system as that used in Liu et al. (2009), but a smaller forcing is obtained when both aerosol number and mass (which leads to improvements in the prediction of aerosols) instead of just aerosol mass is simulated in their global aerosol model.

Potential cirrus modifications caused by aircraft-produced soot particles via heterogeneous ice nucleation were studied in a global model by Hendricks et al. (2005). Provided that soot particles from aviation serve as efficient heterogeneous IN, Hendricks et al. (2005) showed that aircraft soot decreases ice crystal number concentration by 10-40% at northern midlatitudes in an environment dominated by homogeneous freezing, but the opposite is true in an environment dominated by heterogeneous freezing. In the study by Liu et al. (2009), where both homogeneous and heterogeneous freezing are allowed and both aircraft soot and soot originating from surface sources act as efficient IN, a 30% increase in ice crystal number concentration in the NH extratropics (north of 50°N) was simulated when aircraft soot was added, which may indicate an environment dominated by heterogeneous freezing in their model. The opposite is simulated in Penner et al. (2009) when both aerosol mass and number are predicted. Instead a significant decrease in ice crystal number concentration occurs at the highest altitudes (above ~200 hPa) when aircraft soot is added, which indicates a background environment dominated by homogeneous freezing in Penner et al. (2009). As discussed in Penner et al. (2009) and

Liu et al. (2009), differences in simulated *RHi* may partly explain these results, since *RHi* is critical in determining the freezing mode and was treated as a sub-grid scale feature in Penner et al. (2009) but not in Liu et al. (2009).

The effects of anthropogenic soot originating from surface sources (fossil fuel and biomass burning) on cirrus clouds were also studied in Penner et al. (2009) and Liu et al. (2009). In Liu et al. (2009), surface soot has a similar effect on cirrus clouds as aircraft soot, acting to increase ice crystal number concentration, and with a large magnitude. In Penner et al. (2009), when both aerosol mass and number are predicted, surface soot also has a similar effect on cirrus clouds as does the aircraft soot does at high altitudes, acting to decrease ice crystal number concentration. However, surface soot increases ice crystal number concentration at lower altitudes in the NH, where heterogeneous freezing dominates, because of the higher temperatures.

In the GCM studies discussed above (Lohmann and Kärcher, 2002; Hendricks et al., 2005; Liu et al., 2009), the individual GCMs were updated to allow supersaturation with respect to ice, which removes the need for saturation adjustments (i.e., the immediate conversion of supersaturation into condensate mass) that is still used in most global climate models as a simplification. Grid-mean supersaturation with respect to ice is predicted in these models, and is used to determine when freezing occurs, but the cloud fraction is still diagnosed based on grid-mean relative humidity and assumes equal humidity inside and outside of cirrus clouds. This leads to a cloud fraction that is either 0 (if ice crystals have not formed in the previous time step) or 1 (if ice crystals formed in the previous time step) when the grid mean *RHi* is larger than 100%. Partial cloud cover is only diagnosed when subsaturation subsequently occurs. Also, assumptions have to be

made regarding when vapor deposition occurs. More importantly, the representation of subgrid-scale fluctuations of temperature, humidity, and cooling rate that are believed to control cirrus cloud formation and the related microphysical properties, are highly simplified in these studies. The simulated effects of the subgrid-scale fluctuations are only represented in the calculation of ice crystal number concentration by the use of a single vertical velocity that is diagnosed from kinetic turbulence energy (Lohmann and Kärcher, 2002) or a probability distribution of vertical velocities that has a normal distribution with a prescribed constant variance (Liu et al., 2009; see discussion in section 4.2.2). The simplifications in these models limit their capability to study aerosol indirect effects on cirrus clouds.

To address the inconsistency between the diagnosis of cloud fraction and the prediction of ice supersaturation in cirrus cloud schemes that allow supersaturation, Tompkins et al. (2007) used a prognostic cloud fraction that is consistent with their predicted ice supersaturation in the European Centre for Medium-Range Weather Forecasts (ECMWF) Integrated Forecast System. This scheme uses clear sky relative humidity to determine when ice freezing occurs and how much cloud fraction increases. However, this scheme has highly simplified ice microphysics (no ice crystal number is predicted). Moreover, this study assumed vapor saturation in cloudy air. In observations, both ice supersaturation and subsaturation conditions can occur in cloudy air (Ström et al., 2003). For example, significant supersaturation can occur when ice crystal number concentration is low (Krämer et al., 2008), and subsaturation can occur when ice crystal particles are large (Hall and Pruppacher, 1976).

Kärcher and Burkhardt (2008, hereafter KB08) presented a statistical cloud scheme for non-convective cirrus formed by homogeneous freezing of supercooled aerosols, which treats cloud growth and decay based on a subgrid-scale distribution of temperature and total water. The scheme is based on separate probability distribution functions for total water for representing the clear-sky and in-cloud conditions. These distributions are based on *in situ* observations. Both sub- and supersaturation conditions with respect to ice are allowed to occur in cloud-free air and inside cirrus. This scheme was tested in a box model in KB08, which produced nucleated ice crystal number concentrations and sizes in good agreement with observations.

In this chapter, the cirrus cloud scheme in KB08 is implemented in the updated version of NCAR CAM3 (Liu et al., 2007, hereafter LIU07) which has been coupled with the LLNL/UMich IMPACT aerosol model (see Chapter II for the details of the coupling method), in order to replace the cirrus cloud treatment in LIU07. The same coupled model with the cirrus cloud treatment of LIU07 has been used to study aerosol indirect effects on cirrus clouds in Liu et al. (2009), as discussed above.

In implementing the cirrus cloud scheme of KB08 into our model, both homogeneous freezing and heterogeneous freezing are included. Anvil clouds from convective detrainment are also included and compete for clear sky water vapor with large scale cirrus clouds. The coupled model and the implementation of KB08 are presented in section 4.2, and model results in the case of homogeneous freezing only are shown in section 4.3. The effects of heterogeneous IN and subgrid scale temperature perturbations are examined in section 4.4. Finally, section 4.5 contains a discussion and conclusions.

4.2. Model description and set-up of simulations

In this chapter, the coupled IMPACT/CAM3 model described in Chapter II is used, but CAM3 has been updated with a new cloud treatment. The aerosol microphysics version of the IMPACT has been replaced with the mass-only version.

4.2.1. The IMPACT Global Aerosol Model

In this study, the mass-only version of the Lawrence Livermore National Laboratory (LLNL)/University of Michigan IMPACT model is used, which predicts aerosol mass, but not number (Liu and Penner, 2002). We choose this mass-only version of the IMPACT model instead of the more full aerosol microphysics version used in Chapters II and III because the mass-only version of the model is computationally fast and allows us to run more sensitivity studies with the available computational resources.

The mass-only version of IMPACT includes prognostic variables for sulfur and related species: dimethylsulfide (DMS), sulfur dioxide (SO_2), sulfate aerosol (SO_4^{2-}), and hydrogen peroxide (H_2O_2); aerosols from biomass burning BC and organic matter (OM), fossil fuel BC and OM, natural OM, aircraft BC (soot), mineral dust, and sea salt are also included. Sulfate aerosol is divided into three size bins with radii varying from 0.01-0.05 μm, 0.05-0.63 μm and 0.63-1.26 μm, while mineral dust and sea salt are predicted in four bins with radii varying from 0.05-0.63 μm, 0.63-1.26 μm, 1.26-2.5 μm, and 2.5-10 μm. Carbonaceous aerosol (OM and BC) is currently represented by a single submicron size bin. Emissions of primary particles and precursor gases, gas-phase oxidation of precursor gases, aqueous-phase chemistry, rain-out and washout, gravitational settling, and dry deposition are treated. The mass-only version of the IMPACT aerosol model driven by

meteorological fields from the NASA Data Assimilation Office (DAO) participated in the AEROCOM (http://nansen.ipsl.jussieu.fr/AEROCOM/) phase A and B evaluations (Kinne et al., 2006; Textor et al., 2006; Schulz et al., 2007), where it has been extensively compared with *in situ* and remotely sensed data for different aerosol properties.

Emissions of aerosol species and their precursors are described in detail in Chapter II. Prescribed size distributions from observations are used to calculate the number concentrations of sulfate, dust and soot particles that are used in the ice freezing parameterization in section 4.2.2. Sulfate particles are assumed to have a lognormal size distribution with a mode radius of 0.02 μm and a geometric standard deviation of 2.3 (Jensen et al., 1994). For soot particles emitted from the Earth's surface (i.e., biomass burning and fossil fuel combustion), we assumed a size distribution with a mode radius of 0.07 μm and a geometric standard deviation of 1.5 (Pueschel et al., 1992). Aircraft soot has a much smaller size with a mode radius of 0.023 μm and a geometric standard deviation of 1.5 (Petzold and Schrμder, 1998). The size distribution of dust particles (Table 4.B1) is taken from De Reus et al. (2000).

4.2.2. NCAR CAM3

The NCAR Community Atmospheric Model (CAM3) is a part of the Community Climate System Model 3 (CCSM3; Collins et al., 2006a, b). It predicts both cloud liquid water and cloud ice water (Boville et al., 2006). Cloud condensate detrained from deep and shallow convection is added into stratiform clouds. The gravitational settling as well as large-scale transport of cloud condensates is treated for cloud liquid and ice (Boville et al., 2006). However, in the standard CAM3 as used in Chapters II and III, the partitioning between cloud liquid and cloud ice depends only on temperature (T), and both the cloud

droplet number and ice crystal number used in the cloud microphysics scheme are prescribed. Therefore, CAM3 is not able to represent a variety of processes (e.g., the Bergeron-Findeisen process, ice nucleation, droplet nucleation) that are important to the study of aerosol-cloud interactions.

The standard CAM3 version has been updated in Liu et al. (2007) (hereafter, LIU07), by introducing a two-moment cloud microphysics scheme for ice cloud, in which cloud ice number concentrations are predicted by a prognostic equation. The two-moment scheme treats ice nucleation, coagulation, evaporation, and melting. LIU07 also has a more physically-based representation of the liquid/ice partitioning in mixed-phase clouds than that used in the standard version of CAM3. This is accomplished by explicitly treating the liquid mass conversion to ice due to the depositonal growth of cloud ice at the expense of liquid water (the Bergeron-Findeisen process) using the scheme of Rotstayn et al. (2000). This replaces the simple temperature-dependent liquid/ice partitioning in the standard CAM3. The cloud condensation and evaporation (C-E) scheme of Zhang et al. (2003) in the standard CAM3 is used only for liquid water in warm ($T > 0$ºC) and mixed-phase (-35ºC $< T < 0$ºC) clouds, which removes any supersaturation above that of liquid water. Vapor deposition and sublimation of cloud ice is treated based on Rotstayn et al. (2000). With these modifications, supersaturation over ice was allowed in the upper troposphere. The coupled model with the ice cloud treatment in LIU07 has been used to study the effects of aerosols on cirrus clouds (Liu et al., 2009).

In LIU07, although supersaturation with respect to ice is allowed in the model to predict ice freezing, cirrus cloud fraction is still diagnosed based on the relative humidity, as described in Rasch and Kristjánsson (1998). This may lead to an inconsistency

between cirrus cloud fraction and ice freezing. For example, ice freezing may occur with a *RHi* of about 125% (heterogeneous freezing) or 150% (homogeneous freezing), but the cloud fraction begins to increase at a *RHi* of 90%. This caused a very large amount of high clouds to be formed in LIU07 (56.8%, compared with 32.2% in the standard CAM3). Moreover, the grid-mean saturation ratio was used to determine whether homogeneous freezing or heterogeneous freezing occurs in LIU07, although in the atmosphere ice freezing is controlled by mesoscale motions such as gravity waves (Hoyle et al., 2005; Kärcher and Ström, 2003; Haag and Kärcher, 2004; Jensen and Pfister, 2004). Here, in order to treat cirrus cloud formation in a consistent manner in the upper troposphere, the statistical cirrus cloud scheme presented in KB08 was implemented in CAM3 replacing the cirrus cloud treatment of LIU07. This new scheme has subgrid-scale features for clear sky temperature and in-cloud total water, which is more realistic since it captures more of the sub-grid scale physics.. Below we describe how the new cirrus cloud scheme is incorporated into CAM3. Some important formulas other than those listed in this section are listed in Appendix 4.A, and readers are referred to KB08 for more details.

In the new cirrus cloud scheme, the specific humidity in both the clear sky areas (q_{ve}) and cloudy areas (q_{vc}) within a grid is predicted in the model. The specific humidity in clear sky areas is used to determine whether freezing occurs and how much cloud fraction will increase as a result of any freezing, while the specific humidity in the cloudy part of the grid box is used to determine whether vapor deposition or evaporation occurs. The specific humidity in the cloudy part of the grid is used to determine how much cloud fraction decreases in the case of evaporation. The grid mean specific humidity (q_v) is calculated as $aq_{vc}+(1-a)q_{ve}$, where a is the cloud fraction.

Cloud growth is determined by the mean specific humidity in the clear part of a grid box using an assumed subgrid variation profile for temperature. As shown in previous studies (KB08; Hoyle et al., 2005; Kärcher and Ström, 2003; Haag and Kärcher, 2004; Jensen and Pfister, 2004), the use of large scale temperature fluctuations alone is not sufficient for ice nucleation in cirrus clouds, and mesoscale temperature fluctuations from small scale motions such as gravity waves are critical to cirrus cloud generation and to the determination of cirrus cloud properties. These mesoscale temperature fluctuations cover horizontal length-scales 1-100 km (Ström et al., 1997; Bacmeister et al., 1999) and arise from a variety of sources. These sources include intense gravity waves released by mesoscale convective systems, high amplitude lee waves induced by high mountain ridges, or high amplitude lee waves induced in the area of jet streams and storm tracks (KB08). Even away from main source areas, there appears to be a persistent background of mesoscale temperature fluctuations driven by mesoscale gravity waves (Gary, 2006; 2008).

In this new cirrus cloud scheme, a probability density function (PDF) of temperature is used to represent mesoscale temperature perturbations in the clear sky part of a grid. The PDF of temperature (dP_T/dT) is assumed to be a constrained normal distribution with a mean temperature (T_0) that is predicted by the GCM, and a standard deviation of δT that is prescribed (see Equation 4.A1 in Appendix A). This normal distribution is shown to be an excellent approximation to the mesoscale distribution of temperature in background conditions in the middle latitudes of both hemispheres (KB08). The PDF of the temperature distribution is then transformed into a PDF of the saturation ratio (S) (dP_S/dS) (Equation 4.A2) using the saturation vapor pressure over pure hexagonal ice (Murphy

and Koop, 2005) and the mean specific humidity in the clear sky part of the grid (q_{ve}). By comparing this PDF of S with the freezing threshold saturation ratio (S_{cr}), we can determine the portion of the distribution that is located above S_{cr} as:

$$f(S > S_{cr}) = \int_{S_{cr}}^{S_{3+}} \frac{dP_S}{dS} dS, \tag{4.1}$$

where S_{3+} is the upper bound of the saturation ratio over which dP_S/dS is defined (see Equation 4.A2). Ice crystals form when dPs/dS extends above the freezing threshold. After taking account of the clear sky fraction ($1-a$), we have cloud fraction increases from ice freezing defined as

$$\Delta a=(1-a)f(S>S_{cr}). \tag{4.2}$$

The increases in the grid-mean ice crystal number concentration (n_i) from ice freezing are then

$$\Delta n_i=N_i\Delta a, \tag{4.3}$$

where N_i is the in-cloud ice crystal number concentration from homogeneous freezing and/or heterogeneous freezing. When both homogeneous freezing and heterogeneous freezing is allowed, if S is greater than the critical saturation ratio for heterogeneous freezing, but lower than that required for homogeneous freezing, then N_i is determined by the number of heterogeneous nuclei. If S is greater than the critical saturation ratio for homogeneous freezing, then Ni is set to the sum of the heterogeneous nuclei plus the homogeneous nuclei, as discussed in detail later (Equations 4.6-4.9).

To calculate N_i, vertical velocities or cooling rates are needed, and they are parameterized based on a probability distribution for δT. The mean cooling rate ϖ, induced by mesoscale temperature fluctuations, is approximated by

$$\varpi\ [\mathrm{Kh^{-1}}]=8.2\delta T[\mathrm{K}], \tag{4.4}$$

as in Hoyle et al. (2005); then the mean vertical velocity ($\overline{w}$) is deduced by assuming that the cooling takes place in a parcel lifting adiabatically. This cooling rate or vertical velocity is then used to calculate ice crystal number concentration. For homogeneous freezing, the resulting ice crystal number density N_{i_homo} is approximated as

$$N_{i\_homo} \approx 2\ \mathrm{n}(\overline{w}), \tag{4.5}$$

where $n(\overline{w})$ is the ice crystal number concentration from the homogeneous freezing parameterization for the vertical velocity, $\overline{w}$. This formula is based on the integration of a PDF of vertical velocity or cooling rates, and takes account of the following two factors: (a) most of the small cooling rates do not contribute to freezing on average, and (b) high ice crystal concentrations resulting from high cooling rates are more effective at suppressing subsequent supersaturation (KB08).

KB08 demonstrated that a δT of 1K reproduces the observed distribution of saturation ratios at temperatures near 225K, as measured in the middle latitudes of both hemispheres from INCA field data (Kärcher and Ström, 2003; KB08). A δT of 1K is also close to average mesoscale temperature amplitudes associated with mean mesoscale altitude displacements of air parcels of ~ 100 m as inferred from the Microwave Temperature Profiler from the analysis of more than 4000 aircraft flight hours taken in the altitude range 7-22 km and with a variety of underlying topography, spanning the latitude range 70°S to 80°N (Gary, 2006; 2008). Gary (2006) also showed that the mesoscale temperature amplitudes increase with altitude, which is consistent with the gravity wave theory (Fritts and Alexander, 2003).

By using Equation 4.4, the δT of 1K gives a cooling rate of 8.2 K/hour and a vertical velocity of 23 cm/s, which is close to the mean vertical velocity of 26 cm/s measured in

the updraught regions in the INCA campaign (Kärcher and Ström, 2003). However, Equation 4.4 is derived based on data from the Subsonic Aircraft: Contrail and Cloud Effects Special Study (SUCCESS) campaign (Hoyle et al., 2005). Whether the resulting mean updraft velocity of 23 cm/s is representative at other temperatures and at other locations is not yet known. It is most likely that this mean mesoscale vertical velocity is not applicable for all locations and for all temperatures, given the fact that a variety of mechanisms are responsible for mesoscale fluctuations. For example, a vertical velocity of ~20 cm/s would predict very high ice crystal number concentration at lower temperatures from homogeneous freezing, which is not supported by field observations. By examining aircraft in-situ observations of ice crystal number concentration during 28 flights in tropical, midlatitude, and Arctic field experiments in the temperature range of 183-250K, Krämer et al. (2008) showed a decreasing ice crystal number concentration with decreasing temperature. This decreasing ice crystal number concentration cannot be reproduced by homogeneous freezing if a constant vertical velocity is assumed. A vertical velocity as low as 1 cm/s is able to explain the observed ice crystal number concentrations at very low temperatures if homogeneous freezing is assumed. It is also noted that vertical velocities around 1 cm/s were used in Khvorostyanov et al. (2006) and Jensen et al. (2008), and that these were able to reproduce the observed ice crystal number concentration for thin tropopause cirrus from homogeneous freezing during the 2004 CRYSTAL-FACE and 2006 CRAVE campaigns, respectively.

A constant vertical velocity of ~20 cm/s is also not able to simulate realistic stratospheric water vapor concentrations in our model if homogeneous freezing is assumed. A test run with a constant vertical velocity of ~20 cm/s simulated very high ice

crystal number concentrations at low temperatures, which lead to strong heating at the tropical tropopause and resulted in unrealistically high concentrations of stratospheric water vapor (not shown).

Given that observed ice crystal number concentration decreases linearly with decreasing temperature and that the information about mesoscale vertical velocities and temperature perturbations are not available in global climate models, we simply use a mean mesoscale vertical velocity that decreases with decreasing temperature from 23 cm/s at 238K to 1.2 cm/s at 193 K and remains constant above these extremes in our simulations. This results in a mesoscale temperature perturbation of 1 K at 238K and 0.05 K at 193 K (or below) using Equation 4.4.

In KB08, homogeneous freezing is the only freezing mode for cirrus clouds. In this study, an additional scenario that allows competition between homogeneous and heterogeneous freezing is included. When homogeneous freezing is the only freezing mode, ice crystal number concentration from ice freezing (N_{i_homo}) and the threshold freezing saturation ratio (S_{cr_homo}) are parameterized based on Liu and Penner (2005), and are used in Equations 4.2 and 4.3 (with N_{i_homo} adjusted by a factor of 2 to account for the increase in ice crystal number concentrations, see Equation 4.5) to calculate increases in cloud fraction and grid-mean ice crystal number concentration. In the scenario where the competition between homogeneous freezing and heterogeneous freezing is allowed, S_{cr_homo} and N_{i_homo} (Equation 4.5) are still used to determine how much of the cloud fraction and ice crystal number concentration increases are due to homogeneous freezing. When heterogeneous IN number concentration (N_{in}) exceeds the threshold IN number concentration (N_{in_cr}) derived in Gierens (2003), heterogeneous freezing is also allowed.

The heterogeneous freezing threshold saturation ratio (S_{cr_hete}) and ice crystal number concentration from heterogeneous ice freezing (N_{i_hete}) that are parameterized based on Liu and Penner (2005) are then used to calculate total cloud fraction increase, and the ice crystal number concentration increase from heterogeneous freezing. The heterogeneous number concentration is not multiplied by a factor of 2, since the factor of 2 applied in the homogeneous freezing is primarily used to account for the nonlinear dependence of ice crystal number concentrations on vertical velocity during homogeneous freezing and since heterogeneous freezing is less sensitive to vertical velocity due to the low number of heterogeneous IN number concentrations. For example, at temperature 225 K, when vertical velocities increase from 10 cm/s to 50 cm/s, heterogeneous ice crystal number concentrations that are parameterized based on Liu and Penner (2005) change very little (state percentage how much) for a soot number concentration less than 0.1/cm^3, while homogeneous ice crystal number concentrations that are parameterized based on Liu and Penner (2005) increase from 0.20 /cm^3 to 2.50 /cm^3 for a sulfate particle number concentration of 50 /cm^3. So, the cloud fraction increase and ice crystal number concentration increases in this scenario will be defined as:

$$\Delta a=(1-a)f(S>S_{cr\_homo}), \tag{4.6}$$

$$\Delta n_i=N_{i\_homo}\Delta a, \quad \text{when } N_{in} < N_{in\_cr} \tag{4.7}$$

and

$$\Delta a=(1-a)f(S>S_{cr\_hete}), \tag{4.8}$$

$$\Delta n_i=N_{i\_hete}\Delta a+ N_{i\_homo}(1-a)\, f(S>S_{cr\_homo}), \text{ when } N_{in} > N_{in\_cr}. \tag{4.9}$$

where N_{i_homo} (increased by a factor of 2, see Equation 4.5) and N_{i_hete} are evaluated at the average updraft velocity $\overline{w}$.

In the treatment of the competition between homogeneous freezing and heterogeneous freezing, heterogeneous freezing is only allowed to occur when the concentration of heterogeneous IN exceeds the critical heterogeneous IN concentration. However, in the real atmosphere, when the saturation ratio exceeds the freezing threshold saturation ratio, heterogeneous freezing occurs once the heterogeneous IN are present, regardless of the concentration of the heterogeneous IN. This implies that Equations 4.8 and 4.9 should be always applied when the saturation ratio is larger than the freezing threshold saturation ratio. But given the large time step used in the NCAR CAM3 (30 minutes), the application of Equations 4.8 and 4.9 without the limitation set by heterogeneous IN concentrations will significantly decrease supersaturation levels in the model and result in very few homogeneous freezing events even when the concentration of heterogeneous IN is very low (<1/L). So in our treatment, the competition between homogeneous freezing and heterogeneous freezing is partially parameterized by using the critical heterogeneous IN concentrations derived by Gierens (2003) to determine whether heterogeneous freezing will occur. When the heterogeneous IN concentration is lower than the critical heterogeneous IN concentrations, heterogeneous freezing will not occur and the heterogeneous IN concentration is assumed to have no effect on homogeneous freezing.

At a single time step, parcel model results may be used to quantify how accurate the treatment given in Equations 4.8 and 4.9 is. Using a parcel model, Liu and Penner (2005) showed that when heterogeneous IN concentration is larger than N_{in_cr}, ice crystal number concentration is determined by heterogeneous freezing. Then there is a factor of 10 transition region for heterogeneous IN number concentration from $N_{in\_cr}/10$ to N_{in_cr}, in which ice crystal number concentration gradually decreases from that of homogeneous

freezing to that of heterogeneous freezing. When heterogeneous IN concentration is lower than $N_{in\_cr}/10$, ice crystal number concentration is determined by homogeneous freezing. Compared with the results from the parcel model in Liu and Penner (2005), our treatment is generally good for low IN concentration ($< N_{in\_cr}/10$) and for high IN concentration ($> N_{in\_cr}$). For the case where heterogeneous IN concentration is low ($< N_{in\_cr}/10$), our treatment assumes that heterogeneous IN has no effect on ice crystal number concentration and that ice crystal number concentration is determined by homogeneous freezing, which is consistent with the results of the parcel model. When heterogeneous IN number concentration is higher than the critical heterogeneous IN (N_{in_cr}), heterogeneous freezing is allowed to occur, which usually inhibit the occurrence of homogeneous freezing. So ice crystal number concentration in this case is usually determined by heterogeneous freezing, which is also consistent with the results from the parcel model. But when the concentration of heterogeneous IN is in the transition regions (from $N_{in\_cr}/10$ to N_{in_cr}), heterogeneous freezing is not allowed in our treatment, and ice crystal number concentration is determined by homogeneous freezing. Ice crystal number concentrations may then may be overestimated, and biased toward the ice crystal number concentration given by homogeneous freezing.

However, the errors at subsequent time steps are difficult to quantify. The errors at subsequent time steps largely depend on the simulated subgrid-scale supersaturation at the subsequent time steps. Without knowing the history of the large scale temperature and water vapor in the model, it is difficult to quantify how accurately the subgrid-scale supersaturation is simulated at the subsequent time step. The simulated supersaturation level also depends on how gravitational settling is treated in the model. To better quantify

the overall errors in models, a comparison between a single column version of the GCM and a cloud resolving model would provide valuable information about whether the treatment of the competition between homogeneous freezing and heterogeneous freezing is adequate. A cloud resolving model that is capable of simulating the competition between homogeneous freezing and heterogeneous freezing, such as the one from Spichtinger and Gierens (2009), would be an ideal tool for such a comparison.

The threshold IN number concentration (N_{in_cr}) is a function of $S_{cr\_homo,}$ $S_{cr\_hete,}$ vertical velocity, temperature, and pressure (Gierens, 2003). Liu and Penner (2005) obtained a similar formula by empirically fitting N_{in_cr} as a function of vertical velocity from their parcel model simulations. As shown in Liu and Penner (2005), the two formulas give similar N_{in_cr} for vertical velocities larger than 20 cm/s. It was further shown by Liu et al. (2009) that simulated changes in cirrus cloud properties and cloud forcing due to anthropogenic aerosols are very similar from these two formulas, when a subgrid scale PDF of vertical velocities with a mean of 0 and a standard deviation of 25 cm/s is used. However, at low vertical velocities (less than 5 cm/s), N_{in_cr} from Liu and Penner (2005) is much smaller than that from Gierens (2003). For example, at 193 K, with a vertical velocity of 1.2 cm/s, N_{in_cr} is $6.13 \times 10^{-6}/cm^3$ in Liu and Penner (2005) and is 6.12×10^{-3} in Gierens (2003). Heterogeneous freezing occurs exclusively at very low vertical velocities when the formula in Liu and Penner (2005) is used. Here, we choose the formula of Gierens (2003) over that in Liu and Penner (2005) mainly because low vertical velocities are used at low temperatures in this study and the use of the Liu and Penner (2005) values for N_{in_cr} would lead to concentrations of ice crystal number concentrations that are lower than the observations of Krämer et al. (2008) when heterogeneous IN number

concentrations are low. The source of heterogeneous IN used in the model is discussed in section 4.2.3.

An initial ice crystal mass of 10^{-12} kg is assumed for newly formed ice particles. This is a simplification of the treatment used in KB08, where new ice crystal sizes are parameterized based on homogeneous freezing. Because the time step of the GCM is large (about half an hour), all supersaturation in newly formed clouds is usually removed and the in-cloud saturation ratio with respect to ice is close to 1.0, which makes the initial ice crystal mass less important. After the removal of the initial ice crystal mass, the remaining water vapor in the new clouds is then moved into the cloudy portion of the grid and the in-cloud specific humidity q_{vc} is updated.

Ice crystals grow through vapor deposition in cloudy areas and in-cloud water vapor q_{vc} is transferred to ice crystals via gas phase diffusion,

$$(\Delta q_{vc})_{dep} = -(q_{vc} - q_{sat})\{1 - \exp(-\tau / \tau_s)\}, \tag{4.10}$$

where q_{sat} is the saturation specific humidity, τ is the time step, and τ_s is the instantaneous relaxation time scale (see Equation 4.A7 in Appendix 4.A), which determines how long the supersaturation (S_{cr}-1) lasts after freezing. The change in the grid averaged ice water content through vapor deposition is $-a(\Delta q_{vc})_{dep}$.

Cloud decay is determined by the in-cloud specific humidity, ice water content, and a PDF of the in-cloud total water mass mixing ratio (q_{totc}) (see Equation 4.A9). In-cloud specific humidity has a homogeneously distributed PDF in the form of a delta function, $\delta(q-q_{vc})$. The PDF of the total water mass mixing ratio (dP_{qtot}/dq_{tot}) is then determined by the PDF of the in-cloud ice water content (see Equation 4.A8). Cloud decay occurs when in-cloud air becomes subsaturated (in-cloud saturation ratio $S_c < 1$) due to warming or

drying out. This subsaturation will lead to sublimation of ice crystals. The smallest ice crystals experiencing the highest subsaturations will completely sublimate first. The sublimation (Δq_{vc}) is calculated based on Equation 4.10 when q_{vc} is less than q_{sat}. Cloud fraction decrease is determined by the portion of the PDF of ice water in which ice water is less than Δq_{vc}, and is calculated as:

$$\Delta a = a\int_{q_{vc}}^{q_{vc}+\Delta q_{vc}} \frac{dP_{q_{totc}}}{q_{totc}} dq_{totc} = -erf(\xi)a, \ \xi = a\Delta q_{vc}/(q_i\pi^{0.5}), \tag{4.11}$$

where *erf(x)* is the error function (see Equation 4.A5). The change in ice water content is determined by the following formula:

$$\Delta q_i = -q_i[1-exp(-\xi^2)+\pi^{0.5}\xi\{1-erf(\xi)\}]. \tag{4.12}$$

The decrease in ice crystal number concentration (Δn_i) is assumed to be proportional to the cloud fraction decrease, and is calculated as

$$\Delta n_i = n_i \Delta a/a. \tag{4.13}$$

In CAM3, detrained cloud water is added into large scale clouds along with the convective cloud fraction (a_{conv}) that is diagnosed from convective mass fluxes (Boville et al., 2006). This is the case for warm clouds and mixed-phase clouds treated in this study, where cloud droplet and ice crystal number from detrained cloud water are also added into large scale clouds by using a prescribed volume mean radius (see Appendix 4.B for details). For cirrus clouds, detrained cloud ice mass and crystal number are still added into large scale clouds in the same way as in warm and mixed-phase clouds. But since cloud fraction in cirrus clouds is prognostic rather than diagnostic, cloud fraction increases from the convective source are calculated at each time step in the following way:

$$(\Delta a)_{conv} = (1-a)a_{conv}, \tag{4.14}$$

The factor *1-a* in Equation 4.14 appears because convective air detrains simultaneously into cloud-free air, as well as into already existing clouds, ensuring realistic limits at zero cloud cover and at cloud cover 1, following the same assumption as in Tiedtke (1993). This new cloud is assumed to be at saturation with respect to ice (the same assumption is used in the standard CAM3, see Boville et al., 2006), which also sets the upper limit of cloud fraction increase from convective cloud as $(1-a)q_{ve}/q_{sat}$ (i.e., the water vapor in the new cloud ($a_{conv}\ q_{sat}$) will not exceed the available water vapor in the clear sky(q_{ve})). After cloud fraction is updated from convective clouds, the in-cloud specific humidity is updated as

$$q_{vc}=(q_{vc}a+q_{sat}(\Delta a)_{conv})/(a+(\Delta a)_{conv}). \tag{4.15}$$

In the standard CAM3 and the version updated in LIU07, only grid-mean specific humidity (q) is predicted, using:

$$\frac{\partial q}{\partial t} = A_q - Q + E_r\,, \tag{4.16}$$

where A_q is the tendency of water vapor from processes other than large-scale condensation and evaporation of cloud and rain water, Q is the net condensation rate, and E_r is the evaporation of rain water. In order to predict in-cloud specific humidity (q_{vc}), we assume that A_q is uniformly applied to the whole model grid cell, which is also the assumption made in the condensation-evaporation scheme in CAM3 (Zhang et al., 2003). The in-cloud specific humidity is then predicted together with cloud growth (both large scale and convective clouds), decay, and in-cloud vapor deposition/evaporation.

Both cloud ice mass and ice crystal number are advected as in LIU07. As discussed in Boville et al. (2006), advection of cloud condensate is important in the tropical upper troposphere where the mass of ice and vapor phases of water are similar and the lifetime

of cloud ice is relatively long. The tendencies of cloud ice mass (A_{qi}) and ice crystal number (A_{ni}) from processes other than large-scale formation or decay of clouds, detrainment, and sedimentation are also assumed to be uniformly applied to the whole model grid cell. It is assumed that the part of these tendencies that falls into the clear sky portion of the grid is evaporated (the same assumption as that used in Zhang et al., 2003). For simplicity, the cloud fraction predicted here is not advected. As a consequence, cloud ice may be advected to grids that have no cloud fraction or partial cloud fraction. If this is the case, the cloud ice that is advected into the clear sky portion of the grid will be evaporated.

In addition to the new cirrus cloud scheme, several other updates have been made in the version of CAM3 used in this study compared with the version used in LIU07. These include a prognostic liquid droplet number equation that takes into account droplet activation, coagulation, evaporation, and freezing, which, together with the ice cloud treatment, consists of a complete set of equations for the two-moment treatment of cloud microphysics in NCAR CAM3. Also the direct conversion from liquid to ice in mixed-phase clouds which was not allowed in LIU07 but was used in simulating observed clouds in the Mixed-Phase Arctic Cloud Experiment (M-PACE) in a single column model (Liu et al., 2007) and in a short-range weather forecasting approach (Xie et al. 2008) was included. Also, a new package of aerosol optical properties that replaces the one used in the standard CAM3 was added to be consistent with the aerosol fields simulated in IMPACT and to include a treatment of internal mixing of black carbon and organic carbon. These updates are described in detail in Appendices 4.B and 4.C.

4.2.3 Set-up of simulations and experimental design

We used 26 vertical levels and a horizontal resolution of 2 × 2.5 degrees for both the CAM3 and IMPACT models in this study. The time step for CAM3 was 30 minutes, and the time step for advection in IMPACT was 1 hour. The finite volume dynamical core was chosen for CAM3.

We ran several simulations as described in Table 4.1. In case 'HOM', only homogeneous freezing on sulfate particles was considered. All other simulations take into account both homogeneous and heterogeneous freezing, but with varied IN concentrations and varied subgrid-scale temperature perturbations.

Three cases are used to study how cirrus cloud properties change with different IN concentrations. The freezing capabilities of different aerosol particles acting as IN are not well understood and conflicting results exist (see discussion in section 4.1). This justifies the approach of using sensitivity tests to study their effects on cirrus clouds. The same temperature perturbation as that used in the HOM case is applied, but with 1%, 10%, and 100% of soot and dust particles acting as heterogeneous IN in HMHT_0.01IN, HMHT_0.1IN, and HMHT_1IN, respectively. The 1% value is consistent with the report by Seifert et al. (2003) that scavenging ratios were < 1% in the INCA campaign. The 100% value represents the case where soot and dust particles are very efficient IN, which was assumed in several previous modeling studies (e.g., Hendricks et al., 2005; Liu et al., 2009). Additionally, two cases are used to study how different temperature perturbations will change cirrus cloud properties. These two cases have the same IN concentration as in the case HMHT_0.01IN, but temperature perturbations have been decreased/increased by 25% in HMHT_0.75dT and HMHT_1.25dT, respectively. These results are also

compared with the results from the standard version of CAM3 (CAM3) and LIU07. In LIU07, the treatment of ice clouds does not include the subgrid parameterization of supersaturation and cloud droplet number concentrations in liquid clouds are prescribed as in the standard version of CAM3.

Table 4.1: Descriptions of simulations

Case names	Descriptions
HOM	Homogeneous freezing on sulfate particles.
HMHT_0.01IN	Same as HOM, but 1% of soot and dust particles are included to act as heterogeneous IN.
HMHT_0.1IN	Same as HMHT_0.01IN, but 10% of soot and dust particles acts as heterogeneous IN.
HMHT_1IN	Same as HMHT_0.01IN, but 100% of soot and dust particles act as heterogeneous IN.
HMHT_0.75dT	Same as HMHT_0.01IN, but temperature perturbation is decreased by 25%.
HMHT_1.25dT	Same as HMTH_0.01IN, but temperature perturbation is increased by 25%.

4.3. Model results for the HOM case

Since homogeneous freezing is believed to be the dominant freezing mechanism in pristine environments, we show simulated results for the HOM case in this section and model results are compared with observations when available. Cloud-top quantities are estimated as seen by satellite instruments using a modification of the maximum/random cloud overlap assumption that is used in the radiative transfer calculations in the NCAR CAM3 (Collins et al., 2001) to obtain the two-dimensional field (Quaas et al., 2004). The sampling procedure accounts for the contribution of each layer to the two-dimensional distribution seen at each grid point and time step from above (Quaas et al., 2004; the code to sample cloud-top quantities is available from

http://wiki.esipfed.org/index.php/Indirect_forcing). The contribution of a layer to cloud top quantities is based on the increase in the total cloud fraction due to the addition of this layer, where the total cloud fraction from the model top to the current layer is calculated based the maximum/random overlap assumption. This approach assumes that for the subgrid column that results from the addition of the current layer, only clouds at the current layer contribute to the cloud top quantities, so any layer that is below this top layer will have no contribution to the cloud top quantities. For the comparison with the satellite data listed in Table 4.2, cloud top quantities (liquid droplet radius and ice crystal radius) are sampled only for clouds with optical depth larger than 0.3, and are also only sampled once per day at the over pass time of MODIS Aqua satellite (1:30 p.m., local time). For cloud droplet radius, the samples are limited to warm clouds (cloud top temperature larger than 273.16 K), and for ice crystal radius, is the samples are limited to cold cirrus clouds (cloud top temperature less than 238.16 K).

Tables 4.2 and 4.3 show the annual global mean values for several parameters in our simulations along with results from the standard CAM3 and observations. The liquid water path is 77 g/m^2, much less than that simulated in LIU07 and in the standard CAM3, and close to the observed range of 50-84 g/m^2; this is also close to that simulated by Gettleman et al. (2008) in a modified version of CAM3 that includes a two moment cloud physics treatment (74 g/m^2). The large decrease in liquid water path compared with that in the standard CAM3 is mainly caused by the Bergeron-Findeisen process where ice crystals grow at the expense of liquid droplets. Because ice crystals are more efficient at producing precipitation, the inclusion of this process decreases liquid water path significantly. In the treatment here, a direct conversion from liquid to ice is assumed and

the in-cloud vapor pressure that is used to calculate vapor deposition on ice crystals is the saturation vapor pressure over liquid and ice with each weighted by the proportions of ice and liquid water mass (Xie et al., 2008). Even though the Bergeron-Findeisen process was also included in LIU07, the conversion occurs first as a result of supersaturation with respect to ice, and grid-averaged vapor pressure is used to calculate vapor deposition based on Rotstayn et al. (2000). Then the liquid water is evaporated because of subsaturation with respect to liquid water, parameterized based on Zhang et al. (2003) and further deposition takes place. Because grid-averaged vapor pressure is usually less than the saturation vapor pressure that is weighted by the proportion of ice and liquid water mass, the treatment in LIU07 results in a smaller conversion rate from liquid to ice in mixed-phase clouds than that used in this study (Xie et al., 2008; Appendix 4.B), which explains why the liquid water path is still high in LIU07. The column integrated droplet number concentration averaged over 50°S-50°N is $2.3\times10^{10}/m^2$, and is underestimated compared with AVHRR observations ($4.0\times10^{10}/m^2$). However, our simulated cloud top droplet effective radius for warm clouds (cloud top temperature > 273.16 K) is 11.1 μm, which matches well with AVHRR observations (11.40 μm), but is lower than that from MODIS observations (15.7 μm).

The ice water path is 21 g/m^2, which is comparable to satellite observations (Figure 18 in Waliser et al., 2009). The column integrated ice crystal number concentration is about $0.022\times10^{10}/m^2$, which is much smaller than that predicted by Lohmann et al. (2007) ($0.1\text{-}0.7\times10^{10}/m^2$). The large difference mainly comes from the difference in the treatments of mixed-phase clouds. In our model, deposition/condensation freezing and contact freezing are included in mixed-phase clouds. Deposition/condensation freezing is parameterized

Table 4.2. Annual global mean cloud properties and their interannual variations (standard deviations). The liquid water path (LWP, g/m^2) observations are from SSM/I (for the years 1987-1994, Ferraro et al., 1996; for August 1993 and January 1994, Weng and Grody, 1994; and for August 1987 and February 1988, Greenwald et al., 1993) and ISCCP for the year 1987 (Han et al., 1994). SSM/I data are restricted to oceans. Ice water path (IWP, g/m^2) has been derived from ISCCP data for the years 1983-2000 (Storelvmo et al., 2008). N_d and N_i refer to the vertically integrated cloud droplet and ice crystal number concentration ($10^{10}/m^2$), and r_{effl} (μm) refers to the cloud top effective radius. Observations of N_d are obtained from ISCCP for the year 1987 (Han et al., 1998) and observations of r_{effl} are obtained from ISCCP for the year 1987 (Han et al, 1994) and from MODIS (version 4) for the year 2001 (Platnick et al., 2003), and are limited to 50ºN to 50ºS. r_{effi} and N_{itop} refer to ice crystal radius and number at the top of cirrus clouds, respectively. Observations of r_{effi} are from MODIS data (version 4) for the year 2001. Total cloud cover (TCC) was obtained from ISCCP for the years 1983-2001 (Rossow and Schiffer, 1999) and MODIS data for the years 2001-2004 (Platnick, 2003). High cloud cover (TCCHGH) was obtained from ISCCP data for the years 1983-2001. TCCLOW refers to low level cloud cover.

	HOM	HMHT 0.01IN	HMHT 0.1IN	HMHT 1IN	HMHT 1.25dT	HMHT 0.75T	LIU07	CAM3	Obs
LWP	77.45±0.53	76.44±0.42	75.26±0.15	82.00±0.36	78.15±0.28	75.38±0.65	141	121	50-87
IWP	20.94±0.01	21.03±0.03	21.14±0.07	21.79±13	21.39±0.06	20.92±0.06	21.8	15.6	26.7
N_d	2.28±0.017	2.24±0.025	2.24±0.009	2.48±0.011	2.32±0.007	2.20±0.09	#	#	4
N_i	0.022 ±9.82e-5	0.016 ±2.55e-4	0.0085 ±2.70e-5	0.051 ±1.47e-3	0.024 ±5.08e-4	0.0089 ±2.40e-4	0.027	#	
r_{effl}	11.09±0.01	11.10±0.01	11.10±0.02	11.06±0.02	11.08±0.01	11.12±0.01	#	#	11.4-15.7
r_{effi}	39.63±0.28	43.91±0.20	43.09±0.19	35.11±0.09	40.99±0.55	47.77±0.13	#	#	25.21
N_{itop}	0.28± 2.81e-3	0.17± 2.10e-3	0.067± 6.60e-4	0.50± 7.72e-3	0.31± 1.65e-3	0.081± 1.51e-3		#	
TCC	66.41±0.10	67.33±0.13	68.40±0.08	68.46±0.10	67.14±0.09	68.19±0.14	77.90	58.6	65-67
TCCHGH	35.82±0.12	38.18±0.08	40.22±0.10	39.92±0.16	37.20±0.16	39.60±0.11	56.80	32.2	21
TCCLOW	44.24±0.11	43.87±0.18	43.63±0.02	45.30±0.12	44.50±0.03	43.67±0.11			

Table 4.3. Annual global mean shortwave cloud forcing (SWCF, W/m^2), longwave cloud forcing (LWCF, W/m^2), net cloud forcing (CF, W/m^2), total precipitation (Ptot, mm/day), water vapor mass (WVM, kg/m^2), net incoming radiation at the top of the atmosphere (FNT, W/m^2), and clear sky net long wave radiation at the top of the atmosphere (FLNTC, W/m^2, negative values mean outgoing) and their interannual variations (standard deviations). The shortwave (SWCF) and longwave cloud forcing (LWCF) estimates are taken from ERBE for the years 1985-1989 (Kiehl and Trenberth, 1997) and CERES for the years 2000-2005 (http://science.larc.nasa.gov/ceres). Total precipitation (P_{tot}) is taken from the Global Precipitation Data Set for the years 1979-2002 (http://precip.gsfc.nasa.gov). Water vapor mass (WVM) data is from MODIS for the years 2001-2004 (King et al., 2003).

	HOM	HMHT_ 0.01IN	HMHT_ 0.1IN	HMHT_ 1IN	HMHT_1.2 5dT	HMHT_ 0.75T	LIU07	CAM3	Obs
SWCF	-52.21±0.12	-51.47±0.31	-50.65±0.12	-55.83±0.24	-52.72±0.04	-50.40±0.25	-59.1	-54.6	-47 to -54
LWCF	27.60±0.07	26.72±0.03	26.22±0.03	31.53±13	28.19±0.13	25.43±0.09	31.9	30.6	29to 30
CF	-24.61±0.16	-24.75±0.20	-24.43±0.10	-24.30±0.22	-24.53±0.15	-24.97±0.17	-27.2	-24.0	
Ptot	2.89±0.001	2.92±0.006	2.94±0.004	2.81±0.005	2.88±0.004	2.96±0.007	#		2.61
WVM	24.42±0.07	24.15±0.03	23.95±0.05	25.26±0.08	24.43±0.06	23.92±0.02			22.80
FNT	2.63±0.05	2.14±0.21	1.71±0.17	3.94±0.21	2.86±0.04	1.59±0.26			
FLNTC	-261.94 ±0.15	-262.33 ±0.19	-262.95 ±0.17	-261.05 ±0.32	-261.82 ±0.14	-262.58 ±0.13			

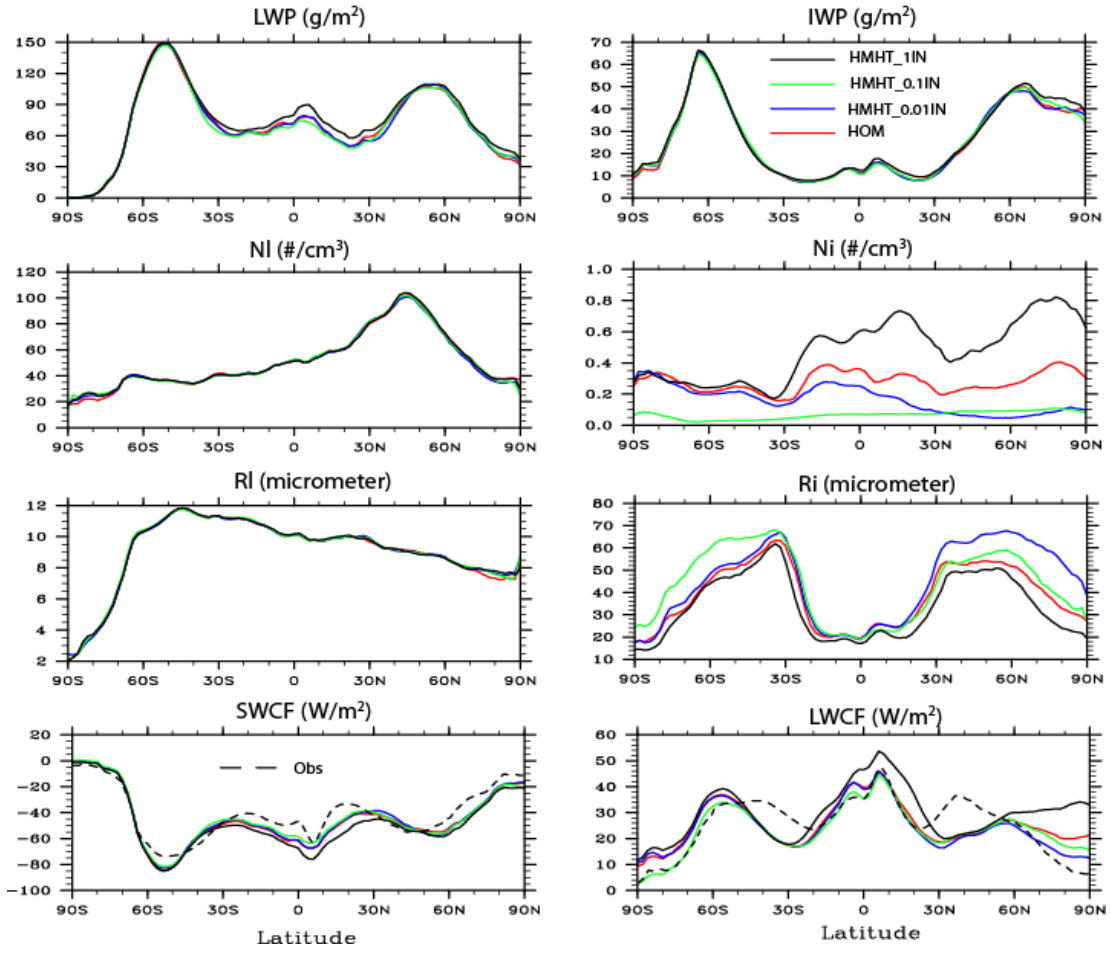

Figure 4.1: Annual zonal means of liquid water path (LWP, g/m^2), ice water path (IWP, g/m^2), cloud top in-cloud liquid droplet number concentration (N_l, #/cm^3), cloud top liquid droplet effective radius (R_l, μm), cirrus cloud top in-cloud ice crystal number (N_i, #/cm3), and cirrus cloud top ice crystal radius (R_i, μm), shortwave cloud forcing (SWCF, W/m^2), and longwave cloud forcing (LWCF, W/m^2) in four cases: HOM, HMTH_0.01IN, HMHT_0.1IN, HMHT_1IN. For shortwave and long wave cloud forcing, observations from CERES data for the years 2000-2005 (http://science.larc.nasa.gov/ceres) are included as the dashed black line.

based on Meyers et al. (1992) and is a function of ice supersaturation. Mineral dust particles are the only contact freezing ice nuclei. The simulated ice crystal number concentration in mixed-phase clouds is generally less than 1/L, which compares well with observations from the M-PACE field experiments. In Lohmann et al. (2007), both

mineral dust and soot particles act as contact freezing ice nuclei. Moreover, Lohmann et al. (2007) included an immersion freezing scheme that has a freezing fraction of 1 for dust particles at temperatures lower than -15°C and has a freezing fraction of 1 for soot particles at temperatures lower than -25°C (Figure 10 in Phillips et al., 2008), which probably explains why Lohmann et al. (2007) simulated much higher ice crystal number concentrations than that simulated here in mixed-phase clouds.. The average cloud top ice crystal radius for cold cirrus clouds (cloud top temperature less than -35ºC) is 39.6 μm, larger than the observed value from the MODIS satellite (25.21 μm).

Total cloud fraction is 66% and compares well with the observations. The new cirrus cloud scheme simulates significantly fewer high clouds than LIU07 and improves the model results compared with observations. Shortwave cloud forcing is -52 W/m^2, and is comparable to ERBE (-54 W/m^2) and CERES (-47 W/m^2) observations. Long wave cloud forcing is 28 W/m^2, which is also comparable to ERBE (30 W/m^2) and CERES (29 W/m^2) observations. The precipitation rate is 2.89 mm/day, slightly higher than observations.

Figure 4.1 shows the annual average zonal mean liquid water path, ice water path, cloud top droplet number concentration and droplet effective radius for liquid clouds, cloud top in-cloud ice crystal number and ice crystal effective radius of cirrus clouds (for cloud top temperatures less than -35ºC), shortwave cloud forcing, and longwave cloud forcing. Cloud top droplet number concentrations have a strong north-south contrast with a larger number concentration in the NH, which is consistent with data derived from MODIS observations (Quaas et al., 2006), and is mainly caused by anthropogenic aerosols in the model. Correspondingly, cloud top droplet effective radius has a larger value in the SH than in the NH, which is consistent with the AVHRR observations (Han

et al., 1994). Liquid water path has larger values in the middle latitude storm track over both hemispheres, which is consistent with SSM/I data (Ferraro et al., 1996). The ice water path has two peak values in the middle latitudes of both hemispheres, which is consistent with ISCCP observations (Storelvmo et al., 2008). For cirrus clouds, cloud top ice crystal number concentration is large over the tropics and the two polar regions. The ice crystal effective radius has two peaks in the middle latitudes of both hemispheres, with minima in the tropics and the two polar regions. The minima in the tropics is not consistent with MODIS data, which have a larger ice crystal radius in tropics than that in the middle latitudes. Short wave cloud forcing and long wave cloud forcing have latitudenal variations that agree with the CERES observations.

Figure 4.2 shows annual, latitude-pressure cross sections for grid-averaged droplet number concentration, liquid water content, ice crystal number concentration, and ice water content. Liquid water content shows two peaks in the storm tracks of both hemispheres, which extend into the middle troposphere. Liquid droplet number concentrations show a similar pattern: two peaks in the middle latitudes in both hemispheres, but the influence of anthropogenic aerosols is also evident: there is a stronger peak in the NH than in the SH. For ice clouds, large ice crystal number concentrations are found over the upper troposphere in tropical regions and at both poles.. The simulated grid mean ice crystal number concentrations are comparable to results from Lohmann et al. (2007), except that they simulated higher ice crystal number concentrations in mixed-phase clouds, as mentioned above. Large ice water content can be found in the lower troposphere over high latitudes in both hemispheres and in the upper troposphere in the tropics.

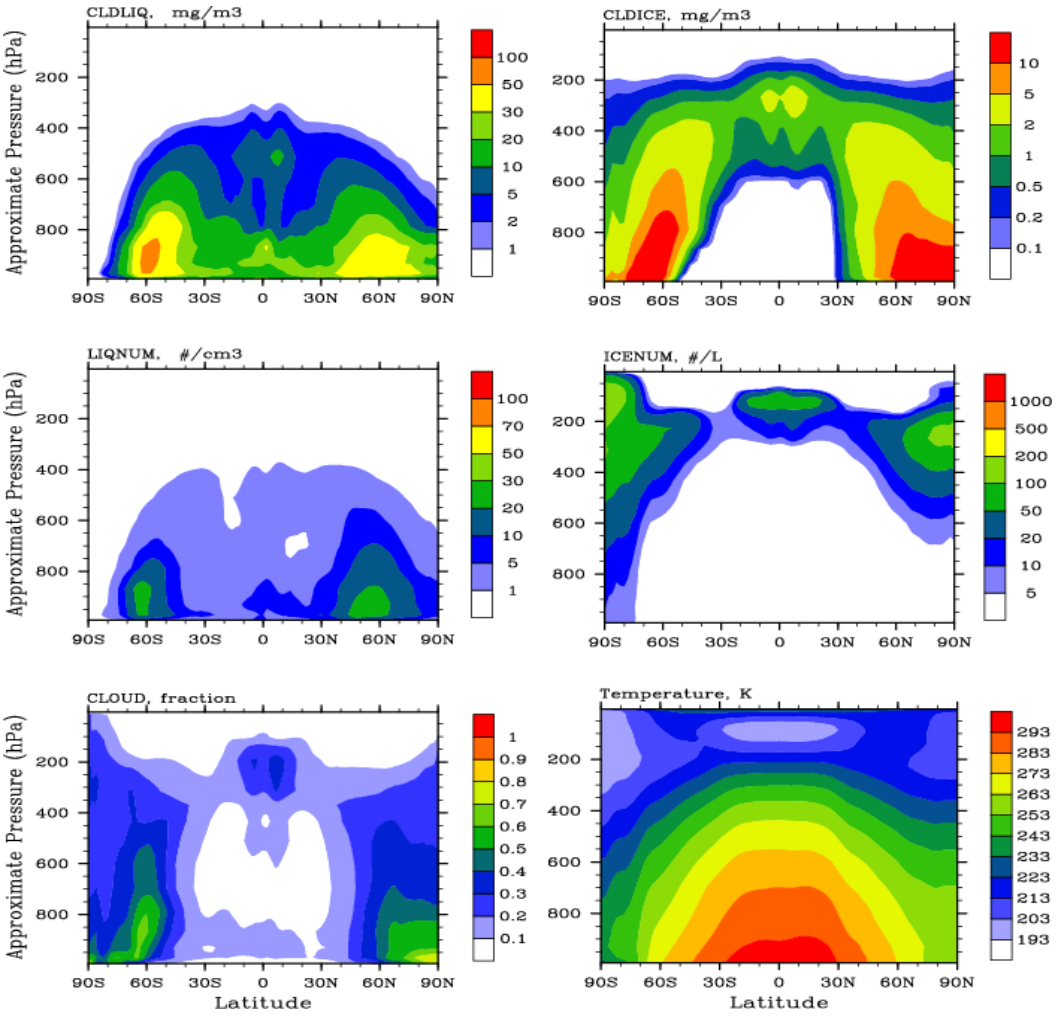

Figure 4.2: Annual zonal mean latitude versus pressure plots of grid-mean cloud liquid water content (CLDLIQ, mg/m^3), cloud ice water content (CLDICE, mg/m^3), cloud liquid droplet number (LIQNUM, #/cm^3), cloud ice crystal number (ICENUM, #/L), cloud fraction (CLOUD) and temperature (K).

Ice water content (IWC) in the upper troposphere is compared with that from the Microwave Limb Sounder (MLS) onboard the Aura Satellite (Wu et al., 2006) in Figure 4.3. The MLS ice water content data have a vertical resolution of ~ 3.5 km and a horizontal resolution of ~160 km for a single MLS measurement along an orbital track (Wu et al., 2006; 2009). The data used here for comparison are monthly means from September 2004 to August 2005. The model broadly captures the spatial and zonal distribution of ice water content in the upper troposphere, but it underestimates ice water

content in tropical regions by a factor of 2 to 4, which is also true in the standard CAM3 model (Li et al., 2005). The model ice water content is larger at the poles than in MLS data, a feature that is improved when heterogeneous IN are included in the model (see section 4.4.1). We notice that the ice water content simulated in LIU07 is larger in tropical regions than that simulated here and is in better agreement with MLS data, but the reasons for this are not known. The cirrus treatment in this study is different with that in LIU07 in many respects, such as different treatments of cloud growth and cloud decay as described above. In addition, we apply a mean vertical velocity rather than a PDF of vertical velocities, and anvil cloud fraction is added as one source term in the predicted total cloud fraction using Equation 4.14 in our treatment while in LIU07 the total cloud fraction is the sum of the diagnostic large scale cloud fraction and the anvil cloud fraction, which is the same treatment as that in the standard CAM3 (Boville et al., 2006). These differences make it difficult to attribute differences in the simulated ice water content between this study and LIU07 to any of the individual processes. Increasing the temperature variations in our treatment, as is done in Section 4.4.2, does not alleviate this problem.

Figure 4.4 shows annual average zonal mean latitude-pressure cross sections for the in-cloud ice crystal number concentration immediately after the initial ice nucleation, and that simulated from the prognostic ice crystal equation which also takes account of ice sublimation, gravitational settling, precipitation removal, and advection. Ice crystal number concentration from the initial nucleation of ice ranges from 0.5 to 5/cm^3, and slowly increases with decreasing temperature although at very low temperatures it decreases with decreasing temperature (Compare the temperatures in Figure 4.2 with

N_{i_homo} in Figure 4.4b). The decrease is caused by the low vertical velocity we used at low temperatures (section 4.2.2). In our treatment, mean vertical velocities linearly decrease from 23 cm/s at 238 K to 1.2 cm/s at 193 K. Based on the homogeneous freezing parameterization of Liu and Penner (2005), ice crystal number concentration from homogeneous freezing is then at its maximum at around 200 K, which explains why ice crystal number concentration decreases with decreasing temperature at very low temperature (lower than 200 K). After taking into account sublimation, gravitational settling, precipitation removal, and advection, the ice crystal number concentrations predicted from the prognostic ice crystal equation are lower by a factor of 2 to 5 compared to the initial concentrations predicted by ice nucleation, which points to the importance of including a prognostic ice crystal equation. As shown later in section 4.4, different freezing mechanisms lead to different ice crystal number concentrations in the upper troposphere.

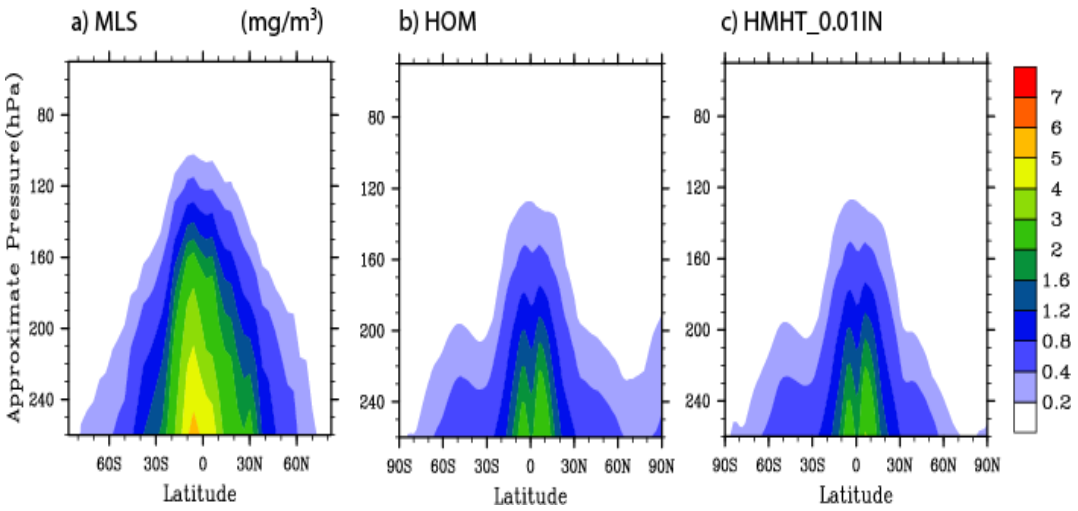

Figure 4.3: Annual zonal mean latitude versus pressure plots of (a) volume-averaged ice water content that measured by the Aura MLS instrument, (b) grid-averaged ice water content that predicted by HOM, and (c) that predicted by HMHT_0.01IN (mg/m^3).

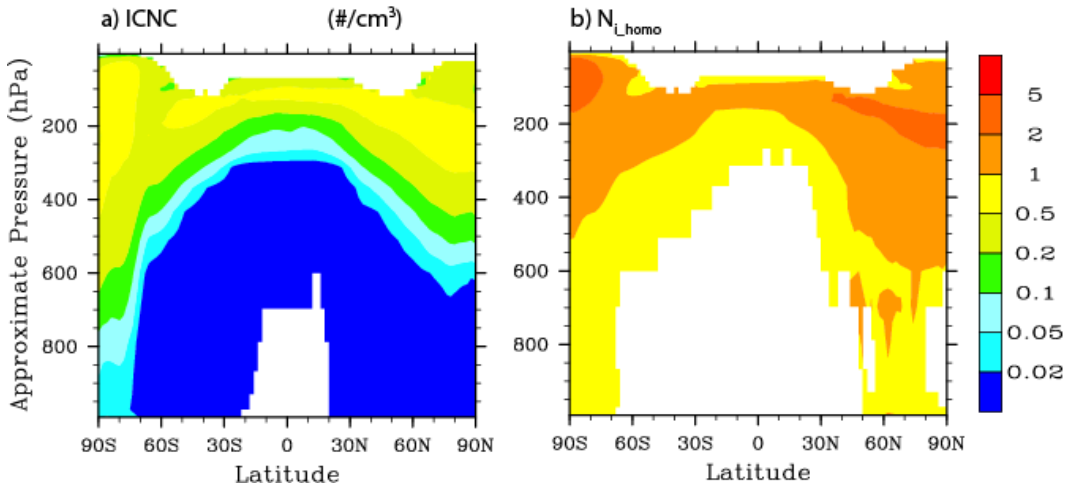

Figure 4.4: Annual zonal mean latitude versus pressure plots of (a) in-cloud ice crystal number concentration (#/cm^3) predicted by the prognostic ice crystal equation and (b) that calculated from the initial nucleation by the homogeneous freezing parameterization in the HOM case.

Table 4.4 compares the simulated ice crystal number concentration from the prognostic ice crystal equation in our model with those measured during the INCA campaign (Gayet et al., 2004). Ice crystal number concentrations were measured in middle latitude cirrus clouds at temperature -33°C and -60°C during the INCA campaign over Punta Arenas in the SH (Chile, in March/April) and over Prestwick in the NH (Scotland, in September/October). Most flight patterns during the campaign were designed to probe young cirrus clouds (Kärcher and Ström, 2003). The measured ice crystal number concentrations in the SH and NH have a median of 1.4 and 2.2 /cm^3, respectively (Gayet et al., 2004). Simulated mean ice crystal number concentrations from the prognostic ice crystal equation in the HOM case are 0.34 and 0.33 /cm^3 in the SH and NH, respectively, and are significantly lower than those observed during the INCA campaign. Lower ice crystal number concentrations in the model are not surprising since ice crystal number concentrations from the prognostic ice crystal equation account for removal processes such as gravitational settling, advection and coagulation, and therefore

represent both aged and young cirrus clouds, and since the INCA observations mainly represented young cirrus clouds. Ice crystal number concentrations immediately after the initial ice nucleation from homogeneous freezing (shown in the parenthesis for the HOM case in Table 4.4), which is more representative for young cirrus clouds, are 1.2 and 1.6 /cm^3 in the SH and NH, respectively, and are in much better agreement with the INCA observations.

Figure 4.5 shows in-cloud ice crystal number concentration (ICNC) and ice crystal effective radius (REI) versus temperature. Model results are sampled every six hours over six flight regions (Kiruna, Sweden in January and February; Hohn, Germany in November and December; Forli, Italy in Octorber; Mahe, Seychelles, in February and March; Darwin, Australia, in November; Aracabuta, Brazil in January and February) where the observations reported in Krämer et al. (2008) were collected (See Table 3 in Krämer et al. (2008) for the flight information). The median, 25% percentile, and 75% percentile are shown for each 1 K temperature bins. In-cloud ice crystal number concentrations in the HOM case increase with decreasing temperature (the median ice crystal number concentration is 0.08/cm^3 at 230K and is 0.13/cm^3 at 200 K), although vertical velocities used in our model decrease with decreasing temperature (19.1 cm/s at 230 K and 4.5 cm/s at 200 K). In Kramer et al. (2008) (Figure 9 in their paper), ice crystal number concentration increases with decreasing temperature, with a mean value ~0.2/cm^3 at 230 K and ~0.1/cm^3 at 200 K. The model results show that a decreasing vertical velocity with decreasing temperature as treated in our model is still not able to simulate decreasing ice crystal number concentration with decreasing temperature when only homogeneous freezing is included. Simulated ice crystal radius increases with

increasing temperature, which is consistent with the results reported in Krämer et al. (2008) (Figure 9 in their paper), although ice crystal radius increases faster with temperature than that in observations.

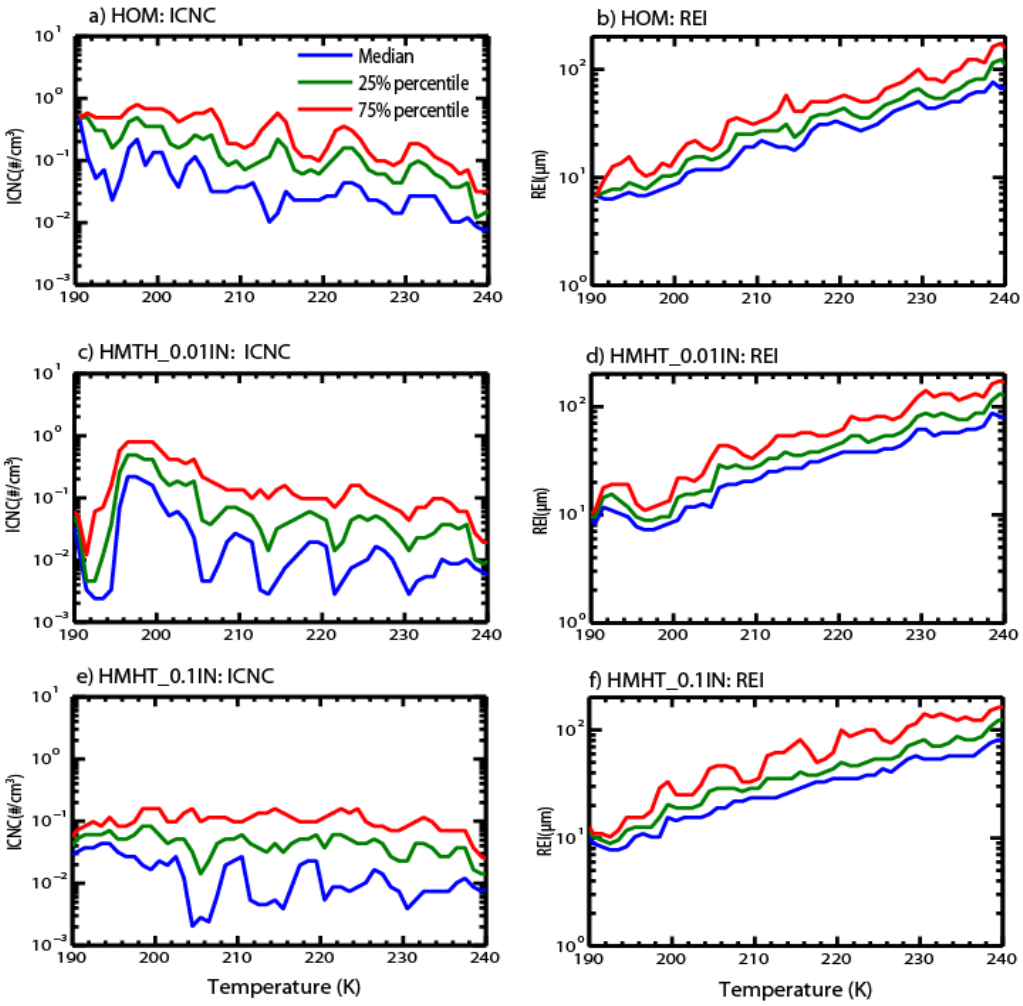

Figure 4.5: In-cloud ice crystal number concentration (ICNC, #/cm^3) and ice crystal effective radius (REI, μm) versus temperature. Model results are sampled every six hours over six flight regions (Kiruna, Sweden in January and February; Hohn, Germany in November and December; Forli, Italy in Octorber; Mahe, Seychelles, in February and March; Darwin, Australia, in November; Aracabuta, Brazil in January and February) where the observation reported in Krämer et al. (2008) were collected (See Table 3 in Krämer et al. (2008) for the flight information). The 50 percentile (green line), 25% percentile (blue line), and 75% percentile (red line) are shown for each 1 K temperature bins. The upper panel is for the HOM case; the middle panel is for the HMHT_0.01IN case; and the low panel is for the HMHT_0.1IN case.

Table 4.4. Comparison of measured ice crystal number concentration ('Obs') during the INCA campaign (Gayet et al., 2004) over the SH (Punta Arenas, Chile, in March/April) and over the NH (Prestwick, Scotland, in September/October) with those simulated from the prognostic ice crystal equations in the model. Median values from the observations are shown. For the model simulations, monthly mean results are used, and are averaged over 60°-50°S, 70°-85°W, from March to May in Chile, and over 50°-60°N, 10°W-5°E, from September to November in Scotland. Model results are restricted to pressure levels from 200 hpa to 300 hPa, and to temperatures from -35°C to -60°C.

	HOM	HMHT_ 0.01IN	HMHT_ 0.1IN	HMHT_ 1IN	HMHT_ 1.25dT	HMHT_ 0.75dT	Obs
Chile, SH	0.34 (1.16)[a]	0.32	0.05	0.28	0.43	0.21	1.45 (0.58-3.01)[b]
Scotland, NH	0.33 (1.60)[a]	0.06	0.11	0.58	0.22	0.02	2.23(0.84-4.74)[b]

[a]Numbers in parentheses are ice crystal number concentrations immediately after the initial homogeneous freezing.
[b]Numbers in parentheses represent 25 to 75 percentile.

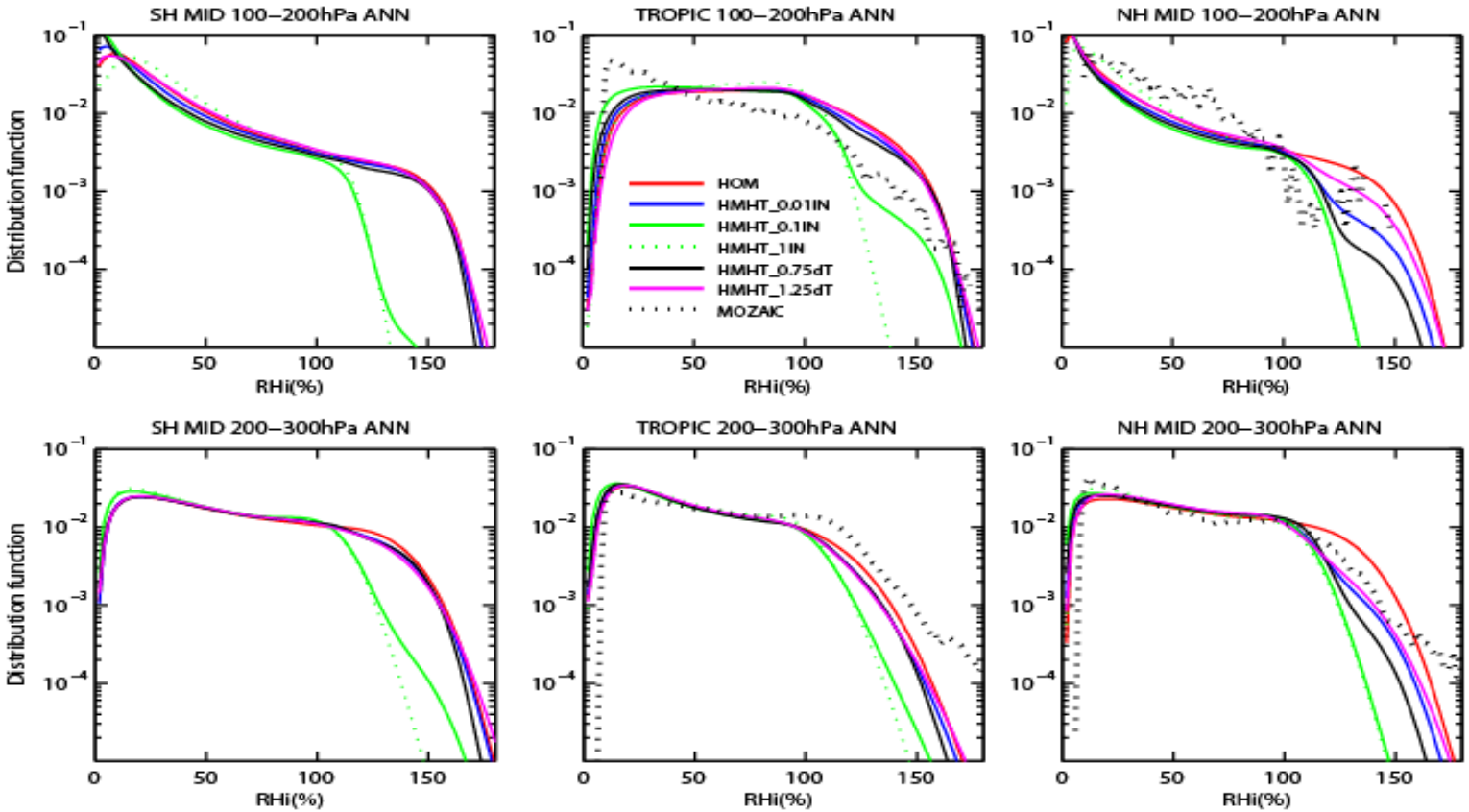

Figure 4.6: Frequency of occurrence of *RHi* in the SH middle latitudes (60ºS-30ºS) (SH MID, left panel), in the tropics (30ºS-30ºN) (TROPIC, middle panel), and the NH middle latitudes (30ºN-60ºN) (NH MID, right panel) at 100-200 hPa (upper panel) and at 200-300 hPa (lower panel) from all simulations listed in Table 4.1. Observations from MOZAIC data in the tropics and in the NH middle latitudes are also shown.

Figure 4.6 shows the simulated PDF of *RHi* outside of cirrus clouds within two layers (100-200 hPa, and 200-300 hPa) and in three regions (the SH middle latitudes: 60ºS-30ºS; the tropics: 30ºS-30ºN; and the NH middle latitudes: 30ºN-60ºN). One year of model results are sampled every six hours. The PDF of the clear-sky *RHi* is calculated based on the clear-sky mean *RHi* and the prescribed temperature perturbations used in the model (section 4.2.2), weighted by the clear sky fraction (1-*a*). Also shown in Figure 4.6 is the PDF of *RHi* from the Measurement of Ozone and Water Vapor by Airbus In-service Aircraft (MOZAIC) campaign (Spichtinger et al., 2004) in two regions: the NH middle latitudes and the tropics. MOZAIC data sampled both clear sky and cloudy sky conditions. The reason why we use *RHi* in clear sky conditions instead of *RHi* in both clear sky and cloudy sky conditions in the simulations comes from the following two factors. First, the model does not treat subgrid-scale supersaturation under cloudy sky conditions. As we mentioned in section 4.2.2, in-cloud specific humidity is assumed to have a uniform distribution, and so no subgrid-scale supersaturation is available under cloudy sky conditions. Moreover, the large time step used in the GCM makes the saturation ratio under cloudy sky conditions very close to 1. So if we account for *RHi* under cloudy sky conditions in the PDF of *RHi*, this will bias the distribution of *RHi* towards 100%. Second,the subgrid-scale *RHi* under clear sky conditions is calculated based on the clear-sky mean *RHi* and the prescribed temperature perturbations using Equation 4.A2, and *RHi* are sampled across the whole PDF spectrum using Equation 4.A2, regardless of whether the value of *RHi* exceeds the heterogeneous freezing or homogeneous freezing threshold. By doing this, the in-cloud conditions sampled in the MOZAIC data are also partly taken account in the model data.

The homogeneous freezing-only case (HOM) reproduces the shape of the PDF of *RHi* from MOZAIC data well. *RHi* in the range from 20-100% occurs with large frequency, and the frequency has an almost exponential decay from *RHi*=100% to around *RHi*=150%, a feature that is consistent with the MOZAIC data and is believed to be mainly caused by temperature variations in combination with heterogenous and homogeneous freezing (Kärcher and Haag, 2004). Beyond 150%, the HOM case simulates a faster decay of *RHi* than that in the MOZAIC data. This fast decay in the HOM case is caused by homogeneous ice freezing that has a threshold *RHi* near 150%.

Figure 4.7 shows the geographical distribution of the frequency of occurrence of ice supersaturation in clear sky regions in the HOM case and in the Microwave Limb Sounder (MLS) satellite data (Spichtinger et al., 2003) at pressure levels 147 hPa (139 hPa is shown for the model) and 215 hPa (192 hPa is shown for the model). The frequency of occurrence of ice supersaturation for a given grid point is calculated as the number of samples with *RHi* > 100% divided by the total number of samples for a given period (one year in the model, September 1991 to June 1997 for MLS data), weighted by the clear sky fraction (1-*a*). In contrast with the comparison to the MOZAIC data, the mean clear-sky *RHi* instead of the subgrid-scale *RHi* in the model is used to calculate the ice supersaturation frequency because of the large field of view of the MLS (about 100×200 km^2 perpendicular and parallel to the line of sight and 3 km vertically). At the 147 hPa level, observed ice supersaturation occurs most frequently in the tropics between 20ºS and 20ºN and over Antarctica. Compared with the MLS data, the model with homogeneous freezing only (HOM) reproduces the observations well in terms of the spatial distribution, but gives a higher ice supersaturation frequency than in the MLS data.

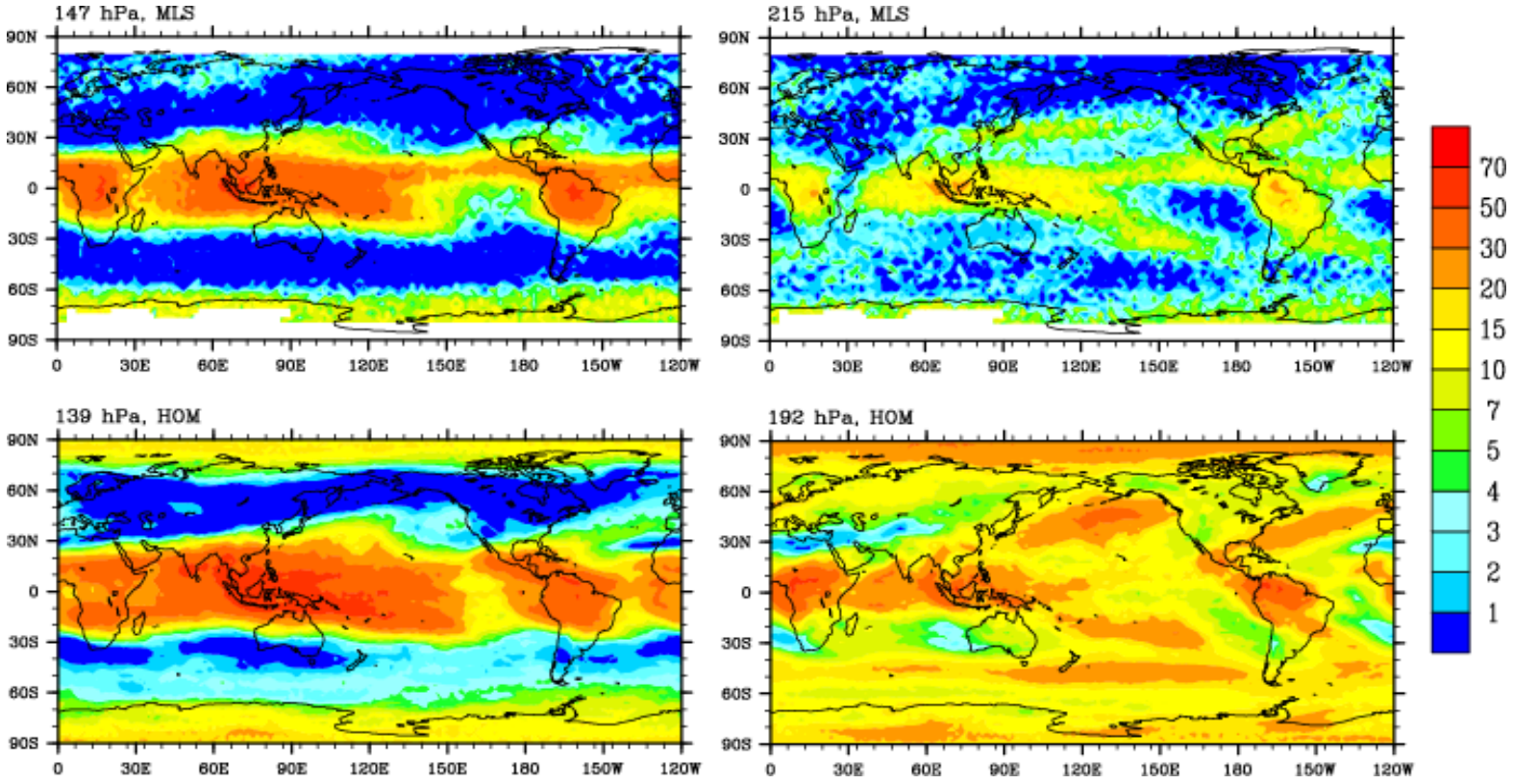

Figure 4.7: Annual-average frequency of occurrence of ice supersaturation from MLS data (upper panel) and the case of HOM (lower panel) at 147 hPa (139 hPa for model) (left panel) and 215 hPa (192 hPa for model) (lower panel).

At the 215 hPa level, the observed ice supersaturation occurs most frequently in the same regions as at the 149 hPa level, although the ice supersaturation region also extends toward high latitudes at 215 hPa, mainly over the storm track regions in both hemispheres. The model produces a similar spatial distribution as that in the MLS observations but with an even larger overestimation than that at 147 hPa, and the ice supersaturation region extends even more towards high latitudes in the model. For example, the model simulates a high frequency of ice supersaturation occurrence in the SH storm track (around 45ºS), which is not present in the MLS observations. As pointed out by Spichtinger et al. (2003), there are considerable data gaps in the middle latitudes of the summer hemispheres in the MLS data. This may prevent us from drawing further conclusions about whether the simulated ice supersaturation regions over the storm track at the 215 hPa level is reasonable or not. To summarize the model performance regionally, averaged supersaturation frequencies in five regions (global, Northern Hemisphere, tropics, Southern Hemisphere, and Antarctic) in both the MLS data and our model are shown in Figure 4.8. This confirms that geographical variations in supersaturation frequency are broadly captured, but with a significant overestimation, especially at 215 hPa, a feature that is improved when heterogeneous IN are included (section 4.4.1).

The simulated supersaturation frequencies also depend on the mesoscale temperature perturbations used in the model. A large temperature perturbation produces more ice, which decreases the clear sky relative humidity and decreases the supersaturation frequency simulated in the model. A larger temperature perturbation, then, would improve the comparison with MLS data, especially at l39 hPa, since quite small

temperature perturbations were used due to the low temperatures there (section 4.2.2). Larger mesoscale temperature perturbations at higher altitude is also consistent with gravity wave theory (Fritts and Alexander, 2003) and observations (Gary et al., 2006) although larger vertical velocities resulting from larger temperature perturbations by using Equation 4.2 would produce too many ice crystals that would lead to unrealistically high water vapor in the stratosphere, as discussed in section 4.2.2.

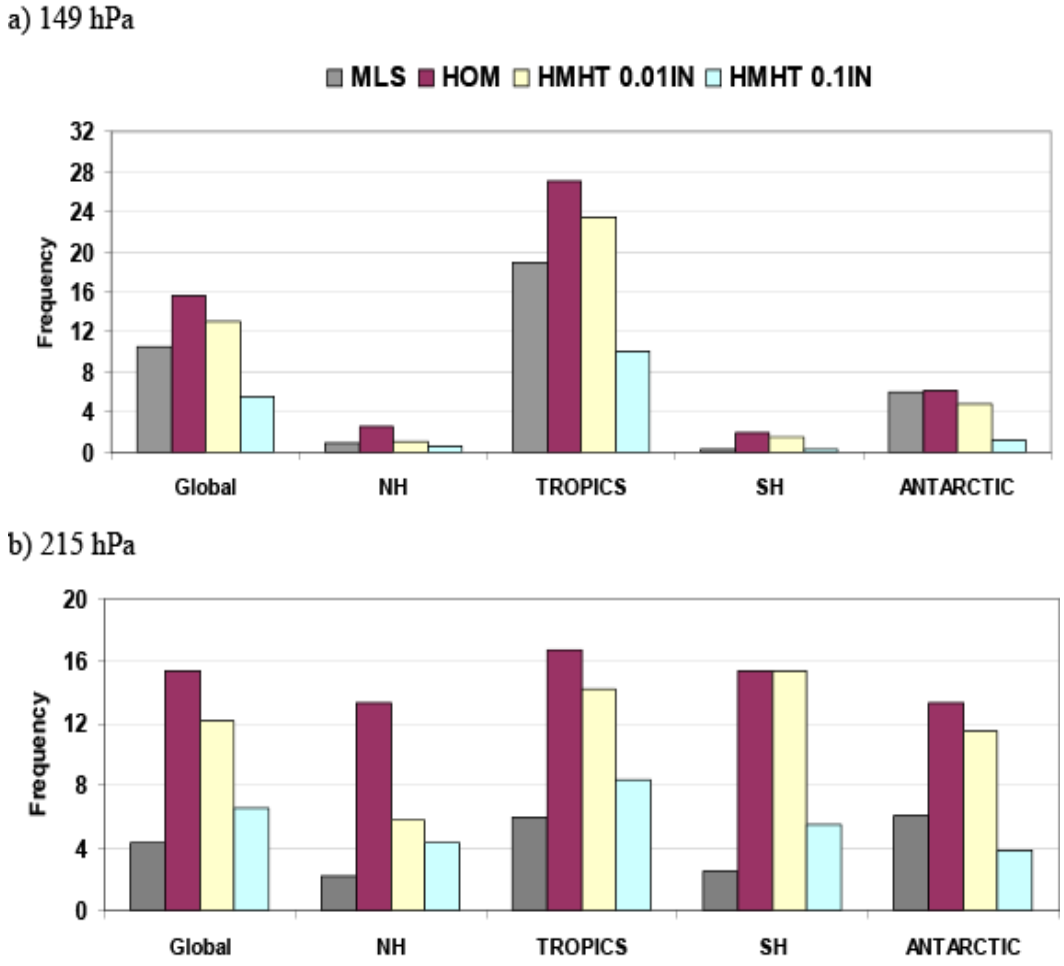

Figure 4.8: Regionally-averaged frequency of occurrence of ice supersaturation from MLS data and from three simulations: HOM, HMHT_0.01IN, and HMHT_0.1IN, (a) at 149 hPa (139 hPa for model) and at (b)215 hpa (192 hPa for model) over five regions: Global (80ºS-80ºN), NH(North Hemisphere, 30ºN-80ºN), TROPICS (30ºN-30ºS), SH(Southern Hemisphere, 55ºS-30ºS), and Antarctic (80ºS-55ºS).

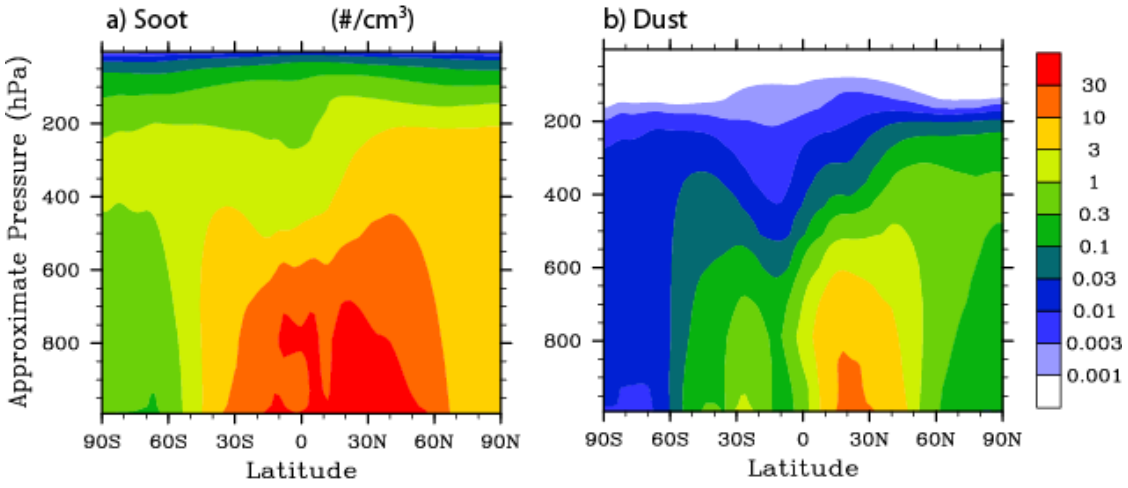

Figure 4.9: Annual zonal mean latitude versus pressure plots of (a) soot and (b) dust number concentration (#/cm^3).

4.4. Effects of heterogeneous IN and mesoscale temperature perturbations

4.4.1 Effects of heterogeneous IN

The effects of heterogeneous IN on cirrus cloud properties are studied using the three sensitivity tests HMHT_0.01IN, HMHT_0.1IN, and HMHT_1IN, where IN concentrations are assumed to be 1%, 10%, and 100% of the total number concentration of soot and dust particles, respectively, as described in Table 4.1. The annual average zonal mean distributions of dust and soot number concentrations are shown in Figure 4.9. Soot particles have a high concentration in the NH upper troposphere (100 hPa to 400 hPa) with a range of 1-10/cm^3, which is caused by anthropogenic emissions. Soot number concentrations in the upper troposphere decrease with latitudes from north to south. In the upper troposphere of the SH, their concentrations can range from 0.3 to 1/cm^3. Dust particles show a much lower number concentration and a stronger gradient with altitude from the surface to the upper troposphere than soot particles because of their larger sizes

and lack of local sources. The number concentrations of dust particles range from 0.001 to 1 /cm^3 in the NH upper troposphere, and range from 0.001 to 0.03/cm^3 in the SH upper troposphere.

4.4.1.1 Effects on humidity fields

We first examine how these heterogeneous IN affect the PDF of *RHi* in Figure 4.6. Heterogeneous IN decrease the frequency of occurrence of very high supersaturation due to the lower required threshold *RHi* which is assumed to be between 120-130% in the parameterization of Liu and Penner (2005). When only 1% of soot and dust particles act as IN in the HMHT_0.01IN case, heterogeneous freezing has little effect in the tropics and in the SH because the IN concentration is too low in these regions to affect homogeneous freezing. However, in the NH middle latitudes, the IN concentration is high enough to meet the critical IN concentration from Gierens (2003), and heterogeneous freezing is allowed to occur. This decreases the frequency of occurrence of very high supersaturation. The simulated hemispheric contrast in the PDF of the *RHi* in this case is consistent with that observed in the INCA field campaign (Haag et al., 2003). When the IN concentration increases by a factor of 10 in the HMHT_0.1IN case, heterogeneous freezing occurs more frequently. In the middle latitudes of the NH, heterogeneous freezing shuts off homogeneous freezing, as evidenced by the very low frequency of *RHi* values higher than 150%. In the middle latitudes of the SH, homogeneous freezing still occurs but with a much lower frequency than that in the HMHT_0.01IN case. When 100% of soot and dust particles act as heterogeneous IN in the case of HMHT_1IN, homogeneous freezing is shut down almost everywhere because of the very high concentration of IN.

The effects of heterogeneous IN on relative humidity fields can also be seen in the simulated regionally averaged supersaturation frequency at 139 hPa and 192 hPa in Figure 4.8. When 1% of dust and soot particles act as heterogeneous IN (HMHT_0.01IN), simulated supersaturation frequencies decrease, with larger decreases over the NH than the SH, and larger decreases at 215 hPa than 147 hPa because of higher IN concentrations there. For example, at 215 hPa, the simulated supersaturation frequencies in the HOM case and the HMHT_0.01IN case are almost the same in the SH middle latitudes, but decrease from 13% in the HOM case to 5.83% in the HMHT_0.01IN case in the NH middle latitudes. When heterogeneous IN concentrations increase by a factor of 10 in the HMHT_0.1IN case, supersaturation frequencies in all regions and at both 147 hPa and 215 hPa decrease significantly. These model results show that ice microphysics is important for simulating supersaturation frequencies in the upper troposphere. Including heterogeneous IN decreases simulated supersaturation frequencies in the model, and gives a better comparison with the frequencies of supersaturation from the MLS data at 215 hPa. But this conclusion has to be treated cautiously given the uncertainties associated with the MLS retrievals. Read et al. (2001) showed that the global-averaged accuracy of *RHi* from the MLS retrievals are 22% and 23% *RHi* at 147 hPa and 215 hPa, repectively.

4.4.1.2 Effects on cloud fields

Since heterogeneous freezing requires lower *RHi*, we expect that adding heterogeneous IN will lead to cloud fraction increases, which is indeed what we find in the model (Table 4.2). Total cloud fraction increases from 66.4% in the HOM case to 67.3% in the HMHT_0.01IN case, and further increases to 68.40% in the HMHT_0.1IN

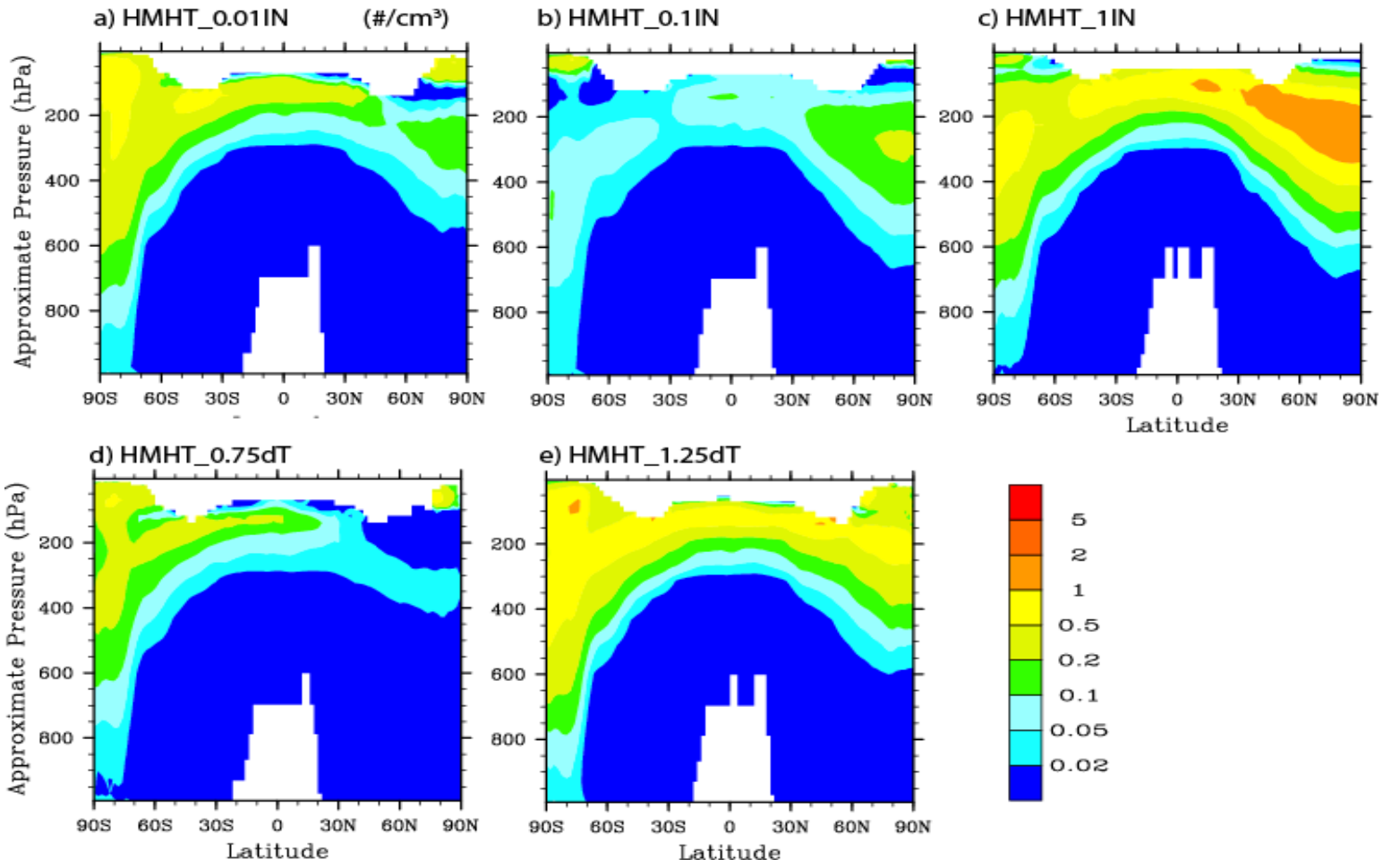

Figure 4.10: Annual zonal mean latitude versus pressure plots of ice crystal number concentration in all five cases that allow the competition between homogeneous freezing and heterogeneous freezing. All cases are described in Table 4.1.

case. Since heterogeneous freezing already dominates in the HMHT_0.1IN case, further increases in the number of heterogeneous IN has little or no effect on cloud fraction.

Heterogeneous IN can significantly affect the simulated ice crystal number concentration, as evident in Table 4.4 and Figure 4.10. Figure 4.10 shows simulated annual latitude-pressure cross sections of in-cloud ice crystal number concentration in all cases where the competition between homogeneous freezing and heterogeneous freezing is allowed. The results show that in an environment dominated by homogeneous freezing, the addition of heterogeneous IN decreases the ice crystal number concentration. In both the HOM case and the HMHT_0.01IN case homogeneous freezing dominates, as seen in the PDF of *RHi* (Figure 4.6). This explains why we see a 27% decrease in column-integrated ice crystal number concentration from the HOM case ($0.022\times10^{10}/m^2$) to the HMHT_0.01IN case ($0.016\times10^{10}/m^2$), and a 47% decrease from the HMHT_0.01IN case ($0.016\times10^{10}/m^2$) to the HMHT_0.1IN case ($0.0085\times10^{10}/m^2$) (Table 4.2). Regionally, when 1% of soot and dust particles are added as heterogeneous IN to the HOM case (compare Figure 4.10a and Figure 4.4b; Table 4.4), the frequency of homogeneous freezing in the NH decreases and therefore the ice crystal number concentration decreases, which results in a higher ice crystal number concentration in the SH than in the NH for HMHT_0.01IN (also see Table 4.4). When IN concentrations are increased by a factor of 10 from the HMHT_0.01IN to the HMHT_0.1IN case (compare Figure 4.10b and Figure 4.10a), the frequency of homogeneous freezing decreases significantly everywhere and heterogeneous freezing dominates (Figure 4.6). Then a higher ice crystal number concentration is simulated in the NH than in the SH in HMHT_0.1IN (Figure 4.10b and Table 4.4) because the heterogeneous IN concentration is higher in the NH (Figure 4.9).

When the environment is dominated by heterogeneous freezing, adding heterogeneous IN increases ice crystal number concentrations. Since heterogeneous freezing dominates in the HMHT_0.1IN case, there is a significant increase in ice crystal number concentration in the HMHT_1IN case compared with that in HMHT_0.1IN (Figure 4.10c and Figure 4.10b; Table 4.4). Column-integrated ice crystal concentration is increased by a factor of 5 from $0.0085\times10^{10}/m^2$ in HMHT_0.1IN to $0.051\times10^{10}/m^2$ in HMHT_1IN (Table 4.2). Because of the very high IN concentration in this case (Figure 4.8), homogeneous freezing rarely occurs, and ice crystal number concentration is almost completely determined by heterogeneous freezing. Our results show that the background ice freezing mode determines the sign of the change in ice crystal number concentration from the addition of heterogeneous IN, which is consistent with previous studies (e.g., Hendricks et al., 2005; Penner et al., 2009).

When 1% of soot and dust particles are added as heterogeneous IN to the HOM case, ice crystal number concentration decreases with decreasing temperature at low temperatures (<195K) (see Figure 4.5c), a feature that is consistent with Krämer et al. (2008), although ice crystal number concentration still increase as they do in the homogeneous case with increasing temperature at higher temperatures. At low temperatures, because of the low vertical velocities and low mesoscale temperature perturbations, heterogeneous IN decreases the frequency of homogeneous freezing significantly, and decreases ice crystal number concentrations, while at higher temperatures (~200K), because of the relatively higher vertical velocities and mesocale temperature perturbations, heterogeneous IN have much smaller effects. When 10% of

soot and dust particles are added as heterogeneous IN (Figure 4.5e), the simulated ice crystal number concentration is less dependent on temperature.

Changes in the ice crystal number concentrations from the addition of heterogeneous IN affect ice crystal radius. Larger ice crystal number concentrations lead to smaller ice crystal radii. The HMHT_1IN case has the largest ice number concentration, which leads to the smallest ice crystal radii at the tops of cirrus clouds (34.56 μm in Table 4.2). One exception is the HMHT_0.1IN case. Although this case leads to the smallest column-integrated ice number concentration, it has a cloud top ice crystal radius of 42.6 μm which is slightly larger than that in HMHT_0.01IN (43.6 μm). This can be explained by regional differences between HMHT_0.01IN and HMHT_0.1IN. Although on average the HMHT_0.1IN case has smaller ice crystal number concentrations than does HMHT_0.01IN, it has larger ice crystal number concentration at the highest levels in the tropics and in the NH, which leads to lightly smaller ice crystal radii at the tops of cirrus clouds (compare Figure 4.10 b and Figure 4.10a).

Since ice crystal radius determines the settling velocity of ice crystals, and since gravitational settling is a very important removal mechanism for cirrus clouds in the upper troposphere, changes in ice crystal radii lead to changes in cirrus cloud lifetimes and ice water content in the upper troposphere. One example is shown in Figure 4.3. When ice crystal number concentrations decrease from the HOM case to the HMHT_0.01IN case (compare Figure 4.3 c and Figure 4.3b), ice crystal radius increases, which increases the gravitational settling and decreases ice water content in the upper troposphere. The excessive ice water simulated over the Arctic in HOM is decreased in the HMHT_0.01IN case, which improves the comparison with MLS observations.

The change in ice crystal size also affects liquid clouds by moistening lower levels in the atmosphere (e.g., Wu, 2002; Grabowski, 2000; Sanderson et al., 2008). Simulated liquid water path and low level cloud fraction are always positively correlated with column-integrated ice crystal number concentration in all our simulations (Table 4.2). For example, when ice crystal number concentration increases from the HMHT_0.1IN case to the HMHT_1IN case, the liquid water path increases by 9% from 75.3 g/m^2 to 82.0 g/m^2. More ice crystals lead to smaller ice crystal radii, which lead to longer cloud lifetimes in the atmosphere. The longer cloud lifetimes lead to more evaporation from ice crystal and more moisture is transported to the lower atmosphere. This increases low level cloud fraction and the liquid water path. Our results here are consistent with those of Wu (2002) and Grabowski (2000). Both of these studies found that a model with low ice crystals falling and evaporating would produce a warm, cloudy, moist lower troposphere with less precipitation. This change in liquid clouds in the lower troposphere can have important implications for the simulated net cloud forcing as we show below.

4.4.1.3 Effects on radiative fluxes

As shown above, heterogeneous IN affect both high cirrus clouds and lower level liquid clouds through their effects on ice crystal number concentration. We will show below that changes in both high cirrus clouds and lower level liquid clouds determine the effects of heterogeneous IN on the net cloud radiative forcing.

Both changes in longwave and shortwave cloud forcing closely follow changes in simulated ice crystal number concentrations (Tables 4.2 and 4.3). Larger ice crystal number concentrations lead to smaller ice crystal radii and more ice water content in the upper troposphere, and a larger liquid water path in the lower level atmosphere (section

4.4.1.2). All these changes lead to a larger longwave cloud forcing (warming) and larger shortwave cloud forcing (cooling). The HMHT_0.1IN case simulates the smallest longwave cloud forcing (26.22 W/m^2) and the smallest shortwave cloud forcing (50.65 W/m^2) because it has the smallest ice crystal number concentration. The opposite is true for the HMHT_1IN case, which simulates the largest longwave and shortwave cloud forcing.

The simulated net cloud forcing is more complicated. Although both longwave and shortwave cloud forcing are affected by changes in both high level cirrus clouds and lower level liquid clouds, changes in high level cirrus clouds have a larger effect on longwave cloud forcing and changes in low level liquid clouds have a larger effect on shortwave cloud forcing (e.g., Chen et al., 2000). So changes in the net cloud forcing depend on whether changes in high cirrus clouds or changes in low level liquid clouds dominate. When column-integrated ice crystal number concentrations decrease by 27% from the HOM case to the HMHT_0.01IN case, the net cloud forcing changes from -24.61 W/m^2 to -24.75 W/m^2 so that a net cooling of 0.14 W/m^2 is simulated, which indicates that the cooling is caused by increases in ice crystal radius and decreases in ice water in high cirrus clouds which dominate the effects on liquid water clouds. But when columned-integrated ice crystal number concentration decreases further by 47% from the HMHT_0.01IN case to the HMHT_0.1IN case, a net warming of 0.32 W/m^2 is simulated, which indicates that the warming is caused by decreases in low level liquid clouds that dominate the effects on cirrus clouds. Compared with the HMHT_0.01IN case, the HMHT_0.1IN case simulates a 1.5% decrease in liquid water path (75.26 vs. 76.44 g/m^2),

which is due to the moistening effects of ice crystals on the low level atmosphere, as discussed in section 4.4.1.2.

The moistening effect of ice crystals on the low level atmosphere is caused by ice crystal gravitational settling, which has long been recognized (e.g., Wu, 2002; Grabowski, 2000; Sanderson et al., 2008). Our results suggest that the sign of the change in the net cloud forcing caused by heterogeneous IN is determined not only by the ice freezing mode in the background atmosphere, but also by the change in liquid clouds from this moistening effect. The effects of liquid cloud changes caused by the moistening effect tend to counteract the effects of high level cirrus cloud changes. So the change in the net cloud forcing is relatively less sensitive to changes in ice crystal number concentrations caused by heterogeneous IN or even by changes in mesoscale dynamics, as will be discussed in next section. The net cloud forcing in the four simulations discussed here ranges from -24.30 W/m^2 to -24.75 W/m^2, with a maximum change of 0.45 W/m^2, which is a small change considering the fact that a two order of magnitude change in IN concentrations was imposed.

Although the net change in cloud forcing is relatively small and the sign of the cloud forcing change depends on the competition between changes in high cirrus clouds and changes in low level liquid clouds, the change in the net radiative fluxes (FNT) at the TOA is large, with a maximum change of 2.2 W/m^2 between the four cases discussed here. This change closely follows the changes in ice crystal number concentration, as shown in Table 4.2, i.e., more ice crystals leads to more warming at the TOA. The large change in net radiative fluxes at the TOA mainly comes from the change in clear sky long wave radiation due to changes in water vapor in the atmosphere, especially in the upper

troposphere. More ice crystals lead to smaller ice crystal radius, which leads to longer cloud lifetimes and therefore more water vapor in the upper troposphere. Also, heating from more ice crystals warms the upper troposphere and leads to higher temperatures and to more water vapor in both the upper troposphere and stratosphere. The greenhouse effect of water vapor depends more on the relative change and less on the absolute change in water vapor (Raval and Ramanathan, 1989). Although the absolute change in the water vapor concentration in the upper troposphere is small between the different cases, the relative change can be large. For example, the integrated water vapor mass from 100 hPa to 300 hPa decreases by 12% from the HOM case to the HMHT_0.1IN case, which contributes most to the clear sky longwave cooling of 1 W/m^2. This overrides the warming in the net cloud forcing and leads to a net cooling of 0.92 W/m^2 at the TOA. Stratospheric water vapor also decreases significantly from the HOM case to the HMHT_0.1IN case (~35%), but results from a 1D radiative transfer model calculation with a typical tropical profile in winter from the GCM show that the change in stratospheric water vapor has little effect on the clear sky TOA longwave radiative flux (i.e., removal of 35% of the stratospheric water vapor had a similar TOA longwave flux as that with the full profile) though the change in stratospheric water vapor can have important effects on the clear sky radiative fluxes at the tropopause, which is consistent with Forster and Shine (2002). The 1 D radiative transfer calculation showed that a 35% decrease in the stratospheric water vapor leads to a cooling of 0.70 W/m^2 at the tropopause.

In summary, changes in ice crystal number concentrations, caused by either homogeneous freezing or heterogeneous freezing, change the TOA radiative fluxes

through three effects: net changes dominated by the change in the longwave cloud radiation caused by changes in high level cirrus clouds, net changes dominated by the changes in shortwave cloud radiation caused by changes in low level liquid clouds, and changes in the clear sky long wave radiation caused by changes in water vapor in the upper troposphere. The first and the third effects act in the same direction, but the second effect acts in the opposite direction. Due to the cancellation of the first and second effects, the net change in cloud forcing is less sensitive to changes in ice crystal number concentration and the net flux change at the TOA is mainly controlled by the third effect in this study.

4.4.2 Effects of mesoscale temperature perturbations

The effects of mesoscale temperature perturbations on simulated cirrus cloud properties are examined by using two additional sensitivity tests (HMHT_0.75dT and HMHT_1.25dT). These two cases have the same IN concentration as in the HMHT_0.01IN case where 1% of the soot and dust particles act as heterogeneous IN, but here the temperature perturbation decreases or increases by 25%.

A 25% higher temperature perturbation in the HMHT_1.25dT case leads to a 25% higher cooling rate and vertical velocity since these latter two parameters are proportional to the temperature perturbation in our treatment (see Equation 4.4 in section 4.2.2). Higher cooling rates and vertical velocities limit the influence of heterogeneous IN, and lead to more homogeneous freezing, as seen in the simulated PDF of *RHi* in the NH middle latitudes at both 100-200 hPa and 200-300 hPa (Figure 4.6), and therefore lead to higher frequencies of *RHi* > 150% than in the HMHT_0.01IN case. The opposite is true when the temperature perturbation is decreased by 25% in the HMHT_0.75dT case,

which increases the influence of heterogeneous IN and leads to less homogeneous freezing (Figure 4.6).

Simulated ice crystal number concentrations in HMHT_1.25dT are higher than in HMHT_0.01IN (compare Figure 4.10a and e; Table 4.4). Two factors contribute to high ice crystal concentrations in this case. One is the high frequency of occurrence of homogeneous freezing, as discussed above. The second is the higher cooling rate, which leads to higher ice crystal numbers generated from homogeneous freezing. Column-integrated ice crystal number concentration increases by 50% from $0.016\times10^{10}/m^2$ in the HMHT_0.01IN case to $0.024\times10^{10}/m^2$ in the HMHT_1.25dT case. The opposite is true for the HMHT_0.75dT case (compare Figure 4.10a and d; Table 4.4). Homogeneous freezing occurs less often so that the simulated column integrated ice crystal number concentration decreases by 50% from $0.016\times10^{10}/m^2$ in the HMHT_0.01IN case to $0.0089\times10^{10}/m^2$ in the HMHT_0.75dT case.

Simulated changes in radiative fluxes depend on changes in ice crystal number concentration, as discussed in section 4.4.1.3. A net warming of 0.46 W/m^2 in the cloud forcing is simulated in going from the HMHT_0.75dT case to the HMHT_1.25dT case, but this only contributes about one third to the increase in the simulated net TOA flux difference, which is 1.27 W/m^2. The remaining two thirds of the increase comes from the greenhouse effect of increased water vapor in the upper troposphere from the decreased crystal size, which results from an increase in the ice crystal number concentration.

The magnitude of simulated changes in net cloud forcing and net TOA fluxes from different mesoscale temperature perturbations are comparable to those simulated from different heterogeneous IN concentrations (section 4.4.1.3). For example, a 25% decrease

in the temperature perturbation from the HMHT_0.01IN case to the HMHT_0.75dT case leads to a net cooling of 0.22 W/m^2 in the cloud forcing and a net TOA cooling of 0.54 W/m^2, while a factor of 10 increase in the heterogeneous IN concentration from the HMHT_0.01IN case to the HMHT_0.1IN case leads to a net warming 0.32 W/m^2 in the cloud forcing and a net TOA cooling of 0.43 W/m^2. This points to the importance of mesoscale dynamics and subgrid scale variations in studying aerosol indirect effects on cirrus clouds (Haag and Kärcher, 2004; Penner et al., 2009).

4.5. Conclusions and discussion

In this study, the statistical cirrus cloud scheme presented in KB08 is implemented in the NCAR CAM3 atmospheric circulation model component of the coupled IMPACT/CAM model. This cirrus cloud scheme has a subgrid scale feature for total water in both clear sky and cloudy sky, and has a consistent treatment of ice freezing and cloud fraction. The coupled model with the new cirrus cloud scheme is evaluated by comparing model results with observations, and the effects of heterogeneous IN and mesoscale temperature perturbations are examined using sensitivity tests.

The simulated model fields, including the liquid water path, ice water path, short wave cloud forcing, long wave cloud forcing, cloud fraction, and precipitation are in reasonable agreement with observations. The direct conversion from liquid water to ice water in mixed-phase clouds decreases liquid water path significantly compared to the standard CAM3, and the resulting liquid water path in different cases ranges from 75 to 82 g/m^2, which agrees better with observations than that simulated by the standard CAM3. The new cirrus cloud scheme simulates significantly smaller high cloud fractions than in LIU07, where cloud fraction was diagnosed based on relative humidity. The simulated

total cloud fraction ranges from 66.4% to 68.5% in all cases, and agrees well with observations. The simulated ice water content in the homogeneous freezing only case (HOM) broadly captures the spatial and zonal distribution of ice water content in the upper troposphere in the MLS data, but it underestimates ice water content in the tropics by a factor of 2 to 4. Ice water simulated in this case also spreads more toward the poles than in the MLS data, a feature that is improved when 1% of soot and dust particles are added as heterogeneous IN.

When only homogeneous freezing is included in the model, the simulated PDF of *RHi* outside of cirrus clouds has an exponential decay from 100% *RHi* to 150% *RHi* which agrees with MOZAIC field data and with a faster decay beyond 150% which is due to homogeneous freezing above 150% *RHi.* Including heterogeneous IN can change the PDF of the *RHi* significantly. When 1% of soot and dust particles act as heterogeneous IN with a low threshold freezing humidity of about 120-130% *RHi*, the frequency of occurrence of very high *RHi* at 200-300 hPa in the NH middle latitudes decreases, but there is little effect in the SH and tropics, and at high altitudes. The simulated hemispheric contrast in the PDF of the *RHi* in this case is consistent with that observed in the INCA field campaign (Haag et al., 2003). When heterogeneous IN concentrations are increased by a factor of 10, the frequency of high *RHi* decreases significantly in both hemispheres, which is not supported by the MOZAIC data.

The simulated supersaturation frequency at 139 hPa and 192 hPa agrees well with satellite observations in terms of its spatial distribution, but the model overestimates the magnitude of supersaturation frequency when only homogeneous freezing is included, especially at 192 hPa. Including heterogeneous IN in the model decreases simulated

supersaturation frequency and improves the comparison with satellite observations at 192 hPa, which supports the notion that heterogeneous freezing plays a role in ice freezing.

Simulated ice crystal number concentrations from the prognostic ice crystal equation are lower than those immediately after initial ice nucleation by a factor of 2-5, which points to the importance of having a prognostic ice crystal equation in the model. Ice crystal number concentrations immediately after the initial ice nucleation from homogeneous freezing are comparable with those from the INCA observations, which represent young clouds that have not undergone aging.

Heterogeneous IN affect cirrus cloud properties significantly, and their exact effects depend on the background freezing modes. In an atmosphere dominated by homogeneous freezing, as is the case in HOM and HMHT_0.01IN, adding heterogeneous IN decreases ice crystal concentrations and increases cirrus cloud fraction. This explains the 27% decrease in simulated column-integrated ice crystal concentration from the HOM case to the HMTH_0.01IN case, as well as the 47% decrease from the HMTH_0.01IN case to the HMHT_0.1IN case. But in an atmosphere dominated by heterogeneous freezing, as is the case in HMHT_0.1IN, adding heterogeneous IN increases the ice crystal number concentration and has little effect on the cirrus cloud fraction. This explains the factor of 5 increase in simulated column-integrated ice crystal number concentration in HMHT_1IN compared with HMHT_0.1IN.

Changes in mesoscale temperature perturbations also change ice crystal number concentrations significantly. Large temperature perturbations produce higher cooling rates and therefore more homogeneous freezing and higher ice crystal number concentrations, while small temperature perturbations produce lower cooling rates and

therefore less homogeneous freezing and less ice crystal number concentrations. Column-integrated ice crystal number concentration increases by 50% from the HMHT_0.01IN case to the HMHT_1.25dT case when the mesoscale temperature perturbation is increased by 25%, while it decreases by 50% from the HMHT_0.01IN case to the HMHT_0.75dT case when the mesoscale temperature perturbation decreases by 25%. Changes in ice crystal number concentrations from a 25% change in the temperature perturbation have a magnitude similar to those caused by a factor of 10 change in the heterogeneous IN concentrations. This reinforces the importance of having a better representation of mesoscale dynamic forcing in the treatment of cirrus clouds and in studies of the indirect effects of aerosols on cirrus clouds (Haag and Kärcher, 2004).

Changes in the ice crystal number concentration, caused by either heterogeneous IN or by mesoscale temperature perturbatrions, affect ice crystal radius, ice water content, low level liquid clouds, and water vapor in the atmosphere. More ice crystals lead to smaller ice crystal radii and smaller ice settling velocities. This leads to not only more ice water and more water vapor in the upper troposphere, but also a more cloudy and more moist lower troposphere. This moistening effect on low level clouds is ubiquitously seen across all simulations, since the liquid water path and low level cloud fraction are always positively correlated with the simulated ice crystal number concentration (i.e., smaller ice crystal number concentration leads to smaller low level cloud fraction and to smaller liquid water path).

Changes in the net radiative fluxes at the TOA are determined by the following three changes: 1) the change in the net radiation caused by the change in high level cirrus clouds; 2) the change in the net radiation caused by the change in low level liquid clouds;

and 3) the change in the clear sky longwave radiation caused by the change in water vapor in the upper troposphere. The first and the third effects act in the same direction, but the second effect acts in the opposite direction. Due to the cancellation of the first and second effects, the net change in cloud forcing is less sensitive to changes in ice crystal number concentration (a maximum change of 0.67 W/m^2 in the net cloud forcing is simulated across all cases in this study) while the sign of the change in cloud forcing depends on which of these two effects dominates. Our results show that either of these two effects can dominate. A net cooling of 0.14 W/m^2 is simulated in going from the HOM case to the HMHT_0.01IN case, which indicates that the first effect dominates, while a net warming of 0.32 W/m^2 is simulated in going from the HMHT_0.01IN case to the HMTH_0.1IN case, which indicates the second effect dominates, though ice crystal number concentration increases in both scenarios. The reason for this difference is not immediately clear, but it may depend on the differences in the simulated ice crystal number concentration changes with altitude. For example, ice crystal number concentrations at the uppermost level in the tropics increase, but they decrease at most of the other levels in the second scenario, while ice crystal number concentrations decrease at all levels in the first scenario (see Figure 4.4a and Figure 4.10a-b).

Because the net change in cloud forcing is less sensitive to changes in ice crystal number concentration due to the competition between the first and second effects, the net flux changes at the TOA are mainly controlled by the third effect in this study and closely follow the change in the ice crystal number concentration (more ice crystals lead to more warming). A maximum change of 2.35 W/m^2 is simulated across all cases in this study, where the net cloud forcing change contributes 0.65 W/m^2 to the change, and the

remaining 1.67 W/m^2 is caused by the changes in the greenhouse effects of water vapor, mainly in the upper troposphere because of its large relative change there. The large change in the greenhouse effects of water vapor may point to a problem in studies of aerosol indirect effects on cirrus clouds that only examine the change in cloud forcing.

Our study shows that ice crystal gravitational settling plays a central role in determining the aerosol indirect effects on clouds. This points to the urgent need to improve global climate models in this respect, as has been highlighted in several recent studies (e.g., Sanderson et al., 2008; Mitchell et al., 2008).

Appendix 4.A Equations used in the cirrus cloud scheme

We listed the key equations used in the cirrus cloud scheme of KB08 in this Appendix, and refer to KB08 for details.

The PDF of clear sky temperature is approximated by a constrained normal distribution with mean temperature (T_0) and standard deviation δT:

$$\frac{dP_T}{dT} = \frac{1}{N_T}\frac{1}{\delta T}\frac{1}{\sqrt{2\pi}}\exp\{\frac{-(T-T_0)}{2\delta T^2}\} \quad , \tag{4.A1}$$

where $dP_T/dT=0$ outside of $T_0 \pm 3\delta T$ and N_T is a normalization factor accounting for the finite limits over which Equation 4.A1 is defined.

By using the saturation vapor pressure over pure hexagonal ice which is calculated based on Murphy and Koop (2005), the PDF of clear sky temperature is then transformed into the PDF of clear sky saturation ratio (S):

$$\frac{dP_s}{dS} = \frac{1}{N_S}\frac{1}{\sigma_S\sqrt{2\pi}}\frac{1}{S\ln^2(S/\alpha)} \times \exp[-\beta_S\{\frac{1}{\ln(S/\alpha)} - \frac{1}{\ln(S_0/\alpha)}\}^2], \tag{4.A2}$$

where $\beta_s = 1/(2\sigma_S^2)$, $\sigma_S=\delta T/\theta$, θ=6132.9 K, $\alpha=p_v/\varphi$, φ=3.4452x1010 hPa, and p_v is the water vapor partial pressure. S_0 is the mean clear sky saturation ratio and N_S is the normalized factor, which is calculated as

$$N_S = \frac{1}{2}(erf[\sqrt{\beta_S}\{\frac{1}{\ln(S_0/\alpha)} - \frac{1}{\ln(S_{3+}/\alpha)}\}] - erf[\sqrt{\beta_S}\{\frac{1}{\ln(S_0/\alpha)} - \frac{1}{\ln(S_{3-}/\alpha)}\}], \quad (4.A3)$$

where S_{3+} and S_{3-} are the upper and lower bounds of S at which dP_s/dS is defined (i.e., dP_s/dS=0 outside of [S_{3-}, S_{3+}]) and $S_{3\pm}$ is calculated as:

$$S_{3\pm} \approx S_0 \exp(\frac{\pm 3\delta T\theta}{T_0^2}). \quad (4.A4)$$

Here, *erf(x)* is the error function and is defined as:

$$erf(x) = (2/\sqrt{\pi})\int_0^x \exp(-t^2)dt. \quad (4.A5)$$

The in-cloud vapor deposition/evaporation is calculated as

$$(\frac{\partial q_{vc}}{\partial t})_{dep} = -4\pi D N_i r \beta C \phi (q_{vc} - q_{sat}) = -\frac{q_{vc} - q_{sat}}{\tau_s}, \quad (4.A6)$$

where *Ni* is the in-cloud ice crystal number concentration, r is the volume mean radius, D is the diffusion coefficient of water molecules in air, C and ϕ are the ice crystal capacitance and ventilation factors, β accounts for gas kinetic corrections, and τ_s is the instantaneous relaxation time-scale given by:

$$\tau_s = \frac{1}{4\pi D N_i r \beta C \phi}. \quad (4.A7)$$

C , ϕ, and β are set equal to unity in this study. Integrating Equation 4.A5 over a time step τ yields the vapor deposition formula given in Equation 4.8.

The PDF of in-cloud ice water content (m) (dP_m/dm) is represented by the following formula:

$$m\frac{dP_m}{dm} = \frac{2}{\sqrt{\pi}}\left(\frac{m}{m_0}\right)\exp\{-\left(\frac{m}{m_0}\right)^2\},\ m_0 = \sqrt{\pi}\,\overline{m}, \tag{4.A8}$$

where $\overline{m}$ is the mean ice water content. This PDF of in-cloud ice water content is shown to be a good approximation of the cirrus ice water content observed over Punta Arenas, Chile (Ström et al., 2003; KB08). The PDF of in-cloud water vapor is assumed to be composed of homogeneously distributed vapor PDF in the form of a delta function. So the PDF of the total water mass mixing ratio in cloudy areas (q_{totc}) is:

$$\frac{dP_{q_{totc}}}{dq_{totc}} = \frac{2}{\sqrt{\pi}}\frac{1}{q_0}\exp\{-\left(\frac{q_{totc}-q_{vc}}{q_0}\right)^2\},\ \ q_0 = \sqrt{\pi}\,\frac{q_i}{a}, \tag{4.A9}$$

where q_i/a denotes the simulated in-cloud ice mass mixing ratio and $q_{totc} \geq q_{vc}$. With the help of this PDF for the total water vapor mixing ratio, changes in cloud fraction and ice water content are then calculated by Equations 4.9 and 4.10, respectively.

Appendix 4.B A two-moment treatment of cloud microphysics for warm and mixed-phase clouds

In the version of the model used in this study, a prognostic cloud droplet number concentration (n_l) equation for liquid cloud is added. Together with the prognostic liquid water mass (q_l), ice water mass (q_i), and ice crystal number concentration (n_i), the complete set of equations for the two-moment treatment of cloud microphysics for liquid clouds and mixed-phase clouds are:

$$\frac{\partial q_l}{\partial t} = A(q_l) + DTR(q_l) + Q_{cond} - Q_{liq2pr} - Q_{liq2ice}, \tag{4.B1}$$

$$\frac{\partial q_i}{\partial t} = A(q_i) + DTR(q_i) + Q_{liq2ice} + Q_{vap2ice} - Q_{ice2pr}, \tag{4.B2}$$

$$\frac{\partial n_l}{\partial t} = A(n_l) + DTR(n_l) + N_{nucl} - N_{self} - N_{liq2pr} - N_{evapl} - N_{liq2ice} \quad (4.B3)$$

$$\frac{\partial n_i}{\partial t} = A(n_i) + DTR(n_i) + N_{nuci} + N_{frz} + N_{\sec} - N_{ice2pr} - N_{evapi}, \quad (4.B4)$$

where the A operator on the left side of Equations 4.B1-4.B4 represents the advective, turbulent, and convective transports, as well as the gravitational settling, and the DTR operator represents the detrained cloud liquid and ice from both deep and shallow convection.

Q_{cond} represents the net condensation rate for liquid clouds in warm and mixed-phase clouds as diagnosed by the fractional cloud closure scheme of Zhang et al. (2003), and this removes supersaturation in terms of water (LIU07). Q_{liq2pr} and Q_{ice2pr} are the loss rates of cloud liquid mass and ice mass from the conversion of cloud condensate into precipitation, which include the autoconversion of cloud liquid and ice and the collection of cloud liquid and ice by rain and snow (Rasch and Kristjánsson, 1998). $Q_{vap2ice}$ represents the deposition on ice crystals from the water vapor form when there is supersaturation over ice or evaporation (LIU07). $Q_{liq2ice}$ represents the growth of ice water at the expense of liquid water due to the Bergeron-Findeisen process in the mixed-phase clouds, and depends on ice crystal number concentrations and ice supersaturation. The in-cloud vapor pressure used to calculate ice supersaturation in mixed-phase clouds is the saturation vapor pressure that is weighted by the proportions of ice and liquid water mass. This direct conversion from liquid to ice was not allowed in LIU07 who assumed a conversion from water vapor to ice which resulted in a smaller conversion rate of liquid to ice in mixed-phase clouds. But this direct conversion was used in simulating observed clouds in the Mixed-Phase Arctic Cloud Experiment (M-PACE) in a single column

model (Liu et al., 2007) and in a short-range weather forecasting approach (Xie et al. 2008).

Table 4.B1 Size distribution parameters for aerosols

Aerosol component	Ni	Ri, um	Sigma
Sulfate[a]	1.0	0.05	1.9
Fossil fuel OM/BC[a]	1.0	0.05	1.9
Biomass OM/BC and natural OM[b]	1.0	0.08	1.65
Sea Salt[c]	0.965	0.035	1.92
	0.035	0.41	1.70
Dust[d]	0.152	0.01	2.3
	0.727	0.045	1.6
	0.121	0.275	2.5

[a]The size distribution of sulfate and internal mixture fossil fuel OM/BC is the fossil fuel size distribution taken from Penner et al. (2001, Table 5.1).
[b]The size distribution of internal mixture biomass burning OM and BC is the biomass burning size distribution from Penner et al. (2001, Table 5.1).
[c]The size distribution of sea slat is taken from Quinn and Coffman (1998).
[d]The size distribution of dust is taken from de Reus et al. (2000).

Detrained cloud mass from convection is assumed to be in liquid phase for clouds warmer than -35ºC, and is assumed to be in ice phase for cirrus clouds. The conversion of this detrained condensate from liquid phase into ice phase in the mixed-phase clouds is completed through the Bergeron-Findeisen process. Detrained cloud droplet and ice crystal number are calculated from detrained cloud liquid and ice mass by assuming a spherical particle with constant volume-mean radius for both cloud droplets and ice crystals. These volume-mean radii for liquid droplets and ice crystals are calculated from the effective radius used in the standard CAM3 (Bovile et al., 2006), following the treatment LIU07 applied to ice crystals.

Microphysical terms of cloud droplet number (n_l) include cloud droplet sources from droplet activation (N_{nucl}), and droplet sinks from precipitation (N_{liq2pr}), evaporation (N_{evapl}), self-collection (N_{self}), and freezing ($N_{liq2ice}$) processes. The loss rate of cloud

droplet number from precipitation is assumed to be proportional to the loss rate of liquid water mass from precipitation, and is calculated as

$$N_{liq2pr} = \frac{Q_{liq2pr}}{q_l} n_l . \tag{4.B5}$$

The same assumption is applied to the loss rate of cloud droplet number from evaporation. In CAM3, only net evaporation rate of cloud liquid mass (Q_{cond}) is diagnosed from the scheme of Zhang et al. (2003), which includes the evaporation due to the decreases in relative humidity of a grid box and the evaporation of cloud liquid that transports into the clear sky part of a grid box. Here we assume that the evaporation of cloud droplets only happens when there is net evaporation of cloud liquid mass, and is calculated as:

$$N_{evapl} = \frac{-\min(0, Q_{cond})}{q_l} n_l . \tag{4.B6}$$

The depletion of liquid droplets from the freezing process ($N_{liq2ice}$) includes the initial freezing of liquid droplets into ice crystals from contact freezing (N_{fr}), and the depletion of cloud droplets from evaporation due to the subsequent growth of ice crystals from the Bergeron-Findeisen process. The fraction of depleted cloud liquid droplet number from the Bergeron-Findeisen process is assumed to be half of the fraction of depleted cloud liquid mass ($Q_{liq2ice}$) except for the complete depletion of cloud liquid mass, where the total droplet number is also depleted. With this treatment, we assumed a part of the depleted cloud mass from the Bergeron-Findeisen process comes from the shrinking of cloud droplets.

For the nucleation term, new droplets are formed only when the number that would be activated exceeds the number of preexisting cloud droplets and when net condensation occurs (Lohmann et al., 1999):

$$N_{nucl} = \max[\frac{1}{\Delta t}(N_{ac} f - n_{old}),0] \text{, when } Q_{cond} > 0 \text{ ,} \quad (4.B7)$$

where N_{ac} is the number concentration of cloud droplets activated from aerosol particles, and n_{old} is the number concentration of cloud droplet in the previous time step. N_{ac} is calculated from aerosol fields using a parameterization based on Köhler theory (Abdul-Razzak and Ghan, 2000; 2002) as was done in Chapter III. This parameterization combines the treatment of multiple aerosol types and a sectional representation of size to deal with arbitrary aerosol mixing states and arbitrary aerosol size distributions. Five categories of aerosols are externally mixed: sulfate, biomass burning OM/BC, fossil fuel OM/BC, sea salt, and dust. The bulk hygroscopicity parameter for each category of aerosol is the volume-weighted average of the parameters for each component taken from Ghan et al. (2001a) (see Table 3.1 in Chapter III). The size distributions of the five types of aerosols are prescribed as in Table 4.B1. The vertical velocity (w) used in calculating N_{ac} is calculated from $w = \overline{w} + c \times \sigma_w$, where $\overline{w}$ is the large-scale vertical velocity, σ_w is the subgrid variance of the vertical velocity diagnosed from the eddy diffusivity and the mixing length, and c is a coefficient that depends on σ_w, as described in Chapter III.

The self-collection of cloud droplets follows the treatment of Beheng (1994) and is parameterized as

$$N_{self} = 1.29 \times 1.0e10 \times b(\rho \frac{q_l}{f})^2, \quad (4.B8)$$

where ρ is the air density (kg/m^3).

The source and sink terms of ice crystal number concentration include deposition/condensation freezing (N_{nucl}), contact freezing of cloud droplets from dust particles (N_{frz}), the secondary ice production by ice splintering between -3 and -8 ºC (N_{sec}), the loss from precipitation (N_{ice2pr}), and the loss from sublimation of ice crystal particles (N_{sublim}). These source and sink terms are described in LIU07, with modifications described as follows. In LIU07, ice particles are assumed to evaporate completely only when cloud dissipates as the cloud fraction (a) decreases. In addition to the evaporation assumed in LIU07, we assumed in this study that ice crystal particles that are transported into the clear part of a grid box also evaporate, which is consistent with the treatment of liquid mass from the scheme of Zhang et al. (2003).

The effective radii of ice crystals are parameterized from ice crystal number concentration, ice water content, and temperature as described in Yang (2006) and LIU07. The cloud droplet effective radius (r_{el}) is calculated from the volume-mean cloud droplet radius (r_{vl}) based on the parameterization of Rotstayn and Liu (2003), which takes account of the change in the dispersion of the cloud droplet size distribution due to the change in the cloud droplet number. r_{el} is calculated as:

$$r_{el} = \beta r_{vl}, \tag{4.B9}$$

where β is the droplet size spectral shape factor. β is approximated as:

$$\beta = \frac{(1+2\varepsilon^2)^{2/3}}{(1+\varepsilon^2)^{1/3}}, \tag{4.B10}$$

where ε is the relative dispersion of the size distribution of cloud droplets and is approximated as:

$$\varepsilon = 1 - 0.7\exp(-\alpha N_l)\,, \tag{4.B11}$$

where N_l is the in-cloud droplet number concentration, and α is a coefficient. A value of α = 0.003 is used in this study, which represents the middle curve that fits observed ε and N_l in Fig. 1 of Rotstayn and Liu (2003).

Appendix 4.C Aerosol optical properties

A new package of aerosol optical properties replaces the standard one used in CAM3. Aerosol size distributions and mixing states are assumed to be the same as those used for the activation parameterization of cloud droplets (Table 4.B1). The refractive index of each aerosol species and their extinction coefficients, single scattering albedos, and asymmetry factors at 550nm from Mie calculations are shown in Table 4.C1. The optical properties of sulfate, sea salt, and biomass burning OM and BC account for aerosol hygroscopic growth, based on Kohler theory. Sulfate is assumed to have the hygroscopic growth behavior of ammonium sulfate. Biomass burning OM and BC is assumed to consist of 30% soluble material, and with the hygroscopic growth behavior of ammonium sulfate. The treatment of hygroscopic growth of sea salt aerosols follows Gerber (1985).

Lookup tables are developed to take account of the dependence of aerosol optical properties on relative humidity (and BC fraction for carbonaceous aerosol). Mie calculations were performed to generate tables of aerosol-specific extinction, single-scattering albedo (SSA), and asymmetry parameter in each shortwave band used in

Table 4.C1: Physical and optical properties at 550 nm for aerosol species[a]

Aerosol type	$k_e, m^2 g^{-1}$	ϖ	g	Refractive Index[c]
Sulfate	3.508 (11.490)	1.000 (1.000)	0.6278 (0.744)	1.53-1.0e-7i
BC				1.80-0.50i
OC				1.53-1.0e-7i
Fossil Fuel BC+OC (f_{vbc}[b]=0.04)	5.347	0.896	0.634	
BB BC+OC (f_{vbc}=0.08)	5.877 (8.399)	0.824 (0.875)	0.637 (0.689)	
Dust				1.53-0.0014i
(0.05-0.63um)	2.460	0.990	0.710	
(0.63-1.25um)	0.786	0.967	0.704	
(1.25-2.5um)	0.381	0.942	0.785	
(2.5-10.0um)	0.118	0.865	0.841	
Sea Salt				1.38-5.8e-7i
(0.05-0.63um)	2.500 (10.354)	1.000 (1.000)	0.788 (0.761)	
(0.63-1.25um)	0.903 (4.012)	1.000 (1.000)	0.692 (0.820)	
(1.25-2.5um)	0.501 (2.060)	1.000 (1.000)	0.802 (0.840)	
(2.5-10.0um)	0.254 (1.064)	1.000 (1.000)	0.834 (0.857)	

[a]k_e is extinction coefficient; w is single scattering albedo; g is asymmetry factor.
For k_e, w, g, the values in the parenthesis are given at 80% relative humidity for hydrophilic or soluble aerosol, and all other values are given at dry conditions. Size distributions are given in Table 4.B1 and aerosol density is given in Table 3.2.
[b]Here, f_{vbc} is dry volume fraction of BC in the internal mixture.
[c]References for refractive indices: Toon et al. (1976) for sulfate, Twitty and Weinman (1971) for BC, Toon et al. (1976) for OM, Myhre et al. (2003) for dust, and d'Almeida et al. (1991) for sea salt.

CAM3, at 21 relative humidities ranging from 0 to 99% (in increments of 5% from 0 to 95%). For carbonaceous aerosols, these tables were generated for 16 equally spaced BC volume fractions ranging from 0 to 30%. In the GCM, linear interpolation in relative humidity (and BC volume fraction) was used to determine the optical properties of each aerosol species.

This new package of aerosol optical properties is more consistent with aerosol fields simulated from the IMPACT aerosol model. The internal mixture between BC and OM is also more physically realistic than the external mixing assumed in the standard CAM3.

The package of aerosol optical properties have been used in Rotstayn et al. (2007) and Liu et al. (2007) with some modifications, and it has been shown that it simulates aerosol optical depths in reasonable agreement with satellite data.

CHAPTER V

SUMMARY AND FUTURE WORK

5.1 Summary

The aerosol indirect effect is still not well understood and remains one of the largest uncertainties in the projection of the future climate change. This is because of the complex nature of both aerosols and clouds; it is a challenge to represent these elements in global climate models. Improvements in both aerosol and cloud treatments in global climate models are therefore critical to advancing our understanding of aerosol indirect effects. In this dissertation, improvements are made for both aerosol and cloud treatments in the coupled IMPACT/CAM aerosol and atmospheric circulation model, and these improved treatments are used to study aerosol indirect effects.

In the first half of this dissertation, the focus is on the aerosol treatment, and in particular the treatment of aerosol nucleation in global models. An empirical aerosol nucleation parameterization is implemented into the aerosol model component of the coupled IMPACT/CAM model to simulate aerosol nucleation events in the boundary layer, which are observed to occur widely but can not be simulated with the traditional binary homogeneous nucleation of sulfuric acid and water vapor alone. Although this parameterization was derived by an empirical fit of the concentration of newly formed

particles and sulfuric acid vapor based on long-term observations of aerosol formation events at a boreal forest site (Kulmala et al, 2006; Sihto et al., 2006; Riipinen et al., 2007), this parameterization is shown to fit the records of nucleation events measured in a variety of continental and marine atmospheric environments well (Kuang et al., 2008). This boundary layer nucleation, together with the binary homogeneous nucleation in the free troposphere, and primary-emitted sulfate particles from anthropogenic sulfur are the basic generation mechanisms for secondary particles in our model. Then, the first three questions (Q1-Q3) originally raised in section 1.6 can be examined by using the coupled model with these three secondary particle generation mechanisms. Here are the results:

Q1. How well does this empirical nucleation mechanism reproduce observed aerosol sizes and number concentration?

The results showed that the inclusion of this boundary layer nucleation mechanism improves the comparison of simulated aerosol size distributions with observations, especially over the marine boundary layer and over the SH. Its effect at the polluted NH sites strongly depends on whether primary-emitted sulfate particles are included. When primary-emitted sulfate particles are included, the effect of boundary layer nucleation is small because of the condensation depletion of sulfuric acid gas by the large amount of primary particles.

Q2. How do different generation mechanisms of secondary articles (primary-emitted sulfate, nucleation in the upper troposphere, and nucleation in the boundary layer) contribute to CCN concentration?

Simulated CCN concentrations in the boundary layer range from 70 to 169/cm^3 from different nucleation mechanisms. The effect of the empirical boundary layer nucleation

scheme on CCN concentration depends in an important way on the assumed and simulated primary particles. Including the empirical boundary layer nucleation increases global average CCN concentrations in the boundary layer by 31.4% when the primary sulfate particles are excluded and by 5.3% when primary-emitted sulfate particles are included.

This study also shows that the inclusion of the empirical boundary layer nucleation scheme in the model decreases the effects of binary homogeneous nucleation in the free troposphere on CCN concentrations in the marine boundary layer, as well as the effects of primary sulfate particles. When no boundary layer nucleation is included, the inclusion of binary homogeneous nucleation in the free troposphere in the model increases CCN concentrations in the marine boundary layer by more than 150%, but when the empirical boundary layer nucleation scheme is included in the model, binary homogeneous nucleation in the free troposphere has a much smaller effect on CCN concentrations. The inclusion of primary-emitted sulfate particles always increases CCN concentrations in the boundary layer, although the inclusion of the empirical boundary layer nucleation scheme decreases the percentage increases in CCN associated with primary-emitted sulfate from 53% to 23%.

Q3. How do different generation mechanisms of secondary particles affect the estimation of aerosol indirect effects?

The effect of including a nucleation mechanism (either boundary layer nucleation or free troposphere nucleation) in the model on the first aerosol indirect forcing largely depends on the competition for sulfuric acid gas between condensation on pre-existing particles and nucleation. When the relative increase in the precursor gas species (SO_2)

between the present day and preindustrial simulations is large and the relative increase in pre-existing particles is not that large, the inclusion of nucleation tends to increase the aerosol indirect forcing. In contrast, when the relative increase in the precursor gas species (SO_2) between the PD and PI simulations is small but the relative increase in pre-existing particles is not that small, the inclusion of nucleation tends to decrease the aerosol indirect forcing. This contrast explains why the empirical boundary layer nucleation scheme changes the spatial pattern of the first indirect forcing and shifts more of the contribution of the first aerosol indirect effect to land. The magnitude of the relative increase in SO_2 and pre-existing particles between the PD and PI simulations causes a large decrease in the first indirect forcing over ocean and small decreases or even increases in the first indirect forcing over land in the simulations with boundary layer nucleation compared to those without boundary layer nucleation.

The inclusion of primary-emitted sulfate increases the first aerosol indirect forcing significantly, because primary-emitted sulfate forms CCN-size particles more efficiently than do particles that nucleate from the gas phase, and because the percentage change in primary-emitted sulfate particles between the PD and PI simulations is larger than the percentage change in other primary particles. When boundary layer nucleation is included, the effect of primary-emitted sulfate particles is smaller, but still significant.

The forcing from various treatments of aerosol nucleation ranges from -1.22 to -2.03 W/m^2. As a comparison, the uncertainty range of the best estimate of the first aerosol indirect forcing in IPCC (2007) from a variety of models is -0.3 to -1.8 W/m^2, which represents the 5% to 95% confidence range (Figure 1.3). The high end of our estimate is even larger than that from the IPCC (2007). So although the physically-based treatment

of aerosol size and composition in our model represents an improvement over the prescribed aerosol sizes used in most model estimates included in IPCC (2007), this predicted size-resolved composition would increase the uncertainty range in the best estimate of the IPCC (2007), since the latter is estimated based on the existing model estimates in the literature. This is partly because the more physically-based prediction of size-resolved aerosol composition in the model brings additional uncertainties into the simulated aerosol sizes and compositions. More efforts are needed to constrain the uncertainties in the simulated aerosol size associated with different aerosol nucleation treatments, which will help us to decrease the uncertainties in the estimate of aerosol indirect forcing associated with the representation of aerosol size distributions.

In the second half of this dissertation, we focus on cloud treatment, and in particular, subgrid-scale treatment of supersaturation and cloud formation in cirrus clouds in global models. The statistical cirrus cloud scheme in KB08 is implemented in the atmospheric circulation model component of the coupled IMPACT/CAM model. This statistical cirrus cloud scheme has subgrid-scale features for the clear sky temperature and in-cloud total water, which improves the treatment of ice freezing and cloud decay. It also has a consistent treatment for cloud fraction and ice freezing, which is absent in previous studies that examined aerosol effects on cirrus clouds. Then, the last three questions (Q5-Q6) raised in section 1.6 are addressed using the coupled model with the new cirrus cloud scheme. Here are the results:

Q4. How well does the model reproduce observed supersaturation?

The simulated PDF of *RHi* outside of cirrus clouds demonstrates an exponential decay from the *RHi* of 100% to the *RHi* of 150%, which agrees well with the MOZAIC field data when only homogeneous freezing is included. A faster decay beyond the *RHi* of 150% is simulated in the model than that in the MOZAIC data, which may be due to the too rapid depletion of water vapor by homogeneous freezing in the model. Including heterogeneous IN can change the PDF of *RHi* significantly. When 1% of soot and dust particles act as heterogeneous IN with a lower threshold freezing humidity of ~ 120-130% *RHi*, the frequency of occurrence of very high *RHi* at 200-300 hPa in the NH middle latitudes decreases, but there is little effect in the SH and tropics, and at high altitudes. The hemispheric contrast simulated in this case is consistent with that observed in the INCA field campaign (Haag et al., 2003). When heterogeneous IN concentrations increase by a factor of 10, the frequency of high *RHi* decreases significantly in both hemispheres, which is not supported by the MOZAIC data.

The simulated supersaturation frequencies at 139 hPa and 192 hPa agree well with satellite observation in terms of their spatial distribution, but the model overestimates the magnitude of the supersaturation frequency when only homogeneous freezing is included, especially at 192 hPa. Including heterogeneous IN in the model decreases the simulated supersaturation frequency and improves the comparison with satellite observations at 192 hPa, which supports the notion that heterogeneous freezing plays a role in ice freezing.

Q5. How do different IN concentrations affect cirrus cloud properties?

Our results showed that heterogeneous IN affect ice crystal number concentrations significantly and that their exact effects depend on the background freezing modes. In an

atmosphere dominated by homogeneous freezing, adding heterogeneous IN decreases ice crystal concentrations and increases cirrus cloud fraction. But in an atmosphere dominated by heterogeneous freezing, adding heterogeneous IN increases the ice crystal number concentration and has little effect on the cirrus cloud fraction.

Changes in the ice crystal number concentration affects ice crystal radius, ice water content, low level liquid clouds, and water vapor in the atmosphere. More ice crystals leads to smaller ice crystal radius and smaller ice falling velocity. This leads to not only more ice water and more water vapor in the upper troposphere, but also a more cloudy, and more moist lower troposphere. This moistening effect on low level clouds is ubiquitously seen across all our simulations, since the liquid water path and low level cloud fraction are always positive correlated with simulated ice crystal number concentration.

The changes in net cloud forcing are not very sensitive to the changes in ice crystal number concentrations because changes in high cirrus clouds and low level liquid clouds tend to cancel. A maximum change of 0.67 W/m^2 in the net cloud forcing is simulated across all the cases used in this study. The sign of the changes in the net cloud forcing depends on whether the changes in high cirrus clouds or changes in low level liquid clouds dominate. Our results show that either of these two effects can dominate.

The net radiative flux changes at the top of atmosphere are still large because of the changes in the greenhouse effect of water vapor, and closely follow the changes in ice crystal number concentration (more ice crystals lead to more warming). A maximum change of 2.35 W/m^2 is simulated across all the cases in this study, where the net cloud forcing change contributes 0.67 W/m^2 to the change, and the remaining 1.68 W/m^2 is

caused by the change in the greenhouse effect of water vapor, mainly in the upper troposphere because of the large relative change in mixing ratio there.

Q6. How do changes in mesoscale dynamics affect cirrus cloud properties and how does this effect compare with changes induced by different IN concentrations?

The changes in mesoscale temperature perturbations result in significant changes in ice crystal number concentration, which therefore further change the simulated radiative fluxes. Larger temperature perturbations lead to higher cooling rates and therefore more homogeneous freezing and higher ice crystal number concentrations, while smaller temperature perturbations lead to lower cooling rates and therefore less homogeneous freezing and lower ice crystal number concentrations. Changes in ice crystal number concentrations and radiative fluxes from different temperature perturbations are comparable to the changes caused by a factor of 10 change in heterogeneous IN concentrations.

The cirrus part of the dissertation represents the first serious attempt to better represent subgrid-scale supersaturation in global climate models, whereas previous treatments of ice nucleation in global models only predicted grid-mean supersaturation which does not sufficiently describe ice nucleation in cirrus clouds. This subgrid-scale supersaturation enables us to treat the competition between homogeneous freezing and heterogeneous more realistically. Although the effects of anthropogenic aerosols on cirrus clouds is not directly examined in this study and therefore the sign of aerosol indirect effects on cirrus clouds is still unknown, the potential effects of aerosols on cirrus clouds are explored using several sensitivity tests. The role of ice crystal number concentration and therefore the role of ice crystal gravitational settling on low level liquid clouds and the TOA

radiative fluxes are clearly demonstrated, which has not been analyzed in previous studies of aerosol effects on cirrus clouds. A best case, in which 1% of soot and dust particles act as heterogeneous IN, is also identified by comparing the simulated relative humidity fields with observations. This choice for ice nuclei number concentrations, with observations, can be used in the future to quantify the effects of anthropogenic aerosols on cirrus clouds, although improvements in the comparison of simulated cloud quantities (e.g., ice crystal number concentration and ice water content) are needed.

5.2 Future work

The study in this dissertation lays the foundation for further work on aerosol indirect effects and also points to some directions for future work, which are discussed below.

A better representation of condensable gases other than sulfate is needed. In our study, the only condensing vapor was sulfuric acid gas. However, observational data has shown that other species may also contribute to the growth of nanoparticles (e.g., Stolzenburg et al., 2005). In particular, a number of theoretical (Kerminen et al., 2000; Zhang and Wexler, 2002) and experimental (e.g., Allan et al., 2006; Smith et al., 2008) studies support the notion that organic species play a crucial role in the growth of nanoparticles. For example, Smith et al. (2008) showed that the condensation of sulfuric acid gas could have accounted for only about 10% of the growth that was observed in their measurements, and that oxygenated organics and nitrogen-containing organics can play a dominant role in the growth of nanoparticles. Including the contribution of condensational growth of organic compounds in the model will increase the growth rate of nanoparticles, which will lead to an increase in the number of larger particles (e.g.,

CCN) and may also improve the comparison with observations (Spracklen et al., 2008; Pierce and Adams, 2009; Makkonen et al., 2009).

A better representation of aerosol nucleation is needed. Although the form of the empirical parameterization for nucleation used in this study is generally applicable, variations of several orders of magnitude in the prefactors A and K have been observed, depending on location and the environmental conditions (Sihto et al.; 2006; Riipinen et al., 2007; Kuang et al., 2008). This indicates that species other than sulfuric acid may play a role in nucleation. For example, biogenic iodine oxides (O'Dowd et al., 2002b), organic species (Zhang et al., 2004), and ammonia (Korhonen et al., 1999) can be important in particle formation. In addition, ion mediated nucleation may be also important (Yu et al., 2008a). If factors other than sulfuric acid are important to aerosol nucleation, the effects of including a boundary layer nucleation mechanism on aerosol indirect forcing can differ from that calculated in this study. For example, the ion-mediated nucleation mechanism suggested by Yu (2006) leads to less nucleation at higher temperatures (Yu et al., 2008b). This suggests that including a boundary layer nucleation scheme would lead to a smaller increase and a larger decrease in the anthropogenic fraction of CCN than shown in this study, if this ion-mediated nucleation mechanism were used and the increase in temperature from the PI to the PD were also included.

A better representation of aerosol sizes and mixing states in the model is needed. A modal approach is used to represent the aerosol size distribution in this study. Although the modal approach is capable of efficiently representing multiple aerosol types under many conditions, the inherent assumption of a lognormal size distribution for each mode can break down (e.g., aerosol activation into cloud droplets will separate aerosol particles

into two separate groups of particles) (Ghan and Schwartz, 2007). Possible solutions to this problem are provided by more general and more accurate sectional (e.g., Adams and Seinfeld, 2002), the quadrature method of moments (QMOM) (McGraw 1997), or piecewise lognormal (Von Salzen, 2006) schemes, with differing computational burdens. QMOM is more general than the modal approach in that it does not assume a lognormal size distribution and the aerosol properties and their evolutions are calculated from the moments of the particle size distribution by Gaussian quadrature. This approach is also more computationally efficient than the sectional approach. The QMOM approach has been used in the GISS model and has shown some promising features for representing aerosol sizes and size-dependent composition (Bauer et al., 2008).

To better represent aerosols in global models, a better representation of the emission of primary particles is needed. Primary particles are not only efficient in producing CCN-size particles, but also affect the frequency and intensity of nucleation events and affect the growth of freshly nucleated particles into large CCN-size particles. Therefore, as is evident in this study, primary particles affect how much nucleation will contribute to CCN concentration. This is also demonstrated in Pierce and Adams (2009). Not only the emission of the mass concentrations of primary particles is needed, but also the emission of the number concentration of primary particles is needed, and the latter has much larger uncertainties.

For cirrus cloud treatment, a better representation of mesoscale motions in global models is highly desirable. Our results showed that a 25% change in mesoscale temperature perturbations leads to an even larger change in simulated ice crystal number concentration than produced by a one-order of magnitude change in heterogeneous IN

concentrations. The treatment of mesoscale temperature variations was highly simplified in our model. The mesoscale perturbations caused by orography has been addressed in recent papers (e.g., Dean et al., 2007; Joos et al., 2008).

A better representation of the gravitational settling of ice crystals is also needed. Our study shows that ice crystal gravitational settling plays a central role to determining changes in radiative fluxes at the top of the atmosphere. Large uncertainties remain in determining how to parameterize ice settling velocities from ice crystal size, mass, and temperature (e.g., Deng and Mace, 2008). A separate treatment of ice settling for ice crystals from homogeneous versus heterogeneous freezing may also desirable, since the size difference between ice crystals from these two freezing mechanisms can be large.

A better representation of cirrus cloud transport is also important. Cirrus clouds tend to have long lifetimes in the upper troposphere, and therefore the advection of cirrus is important, particularly for modeling upper tropospheric humidity. In our study, only ice crystal mass and ice crystal number are advected, but cloud fraction is not. So, ice crystals that move to clear sky areas will evaporate. This treatment may overestimate the role of ice nucleation in the model and underestimate the role of deposition growth.

A better representation of ice freezing in the model is also highly desirable. Although we improved this aspect by including a parameterization of the subgrid-scale supersaturation, more has to be done. For example, we assume that all soot and dust particles have the same freezing capabilities, which may not be true. Soot particles with different sources may have different freezing capabilities, and aerosol particles at different temperatures may also have different freezing capabilities (Kärcher et al., 2007).

APPENDIX

CODE CHANGES MADE FOR THIS DISSERTATION

Here code changes made on both the aerosol model (IMPACT) and atmospheric circulation model (NCAR CAM3) are documented. The original IMPACT and CAM codes have been changed in several aspects:

1. Code changes for the coupling between two model components.
2. Code changes for two-moment treatment of cloud microphysics.
3. Code changes for UMich aerosol optical properties.
4. Code changes for the empirical nucleation mechanisms.
5. Codes for the offline radiative transfer model of NCAR CAM3.

1. Codes for the coupling between two model components.

The coupling between two model components are started by first calling CPL_COMM_INIT in both model components (called in the subroutine of CAM in the CAM model and in the subroutine of MSG_INIT1 in the IMPACT model). This subroutine initializes the communication channels between the two model components and maps the processors to the model components using the MPH (Multi-component Handshaking) Library. Then two modules of CAMPACT_MSG and PACTCAM_MSG

are added into the CAM and IMPACT source codes to handle data exchange between the IMPACT aerosol model and NCAR CAM3 model, respectively.

The module of CAMPACT_MSG defines several public subroutines, and public variables for meteorological data that will be sent to the aerosol model. Here are details:

Public meteorological data: MET2_DATA. These public data are used and updated in the subroutine of PHYSPKG (a subroutine in the original CAM3).

Public subroutines:

CAMPACTINI: This subroutine is called in INITEXT (a subroutine in the original CAM3) to initialize the communication between CAM and IMPACT. It first initializes data used in the module of CAMPACT_MSG. Then it sends time information of the integration periods (e.g., the starting year, month and day, and the ending time of the integration) by calling the subroutine of CAMPACT_MSG_TIME, and it sends the decomposition information of CAM model grids to IMPACT (e.g., the number of model longitudes, the number of model latitudes, and indices of model grids in each MPI processor) by calling the subroutine of CAMPACT_MSG_SENDGRID. Finally it receives the decomposition information of IMPACT model grids (e.g., the number of MPI processors and indices of model grids in each MPI processor in the IMPACT model) and the initial aerosol data from IMPACT model.

CAMPACTSNDMET1: This subroutine is called every two time steps in PHYSPKG to send four basic meteorological fields (zonal wind speed, U (m/s); meridional wind speed, V(m/s); temperature, T(K); and surface pressure, PS (Pa)) to the IMPACT model.

CAMPACTSNDMET2: This subroutine is also called every two time steps in PHYSPKG to send all other meteorological fields (convective precipitation,

CON_PRECIP (mm/day); total precipitation, TOT_PRECIP (mm/day); planetary boundary layer depth, PBL (m); surface friction velocity, USTAR (m/s); surface air temperature, SURF_AIR_TEMP (K); surface roughness, SURF_ROUGH (m); ground temperature, GRND_TEMPERATURE (K); soil wetness, GWET (m^3/m^3); the 10-meter wind speed, U10 (m/s); convective mass flux in downdraft, CMF ($kg/m^2/s$); detrainment rate, DTRN (kg/m2/s); specific humidity, HUMIDITY (g/kg); moisture change due to wet processes, MOISTQ (g/kg/day); vertical diffusion coefficient, KZZ (m^2/s); cloud fraction, RAN_CLOUD; cloud water content, CLOUD_LWC (kg/kg)).

CAMPACTRCVAER2: This subroutine is called every two time steps in PHYSPKG to receive all aerosol fields from the IMPACT model.

GET_AEROSOL_CAMPACT_NEW: This subroutine is used to get aerosol fields from the received aerosol data by CAMPACTRCVAER2 in the calculation of aerosol optical properties in RADCTL (a subroutine in the original CAM3), cloud droplet number concentration in NUCLEATE_AG3 (see section 2), and ice crystal number concentration in NUCLEATI (see section 2)).

For the aerosol model, the module of PACTCAM_MSG has a similar function as that of CAMPACT_MSG, as described below:

PACTCAMINITIME: This subroutine is called in ESM_GENERATE (a subroutine in the original IMPACT) to get the time information of the model integration from CAMPACT_MSG_TIME.

PACTCAMINI: This subroutine is called in ACTM_INTI2 (a subroutine in the original IMPACT) to receive the decomposition information of the CAM model grids (e.g., the number of model longitudes, the number of model latitudes, and indices of

model grids in each MPI processor in the CAM model) and to send the decomposition information of the IMPACT model (e.g., the number of MPI processors and indices of model grids in each MPI processor in the IMPACT model) into the CAM model.

PACTCAMRCVMET1: This subroutine is called in SET_MET1 (a subroutine in the original IMPACT) at the first time step and in CONTROL_MET1_FILE_INPUT (a subroutine in the original IMPACT) at the subsequent time steps to receive the meteorological fields from CAMPACTSNDMET1.

PACTCAMRCVMET2: This subroutine is called in SET_MET1 at the first time step and in CONTROL_MET1_FILE_INPUT at the subsequent time steps to receive the meteorological fields from CAMPACTSNDMET2.

PACTCAMSNDAER2: This subroutine is called in ACTM_INIT2 at the first time step and in DO_MULTIPROC_ADV at the subsequent time steps to send aerosol data (aerosol mass mixing ratio, CONST (kg/kg)) to the CAM model (as received by CAMPACTRCVAER2).

2. Codes for two-moment treatment of cloud microphysics.

Two additional prognostic variables for cloud droplet number concentration (LIQNUM, #1.0^{12}/kg) and cloud ice crystal number concentration (ICENUM, #1.0^{12}/kg) are added. This is done in the subroutine of CLDCOND_REGISTER (a subroutine in the original CAM3). Then the subroutines of CLDCOND_TEND (a subroutine in the original CAM3) and PCOND (a subroutine in the original CAM3) are updated with the source and sink terms that are described in Appendix 4.B.

The subroutine of CLDCOND_TEND first updates cloud liquid and ice by adding the detrained sources from deep and shallow convection. Then activated cloud droplet

number concentration from the cloud droplet activation parameterization for liquid clouds and nucleated ice crystal number concentration from the ice freezing parameterization for mixed-phase clouds are calculated by calling the subroutines of NUCLEATE_AG3 and NUCLEATI, respectively. The input variables for the subroutine NUCLEATE_AG3 are the chunk identifier (LCHNK) (a group of columns in CAM3 is identified as a chunk), the number of atmospheric columns (NCOL), temperature (T, K), model interface pressure (PMID, Pa), model midpoint pressure (PINT, Pa), layer thickness (PDEL, Pa), height at the interface (ZM, meter), height of the planetary boundary layer (PBLHT, meter), eddy diffusivity (KZZ, m^2/s), grid-mean vertical velocity (OMEGA, Pa/s), sea ice fraction (SEAICEF), snow depth over land (SNOWH, meter), the cloud droplet number concentration at the last time step (NOLD, $\#/cm^3$), cloud fraction (CLDN), and the fraction of ice condensate in the total condensate (FICE). The output variables of NUCLEATE_AG3 include the activated droplet number concentration (NUCL, $\#/cm^3$), the variance of the updraft velocity (WSTAR, cm/s), and the grid-mean update velocity (WM, cm/s). The input variables for the subroutine NUCLEAI are chunk identifier (LCHNK), the number of atmospheric columns (NCOL), temperature (T, K), specific humidity (Q), liquid water mixing ratio (QL, kg/kg), model interface pressure (PMID, Pa), model midpoint pressure (PINT, Pa), and layer thickness (PDEL, Pa), height at the interface (ZM, meter), grid-mean vertical velocity (OMEGA, Pa/s), cloud fraction (CLDN), sea ice fraction (ICEFRAC), snow depth (SNOWTH, meter), and ice crystal number concentration at the last time step (NIOLD, $\#/cm^3$). The output variable of NUCLEATI is ice number nucleated (NUCI, $\#/cm^3$). These are then used to update both cloud droplet number concentration and ice crystal number concentration by using

Equation 4.B7 in this thesis and Equation 4 in Liu et al. (2007). Ice crystal number concentration in the mixed-phase clouds are further updated by adding ice crystal number from contact freezing that is parameterized as in Equation 13 in Liu et al. (2007). It then calls the subroutine PCOND to calculate liquid condensate, ice condensate, liquid precipitation, ice precipitation, and ice freezing of cirrus clouds. Finally, sink terms of cloud liquid droplet number and ice crystal number from evaporation and precipitation are updated in CLDCOND_TEND.

The subroutine of PCOND is called in CLDCOND_TEND to handle the partitioning of water vapor, cloud water, and rain water. It first calculates the total liquid from the condensation-evaporation scheme of Zhang et al. (2003) for warm clouds and mixed-phase clouds. Then the in-cloud conversion from liquid phase to ice phase from the Bergeron-Findeisen process is calculated for mixed-phase clouds. The additional water vapor that exceeds ice supersaturation in mixed-phase clouds deposits on ice crystals, which depends on ice crystal number concentration as is calculated by Equation 19 in Liu et al. (2007). Then, cloud growth and cloud decay for cirrus clouds as described in the section of 4.2.2 is treated by calling the subroutine of CIRRUS0D. The input variables of CIRRUS0D include time step (DELTAT, seconds), temperature (T, K), model midpoint pressure (PMID, Pa), specific humidity (Q, kg/kg), in-cloud specific humidity (QC, kg/kg), cloud fraction (CLD), grid-averaged ice water content (QI, kg/kg), grid-averaged ice crystal number concentration (NI, 10^{12}/kg), the number concentration of soot particles (SOOT_NUM, #/cm^3), the number concentration of dust particles (DUST_NUM, #/cm^3), the number concentration of sulfate particles (SO4_NUM, #/cm^3), surface soot mass mixing ratio (BC_MASS, kg/kg), air soot mass mixing ratio (AIRST_MASS, kg/kg),

dust mass mixing ratio in the bin 1 (DST1_MASS, kg/kg), dust mass mixing ratio in the bin 2 (DST2_MASS, kg/kg), dust mass mixing ratio in the bin 3 (DST3_MASS, kg/kg), and dust mass mixing ratio in the bin 4 (DST4_MASS, kg/kg). The output variables of CIRRUS0D include change in specific humidity from ice freezing and decay (DQDT, kg/kg/s), change in in-cloud specific humidity (DQCDT, kg/kg/s), change in cloud fraction (DCLDDT, fraction/s), change in grid-averaged ice water content (DQIDT, kg/kg/s), change in grid-averaged ice crystal number concentration (DNIDT, 10^{12}/kg/s), ice crystal number concentration from homogeneous freezing (NI_NEW_HOMO, #/cm^3), and ice crystal number concentration from heterogeneous freezing (NI_NEW_HETE, #/cm^3). Finally, the partitioning between cloud water and rain water is treated as described in Rasch and Kristjansson (1997) by calling the subroutine of FINDMCNEW (a subroutine in the original CAM3).

The subroutine CIRRUS0D is a part of the module of CLD_CIRRUS, which is added to the CAM3 codes to handle the implementation of Kärcher and Burkhardt's cirrus cloud scheme (see section 4.2.2 in the thesis). The module of CLD_CIRRUS includes five public subroutines (CIRRUS_INIT, CIRRUS_EXPANSION, VAPOR_DEPOSITION2, CIRRUS_DECAY, and CIRRUS0D). The subroutine of CIRRUS_INIT is called in CLDCOND_INIT to define some constant parameters used in the module. The CIRRUS_EXPANSION, VAPOR_DEPOSITION2 and CIRRUS_DECAY subroutines are called in the subroutine CIRRUS0D to treat cirrus cloud growth (Equations 4.4-4.7), vapor deposition/evaporation (Equation 4.8), and cirrus cloud decay (Equation 4.9-4.10), respectively. The subroutine of CIRRUS0D is the major subroutine to treat cirrus clouds, and is called in the subroutine of PCOND as mentioned in the previous paragraph.

The module of OUTPUT_AEROCOM_AIE is added to diagnose variables at the cloud top as described in section 4.3. It includes three subroutines: OUTPUT_AEROCOM_AIE_INIT, AEROCOM_CALC, and OUTPUT_AEROCOM. The OUTPUT_AEROCOM_AIE_INIT subroutine initializes cloud top quantities. The AEROCOM_CALC subroutine diagnoses cloud top quantities using the maximum/random cloud overlap hypothesis to obtain the 2D field as seen by the satellite instruments. The subroutine OUTPUT_AEROCOM outputs all cloud top quantities.

3. Codes for Umich aerosol optical properties.

A lookup table for the aerosol optical properties we described in Appendix 4.C is implemented into the NCAR CAM model. This look-up table is read and stored in the module of AER_OPTICS (a subroutine in the original CAM3). Two subroutines are then added in the module of AER_OPTDEPTH to calculate aerosol optical properties (i.e., optical depth, single scattering albedo, asymmetric factor). One is AER_OPTDEPTH_UMICH, which is called in the subroutine of RADCSWMAX (a subroutine in the original CAM3) and is used to calculate the band-averaged aerosol optical properties for all 19 wave bands in the short wave radiative transfer code in NCAR CAM3. The input variables of AER_OPTDEPTH_UMICH include the model interface pressure (PFLX, Pa) (the boundary between pressure levels), aerosol mass mixing ratio (AERMMR, kg/kg), relative humidity (RH), cloud fraction (CLD), the number of daylight columns (NDAY), the spectral loop index for solar spectrum (NS), and the number of aerosol groups for the calculation of aerosol optical depth (NAER_GROUPS). The output variables include aerosol extinction optical depth (TAUAR), aerosol single scattering albedo (WA), aerosol asymmetry parameter (GA),

aerosol forward scattered fraction (FA), aerosol column optical depth (AERTAU), aerosol column-averaged single scattering albedo (AERSSA), aerosol column-averaged asymmetry parameter (AERASM), and aerosol-column averaged forward scattering (AERFWD. The other is AER_WAV_OPTDEPTH_UMICH, which calculates aerosol optical properties at 550 nm and is called in the subroutine of RADCTL (a subroutine in the original CAM3). The input variables of AER_WAV_OPTDEPTH_UMICH are model interface pressure (PFLX, Pa), aerosol mixing ratio (AERMMR, kg/kg), relative humidity (RH), cloud fraction (CLD), the number of columns (NCOL), and the number of aerosol groups for the calculation of aerosol optical depth (NAER_GROUPS). The output variable of AER_WAV_OPTDEPTH_UMICH is the aerosol column optical depth at 550 nm (AERTAU_WAV).

4. Codes for the empirical nucleation mechanisms.

A new subroutine, NUCLEATION_BOUNDARY, is added into the file of umaerosol.F in the IMPACT codes to treat boundary layer nucleation as we described in the section of 2.3.2. It first calculates the nucleation rate of 1 nm diameter particles by using Equations 2.1-2.2, and it then calculates the nucleation rate of 3 nm particles by using Equation 2.3. The input variables of the subroutine are the number of parcels (NV), temperature (TEMP, K), relative humidity (RELHUM, 0-1), the concentration of sulfuric acid (SO4GAS, #molecules/m^3), the number concentration of sulfate aerosols (SO4AER, #/m^3), the volume-mean radius of sulfate particles (SO4RADV, meter), the Knudson number (SO4KNU). The output variables are FXAER (a vector), which includes the change in sulfuric acid gas (#molecules/m^3), aerosol number concentration (#/m^3) and aerosol mass (#molecules so4/m^3). This subroutine is called in the subroutine of

DERIVATIVE (a subroutine in the original IMPACT) to replace the original binary homogeneous nucleation in the boundary layer. The planetary boundary layer height is calculated by the NCAR CAM3 model, and is transferred into the IMPACT model by the subroutines of CAMPACTSNDMET2 and PACTCAMRCVMET2.

5. Codes for the offline radiative transfer codes of NCAR CAM3.

In order to estimate the first aerosol indirect forcing in Chapter III, the radiative transfer codes of NCAR CAM3 were taken out of the host model CAM3, and interfaces are added to run the radiative transfer model independently. These interfaces include the handling of the input and output data and the parallelization of the code by using a hybrid message passing MPI/OpenMP scheme. This offline radiative transfer model has been used in Wang and Penner (2009) and Penner et al. (2009) to calculate the aerosol indirect forcing for liquid clouds and cirrus clouds, respectively.

The main program file is main.F90. It first calls SPMDINIT to initialize the MPI environment, such as to get the number of processors, and processor IDs. It then calls the subroutine RUNTIME_OPTIONS to read parameters from namelist. Next the subroutines of SET_CHUNK and SPMD_DECOMPOSE are called to decompose the global domain into individual MPI processors. Then meteorological fields, surface albedo, aerosol fields, and ozone) are read by calling the subroutines READ_MET, READ_ALBEDO and READ_AEROSOL_DYNAIR (which reads the aerosol fields), respectively It then calls the subroutine of STEP, which is the main subroutine to perform the radiative transfer calculation for individual domains that are assigned into MPI processors. Finally, it outputs data by calling the subroutines of WSHIST and WRAPUP.

The subroutine STEP first sets up meteorological fields (SET_MET), solar zenith angle (ZENITH), and albedo fields (SET_ALBEDO). It then calculates cloud droplet number concentration (NUCLEATE_AG23), cloud optical properties (PARAM_CLDOPTICS_CALC). Finally, it calculates radiative fluxes by calling the subroutine RADCTL.

BIBLIOGRAPHY

Abbatt, J. P. D., Benz, S., Cziczo, D. J., Kanji, Z., Lohmann, U., and Möhler, O.: Solid ammonium sulfate aerosols as ice nuclei: A pathway for cirrus cloud formation, Science, 313, 1770-1773, DOI 10.1126/science.1129726, 2006.

Abdul-Razzak, H., and Ghan, S. J.: A parameterization of aerosol activation 2. Multiple aerosol types, Journal of Geophysical Research, 105, 6837-6844, 2000.

Abdul-Razzak, H., and Ghan, S. J.: A parameterization of aerosol activation - 3. Sectional representation, Journal of Geophysical Research, 107, 4026, doi:10.1029/2001JD000 483, 2002.

Ackerman, A. S., Kirkpatrick, M. P., Stevens, D. E., and Toon, O. B.: The impact of humidity above stratiform clouds on indirect aerosol climate forcing, Nature, 432, 1014-1017, doi:10.1038/Nature03174, 2004.

Adams, P. J., and Seinfeld, J. H.: Predicting global aerosol size distributions in general circulation models, Journal of Geophysical Research, 107, 4370, doi:10.1029/2001JD001 010, 2002.

Adams, P. J., and Seinfeld, J. H.: Disproportionate impact of particulate emissions on global cloud condensation nuclei concentrations, Geophysical Research Letters, 30, 1239, doi:10.1029/2002GL016303, 2003.

Albrecht, B. A.: Aerosols, cloud microphysics, and fractional cloudiness, Science, 245, 1227-1230, 1989.

Allan, J. D., Alfarra, M. R., Bower, K. N., Coe, H., Jayne, J. T., Worsnop, D. R., Aalto, P. P., Kulmala, M., Hyotylainen, T., Cavalli, F., and Laaksonen, A.: Size and composition measurements of background aerosol and new particle growth in a Finnish forest during QUEST 2 using an aerodyne aerosol mass spectrometer, Atmospheric Chemistry and Physics, 6, 315-327, 2006.

Andreae, M. O., Elbert, W., Cai, Y., Andreae, T. W., and Gras, J.: Non-sea-salt sulfate, methanesulfonate, and nitrate aerosol concentrations and size distributions at Cape Grim, Tasmania, Journal of Geophysical Research, 104, 21695-21706, 1999.

Andreae, M. O., Rosenfeld, D., Artaxo, P., Costa, A. A., Frank, G. P., Longo, K. M., and Silva-Dias, M. A. F.: Smoking rain clouds over the Amazon, Science, 303, 1337-1342, 2004.

Andres, R. J., and Kasgnoc, A. D.: A time-averaged inventory of subaerial volcanic sulfur emissions, Journal of Geophysical Research, 103, 25251-25261, 1998.

Archuleta, C. M., DeMott, P. J., and Kreidenweis, S. M.: Ice nucleation by surrogates for atmospheric mineral dust and mineral dust/sulfate particles at cirrus temperatures, Atmospheric Chemistry and Physics, 5, 2617-2634, 2005.

Arellano, A. F., Kasibhatla, P. S., Giglio, L., van der Werf, G. R., and Randerson, J. T.: Top-down estimates of global CO sources using MOPITT measurements, Geophysical Research Letters, 31, L01104, doi:10.1029/2003gl018609, 2004.

Arimoto, R., Duce, R. A., Savoie, D. L., Prospero, J. M., Talbot, R., Cullen, J. D., Tomza, U., Lewis, N. F., and Jay, B. J.: Relationships among aerosol constituents from Asia and the north Pacific during PEM-WEST A, Journal of Geophysical Research-Atmospheres, 101, 2011-2023, 1996.

Bacmeister, J. T., Eckermann, S. D., Tsias, A., Carslaw, K. S., and Peter, T.: Mesoscale temperature fluctuations induced by a spectrum of gravity waves: A comparison of parameterizations and their impact on stratospheric microphysics, Journal of Atmospheric Science, 56, 1913-1924, 1999.

Bauer, S. E., Wright, D. L., Koch, D., Lewis, E. R., McGraw, R., Chang, L. S., Schwartz, S. E., and Ruedy, R.: Matrix (Multiconfiguration Aerosol Tracker of Mixing State): An aerosol microphysical module for global atmospheric models, Atmos. Chem. Phys., 8, 6003-6035, 2008.

Beheng, K. D.: A parameterization of warm cloud microphysical conversion processes, Atmospheric Research, 33, 193-206, 1994.

Bodhaine, B. A.: Aerosol absorption-measurements at Barrow, Mauna-loa and the south-pole, Journal of Geophysical Research, 100, 8967-8975, 1995.

Bond, T. C., Streets, D. G., Yarber, K. F., Nelson, S. M., Woo, J. H., and Klimont, Z.: A technology-based global inventory of black and organic carbon emissions from combustion, Journal of Geophysical Research, 109, D14203, doi:10.1029/2003JD003697, 2004.

Boville, B. A., Rasch, P. J., Hack, J. J., and McCaa, J. R.: Representation of clouds and precipitation processes in the community atmosphere model version 3 (CAM3), Journal of Climate, 19, 2184-2198, 2006.

Brock, C. A., Washenfelder, R. A., Trainer, M., Ryerson, T. B., Wilson, J. C., Reeves, J. M., Huey, L. G., Holloway, J. S., Parrish, D. D., Hubler, G., and Fehsenfeld, F. C.:

Particle growth in the plumes of coal-fired power plants, Journal of Geophysical Research, 107, 4155, doi:10.1029/2001jd001062, 2002.

Burkhardt, U., Karcher, B., Ponater, M., Gierens, K., and Gettelman, A.: Contrail cirrus supporting areas in model and observations, Geophys Res Lett, 35, L16808, doi: 10.1029/2008gl034056, 2008.

Cakmur, R. V., Miller, R. L., Perlwitz, J., Geogdzhayev, I. V., Ginoux, P., Koch, D., Kohfeld, K. E., Tegen, I., and Zender, C. S.: Constraining the magnitude of the global dust cycle by minimizing the difference between a model and observations, Journal of Geophysical Research, 111, D06207, doi:10.1029/2005jd005791, 2006.

Cantrell, B. K., and Whitby, K. T.: Aerosol size distributions and aerosol volume formation for a coal-fired power-plant plume, Atmospheric Environment, 12, 323-333, 1978.

Cantrell, W., and Heymsfield, A.: Production of ice in tropospheric clouds - a review, Bulletin of the American Meteorological Society, 86, 795-807, 2005.

Chen, Y. L., Kreidenweis, S. M., McInnes, L. M., Rogers, D. C., and DeMott, P. J.: Single particle analyses of ice nucleating aerosols in the upper troposphere and lower stratosphere, Geophysical Research Letters, 25, 1391-1394, 1998.

Chen, T., Rossow, W. B., and Zhang, Y. C.: Radiative effects of cloud-type variations, Journal of Climate, 13, 264-286, 2000.

Chen, Y., and Penner, J. E.: Uncertainty analysis for estimates of the first indirect aerosol effect, Atmospheric Chemistry and Physics, 5, 2935-2948, 2005.

Chen, Y.: Aerosol indirect effects on clouds and global climate, PhD, Department of Atmospheric, Oceanic, and Space Sciences, University of Michigan, Ann Arbor, MI, 218 pp., 2006.

Chuang, C. C., Penner, J. E., Prospero, J. M., Grant, K. E., Rau, G. H., and Kawamoto, K.: Cloud susceptibility and the first aerosol indirect forcing: Sensitivity to black carbon and aerosol concentrations, Journal of Geophysical Research, 107, 4564, doi:10.1029/2000JD000215, 2002.

Chung, S. H., and Seinfeld, J. H.: Global distribution and climate forcing of carbonaceous aerosols, Journal of Geophysical Research, 107, 4407, doi:10.1029/2001JD001397, 2002.

Clarke, A. D., Uehara, T., and Porter, J. N.: Lagrangian evolution of an aerosol column during the Atlantic Stratocumulus Transition Experiment, Journal of Geophysical Research, 101, 4351-4362, 1996.

Clarke, A. D., Davis, D., Kapustin, V. N., Eisele, F., Chen, G., Paluch, I., Lenschow, D., Bandy, A. R., Thornton, D., Moore, K., Mauldin, L., Tanner, D., Litchy, M., Carroll,

M. A., Collins, J., and Albercook, C.: Particle nucleation in the tropical boundary layer and its coupling to marine sulfur sources, Science, 282, 89-92, 1998.

Clarke, A. D., and Kapustin, V. N.: A Pacific aerosol survey. Part I: A decade of data on particle production, transport, evolution, and mixing in the troposphere, Journal of the Atmospheric Sciences, 59, 363-382, 2002.

Clarke, A. D., Owens, S. R., and Zhou, J. C.: An ultrafine sea-salt flux from breaking waves: Implications for cloud condensation nuclei in the remote marine atmosphere, Journal of Geophysical Research, 111, D06202, doi:10.1029/2005JD006565, 2006.

Collins, W. D., Rasch, P. J., Eaton, B. E., Khattatov, B. V., Lamarque, J. F., and Zender, C. S.: Simulating aerosols using a chemical transport model with assimilation of satellite aerosol retrievals: Methodology for INDOEX, Journal of Geophysical Research, 106, 7313-7336, 2001.

Collins, W. D., Bitz, C. M., Blackmon, M. L., Bonan, G. B., Bretherton, C. S., Carton, J. A., Chang, P., Doney, S. C., Hack, J. J., Henderson, T. B., Kiehl, J. T., Large, W. G., McKenna, D. S., Santer, B. D., and Smith, R. D.: The community climate system model version 3 (CCSM3), Journal of Climate, 19, 2122-2143, 2006.

Collins, W. D., Rasch, P. J., Boville, B. A., Hack, J. J., McCaa, J. R., Williamson, D. L., Briegleb, B. P., Bitz, C. M., Lin, S. J., and Zhang, M. H.: The formulation and atmospheric simulation of the community atmosphere model version 3 (CAM3), Journal of Climate, 19, 2144-2161, 2006.

Cooke, W. F., Jennings, S. G., and Spain, T. G.: Black carbon measurements at mace head, 1989-1996, Journal of Geophysical Research, 102, 25339-25346, 1997.

Cziczo, D. J., Murphy, D. M., Hudson, P. K., and Thomson, D. S.: Single particle measurements of the chemical composition of cirrus ice residue during CRYSTAL-FACE, Journal of Geophysical Research, 109, D04201, doi:10.1029/2003JD004032, 2004.

d'Almeida, G., P.Koepke, and E. Shettle: Atmospheric aerosols : Global climatology and radiative characteristics A. Deepak Pub., Hampton, Va., USA 1991.

Dal Maso, M., Kulmala, M., Riipinen, I., Wagner, R., Hussein, T., Aalto, P. P., and Lehtinen, K. E. J.: Formation and growth of fresh atmospheric aerosols: Eight years of aerosol size distribution data from SMEAR II, Hyytiala, Finland, Boreal Environment Research, 10, 323-336, 2005.

de Reus, M., Dentener, F., Thomas, A., Borrmann, S., Ström, J., and Lelieveld, J.: Airborne observations of dust aerosol over the north atlantic ocean during ACE 2: Indications for heterogeneous ozone destruction, Journal of Geophysical Research, 105, 15263-15275, 2000.

Dean, S. M., Flowerdew, J., Lawrence, B. N., and Eckermann, S. D.: Parameterisation of orographic cloud dynamics in a GCM, Climate Dynamics, 28, 581-597, doi:10.1007/s00382-006-0202-0, 2007.

Demott, P. J.: An exploratory-study of ice nucleation by soot aerosols, Journal of Applied Meteorology, 29, 1072-1079, 1990.

DeMott, P. J., Rogers, D. C., and Kreidenweis, S. M.: The susceptibility of ice formation in upper tropospheric clouds to insoluble aerosol components, Journal of Geophysical Research, 102, 19575-19584, 1997.

DeMott, P. J., Chen, Y., Kreidenweis, S. M., Rogers, D. C., and Sherman, D. E.: Ice formation by black carbon particles, Geophysical Research Letters, 26, 2429-2432, 1999.

DeMott, P. J., Sassen, K., Poellot, M. R., Baumgardner, D., Rogers, D. C., Brooks, S. D., Prenni, A. J., and Kreidenweis, S. M.: African dust aerosols as atmospheric ice nuclei, Geophysical Research Letters, 30, 1732, doi:10.1029/2003GL017410, 2003.

DeMott, P.J.: Progress and Issues in Quantifying Ice Nucleation Involving Atmospheric Aerosols, presented at the 17th International Conference on Nucleation and Atmospheric Aerosols, Galway, Ireland, August 13-17, 2007.

Deng, M., and Mace, G. G.: Cirrus cloud microphysical properties and air motion statistics using cloud radar doppler moments: Water content, particle size, and sedimentation relationships, Geophysical Research Letters, 35, L17808, doi:10.1029/2008gl035054, 2008.

Denman, K. L., G. Brasseur, A. Chidthaisong, P. Ciais, P.M. Cox, R.E. Dickinson, D. Hauglustaine, C. Heinze, E. Holland, D. Jacob, U. Lohmann, S Ramachandran, P.L. da Silva Dias, S.C. Wofsy and X. Zhang: Couplings between changes in the climate system and biogeochemistry, in: Climate change 2007: The physical science basis. Contribution of working group I to the fourth assessment report of the intergovernmental panel on climate change, edited by: Solomon, S., D. Qin, M. Manning, Z. Chen, M. Marquis, K.B. Averyt, M.Tignor and H.L. Miller, Cambridge University Press, Cambridge, United Kingdom and New York, NY, USA., 2007.

Diner, D. J., Ackerman, T. P., Anderson, T. L., Bosenberg, J., Braverman, A. J., Charlson, R. J., Collins, W. D., Davies, R., Holben, B. N., Hostetler, C. A., Kahn, R. A., Martonchik, J. V., Menzies, R. T., Miller, M. A., Ogren, J. A., Penner, J. E., Rasch, P. J., Schwartz, S. E., Seinfeld, J. H., Stephens, G. L., Torres, O., Travis, L. D., Wielicki, B. A., and Yu, B.: Paragon - an integrated approach for characterizing aerosol climate impacts and environmental interactions, Bulletin of the American Meteorological Society, 85, 1491, doi:10.1175/Bams-85-10-1491, 2004.

Easter, R. C., Ghan, S. J., Zhang, Y., Saylor, R. D., Chapman, E. G., Laulainen, N. S., Abdul-Razzak, H., Leung, L. R., Bian, X. D., and Zaveri, R. A.: MIRAGE: Model

description and evaluation of aerosols and trace gases, Journal of Geophysical Research, 109, D20210, doi:10.1029/2004JD004571, 2004.

Feichter, J., Roeckner, E., Lohmann, U., and Liepert, B.: Nonlinear aspects of the climate response to greenhouse gas and aerosol forcing, Journal of Climate, 17, 2384-2398, 2004.

Feingold, G., and Chuang, P. Y.: Analysis of the influence of film-forming compounds on droplet growth: Implications for cloud microphysical processes and climate, Journal of the Atmospheric Sciences, 59, 2006-2018, 2002.

Feingold, G.: Modeling of the first indirect effect: Analysis of measurement requirements, Geophysical Research Letters, 30, 1997, doi: 10.1029/2003gl017967, 2003.

Feng, Y., and Penner, J. E.: Global modeling of nitrate and ammonium: Interaction of aerosols and tropospheric chemistry, Journal of Geophysical Research, 112, D01304, doi: 10.1029/2005jd006404, 2007.

Ferraro, R. R., Weng, F. Z., Grody, N. C., and Basist, A.: An eight-year (1987-1994) time series of rainfall, clouds, water vapor, snow cover, and sea ice derived from SSM/I measurements, Bulletin of the American Meteorological Society, 77, 891-905, 1996.

Field, P. R., Heymsfield, A. J., and Bansemer, A.: Shattering and particle interarrival times measured by optical array probes in ice clouds, Journal of Atmospheric and Oceanic Technology, 23, 1357-1371, 2006.

Forrest, J., Garber, R. W., and Newman, L.: Conversion rates in power-plant plumes based on filter pack data - the coal-fired cumberland plume, Atmospheric Environment, 15, 2273-2282, 1981.

Forster, P. M. D., and Shine, K. P.: Assessing the climate impact of trends in stratospheric water vapor, Geophysical Research Letters, 29, 1086, doi: 10.1029/2001gl013909, 2002.

Forster, P., Ramaswamy, V., Artaxo, P., Berntsen, T., Betts, R., Fahey, D. W., Haywood, J., Lean, J., Lowe, D. C., Myhre, G., Nganga, J., Prinn, R., Raga, G., Schulz, M., and Dorland, R. V.: Changes in atmospheric constituents and in radiative forcing, in: Climate change 2007: The physical science basis. Contribution of working group I to the fourth assessment report of the intergovernmental panel on climate change, edited by: Solomon, S., Qin, D., Manning, M., Chen, Z., Marquis, M., Averyt, K. B., Tignor, M., and Miller, H. L., Cambridge University Press, Cambridge, United Kingdom and New York, NY, USA, 2007.

Fridlind, A. M., Ackerman, A. S., Jensen, E. J., Heymsfield, A. J., Poellot, M. R., Stevens, D. E., Wang, D. H., Miloshevich, L. M., Baumgardner, D., Lawson, R. P., Wilson, J. C., Flagan, R. C., Seinfeld, J. H., Jonsson, H. H., VanReken, T. M.,

Varutbangkul, V., and Rissman, T. A.: Evidence for the predominance of mid-tropospheric aerosols as subtropical anvil cloud nuclei, Science, 304, 718-722, 2004.

Fritts, D. C., and Alexander, M. J.: Gravity wave dynamics and effects in the middle atmosphere, Reviews of Geophysics, 41, 1003, doi: 10.1029/2001rg000106, 2003.

Gallagher, M. W., Connolly, P. J., Whiteway, J., Figueras-Nieto, D., Flynn, M., Choularton, T. W., Bower, K. N., Cook, C., Busen, R., and Hacker, J.: An overview of the microphysical structure of cirrus clouds observed during EMERALD-1, Quarterly Journal of the Royal Meteorological Society, 131, 1143-1169, doi:10.1256/Qj.03.138, 2005.

Gary, B. L.: Mesoscale temperature fluctuations in the stratosphere, Atmospheric Chemistry and Physics, 6, 4577-4589, 2006.

Gary, B. L.: Mesoscale temperature fluctuations in the Southern Hemisphere stratosphere, Atmospheric Chemistry and Physics, 8, 4677-4681, 2008.

Gayet, J. F., Auriol, F., Minikin, A., Ström, J., Seifert, M., Krejci, R., Petzold, A., Febvre, G., and Schumann, U.: Quantitative measurement of the microphysical and optical properties of cirrus clouds with four different in situ probes: Evidence of small ice crystals, Geophysical Research Letters, 29, 2230, doi:10.1029/2001gl014342, 2002.

Gayet, J. F., Ovarlez, J., Shcherbakov, V., Ström, J., Schumann, U., Minikin, A., Auriol, F., Petzold, A., and Monier, M.: Cirrus cloud microphysical and optical properties at southern and northern midlatitudes during the INCA experiment, Journal of Geophysical Research, 109, D20206, doi: 10.1029/2004jd004803, 2004.

Gayet, J. F., Shcherbakov, V., Mannstein, H., Minikin, A., Schumann, U., Ström, J., Petzold, A., Ovarlez, J., and Immler, F.: Microphysical and optical properties of midlatitude cirrus clouds observed in the southern hemisphere during INCA, Quarterly Journal of the Royal Meteorological Society, 132, 2719-2748, doi:10.1256/Qj.05.162, 2006.

Gerber, H. E.: Relative-humidity parameterization of the navy aerosol model (NAM). NRL rep. 8956, Naval Res. Lab., Washington, D. C., 13, 1985.

Gettelman, A., Morrison, H., and Ghan, S. J.: A new two-moment bulk stratiform cloud microphysics scheme in the community atmosphere model, version 3 (CAM3). Part II: Single-colunm and global results, Journal of Climate, 21, 3660-3679, 2008.

Ghan, S. J., Leung, L. R., Easter, R. C., and AbdulRazzak, K.: Prediction of cloud droplet number in a general circulation model, Journal of Geophysical Research, 102, 21777-21794, 1997.

Ghan, S., Laulainen, N., Easter, R., Wagener, R., Nemesure, S., Chapman, E., Zhang, Y., and Leung, R.: Evaluation of aerosol direct radiative forcing in MIRAGE, Journal of Geophysical Research, 106, 5295-5316, 2001.

Ghan, S. J., Easter, R. C., Chapman, E. G., Abdul-Razzak, H., Zhang, Y., Leung, L. R., Laulainen, N. S., Saylor, R. D., and Zaveri, R. A.: A physically based estimate of radiative forcing by anthropogenic sulfate aerosol, Journal of Geophysical Research, 106, 5279-5293, 2001.

Ghan, S. J., and Schwartz, S. E.: Aerosol properties and processes - a path from field and laboratory measurements to global climate models, Bulletin of the American Meteorological Society, 88, 1059-1083, doi: 10.1175/Bams-88-7-1059, 2007.

Gierens, K.: On the transition between heterogeneous and homogeneous freezing, Atmospheric Chemistry and Physics, 3, 437-446, 2003.

Ginoux, P., Chin, M., Tegen, I., Prospero, J. M., Holben, B., Dubovik, O., and Lin, S. J.: Sources and distributions of dust aerosols simulated with the GOCART model, Journal of Geophysical Research, 106, 20255-20273, 2001.

Ginoux, P., Prospero, J. M., Torres, O., and Chin, M.: Long-term simulation of global dust distribution with the GOCART model: Correlation with north Atlantic oscillation, Environ Modell Softw, 19, 113-128, 2004.

Giorgi, F., and Chameides, W. L.: Rainout lifetimes of highly soluble aerosols and gases as inferred from simulations with a general-circulation model, Journal of Geophysical Research, 91, 14367-14376, 1986.

Gong, S. L., Barrie, L. A., and Blanchet, J. P.: Modeling sea-salt aerosols in the atmosphere .1. Model development, Journal of Geophysical Research, 102, 3805-3818, 1997.

Gong, S. L., Barrie, L. A., Blanchet, J. P., von Salzen, K., Lohmann, U., Lesins, G., Spacek, L., Zhang, L. M., Girard, E., Lin, H., Leaitch, R., Leighton, H., Chylek, P., and Huang, P.: Canadian aerosol module: A size-segregated simulation of atmospheric aerosol processes for climate and air quality models - 1. Module development, Journal of Geophysical Research, 108, 4007, doi: 10.1029/2001JD002002, 2003.

Gorbunov, B., Baklanov, A., Kakutkina, N., Windsor, H. L., and Toumi, R.: Ice nucleation on soot particles, Journal of Aerosol Science, 32, 199-215, 2001.

Grabowski, W. W.: Cloud microphysics and the tropical climate: Cloud-resolving model perspective, Journal of Climate, 13, 2306-2322, 2000.

Greenwald, T. J., Stephens, G. L., Vonderhaar, T. H., and Jackson, D. L.: A physical retrieval of cloud liquid water over the global oceans using special sensor microwave imager (SSM/I) observations, Journal of Geophysical Research, 98, 18471-18488, 1993.

Guenther, A., Hewitt, C. N., Erickson, D., Fall, R., Geron, C., Graedel, T., Harley, P., Klinger, L., Lerdau, M., Mckay, W. A., Pierce, T., Scholes, B., Steinbrecher, R., Tallamraju, R., Taylor, J., and Zimmerman, P.: A global-model of natural volatile

organic-compound emissions, Journal of Geophysical Research, 100, 8873-8892, 1995.

Guo, H., Penner, J. E., Herzog, M., and Pawlowska, H.: Examination of the aerosol indirect effect under contrasting environments during the ACE-2 experiment, Atmospheric Chemistry and Physics, 7, 535-548, 2007.

Haag, W., Kärcher, B., Ström, J., Minikin, A., Lohmann, U., Ovarlez, J., and Stohl, A.: Freezing thresholds and cirrus cloud formation mechanisms inferred from in situ measurements of relative humidity, Atmospheric Chemistry and Physics, 3, 1791-1806, 2003.

Haag, W., and Kärcher, B.: The impact of aerosols and gravity waves on cirrus clouds at midlatitudes, Journal of Geophysical Research, 109, D12202, doi:10.1029/2004JD004579, 2004.

Hack, J. J.: Parameterization of moist convection in the national center for atmospheric research community climate model (ccm2), Journal of Geophysical Research, 99, 5551-5568, 1994.

Hall, W. D., and Pruppacher, H. R.: Survival of ice particles falling from cirrus clouds in subsaturated air, Journal of the Atmospheric Sciences, 33, 1995-2006, 1976.

Han, Q. Y., Rossow, W. B., Chou, J., and Welch, R. M.: Global variation of column droplet concentration in low-level clouds, Geophysical Research Letter, 25, 1419-1422, 1998.

Han, Q. Y., Rossow, W. B., and Lacis, A. A.: Near-global survey of effective droplet radii in liquid water clouds using ISCCP data, Journal of Climate, 7, 465-497, 1994.

Hansen, J., Sato, M., and Ruedy, R.: Radiative forcing and climate response, Journal of Geophysical Research, 102, 6831-6864, 1997.

Hansen, J., and Nazarenko, L.: Soot climate forcing via snow and ice albedos, Proceedings of the National Academy of Sciences of the United States of America, 101, 423-428, doi:10.1073/pnas.2237157100, 2004.

Harrington, D. Y., and Kreidenweis, S. M.: Simulations of sulfate aerosol dynamics - I. Model description, Atmospheric Environment, 32, 1691-1700, 1998.

He, Y., and Ding, C.: Coupling multi-component models with mph on distributed memory computer architectures, International Journal of High Performance Computing Applications, 19, 329-340, 2005.

Heald, C. L., Jacob, D. J., Park, R. J., Russell, L. M., Huebert, B. J., Seinfeld, J. H., Liao, H., and Weber, R. J.: A large organic aerosol source in the free troposphere missing from current models, Geophysical Research Letters, 32, L18809, doi:10.1029/2005gl023831, 2005.

Hegg, D. A., and Hobbs, P. V.: Measurements of gas-to-particle conversion in the plumes from 5 coal-fired electric-power plants, Atmospheric Environment, 14, 99-116, 1980.

Heintzenberg, J., Covert, D. C., and Van Dingenen, R.: Size distribution and chemical composition of marine aerosols: A compilation and review, Tellus Series B-Chemical and Physical Meteorology, 52, 1104-1122, 2000.

Hendricks, J., Kärcher, B., Dopelheuer, A., Feichter, J., Lohmann, U., and Baumgardner, D.: Simulating the global atmospheric black carbon cycle: A revisit to the contribution of aircraft emissions, Atmospheric Chemistry and Physics, 4, 2521-2541, 2004.

Hendricks, J., Kärcher, B., Lohmann, U., and Ponater, M.: Do aircraft black carbon emissions affect cirrus clouds on the global scale? Geophysical Research Letters, 32, L12814, doi:10.1029/2005gl022740, 2005.

Henning, S., Bojinski, S., Diehl, K., Ghan, S., Nyeki, S., Weingartner, E., Wurzler, S., and Baltensperger, U.: Aerosol partitioning in natural mixed-phase clouds, Geophysical Research Letters, 31, L06101, doi:10.1029/2003gl019025, 2004.

Herzog, M., Weisenstein, D. K., and Penner, J. E.: A dynamic aerosol module for global chemical transport models: Model description, Journal of Geophysical Research, 109, D18202, doi:10.1029/2003jd004405, 2004.

Hewitt, C. N.: The atmospheric chemistry of sulphur and nitrogen in power station plumes, Atmospheric Environment, 35, 1155-1170, 2001.

Heymsfield, A. J.: Precipitation development in stratiform ice clouds - microphysical and dynamical study, Journal of the Atmospheric Sciences, 34, 367-381, 1977.

Heymsfield, A. J., and Sabin, R. M.: Cirrus crystal nucleation by homogeneous freezing of solution droplets, Journal of the Atmospheric Sciences, 46, 2252-2264, 1989.

Hobbs, P. V., Hegg, D. A., Eltgroth, M. W., and Radke, L. F.: Evolution of particles in the plumes of coal-fired power-plants .1. Deductions from field-measurements, Atmospheric Environment, 13, 935-951, 1979.

Holtslag, A. A. M., and Boville, B. A.: Local versus nonlocal boundary-layer diffusion in a global climate model, Journal of Climate, 6, 1825-1842, 1993.

Hoppel, W. A., Frick, G. M., Fitzgerald, J. W., and Wattle, B. J.: A cloud chamber study of the effect that nonprecipitating water clouds have on the aerosol-size distribution, Aerosol Science and Technology, 20, 1-30, 1994.

Hopper, J. F., Worthy, D. E. J., Barrie, L. A., and Trivett, N. B. A.: Atmospheric observations of aerosol black carbon, carbon-dioxide, and methane in the high arctic, Atmospheric Environment, 28, 3047-3054, 1994.

Hoyle, C. R., Luo, B. P., and Peter, T.: The origin of high ice crystal number densities in cirrus clouds, Journal of the Atmospheric Sciences, 62, 2568-2579, 2005.

Hung, H. M., Malinowski, A., and Martin, S. T.: Kinetics of heterogeneous ice nucleation on the surfaces of mineral dust cores inserted into aqueous ammonium sulfate particles, Journal of Physical Chemistry A, 107, 1296-1306, doi:10.1021/JP021593Y, 2003.

Hurrell, J. W., Hack, J. J., Phillips, A. S., Caron, J., and Yin, J.: The dynamical simulation of the community atmosphere model version 3 (CAM3), Journal of Climate, 19, 2162-2183, 2006.

Immler, F., Kruger, K., Fujiwara, M., Verver, G., Rex, M., and Schrems, O.: Correlation between equatorial kelvin waves and the occurrence of extremely thin ice clouds at the tropical tropopause, Atmospheric Chemistry and Physics, 8, 4019-4026, 2008.

IPCC: Climate change 2007: The physical science basis. Contribution of working group I to the fourth assessment report of the intergovernmental panel on climate change, edited by: Solomon, S., D. Qin, M. Manning, Z. Chen, M. Marquis, K.B. Averyt, M. Tignor and H.L. Miller, Cambridge University Press, 996 pp., 2007.

Ito, A., and Penner, J. E.: Global estimates of biomass burning emissions based on satellite imagery for the year 2000, Journal of Geophysical Research, 109, D14S05, doi:10.1029/2003jd004423, 2004.

Ito, A., and Penner, J. E.: Historical emissions of carbonaceous aerosols from biomass and fossil fuel burning for the period 1870-2000, Global Biogeochemical Cycle, 19, GB2028, doi:10.1029/2004GB002374, 2005.

Jensen, E. J., Kinne, S., and Toon, O. B.: Tropical cirrus cloud radiative forcing - sensitivity studies, Geophysical Research Letters, 21, 2023-2026, 1994.

Jensen, E. J., Toon, O. B., Westphal, D. L., Kinne, S., and Heymsfield, A. J.: Microphysical modeling of cirrus .2. Sensitivity studies, Journal of Geophysical Research, 99, 10443-10454, 1994.

Jensen, E. J., Toon, O. B., Westphal, D. L., Kinne, S., and Heysmfield, A. J.: Microphysical modeling of cirrus .1. Comparison with 1986 fire IFO measurements, Journal of Geophysical Research, 99, 10421-10442, 1994.

Jensen, E. J., and Toon, O. B.: The potential impact of soot particles from aircraft exhaust on cirrus clouds, Geophysical Research Letters, 24, 249-252, 1997.

Jensen, E., and Pfister, L.: Transport and freeze-drying in the tropical tropopause layer, Journal of Geophysical Research, 109, D02207, doi: 10.1029/2003JD004022, 2004.

Jensen, E. J., Pfister, L., Bui, T. V., Lawson, P., Baker, B., Mo, Q., Baumgardner, D., Weinstock, E. M., Smith, J. B., Moyer, E. J., Hanisco, T. F., Sayres, D. S., St Clair, J.

M., Alexander, M. J., Toon, O. B., and Smith, J. A.: Formation of large (similar or equal to 100 μm) ice crystals near the tropical tropopause, Atmospheric Chemistry and Physics, 8, 1621-1633, 2008.

Jiang, H. L., and Cotton, W. R.: A diagnostic study of subgrid-scale activation, Journal of Geophysical Research, 110, D16107, doi:10.1029/2004JD005722, 2005.

Jones, A., Roberts, D. L., Woodage, M. J., and Johnson, C. E.: Indirect sulphate aerosol forcing in a climate model with an interactive sulphur cycle, Journal of Geophysical Research, 106, 20293-20310, 2001.

Joos, H., Spichtinger, P., Lohmann, U., Gayet, J. F., and Minikin, A.: Orographic cirrus in the global climate model ECHAM5, Journal of Geophysical Research, 113, D18205, doi:10.1029/2007jd009605, 2008.

Kärcher, B., and Lohmann, U.: A parameterization of cirrus cloud formation: Homogeneous freezing of supercooled aerosols, Journal of Geophysical Research, 107, 4010, doi: 10.1029/2001jd000470, 2002.

Kärcher, B.: Simulating gas-aerosol-cirrus interactions: Process-oriented microphysical model and applications, Atmospheric Chemistry and Physics, 3, 1645-1664, 2003.

Kärcher, B., and Ström, J.: The roles of dynamical variability and aerosols in cirrus cloud formation, Atmospheric Chemistry and Physics, 3, 823-838, 2003.

Kärcher, B., Hendricks, J., and Lohmann, U.: Physically based parameterization of cirrus cloud formation for use in global atmospheric models, Journal of Geophysical Research, 111, D01205, doi: 10.1029/2005JD006219, 2006.

Kärcher, B., Möhler, O., DeMott, P. J., Pechtl, S., and Yu, F.: Insights into the role of soot aerosols in cirrus cloud formation, Atmospheric Chemistry and Physics, 7, 4203-4227, 2007.

Kärcher, B., and Burkhardt, U.: A cirrus cloud scheme for general circulation models, Quarterly Journal of the Royal Meteorological Society, 134, 1439-1461, doi: 10.1002/Qj.301, 2008.

Kay, J. E., and Wood, R.: Timescale analysis of aerosol sensitivity during homogeneous freezing and implications for upper tropospheric water vapor budgets, Geophysical Research Letters, 35, L10809, doi: 10.1029/2007gl032628, 2008.

Kerminen, V. M., Virkkula, A., Hillamo, R., Wexler, A. S., and Kulmala, M.: Secondary organics and atmospheric cloud condensation nuclei production, Journal of Geophysical Research, 105, 9255-9264, 2000.

Kerminen, V. M., and Kulmala, M.: Analytical formulae connecting the "Real" And the "Apparent" Nucleation rate and the nuclei number concentration for atmospheric nucleation events, Journal of Aerosol Science, 33, 609-622, 2002.

Kerminen, V. M., Anttila, T., Lehtinen, K. E. J., and Kulmala, M.: Parameterization for atmospheric new-particle formation: Application to a system involving sulfuric acid and condensable water-soluble organic vapors, Aerosol Science and Technology, 38, 1001-1008, doi:10.1080/027868290519085, 2004.

Kettle, A. J., Andreae, M. O., Amouroux, D., Andreae, T. W., Bates, T. S., Berresheim, H., Bingemer, H., Boniforti, R., Curran, M. A. J., DiTullio, G. R., Helas, G., Jones, G. B., Keller, M. D., Kiene, R. P., Leck, C., Levasseur, M., Malin, G., Maspero, M., Matrai, P., McTaggart, A. R., Mihalopoulos, N., Nguyen, B. C., Novo, A., Putaud, J. P., Rapsomanikis, S., Roberts, G., Schebeske, G., Sharma, S., Simo, R., Staubes, R., Turner, S., and Uher, G.: A global database of sea surface dimethylsulfide (DMS) measurements and a procedure to predict sea surface DMS as a function of latitude, longitude, and month, Global Biogeochemical Cycle, 13, 399-444, 1999.

Kettle, A. J., and Andreae, M. O.: Flux of dimethylsulfide from the oceans: A comparison of updated data seas and flux models, Journal of Geophysical Research, 105, 26793-26808, 2000.

Khain, A., Rosenfeld, D., and Pokrovsky, A.: Aerosol impact on the dynamics and microphysics of deep convective clouds, Quarterly Journal of the Royal Meteorological Society, 131, 2639-2663, Doi 10.1256/Qj.04.62, 2005.

Khvorostyanov, V. I., Morrison, H., Curry, J. A., Baumgardner, D., and Lawson, P.: High supersaturation and modes of ice nucleation in thin tropopause cirrus: Simulation of the 13 July 2002 Cirrus Regional Study of Tropical Anvils and Cirrus layers case, Journal of Geophysical Research, 111, D02201, doi:10.1029/2004JD005235, 2006.

Kiehl, J. T., and Trenberth, K. E.: Earth's annual global mean energy budget, Bulletin of the American Meteorological Society, 78, 197-208, 1997.

Kiehl, J. T.: Twentieth century climate model response and climate sensitivity, Geophysical Research Letters, 34, L22710, doi:10.1029/2007gl031383, 2007.

King, M. D., Menzel, W. P., Kaufman, Y. J., Tanre, D., Gao, B. C., Platnick, S., Ackerman, S. A., Remer, L. A., Pincus, R., and Hubanks, P. A.: Cloud and aerosol properties, precipitable water, and profiles of temperature and water vapor from MODIS, IEEE T Geosci Remote, 41, 442-458, doi:10.1109/Tgrs.2002.808226, 2003.

Kinne, S., Schulz, M., Textor, C., Guibert, S., Balkanski, Y., Bauer, S. E., Berntsen, T., Berglen, T. F., Boucher, O., Chin, M., Collins, W., Dentener, F., Diehl, T., Easter, R., Feichter, J., Fillmore, D., Ghan, S., Ginoux, P., Gong, S., Grini, A., Hendricks, J. E., Herzog, M., Horowitz, L., Isaksen, L., Iversen, T., Kirkavag, A., Kloster, S., Koch, D., Kristjansson, J. E., Krol, M., Lauer, A., Lamarque, J. F., Lesins, G., Liu, X., Lohmann, U., Montanaro, V., Myhre, G., Penner, J. E., Pitari, G., Reddy, S., Seland, O., Stier, P., Takemura, T., and Tie, X.: An AeroCom initial assessment - optical properties in aerosol component modules of global models, Atmospheric Chemistry and Physics, 6, 1815-1834, 2006.

Klein, S. A., and Jakob, C.: Validation and sensitivities of frontal clouds simulated by the ecmwf model, Monthly Weather Review, 127, 2514-2531, 1999.

Koop, T., Luo, B. P., Tsias, A., and Peter, T.: Water activity as the determinant for homogeneous ice nucleation in aqueous solutions, Nature, 406, 611-614, 2000.

Koponen, I. K., Virkkula, A., Hillamo, R., Kerminen, V. M., and Kulmala, M.: Number size distributions and concentrations of the continental summer aerosols in Queen Maud land, Antarctica, Journal of Geophysical Research, 108, 4587, doi:10.1029/2003jd003614, 2003.

Korhonen, P., Kulmala, M., Laaksonen, A., Viisanen, Y., McGraw, R., and Seinfeld, J. H.: Ternary nucleation of H_2SO_4, NH_3, and H_2O in the atmosphere, Journal of Geophysical Research, 104, 26349-26353, 1999.

Krämer, M., Schiller, C., Afchine, A., Bauer, R., Gensch, I., Mangold, A., Schlicht, S., Spelten, N., Sitnikov, N., Borrmann, S., de Reus, M., and Spichtinger, P.: Ice supersaturations and cirrus cloud crystal numbers, Atmos. Chem. Phys. Discuss., 8, 21089-21128, 2008.

Kuang, C., McMurry, P. H., McCormick, A. V., and Eisele, F. L.: Dependence of nucleation rates on sulfuric acid vapor concentration in diverse atmospheric locations, Journal of Geophysical Research, 113, D10209, doi: 10.1029/2007JD009253, 2008.

Kulmala, M., Vehkamäki, H., Petaja, T., Dal Maso, M., Lauri, A., Kerminen, V. M., Birmili, W., and McMurry, P. H.: Formation and growth rates of ultrafine atmospheric particles: A review of observations, Journal of Aerosol Science, 35, 143-176, doi:10.1016/j.jaerosci.2003.10.003, 2004.

Kulmala, M., Lehtinen, K. E. J., and Laaksonen, A.: Cluster activation theory as an explanation of the linear dependence between formation rate of 3nm particles and sulphuric acid concentration, Atmospheric Chemistry and Physics, 6, 787-793, 2006.

Kulmala, M., Riipinen, I., Sipila, M., Manninen, H. E., Petaja, T., Junninen, H., Dal Maso, M., Mordas, G., Mirme, A., Vana, M., Hirsikko, A., Laakso, L., Harrison, R. M., Hanson, I., Leung, C., Lehtinen, K. E. J., and Kerminen, V. M.: Toward direct measurement of atmospheric nucleation, Science, 318, 89-92, 2007.

Laaksonen, A., Hamed, A., Joutsensaari, J., Hiltunen, L., Cavalli, F., Junkermann, W., Asmi, A., Fuzzi, S., and Facchini, M. C.: Cloud condensation nucleus production from nucleation events at a highly polluted region, Geophysical Research Letters, 32, L06812, doi:10.1029/2004GL022092, 2005.

Lance, S., Nenes, A., and Rissman, T. A.: Chemical and dynamical effects on cloud droplet number: Implications for estimates of the aerosol indirect effect, Journal of Geophysical Research, 109, D22208, doi:10.1029/2004jd004596, 2004.

Lauer, A., Hendricks, J., Ackermann, I., Schell, B., Hass, H., and Metzger, S.: Simulating aerosol microphysics with the ECHAM/MADE GCM - Part I: Model description and comparison with observations, Atmospheric Chemistry and Physics, 5, 3251-3276, 2005.

Li, J. L., Waliser, D. E., Jiang, J. H., Wu, D. L., Read, W., Waters, J. W., Tompkins, A. M., Donner, L. J., Chern, J. D., Tao, W. K., Atlas, R., Gu, Y., Liou, K. N., Del Genio, A., Khairoutdinov, M., and Gettelman, A.: Comparisons of eos mls cloud ice measurements with ECMWF analyses and GCM simulations: Initial results, Geophysical Research Letters, 32, L18710, doi:10.1029/2005GL023788 2005.

Li, J. L., Jiang, J. H., Waliser, D. E., and Tompkins, A. M.: Assessing consistency between EOS MLS and ECMWF analyzed and forecast estimates of cloud ice, Geophysical Research Letters, 34, L08701, doi:10.1029/2006GL029022, 2007.

Lihavainen, H., Kerminen, V. M., Komppula, M., Hatakka, J., Aaltonen, V., Kulmala, M., and Viisanen, Y.: Production of "Potential" Cloud condensation nuclei associated with atmospheric new-particle formation in northern Finland, Journal of Geophysical Research, 108, 4782, doi:10.1029/2003JD003887, 2003.

Lin, S. J., and Rood, R. B.: Multidimensional flux-form semi-Lagrangian transport schemes, Monthly Weather Review, 124, 2046-2070, 1996.

LIss, P. S., and Merlivat, L.: Air-sea gas exchange rates: Introduction and synthesis, in: The role of air-sea gas exchange in geochemical cycling, edited by: Menard, P. B., Springer, New York, 113-127, 1986.

Liu, H. Y., Jacob, D. J., Bey, I., and Yantosca, R. M.: Constraints from pb-210 and be-7 on wet deposition and transport in a global three-dimensional chemical tracer model driven by assimilated meteorological fields, Journal of Geophysical Research, 106, 12109-12128, 2001.

Liu, X. H., and Penner, J. E.: Effect of Mount Pinatubo H_2SO_4/H_2O aerosol on ice nucleation in the upper troposphere using a global chemistry and transport model, Journal of Geophysical Research, 107, 4141, doi: 10.1029/2001jd000455, 2002.

Liu, X. H., and Penner, J. E.: Ice nucleation parameterization for global models, Meteorologische Zeitschrift, 14, 499-514, doi:10.1127/0941-2948/2005/0059, 2005.

Liu, X. H., Penner, J. E., and Herzog, M.: Global modeling of aerosol dynamics: Model description, evaluation, and interactions between sulfate and nonsulfate aerosols, Journal of Geophysical Research, 110, D18206, doi: 10.1029/2004JD005674, 2005.

Liu, X., Penner, J. E., Ghan, S. J., and Wang, M.: Inclusion of ice microphysics in the ncar community atmospheric model version 3 (CAM3), Journal of Climate, 20, 4526-4547, 2007.

Liu, X. H., Penner, J. E., Das, B. Y., Bergmann, D., Rodriguez, J. M., Strahan, S., Wang, M. H., and Feng, Y.: Uncertainties in global aerosol simulations: Assessment using three meteorological data sets, Journal of Geophysical Research, 112, D11212, doi: 10.1029/2006jd008216, 2007.

Liu, X. H., Xie, S. C., and Ghan, S. J.: Evaluation of a new mixed-phase cloud microphysics parameterization with CAM3 single-column model and M-PACE observations, Geophysical Research Letters, 34, L23712, doi: 10.1029/2007GL031446, 2007.

Liu, X. H., Penner, J. E., and Wang, M. H.: Influence of anthropogenic sulfate and black carbon on upper tropospheric clouds in the ncar CAM3 model coupled to the IMPACT global aerosol model, Journal of Geophysical Research, 114, D03204, doi: 10.1029/2008JD010492, 2009.

Lohmann, U., Feichter, J., Chuang, C. C., and Penner, J. E.: Prediction of the number of cloud droplets in the ECHAM GCM, Journal of Geophysical Research, 104, 9169-9198, 1999.

Lohmann, U.: A glaciation indirect aerosol effect caused by soot aerosols, Geophysical Research Letters, 29, 1052, doi: 10.1029/2001gl014357, 2002.

Lohmann, U., and Kärcher, B.: First interactive simulations of cirrus clouds formed by homogeneous freezing in the ECHAM general circulation model, Journal of Geophysical Research, 107, 4105, doi: 10.1029/2001jd000767, 2002.

Lohmann, U., and Lesins, G.: Stronger constraints on the anthropogenic indirect aerosol effect, Science, 298, 1012-1015, 2002.

Lohmann, U., and Feichter, J.: Global indirect aerosol effects: A review, Atmospheric Chemistry and Physics, 5, 715-737, 2005.

Lohmann, U., and Diehl, K.: Sensitivity studies of the importance of dust ice nuclei for the indirect aerosol effect on stratiform mixed-phase clouds, Journal of the Atmospheric Sciences, 63, 968-982, 2006.

Lohmann, U., Koren, I., and Kaufman, Y. J.: Disentangling the role of microphysical and dynamical effects in determining cloud properties over the Atlantic, Geophysical Research Letters, 33, L09802, doi: 10.1029/2005gl024625, 2006.

Lohmann, U., Stier, P., Hoose, C., Ferrachat, S., Kloster, S., Roeckner, E., and Zhang, J.: Cloud microphysics and aerosol indirect effects in the global climate model ECHAM5-HAM, Atmospheric Chemistry and Physics, 7, 3425-3446, 2007.

Lucas, D. D., and Akimoto, H.: Evaluating aerosol nucleation parameterizations in a global atmospheric model, Geophysical Research Letters, 33, L10808, doi:10.1029/2006GL025672, 2006.

Mace, G. G., Clothiaux, E. E., and Ackerman, T. P.: The composite characteristics of cirrus clouds: Bulk properties revealed by one year of continuous cloud radar data, Journal of Climate, 14, 2185-2203, 2001.

Makkonen, R., Asmi, A., Korhonen, H., Kokkola, H., JÃ¤rvenoja, S., RÃ¤isÃ¤nen, P., Lehtinen, K. E. J., Laaksonen, A., Kerminen, V. M., JÃ¤rvinen, H., Lohmann, U., Bennartz, R., Feichter, J., and Kulmala, M.: Sensitivity of aerosol concentrations and cloud properties to nucleation and secondary organic distribution in ECHAM5-HAM global circulation model, Atmos. Chem. Phys., 9, 1747-1766, 2009.

Malm, W. C., Pitchford, M. L., Scuggs, M., Sisler, J. F., Ames, R., Copeland, S., Gebhart, K. A., and Day, D. E.: Spatial and seasonal patterns and temporal variability of haze and its constituents in the united states: Report iii, Coop. Inst. for Res., Colorado State University, Fort Collins, 2000.

Manabe, S., and Moller, F.: On the radiative equilibrium and heat balance of the atmosphere, Monthly Weather Review, 503-532, 1961.

Manabe, S., and Wetheral.Rt: Thermal equilibrium of atmosphere with a given distribution of relative humidity, Journal of the Atmospheric Sciences, 24, 241-&, 1967.

Marcolli, C., Gedamke, S., Peter, T., and Zobrist, B.: Efficiency of immersion mode ice nucleation on surrogates of mineral dust, Atmospheric Chemistry and Physics, 7, 5081-5091, 2007.

Mari, C., Jacob, D. J., and Bechtold, P.: Transport and scavenging of soluble gases in a deep convective cloud, Journal of Geophysical Research, 105, 22255-22267, 2000.

Marshak, A., Platnick, S., Varnai, T., Wen, G. Y., and Cahalan, R. F.: Impact of three-dimensional radiative effects on satellite retrievals of cloud droplet sizes, Journal of Geophysical Research, 111, D09207, doi:10.1029/2005jd006686, 2006.

Martensson, E. M., Nilsson, E. D., de Leeuw, G., Cohen, L. H., and Hansson, H. C.: Laboratory simulations and parameterization of the primary marine aerosol production, Journal of Geophysical Research, 108, 4297, doi:10.1029/2002jd002263, 2003.

McGraw, R.: Description of aerosol dynamics by the quadrature method of moments, Aerosol Science and Technology, 27, 255-265, 1997.

Mcmurry, P. H., and Friedlander, S. K.: New particle formation in the presence of an aerosol, Atmospheric Environment, 13, 1635-1651, 1979.

McNaughton, C. S., Clarke, A. D., Howell, S. G., Moore, K. G., Brekhovskikh, V., Weber, R. J., Orsini, D. A., Covert, D. S., Buzorius, G., Brechtel, F. J., Carmichael, G. R., Tang, Y. H., Eisele, F. L., Mauldin, R. L., Bandy, A. R., Thornton, D. C., and Blomquist, B.: Spatial distribution and size evolution of particles in Asian outflow:

Significance of primary and secondary aerosols during ACE-Asia and TRACE-P, Journal of Geophysical Research, 109, D19S06, doi:10.1029/2003JD003528, 2004.

Ming, Y., Ramaswamy, V., Ginoux, P. A., Horowitz, L. W., and Russell, L. M.: Geophysical fluid dynamics laboratory general circulation model investigation of the indirect radiative effects of anthropogenic sulfate aerosol, Journal of Geophysical Research, 110, D22206, doi:10.1029/2005JD006161, 2005.

Ming, Y., Ramaswamy, V., Donner, L. J., Phillips, V. T. J., Klein, S. A., Ginoux, P. A., and Horowitz, L. W.: Modeling the interactions between aerosols and liquid water clouds with a self-consistent cloud scheme in a general circulation model, Journal of the Atmospheric Sciences, 64, 1189-1209, doi:10.1175/Jas3874.1, 2007.

Minikin, A., Petzold, A., Ström, J., Krejci, R., Seifert, M., van Velthoven, P., Schlager, H., and Schumann, U.: Aircraft observations of the upper tropospheric fine particle aerosol in the northern and southern hemispheres at midlatitudes, Geophysical Research Letters, 30, 1503, doi:10.1029/2002gl016458, 2003.

Mitchell, D. L., Rasch, P., Ivanova, D., McFarquhar, G., and Nousiainen, T.: Impact of small ice crystal assumptions on ice sedimentation rates in cirrus clouds and GCM simulations, Geophysical Research Letters, 35, L09806, doi: 10.1029/2008GL033552 2008.

Möhler, O., Buttner, S., Linke, C., Schnaiter, M., Saathoff, H., Stetzer, O., Wagner, R., Kramer, M., Mangold, A., Ebert, V., and Schurath, U.: Effect of sulfuric acid coating on heterogeneous ice nucleation by soot aerosol particles, Journal of Geophysical Research, 110, D11210, doi:10.1029/2004JD005169, 2005.

Möhler, O., Field, P. R., Connolly, P., Benz, S., Saathoff, H., Schnaiter, M., Wagner, R., Cotton, R., Kramer, M., Mangold, A., and Heymsfield, A. J.: Efficiency of the deposition mode ice nucleation on mineral dust particles, Atmospheric Chemistry and Physics, 6, 3007-3021, 2006.

Morrison, H., Curry, J. A., and Khvorostyanov, V. I.: A new double-moment microphysics parameterization for application in cloud and climate models. Part I: Description, Journal of the Atmospheric Sciences, 62, 1665-1677, 2005.

Murphy, D. M., and Koop, T.: Review of the vapour pressures of ice and supercooled water for atmospheric applications, Quarterly Journal of the Royal Meteorological Society, 131, 1539-1565, doi:10.1256/Qj.04.94, 2005.

Myhre, G., Grini, A., Haywood, J. M., Stordal, F., Chatenet, B., Tanre, D., Sundet, J. K., and Isaksen, I. S. A.: Modeling the radiative impact of mineral dust during the Saharan dust experiment (SHADE) campaign, Journal of Geophysical Research, 108, 8579, doi:10.1029/2002JD002566, 2003.

Nenes, A., Charlson, R. J., Facchini, M. C., Kulmala, M., Laaksonen, A., and Seinfeld, J. H.: Can chemical effects on cloud droplet number rival the first indirect effect?, Geophysical Research Letters, 29, 1848, doi:10.1029/2002gl015295, 2002.

Nyeki, S., Baltensperger, U., Colbeck, I., Jost, D. T., Weingartner, E., and Gaggeler, H. W.: The Jungfraujoch high-alpine research station (3454m) as a background clean continental site for the measurement of aerosol parameters, Journal of Geophysical Research, 103, 6097-6107, 1998.

O'Dowd, C., McFiggans, G., Creasey, D. J., Pirjola, L., Hoell, C., Smith, M. H., Allan, B. J., Plane, J. M. C., Heard, D. E., Lee, J. D., Pilling, M. J., and Kulmala, M.: On the photochemical production of new particles in the coastal boundary layer, Geophysical Research Letters, 26, 1707-1710, 1999.

O'Dowd, C. D., Hameri, K., Makela, J. M., Pirjola, L., Kulmala, M., Jennings, S. G., Berresheim, H., Hansson, H. C., de Leeuw, G., Kunz, G. J., Allen, A. G., Hewitt, C. N., Jackson, A., Viisanen, Y., and Hoffmann, T.: A dedicated study of new particle formation and fate in the coastal environment (PARFORCE): Overview of objectives and achievements, Journal of Geophysical Research, 107, 8108, doi:10.1029/2001JD000555, 2002.

O'Dowd, C. D., Jimenez, J. L., Bahreini, R., Flagan, R. C., Seinfeld, J. H., Hameri, K., Pirjola, L., Kulmala, M., Jennings, S. G., and Hoffmann, T.: Marine aerosol formation from biogenic iodine emissions, Nature, 417, 632-636, 2002.

Penner, J. E., Bergmann, D. J., Walton, J. J., Kinnison, D., Prather, M. J., Rotman, D., Price, C., Pickering, K. E., and Baughcum, S. L.: An evaluation of upper troposphere nox with two models, Journal of Geophysical Research, 103, 22097-22113, 1998.

Penner, J. E., Andreae, M. O., Annegarn, H., Barrie, L., Feichter, J., Hegg, D., Jayaraman, A., Leaitch, R., Murphy, D., Nganga, J., and Pitari, G.: Aerosols, their direct and indirect effects, in: Climate change 2001: The scientific basis, contribution of working group i to the third assessment report of the intergovernmental panel on climate change, edited by: Houghton, J. T., Ding, Y., Griggs, D. J., Noguer, M., Van der Linden, P. J., Dai, X., Maskell, K., and Johnson, C. A., Cambridge University Press, New York, 881, 2001.

Penner, J. E., Zhang, S. Y., Chin, M., Chuang, C. C., Feichter, J., Feng, Y., Geogdzhayev, I. V., Ginoux, P., Herzog, M., Higurashi, A., Koch, D., Land, C., Lohmann, U., Mishchenko, M., Nakajima, T., Pitari, G., Soden, B., Tegen, I., and Stowe, L.: A comparison of model- and satellite-derived aerosol optical depth and reflectivity, Journal of the Atmospheric Sciences, 59, 441-460, 2002.

Penner, J. E., Zhang, S. Y., and Chuang, C. C.: Soot and smoke aerosol may not warm climate, Journal of Geophysical Research, 108, 4657, doi:10.1029/2003JD003409, 2003.

Penner, J. E.: Climate change - the cloud conundrum, Nature, 432, 7020, 2004.

Penner, J. E., Quaas, J., Storelvmo, T., Takemura, T., Boucher, O., Guo, H., Kirkevag, A., Kristjansson, J. E., and Seland, O.: Model intercomparison of indirect aerosol effects, Atmospheric Chemistry and Physics, 6, 3391-3405, 2006.

Penner, J. E., Chen, Y., Wang, M., and Liu, X.: Possible influence of anthropogenic aerosols on cirrus clouds and anthropogenic forcing, Atmospheric Chemistry and Physics, 9, 879-896, 2009.

Petzold, A., and Schröder, F. P.: Jet engine exhaust aerosol characterization, Aerosol Science and Technology, 28, 62-76, 1998.

Pusechel, R. F., Blake, D. F., Snetsinger, K. G., Hansen, A. D. A., Verma, S., and Kato, K.: Black carbon (soot) aerosol in the lower stratosphere and upper troposphere, Geophysical Research Letters, 19, 1659-1662, 1992.

Phillips, V. T. J., DeMott, P. J., and Andronache, C.: An empirical parameterization of heterogeneous ice nucleation for multiple chemical species of aerosol, Journal of the Atmospheric Sciences, 65, 2757-2783, doi:10.1175/2007jas2546.1, 2008.

Pierce, J. R., and Adams, P. J.: Global evaluation of ccn formation by direct emission of sea salt and growth of ultrafine sea salt, Journal of Geophysical Research, 111, D06203, doi: 10.1029/2005JD006186, 2006.

Pierce, J. R., Chen, K., and Adams, P. J.: Contribution of primary carbonaceous aerosol to cloud condensation nuclei: Processes and uncertainties evaluated with a global aerosol microphysics model, Atmospheric Chemistry and Physics, 7, 5447-5466, 2007.

Pierce, J. R., and Adams, P. J.: Uncertainty in global ccn concentrations from uncertain aerosol nucleation and primary emission rates, Atmos. Chem. Phys., 9, 1339-1356, 2009.

Platnick, S., King, M. D., Ackerman, S. A., Menzel, W. P., Baum, B. A., Riedi, J. C., and Frey, R. A.: The MODIS cloud products: Algorithms and examples from TERRA, Ieee T Geosci Remote, 41, 459-473, 2003.

Prospero, J. M., Uematsu, M., and Savoie, D. L.: Mineral aerosol transport to the Pacific ocean, in: Chemical oceanography, edited by: Ridley, J. P., Chester, R., and Duce, R. A., Elsevier, New York, 188-218, 1989.

Pruppacher, H. R., and J. D. Klett: Microphysics of cloud and precipitation, Dordrecht, 954 pp., 1997.

Putaud, J., van Dingenen, R., Baltensperger, U., Bruggemann, E., Charron, A., Facchini, M., Decesari, S., Fuzzi, S., Gehrig, R., H.H.-C., Harrison, R. M., Jones, A. M., Laj, P., Lorbeer, G., Maenhaut, W., Mihalopoulos, N., M¨uller, K., Palmgren, F., Querol, X., Rodriguez, S., Schneider, J., Spindler, G., ten Brink, H., Tunved, P., Torseth, K., Wehner, B., Weingartner, E., Wiedensohler, A., Wahlin, P., and Raes, F.: A European

aerosol phenomenology, European Commission Joint Research Center, Ispra, Italy, EUR 20411 EN, 55, 2003.

Quaas, J., Boucher, O., and Breon, F. M.: Aerosol indirect effects in Polder satellite data and the Laboratoire de Meteorologie Dynamique-zoom (LMDZ) general circulation model, Journal of Geophysical Research, 109, D08205, doi: 10.1029/2003jd004317, 2004.

Quaas, J., Boucher, O., and Lohmann, U.: Constraining the total aerosol indirect effect in the LMDZ and ECHAM4 GCMs using MODIS satellite data, Atmospheric Chemistry and Physics, 6, 947-955, 2006.

Quaas, J., Boucher, O., Bellouin, N., and Kinne, S.: Satellite-based estimate of the direct and indirect aerosol climate forcing, Journal of Geophysical Research, 113, D05204, doi:10.1029/2007jd008962, 2008.

Quinn, P. K., Coffman, D. J., Kapustin, V. N., Bates, T. S., and Covert, D. S.: Aerosol optical properties in the marine boundary layer during the first aerosol characterization experiment (ACE 1) and the underlying chemical and physical aerosol properties, Journal of Geophysical Research, 103, 16547-16563, 1998.

Quinn, P. K., and Coffman, D. J.: Local closure during the first aerosol characterization experiment (ACE 1): Aerosol mass concentration and scattering and backscattering coefficients, Journal of Geophysical Research, 103, 16575-16596, 1998.

Quinn, P. K., and Coffman, D. J.: Comment on "Contribution of different aerosol species to the global aerosol extinction optical thickness: Estimates from model results" By Tegen et al., Journal of Geophysical Research, 104, 4241-4248, 1999.

Raes, F., VanDingenen, R., Cuevas, E., VanVelthoven, P. F. J., and Prospero, J. M.: Observations of aerosols in the free troposphere and marine boundary layer of the subtropical northeast Atlantic: Discussion of processes determining their size distribution, Journal of Geophysical Research, 102, 21315-21328, 1997.

Raes, F., Van Dingenen, R., Vignati, E., Wilson, J., Putaud, J. P., Seinfeld, J. H., and Adams, P.: Formation and cycling of aerosols in the global troposphere, Atmospheric Environment, 34, 4215-4240, 2000.

Ramanathan, V., and Collins, W.: Thermodynamic regulation of ocean warming by cirrus clouds deduced from observations of the 1987 El-Nino, Nature, 351, 27-32, 1991.

Ramanathan, V., Chung, C., Kim, D., Bettge, T., Buja, L., Kiehl, J. T., Washington, W. M., Fu, Q., Sikka, D. R., and Wild, M.: Atmospheric brown clouds: Impacts on south asian climate and hydrological cycle, Proceedings of the National Academy of Sciences of the United States of America, 102, 5326-5333, doi:10.1073/pnas.0500656102, 2005.

Ramaswamy, V., O. Boucher, J. Haigh, D. Hauglustaine, J. Haywood, G. Myhre, T. Nakajima, G.Y. Shi, S. Solomon: Radiative forcing of climate change, in: Climate change 2001: The scientifi c basis. Contribution of working group I to the third assessment report of the intergovernmental panel on climate change, edited by: Houghton, J. T., Y. Ding, D.J. Griggs, M. Noguer, P.J. van der Linden, X. Dai, K. Maskell, and C.A. Johnson, Cambridge University Press, 2001.

Randall, D. A., R.A. Wood, S. Bony, R. Colman, T. Fichefet, J. Fyfe, V. Kattsov, A. Pitman, J. Shukla, J. Srinivasan, R.J. Stouffer, A. Sumi and K.E. Taylor: Cilmate models and their evaluation, in: Climate change 2007: The physical science basis. Contribution of working group I to the fourth assessment report of the intergovernmental panel on climate change, edited by: Solomon, S., D. Qin, M. Manning, Z. Chen, M. Marquis, K.B. Averyt, M.Tignor and H.L. Miller, Cambridge University Press, Cambridge, United Kingdom and New York, NY, USA., 2007.

Rasch, P. J., and Kristjansson, J. E.: A comparison of the CCM3 model climate using diagnosed and predicted condensate parameterizations, Journal of Climate, 11, 1587-1614, 1998.

Rasch, P. J., Collins, W. D., and Eaton, B. E.: Understanding the Indian Ocean Experiment (INDOEX) aerosol distributions with an aerosol assimilation, Journal of Geophysical Research, 106, 7337-7355, 2001.

Raval, A., and Ramanathan, V.: Observational determination of the greenhouse-effect, Nature, 342, 758-761, 1989.

Read, W. G., Waters, J. W., Wu, D. L., Stone, E. M., Shippony, Z., Smedley, A. C., Smallcomb, C. C., Oltmans, S., Kley, D., Smit, H. G. J., Mergenthaler, J. L., and Karki, M. K.: Uars microwave limb sounder upper tropospheric humidity measurement: Method and validation, Journal of Geophysical Research, 106, 32207-32258, 2001.

Riipinen, I., Sihto, S. L., Kulmala, M., Arnold, F., Dal Maso, M., Birmili, W., Saarnio, K., Teinila, K., Kerminen, V. M., Laaksonen, A., and Lehtinen, K. E. J.: Connections between atmospheric sulphuric acid and new particle formation during QUEST III-IV campaigns in Heidelberg and Hyyti, Atmospheric Chemistry and Physics, 7, 1899-1914, 2007.

Rissler, J., Vestin, A., Swietlicki, E., Fisch, G., Zhou, J., Artaxo, P., and Andreae, M. O.: Size distribution and hygroscopic properties of aerosol particles from dry-season biomass burning in Amazonia, Atmospheric Chemistry and Physics, 6, 471-491, 2006.

Rosenfeld, D.: TRMM observed first direct evidence of smoke from forest fires inhibiting rainfall, Geophysical Research Letters, 26, 3105-3108, 1999.

Rosenfeld, D., and Woodley, W. L.: Deep convective clouds with sustained supercooled liquid water down to -37.5 degrees C, Nature, 405, 440-442, 2000.

Rossow, W. B., and Schiffer, R. A.: Advances in understanding clouds from ISCCP, Bulletin of the American Meteorological Society, 80, 2261-2287, 1999.

Rotman, D. A., Atherton, C. S., Bergmann, D. J., Cameron-Smith, P. J., Chuang, C. C., Connell, P. S., Dignon, J. E., Franz, A., Grant, K. E., Kinnison, D. E., Molenkamp, C. R., Proctor, D. D., and Tannahill, J. R.: Impact, the LLNL 3-D global atmospheric chemical transport model for the combined troposphere and stratosphere: Model description and analysis of ozone and other trace gases, Journal of Geophysical Research-Atmospheres, 109, D04303, doi:10.1029/2002jd003155, 2004.

Rotstayn, L. D., Ryan, B. F., and Katzfey, J. J.: A scheme for calculation of the liquid fraction in mixed-phase stratiform clouds in large-scale models, Monthly Weather Review, 128, 1070-1088, 2000.

Rotstayn, L. D., and Liu, Y. G.: Sensitivity of the first indirect aerosol effect to an increase of cloud droplet spectral dispersion with droplet number concentration, Journal of Climate, 16, 3476-3481, 2003.

Rotstayn, L. D., Cai, W. J., Dix, M. R., Farquhar, G. D., Feng, Y., Ginoux, P., Herzog, M., Ito, A., Penner, J. E., Roderick, M. L., and Wang, M. H.: Have Australian rainfall and cloudiness increased due to the remote effects of Asian anthropogenic aerosols?, Journal of Geophysical Research, 112, D09202, doi:10.1029/2006jd007712, 2007.

Salam, A., Lohmann, U., Crenna, B., Lesins, G., Klages, P., Rogers, D., Irani, R., MacGillivray, A., and Coffin, M.: Ice nucleation studies of mineral dust particles with a new continuous flow diffusion chamber, Aerosol Science and Technology, 40, 134-143, doi :10.1080/02786820500444853, 2006.

Sanderson, B. M., Piani, C., Ingram, W. J., Stone, D. A., and Allen, M. R.: Towards constraining climate sensitivity by linear analysis of feedback patterns in thousands of perturbed-physics GCM simulations, Climate Dynamics, 30, 175-190, 2008.

Savoie, D. L., Prospero, J. M., and Saltzman, E. S.: Nitrate, nonseasalt sulfate and methanesulfonate over the pacific ocean, in: Chemical oceanography, edited by: Ridley, J. P., Chester, R., and Duce, R. A., Elsevier, New York, 219-250, 1989.

Savoie, D. I., Prospero, J. M., Larsen, R. J., Huang, F., Izaguirre, M. A., Huang, T., Snowdon, T. H., Custals, L., and Sanderson, C. G.: Nitrogen and sulfur species in Antarctic aerosols at Mawson, Palmer station, and Marsh (King George Island), Journal of Atmospheric Chemistry, 17, 95-122, 1993.

Savoie, D. L., Arimoto, R., Keene, W. C., Prospero, J. M., Duce, R. A., and Galloway, J. N.: Marine biogenic and anthropogenic contributions to non-sea-salt sulfate in the marine boundary layer over the north Atlantic ocean, Journal of Geophysical Research-Atmospheres, 107, 4356, doi:10.1029/2001jd000970, 2002.

Schröder, F., Kärcher, B., Duroure, C., Ström, J., Petzold, A., Gayet, J. F., Strauss, B., Wendling, P., and Borrmann, S.: On the transition of contrails into cirrus clouds, Journal of the Atmospheric Sciences, 57, 464-480, 2000.

Schulz, M., Textor, C., Kinne, S., Balkanski, Y., Bauer, S., Berntsen, T., Berglen, T., Boucher, O., Dentener, F., Guibert, S., Isaksen, I. S. A., Iversen, T., Koch, D., Kirkevag, A., Liu, X., Montanaro, V., Myhre, G., Penner, J. E., Pitari, G., Reddy, S., Seland, O., Stier, P., and Takemura, T.: Radiative forcing by aerosols as derived from the aerocom present-day and pre-industrial simulations, Atmospheric Chemistry and Physics, 6, 5225-5246, 2006.

Schwarz, J. P., Gao, R. S., Fahey, D. W., Thomson, D. S., Watts, L. A., Wilson, J. C., Reeves, J. M., Darbeheshti, M., Baumgardner, D. G., Kok, G. L., Chung, S. H., Schulz, M., Hendricks, J., Lauer, A., Kärcher, B., Slowik, J. G., Rosenlof, K. H., Thompson, T. L., Langford, A. O., Loewenstein, M., and Aikin, K. C.: Single-particle measurements of midlatitude black carbon and light-scattering aerosols from the boundary layer to the lower stratosphere, Journal of Geophysical Research, 111, D16207, doi:10.1029/2006jd007076, 2006.

Seifert, M., Ström, J., Krejci, R., Minikin, A., Petzold, A., Gayet, J. F., Schumann, U., and Ovarlez, J.: In-situ observations of aerosol particles remaining from evaporated cirrus crystals: Comparing clean and polluted air masses, Atmospheric Chemistry and Physics, 3, 1037-1049, 2003.

Seinfeld, J. H., and Pandis, S. N.: Atmospheric chemistry and physics: From air pollution to climate change, John Wiely, Hoboken, N. J., 1998.

Sherwood, S.: A microphysical connection among biomass burning, cumulus clouds, and stratospheric moisture, Science, 295, 1272-1275, 2002.

Sihto, S. L., Kulmala, M., Kerminen, V. M., Dal Maso, M., Petaja, T., Riipinen, I., Korhonen, H., Arnold, F., Janson, R., Boy, M., Laaksonen, A., and Lehtinen, K. E. J.: Atmospheric sulphuric acid and aerosol formation: Implications from atmospheric measurements for nucleation and early growth mechanisms, Atmospheric Chemistry and Physics, 6, 4079-4091, 2006.

Singh, H. B., Anderson, B. E., Avery, M. A., Viezee, W., Chen, Y., Tabazadeh, A., Hamill, P., Pueschel, R., Fuelberg, H. E., and Hannan, J. R.: Global distribution and sources of volatile and nonvolatile aerosol in the remote troposphere, Journal of Geophysical Research, 107, 4121, doi:10.1029/2001JD000486, 2002.

Smith, W. L., Ackerman, S., Revercomb, H., Huang, H., DeSlover, D. H., Feltz, W., Gumley, L., and Collard, A.: Infrared spectral absorption of nearly invisible cirrus clouds, Geophysical Research Letters, 25, 1137-1140, 1998.

Smith, S. J., Pitcher, H., and Wigley, T. M. L.: Global and regional anthropogenic sulfur dioxide emissions, Global Planet Change, 29, 99-119, 2001.

Smith, S., Andres, R., Conception, L., and Lurz, J.: Historical sulfur dioxide emissions 1850-2000: Methods and resutls, JGCRI research report PNNL 14537, Pacific Northwest National Laboratory, Richland, WA, USA14537, 16, 2004.

Smith, J. N., Dunn, M. J., VanReken, T. M., Iida, K., Stolzenburg, M. R., McMurry, P. H., and Huey, L. G.: Chemical composition of atmospheric nanoparticles formed from nucleation in Tecamac, Mexico: Evidence for an important role for organic species in nanoparticle growth, Geophysical Research Letters, 35, L04808, doi:10.1029/2007gl032523, 2008.

Spichtinger, P., Gierens, K., and Read, W.: The global distribution of ice-supersaturated regions as seen by the microwave limb sounder, Quarterly Journal of the Royal Meteorological Society, 129, 3391-3410, 2003.

Spichtinger, P., Gierens, K., Smit, H. G. J., Ovarlez, J., and Gayet, J. F.: On the distribution of relative humidity in cirrus clouds, Atmospheric Chemistry and Physics, 4, 639-647, 2004.

Spichtinger, P., and Gierens, K. M.: Modelling of cirrus clouds – part 2: Competition of different nucleation mechanisms, Atmospheric Chemistry and Physics, 9, 2319-2334, 2009.

Spracklen, D. V., Pringle, K. J., Carslaw, K. S., Chipperfield, M. P., and Mann, G. W.: A global off-line model of size-resolved aerosol microphysics: I. Model development and prediction of aerosol properties, Atmospheric Chemistry and Physics, 5, 2227-2252, 2005.

Spracklen, D. V., Pringle, K. J., Carslaw, K. S., Chipperfield, M. P., and Mann, G. W.: A global off-line model of size-resolved aerosol microphysics: II. Identification of key uncertainties, Atmospheric Chemistry and Physics, 5, 3233-3250, 2005.

Spracklen, D. V., Carslaw, K. S., Kulmala, M., Kerminen, V. M., Mann, G. W., and Sihto, S. L.: The contribution of boundary layer nucleation events to total particle concentrations on regional and global scales, Atmospheric Chemistry and Physics, 6, 5631-5648, 2006.

Spracklen, D. V., Pringle, K. J., Carslaw, K. S., Mann, G. W., Manktelow, P., and Heintzenberg, J.: Evaluation of a global aerosol microphysics model against size-resolved particle statistics in the marine atmosphere, Atmospheric Chemistry and Physics, 7, 2073-2090, 2007.

Spracklen, D. V., Carslaw, K. S., Kulmala, M., Kerminen, V. M., Sihto, S. L., Riipinen, I., Merikanto, J., Mann, G. W., Chipperfield, M. P., Wiedensohler, A., Birmili, W., and Lihavainen, H.: Contribution of particle formation to global cloud condensation nuclei concentrations, Geophysical Research Letters, 35, L06808, doi:10.1029/2007GL033038, 2008.

Stephens, G. L., Tsay, S. C., Stackhouse, P. W., and Flatau, P. J.: The relevance of the microphysical and radiative properties of cirrus clouds to climate and climatic feedback, Journal of the Atmospheric Sciences, 47, 1742-1753, 1990.

Stier, P., Feichter, J., Kinne, S., Kloster, S., Vignati, E., Wilson, J., Ganzeveld, L., Tegen, I., Werner, M., Balkanski, Y., Schulz, M., Boucher, O., Minikin, A., and Petzold, A.: The aerosol-climate model ECHAM5-HAM, Atmospheric Chemistry and Physics, 5, 1125-1156, 2005.

Stier, P., Feichter, J., Kloster, S., Vignati, E., and Wilson, J.: Emission-induced nonlinearities in the global aerosol system: Results from the ECHAM5-HAM aerosol-climate model, Journal of Climate, 19, 3845-3862, 2006.

Stolzenburg, M. R., McMurry, P. H., Sakurai, H., Smith, J. N., Mauldin, R. L., Eisele, F. L., and Clement, C. F.: Growth rates of freshly nucleated atmospheric particles in atlanta, Journal of Geophysical Research, 110, D22S05, doi:10.1029/2005jd005935, 2005.

Storelvmo, T., Kristjansson, J. E., Ghan, S. J., Kirkevag, A., Seland, O., and Iversen, T.: Predicting cloud droplet number concentration in community atmosphere model (CAM)-Oslo, Journal of Geophysical Research, 111, D24208, doi:10.1029/2005jd006300, 2006.

Storelvmo, T., Kristjansson, J. E., and Lohmann, U.: Aerosol influence on mixed-phase clouds in CAM-Oslo, J Atmos Sci, 65, 3214-3230, doi:10.1175/2008jas2430.1, 2008.

Ström, J., and Heintzenberg, J.: Water-vapor, condensed water, and crystal concentration in orographically influenced cirrus clouds, Journal of the Atmospheric Sciences, 51, 2368-2383, 1994.

Ström, J., Strauss, B., Anderson, T., Schröder, F., Heintzenberg, J., and Wendling, P.: In situ observations of the microphysical properties of young cirrus clouds, Journal of the Atmospheric Sciences, 54, 2542-2553, 1997.

Ström, J., and Ohlsson, S.: In situ measurements of enhanced crystal number densities in cirrus clouds caused by aircraft exhaust, Journal of Geophysical Research, 103, 11355-11361, 1998.

Ström, J., and Ohlsson, S.: Real-time measurement of absorbing material in contrail ice using a counterflow virtual impactor, Journal of Geophysical Research, 103, 8737-8741, 1998.

Ström, J., Seifert, M., Kärcher, B., Ovarlez, J., Minikin, A., Gayet, J. F., Krejci, R., Petzold, A., Auriol, F., Haag, W., Busen, R., Schumann, U., and Hansson, H. C.: Cirrus cloud occurrence as function of ambient relative humidity: A comparison of observations obtained during the INCA experiment, Atmospheric Chemistry and Physics, 3, 1807-1816, 2003.

Suzuki, K., Nakajima, T., Numaguti, A., Takemura, T., Kawamoto, K., and Higurashi, A.: A study of the aerosol effect on a cloud field with simultaneous use of gcm modeling and satellite observation, Journal of the Atmospheric Sciences, 61, 179-194, 2004.

Takemura, T., Nozawa, T., Emori, S., Nakajima, T. Y., and Nakajima, T.: Simulation of climate response to aerosol direct and indirect effects with aerosol transport-radiation model, Journal of Geophysical Research, 110, D02202, doi:10.1029/2004JD005029, 2005.

Taylor, K. E., and Penner, J. E.: Response of the climate system to atmospheric aerosols and greenhouse gases, Nature, 369, 734-737, 1994.

Textor, C., Schulz, M., Guibert, S., Kinne, S., Balkanski, Y., Bauer, S., Berntsen, T., Berglen, T., Boucher, O., Chin, M., Dentener, F., Diehl, T., Easter, R., Feichter, H., Fillmore, D., Ghan, S., Ginoux, P., Gong, S., Kristjansson, J. E., Krol, M., Lauer, A., Lamarque, J. F., Liu, X., Montanaro, V., Myhre, G., Penner, J., Pitari, G., Reddy, S., Seland, O., Stier, P., Takemura, T., and Tie, X.: Analysis and quantification of the diversities of aerosol life cycles within AeroCom, Atmospheric Chemistry and Physics, 6, 1777-1813, 2006.

Tiedtke, M.: Representation of clouds in large-scale models, Monthly Weather Review, 121, 3040-3061, 1993.

Tompkins, A. M., Gierens, K., and Radel, G.: Ice supersaturation in the ECMWF integrated forecast system, Quarterly Journal of the Royal Meteorological Society, 133, 53-63, 2007.

Toon, O. B., Pollack, J. B., and Khare, B. N.: Optical-constants of several atmospheric aerosol species - ammonium-sulfate, aluminum-oxide, and sodium-chloride, J Geophys Res, 81, 5733-5748, 1976.

Twitty, J. T., and J. A. Weinman Radiative properties of carbonaceous aerosols, J. Appl. Meteorol., 10, 725-731, 1971.

Twohy, C. H., Clement, C. F., Gandrud, B. W., Weinheimer, A. J., Campos, T. L., Baumgardner, D., Brune, W. H., Faloona, I., Sachse, G. W., Vay, S. A., and Tan, D.: Deep convection as a source of new particles in the midlatitude upper troposphere, Journal of Geophysical Research, 107, 4560, doi:10.1029/2001JD000323, 2002.

Twomey, S.: Influence of pollution on shortwave albedo of clouds, Journal of the Atmospheric Sciences, 34, 1149-1152, 1977.

Vaattovaara, P., Huttunen, P. E., Yoon, Y. J., Joutsensaari, J., Lehtinen, K. E. J., O'Dowd, C. D., and Laaksonen, A.: The composition of nucleation and Aitken modes particles during coastal nucleation events: Evidence for marine secondary organic contribution, Atmospheric Chemistry and Physics, 6, 4601-4616, 2006.

Vallina, S. M., Simo, R., Gasso, S., De Boyer-Montegut, C., del Rio, E., Jurado, E., and Dachs, J.: Analysis of a potential "Solar radiation dose-dimethylsulfide-cloud condensation nuclei" link from globally mapped seasonal correlations, Global Biogeochemical Cycle, 21, GB2004, doi:10.1029/2006GB002787, 2007.

Van Dingenen, R., Raes, F., Putaud, J. P., Virkkula, A., and Mangoni, M.: Processes determining the relationship between aerosol number and non-sea-salt sulfate mass concentrations in the clean and perturbed marine boundary layer, Journal of Geophysical Research, 104, 8027-8038, 1999.

Vehkamäki, H., Kulmala, M., Napari, I., Lehtinen, K. E. J., Timmreck, C., Noppel, M., and Laaksonen, A.: An improved parameterization for sulfuric acid-water nucleation rates for tropospheric and stratospheric conditions, Journal of Geophysical Research, 107, 4622, doi:10.1029/2002JD002184, 2002.

Vehkamäki, H., Dal Maso, M., Hussein, T., Flanagan, R., Hyvarinen, A., Lauros, J., Merikanto, J., Monkkonen, P., Pihlatie, M., Salminen, K., Sogacheva, L., Thum, T., Ruuskanen, T. M., Keronen, P., Aalto, P. P., Hari, P., Lehtinen, K. E. J., Rannik, U., and Kulmala, M.: Atmospheric particle formation events at Varrio measurement station in Finnish Lapland 1998-2002, Atmospheric Chemistry and Physics, 4, 2015-2023, 2004.

Volkamer, R., Molina, L. T., Molina, M. J., Shirley, T., and Brune, W. H.: Doas measurement of glyoxal as an indicator for fast voc chemistry in urban air, Geophysical Research Letters, 32, L08806, doi:10.1029/2005gl022616, 2005.

von Salzen, K.: Piecewise log-normal approximation of size distributions for aerosol modelling, Atmos. Chem. Phys., 6, 1351-1372, 2006.

Waliser, D. E., Li, J. L. F., Woods, C. P., Austin, R. T., Bacmeister, J., Chern, J., Del Genio, A., Jiang, J. H., Kuang, Z. M., Meng, H., Minnis, P., Platnick, S., Rossow, W. B., Stephens, G. L., Sun-Mack, S., Tao, W. K., Tompkins, A. M., Vane, D. G., Walker, C., and Wu, D.: Cloud ice: A climate model challenge with signs and expectations of progress, Journal of Geophysical Research, 114, D00A21, doi:10.1029/2008JD010015 2009.

Walton, J. J., Maccracken, M. C., and Ghan, S. J.: A global-scale lagrangian trace species model of transport, transformation, and removal processes, Journal of Geophysical Research, 93, 8339-8354, 1988.

Wang, P. H., Minnis, P., McCormick, M. P., Kent, G. S., and Skeens, K. M.: A 6-year climatology of cloud occurrence frequency from Stratospheric Aerosol and Gas Experiment II observations (1985-1990), Journal of Geophysical Research, 101, 29407-29429, 1996.

Wang, Y. H., Jacob, D. J., and Logan, J. A.: Global simulation of tropospheric o-3-nox-hydrocarbon chemistry 1. Model formulation, Journal of Geophysical Research, 103, 10713-10725, 1998.

Wang, M., and Penner, J. E.: Aerosol indirect forcing in a global model with particle nucleation, Atmospheric Chemistry and Physics, 9, 239-260, 2009.

Wanninkhof, R.: Relationship between wind-speed and gas-exchange over the ocean, Journal of Geophysical Research-Oceans, 97, 7373-7382, 1992.

Webb, M., Senior, C., Bony, S., and Morcrette, J. J.: Combining erbe and isccp data to assess clouds in the hadley centre, ECMWF and LMD atmospheric climate models, Climate Dynamics, 17, 905-922, 2001.

Weisenstein, D. K., Penner, J. E., Herzog, M., and Liu, X.: Global 2-D intercomparison of sectional and modal aerosol modules, Atmospheric Chemistry and Physics, 7, 2339-2355, 2007.

Weng, F. Z., and Grody, N. C.: Retrieval of cloud liquid water using the special sensor microwave imager (SSM/I), J Geophys Res, 99, 25535-25551, 1994.

Wesely, M. L., Cook, D. R., Hart, R. L., and Speer, R. E.: Measurements and parameterization of particulate sulfur dry deposition over grass, Journal of Geophysical Research, 90, 2131-2143, 1985.

Whitby, K. T.: Physical characteristics of sulfur aerosols, Atmospheric Environment, 12, 135-159, 1978.

Whitby, K. T., Cantrell, B. K., and Kittelson, D. B.: Nuclei formation rates in a coal-fired power-plant plume, Atmospheric Environment, 12, 313-321, 1978.

Williamson, D. L.: Time-split versus process-split coupling of parameterizations and dynamical core, Monthly Weather Review, 130, 2024-2041, 2002.

Wilson, J., Cuvelier, C., and Raes, F.: A modeling study of global mixed aerosol fields, Journal of Geophysical Research, 106, 34081-34108, 2001.

Wolff, E. W., and Cachier, H.: Concentrations and seasonal cycle of black carbon in aerosol at a coastal Antarctic station, Journal of Geophysical Research, 103, 11033-11041, 1998.

Wu, X. Q.: Effects of ice microphysics on tropical radiative-convective-oceanic quasi-equilibrium states, Journal of the Atmospheric Sciences, 59, 1885-1897, 2002.

Wu, D. L., Jiang, J. H., and Davis, C. P.: EOS MOS cloud ice measurements and cloudy-sky radiative transfer model, Ieee T Geosci Remote, 44, 1156-1165, 2006.

Wu, D. L., Austin, R. T., Deng, M., Durden, S. L., Heymsfield, A. J., Jiang, J. H., Lambert, A., Li, J.-L., Livesey, N. J., McFarquhar, G. M., Pittman, J. V., Stephens, G. L., Tanelli, S., Vane, D. G., and Waliser, D. E.: Comparisons of global cloud ice from mls, cloudsat, and correlative data sets, Journal of Geophysical Research, 114, D00A24, doi:10.1029/2008JD009946, 2009.

Wylie, D. P., and Menzel, W. P.: Eight years of high cloud statistics using HIRS, Journal of Climate, 12, 170-184, 1999.

Xie, S. C., Boyle, J., Klein, S. A., Liu, X. H., and Ghan, S.: Simulations of arctic mixed-phase clouds in forecasts with CAM3 and AM2 for M-Pace, Journal of Geophysical Research-Atmospheres, 113, D04211, doi: 10.1029/2007JD009225 2008.

Yoon, Y. J., Ceburnis, D., Cavalli, F., Jourdan, O., Putaud, J. P., Facchini, M. C., Decesari, S., Fuzzi, S., Sellegri, K., Jennings, S. G., and O'Dowd, C. D.: Seasonal characteristics of the physicochemical properties of north Atlantic marine atmospheric aerosols, Journal of Geophysical Research, 112, D04206, doi:10.1029/2005jd007044, 2007.

Yu, F. Q., and Turco, R. P.: Ultrafine aerosol formation via ion-mediated nucleation, Geophysical Research Letters, 27, 883-886, 2000.

Yu, F.: From molecular clusters to nanoparticles: Second-generation ion-mediated nucleation model, Atmospheric Chemistry and Physics, 6, 5193-5211, 2006.

Yu, F., and Turco, R.: Case studies of particle formation events observed in boreal forests: Implications for nucleation mechanisms, Atmos. Chem. Phys., 8, 6085-6102, 2008.

Yu, F., Wang, Z., Luo, G., and Turco, R.: Ion-mediated nucleation as an important global source of tropospheric aerosols, Atmospheric Chemistry and Physics, 8, 2537-2554, 2008.

Zhang, G. J., and Mcfarlane, N. A.: Sensitivity of climate simulations to the parameterization of cumulus convection in the Canadian climate center general-circulation model, Atmosphere-Ocean, 33, 407-446, 1995.

Zhang, K. M., and Wexler, A. S.: A hypothesis for growth of fresh atmospheric nuclei, Journal of Geophysical Research, 107, 4577, doi:10.1029/2002jd002180, 2002.

Zhang, M. H., Lin, W. Y., Bretherton, C. S., Hack, J. J., and Rasch, P. J.: A modified formulation of fractional stratiform condensation rate in the NCAR community atmospheric model (CAM2), Journal of Geophysical Research, 108, 4035, doi: 10.1029/2002JD002523, 2003.

Zhang, R. Y., Suh, I., Zhao, J., Zhang, D., Fortner, E. C., Tie, X. X., Molina, L. T., and Molina, M. J.: Atmospheric new particle formation enhanced by organic acids, Science, 304, 1487-1490, 2004.

Zhang, S., Penner, J. E., and Torres, O.: Inverse modeling of biomass burning emissions using total ozone mapping spectrometer aerosol index for 1997, Journal of Geophysical Research, 110, D21306, doi:10.1029/2004JD005738, 2005.

Zhang, R. Y., Li, G. H., Fan, J. W., Wu, D. L., and Molina, M. J.: Intensification of pacific storm track linked to Asian pollution, Proceedings of the National Academy of Sciences of the United States of America, 104, 5295-5299, doi:10.1073/pnas.0700618104, 2007.

Zobrist, B., Koop, T., Luo, B. P., Marcolli, C., and Peter, T.: Heterogeneous ice nucleation rate coefficient of water droplets coated by a nonadecanol monolayer, Journal of Physical Chemistry C, 111, 2149-2155, doi:10.1021/Jp066080w, 2007.

Zuberi, B., Bertram, A. K., Cassa, C. A., Molina, L. T., and Molina, M. J.: Heterogeneous nucleation of ice in (nh4)(2)so4-h2o particles with mineral dust immersions, Geophysical Research Letters, 29, 1504, doi:10.1029/2001gl014289, 2002.